

Trace metal sources and cycling in tropical oxygen minimum zones



Dissertation

vorgelegt von

Insa Rapp

zur Erlangung des akademischen Grades eines Doktors der
Naturwissenschaften

– **Dr. rer. nat** –

an der Mathematisch-Naturwissenschaftlichen Fakultät
der Christian-Albrechts-Universität zu Kiel

Kiel, Mai 2018

Photo credit: Gert van Dijken

1. Gutachter: Prof. Eric P. Achterberg
2. Gutachter: Prof. Martin Frank

Tag der mündlichen Prüfung: 19.09.2018

Abstract

Iron (Fe) and a suite of other trace metals (TMs) are bioessential nutrients in the ocean and their availability in seawater can control both the growth rate and community structure of phytoplankton. Seawater oxygen concentrations have a strong influence on TM biogeochemical cycling by modulating both their supply from sediments and their stability in seawater; this is particularly important for redox-sensitive elements such as Fe. Regions of the ocean with suboxic ($<70 \mu\text{mol L}^{-1} \text{O}_2$) or anoxic ($0 \mu\text{mol L}^{-1} \text{O}_2$) conditions, so called oxygen minimum zones (OMZs), are present at tropical eastern boundary regions of both the Pacific and Atlantic Oceans. These OMZs have expanded in extent and intensity over the past five decades. Such changes are likely to result in major feedbacks on Earth's biogeochemical cycles, but these are difficult to predict due to a lack of supporting observations accompanying OMZ expansion, and the chain of complex processes typically involved in regulating these feedbacks. Because TMs are ocean nutrients, improving our understanding of the impact of OMZ changes on biogeochemical cycles requires detailed investigations of TM sources, sinks and internal cycling in OMZs. The third chapter of this thesis presents a new, accurate, high-throughput method for the simultaneous analysis of a range of seawater TM concentrations at (ultra-)trace levels using isotope dilution for Fe, cadmium (Cd), nickel (Ni), zinc (Zn), copper (Cu) and lead (Pb), and standard addition for cobalt (Co) and manganese (Mn). In the subsequent two chapters this method is employed to investigate TM cycling in two OMZs, one in the Eastern Tropical North Atlantic (ETNA) off the coast of Mauritania, and one in the Eastern Tropical South Pacific (ETSP) off the coast of Peru. Measurements of dissolved and leachable particulate TM fractions revealed a large influence of oxygen concentrations on the distribution of the redox-sensitive elements Fe, Co and Mn. Specifically, seawater concentrations of these TMs were substantially enhanced under reduced oxygen conditions. The contrasting behaviour of these redox-sensitive metals relative to other TMs with so-called 'nutrient-like' behaviour (e.g. Cd, Ni, Zn) emphasized the importance of redox-regulated processes (such as sediment release and oxidation rates) over changes in biological uptake and remineralization in controlling their distributions. In the ETNA, supporting aluminium data (a tracer for dust input), confirmed the dominance of a benthic Fe source over atmospheric deposition sources close to the continental shelf. In the ETSP, supporting concentration measurements of the reduced Fe species (Fe(II)), also revealed a marked

Abstract

shift in the redox speciation of total dissolved Fe towards Fe(III) under elevated oxygen conditions on the shelf. Sample collection in the ETSP serendipitously occurred during a strong, on-going El Niño event. This accentuated spatial variability in oxygen content in the ETSP relative to typical conditions, with much enhanced seawater oxygenation over the North Peruvian coast. This oxygenation was matched by large reductions in concentrations of redox-sensitive TMs. Despite the clear association of redox-sensitive TMs with broad scale patterns in oxygenation in both study regions, a direct correlation between the concentration of these TMs and oxygen was not observed. Furthermore, the two study regions appeared to reveal differences in TM response to oxygen concentrations. Such variability can be attributed to other factors influencing TM distributions in addition to oxygen, including variations in source terms (e.g. atmospheric dust deposition), differences in continental shelf bathymetry and sediment characteristics (e.g. shelf width and organic carbon content), and variations in the amount and type of particles present in the water column that scavenge and/or supply TMs at different rates. The findings in this thesis point towards expanding OMZs enhancing the supply of redox-sensitive TMs to waters over associated continental shelves, with a potential for ensuing biological impacts. However, such changes could be strongly modulated by coincident changes in frequency and intensity of shorter-lived ocean circulation changes (e.g. ENSO), coincident variability in other parts of oceanic TM cycles, and overall changes in the vertical supply rate of TMs from the seawaters overlying the shelf upwards into the sunlit surface ocean.

Zusammenfassung

Eisen (Fe) und eine Reihe anderer Spurenmetalle sind essentielle Nährstoffe im Ozean und ihre Verfügbarkeit kann sowohl die Wachstumsrate als auch die Gemeinschaftsstruktur von Phytoplankton kontrollieren. Sauerstoffkonzentrationen im Meer haben einen starken Einfluss auf den biogeochemischen Kreislauf von Spurenmetallen, indem sie sowohl ihre Freisetzung aus Sedimenten als auch ihre Stabilität im Meerwasser modulieren. Dies ist besonders wichtig für redox-sensitive Elemente wie Fe. Regionen des Ozeans mit suboxischen ($<70 \mu\text{mol L}^{-1} \text{O}_2$) oder anoxischen ($0 \mu\text{mol L}^{-1} \text{O}_2$) Bedingungen, sogenannten Sauerstoffminimumzonen (OMZs), sind in den tropischen östlichen Grenzregionen des pazifischen und atlantischen Ozeans vorhanden. Diese OMZs haben in den letzten fünf Jahrzehnten in Umfang und Intensität zugenommen. Solche Veränderungen werden wahrscheinlich einen großen Einfluss auf die biogeochemischen Kreisläufe der Erde haben. Da es nicht genügend beobachtende Daten in sich ausbreitenden OMZs gibt und die Kette der beteiligten Prozesse sehr komplex ist, sind die genauen Einflüsse jedoch schwer vorherzusagen. Da Spurenmetalle wichtige Nährstoffe im Ozean sind, müssen zur Verbesserung unseres Verständnisses der Auswirkungen von OMZ Veränderungen auf biogeochemische Kreisläufe detaillierte Untersuchungen von Spurenmetall-Quellen, -Senken und internen Kreisläufen in OMZs durchgeführt werden. Das dritte Kapitel dieser Arbeit stellt eine neue, präzise Hochdurchsatzmethode für die simultane Analyse einer Reihe von Meerwasser-Spurenmetall-Konzentrationen im (Ultra-)Spurenbereich unter Verwendung von Isotopenverdünnung für Fe, Cadmium (Cd), Nickel (Ni), Zink (Zn), Kupfer (Cu) und Blei (Pb) und Standardaddition für Cobalt (Co) und Mangan (Mn) vor. In den folgenden zwei Kapiteln wird diese Methode zur Untersuchung von Spurenmetall-Kreisläufen in zwei OMZs eingesetzt, einer im östlichen tropischen Nordatlantik (ETNA) vor der Küste Mauretaniens und einer im östlichen tropischen Südpazifik (ETSP) vor der Küste Perus. Messungen von gelösten und säurelöslichen partikulären Spurenmetall-Fractionen zeigten einen großen Einfluss von Sauerstoffkonzentrationen auf die Verteilung der redox-sensitiven Elemente Fe, Co und Mn. Insbesondere waren die Meerwasserkonzentrationen dieser Spurenmetalle unter reduzierten Sauerstoffbedingungen stark erhöht. Ein gegensätzliches Verhalten dieser redox-sensitiven Metalle gegenüber anderen Spurenmetallen, mit sogenanntem "nährstoffähnlichem" Verhalten (z. B. Cd, Ni, Zn),

Zusammenfassung

unterstrich die Bedeutung redoxregulierter Prozesse (z. B. Sedimentfreisetzung und Oxidationsraten) gegenüber Veränderungen in der biologischen Aufnahme und Remineralisierung. In der ETNA bestätigten unterstützende Aluminiumdaten (ein Tracer für Staubeintrag) die Dominanz einer benthischen Fe-Quelle gegenüber atmosphärischen Quellen in der Nähe des Schelfs. In der ETSP zeigten unterstützende Konzentrationsmessungen der reduzierten Fe-Spezies (Fe(II)) ebenfalls eine deutliche Verschiebung der Redox-Speziation des gesamten gelösten Fe zu Fe (III) unter erhöhten Sauerstoffbedingungen am Schelf. Die Probenahme in der ETSP erfolgte zufällig während eines starken El Niño Ereignisses. Dieses bewirkte eine räumliche Veränderung des Sauerstoffgehalts im ETSP mit stark erhöhter Meerwasseroxygenierung über der nordperuanischen Küste im Vergleich zu typischen Bedingungen. Diese Oxygenierung bewirkte eine starke Reduktion der Konzentrationen von redox-sensitiven Spurenmetallen. Trotz der eindeutigen Assoziation von redox-sensitiven Spurenmetallen mit Mustern in der Oxygenierung in beiden Studienregionen, wurde keine direkte Korrelation zwischen der Konzentration dieser Spurenmetalle und Sauerstoff beobachtet. Darüber hinaus schienen die beiden Studienregionen Unterschiede in der Reaktion von Spurenmetallen auf Sauerstoffkonzentrationen aufzuzeigen. Eine solche Variabilität kann auf andere Faktoren zurückgeführt werden, die die Spurenmetall-Verteilungen zusätzlich beeinflussen. Solche Faktoren sind unter anderen Variationen der Quellterme (z. B. atmosphärische Quellen), Unterschiede in Schelf-Bathymetrie und Sedimentcharakteristika (z. B. Schelfbreite und organischer Kohlenstoffgehalt), sowie Variationen der Menge und Art der in der Wassersäule vorhandenen Partikel, die Spurenmetalle in unterschiedlichem Maße abfangen oder abgeben können. Die Ergebnisse dieser Arbeit deuten auf einen starken Einfluss der Ausdehnung von OMZs hin, welche die Versorgung der Gewässer über dem assoziierten Schelf mit redox-sensitiven TMs erhöht, was möglicherweise große biologische Auswirkungen mit sich bringt. Solche Änderungen könnten jedoch stark durch gleichzeitige Änderungen der Häufigkeit und Intensität kurzlebigerer Veränderungen der Ozeanzirkulation (z. B. ENSO), durch gleichzeitige Schwankungen in anderen Teilen ozeanischer Spurenmetall-Kreisläufen, sowie durch Änderungen der vertikalen Zufuhr rate von Spurenmetallen über dem Schelf nach oben in den sonnenbeschienenen Ozean, moduliert werden.

Acknowledgements

I firstly want to thank my supervisors Eric Achterberg, Christian Schlosser and Martha Gledhill for their guidance, advice and support and for giving me the opportunity to work on an amazing project. This work was only possible through the financial support and resources from GEOMAR, and in particular the collaborative research centre 754 funded by the DFG. I would also like to express my gratitude to ISOS and the CAU Graduate Centre for the opportunity to participate at international conferences by providing travel grants. I also thank the GEOTRACES programme for selecting me to participate in the eye-opening 2017 summer school in Brest.

I would like to thank Peter, Lea and Fabian for their help in the lab and Joaquin for his assistance on my first research cruise. I am very grateful to Birgit and Chris Schelten for their administrative assistance during this project. I am also grateful to Ulrike Westernströer and Institute for Geoscience (Kiel University) for letting us use their ICP-MS before our Element XR was installed at GEOMAR.

I thank the Captains and crew from RV New Horizon (cruise NH1417), RV Sonne (cruise SO243) and RV Meteor (cruise M107) for supporting this research project. In addition chief scientists Mathew Mills and Irina Shilova (NH1417), Stephan Sommer (M107), and Christa Marandino, Tobias Steinhoff and Damian Grundle (SO243) are thanked.

I would like to thank cruise participants that went out of their way to help me on cruises, in particular Emily and Brett for their extensive help with trace metal sampling on NH1417 and Fred on SO243.

I have greatly benefitted from discussion with many colleagues of my working group. Particularly Mark and Tom - thanks for insightful comments and sharing your knowledge. Special thanks to Tom also for helping me to make nice figures in R, proof reading and his patience!

I thank my peer PhD candidates, and in particular my office and clean lab mates Jan-Lukas and Dag who have been there since the beginning! We shared a lot of good times, as well as times of frustration when our instruments where not working or dealing with contamination issues and during thesis writing.

Thanks to Kathrin, Dag, Anna, Jen, Tom, Fred, Jon, Mark, Nick, Matt P., Pablo, Concha, JC, Jean, Lucia, Jan-Lukas, Mario, Ruifang, Brad, Nina, Anja, Ulli, Matthias, Chris and many more great people I met during my PhD for support and all the good times I had and for making the four years in Kiel so much fun!

Finally I would like to thank my family and friends from home who have offered me support during my PhD and came for lots of visits to make my time even greater!

Contents

Abstract	i
Zusammenfassung	iii
Acknowledgements	v
List of Figures	xi
List of Tables.....	xii
1 Introduction.....	1
1.1 Trace metal sources	3
1.2 Trace metal distributions	7
1.2.1 Scavenging.....	8
1.3 Trace metal speciation.....	9
1.3.1 Redox speciation.....	9
1.3.2 Inorganic and organic complexation.....	11
1.4 Characteristics of study areas	13
1.4.1 Upwelling.....	16
1.4.2 Study regions	18
1.5 Thesis objectives and outline.....	19
2 Sample collection and analysis	23
2.1 Plastics and other materials	23
2.2 Operationally defined trace metal fractions	24
2.3 Sampling.....	25
2.4 Trace metal analysis	27
2.4.1 Multielement analysis by ICP-MS after sample preconcentration	27
2.4.2 Chemiluminescence flow injection analysis of Fe(II) and H ₂ O ₂	29
2.5 Stability of the soluble trace metal fraction.....	32
2.6 Iodide and Iodate analysis	34
3 Automated preconcentration of Fe, Zn, Cu, Ni, Cd, Pb, Co, and Mn in seawater with analysis using high-resolution sector field inductively-coupled plasma mass spectrometry	39
Abstract.....	41
3.1 Introduction	43
3.2 Experimental.....	45

Contents

3.2.1 Reagents for sample pre-concentration	45
3.2.2 Spike solutions.....	46
3.2.3 Seawater sample preparation	47
3.2.4 Preconcentration set-up	48
3.2.5 Resins for preconcentration	50
3.2.6 Preconcentration and extraction	50
3.2.7 Blanks	52
3.2.8 ICP-MS	53
3.2.9 Calculation of elemental concentration and uncertainties	54
3.2.10 Reference Material	56
3.3 Results and Discussion.....	57
3.3.1 UV-digestion	57
3.3.2 Recovery and pH	59
3.3.3 Sample carry-over.....	65
3.3.4 Linearity.....	67
3.3.5 Procedural blanks and detection limits	69
3.3.6 Precision and accuracy	70
3.3.7 Environmental Application—vertical oceanic profiles	71
3.4 Conclusion.....	73
4 Controls on redox-sensitive trace metals in the Mauritanian oxygen minimum zone ..	75
Abstract	77
4.1 Introduction	79
4.2 Methods.....	82
4.2.1 Sampling.....	82
4.2.2 Trace metal analysis	83
4.2.3 Aluminum measurements	84
4.2.4 Iodide measurements	85
4.2.5 Oxygen and nutrient analysis	85
4.2.6 Radium analysis.....	86
4.2.7 Turbulence measurements and vertical flux calculations.....	86
4.3 Results & Discussion	89
4.3.1 Oceanographic settings of the study area	89
4.3.2 Spatial distribution of dissolved and leachable particulate trace metals	93

Contents

4.3.3 Classification of different groups of trace metals based on principle component analysis.....	100
4.3.4 Influence of the different sources of Fe, Mn and Co	102
4.3.5 Removal mechanisms and particle interactions.....	109
4.3.6 Temporal variability in redox sensitive trace metals	112
4.4 Conclusion.....	119
5 El Niño reduces Peruvian shelf trace metal supply to the ocean	121
Abstract.....	123
5.1 Introduction	125
5.2 Methods	126
5.2.1 Sampling	126
5.2.2 Trace metal analysis.....	127
5.2.3 Iodide/Iodate analysis	129
5.2.4 Oxygen and nutrient analysis.....	130
5.3 Results & Discussion.....	130
5.4 Conclusion.....	140
6 Conclusions and future directions.....	143
6.1 Summary.....	143
6.2 Comparison of the two study regions	145
6.2.1 Additional TM inputs.....	148
6.2.2 Sediment release	149
6.2.3 Physical transport.....	153
6.2.4 Primary productivity and remineralization	153
6.2.5 Removal rates	154
6.3 Predicting long term effects of ocean deoxygenation on TM distributions	155
6.4 Future directions	157
References	163
Appendix	187
Statement of declaration.....	191
Curriculum Vitae.....	193

List of Figures

Figure 1.1: Schematic of major sources and sinks of TMs in the ocean.....	4
Figure 1.2: The dominant Fe sources to the integrated water column Fe budget as simulated using an ocean biogeochemical model	6
Figure 1.3: Simplified schematic of the cycling of Fe between different species and size fractions in the euphotic zone and the deep ocean after aerosol deposition	13
Figure 1.4: Oxygen minimum zones and their biogeochemical settings	15
Figure 1.5: Schematic of the Ekman spiral and coastal upwelling	17
Figure 2.1: Structure of the CM-PEHA resin.....	28
Figure 2.2: Schematic diagram of a sector-field ICP-MS.....	29
Figure 2.3: Simplified Fe(II) system scheme showing the reagent flow path and alternating valve positions.....	30
Figure 2.4: Test for soluble Fe filtration	34
Figure 3.1: Schematic set-up of SeaFAST system and valve positions.....	49
Figure 3.2: UV digestion efficiency experiment for Co and Cu with Southern Ocean water	58
Figure 3.3: Count rates (cps) for the most abundant isotope of Cd, Pb, Fe, Ni, Cu, Zn, Co and Mn in North Pacific seawater	61
Figure 3.4: Isotope ratios obtained for Cd, Pb, Fe, Ni, Cu and Zn (natural isotopic composition) over a pH range employed during preconcentration	63
Figure 3.5: Carry-over of metals from an enriched North Pacific seawater sample to five following manifold blanks using a WAKO and a NOBIAS resin for preconcentration...	67
Figure 3.6: Linear regressions for high concentrated standard additions	69
Figure 3.7: Depth profiles of eight trace metals.....	73
Figure 4.1: Map of the study area	91
Figure 4.2: Section plots of oxygen, salinity, nitrate and phosphate along the transect off the Mauritanian coast in June 2014.....	93
Figure 4.3: Spatial distributions of dissolved and leachable particulate trace metals and $^{224}\text{Ra}/^{223}\text{Ra}$ across the Mauritanian shelf at 18°20'N in June 2014	98
Figure 4.4: Principle component analysis of the Mauritanian shelf data set	101
Figure 4.5: Dissolved TM concentrations against oxygen for Fe, Mn and Co	102

List of Figures and Tables

Figure 4.6: Distributions of TMs between dissolved and leachable particulate phase and compared to turbidity	112
Figure 4.7: Repeated stations: oxygen concentration, turbidity and dissolved trace metals (Fe, Mn and Co) and temperature vs salinity plots	114
Figure 4.8: Depth profiles of dCd and nitrate (NO_3^-) of repeated stations	115
Figure 4.9: Repeated stations: oxygen concentration, dissolved and LpAl	117
Figure 5.1: Map of sampling sites along the four cross-shelf transects	131
Figure 5.2: Elevated dissolved Fe concentrations under reducing conditions	132
Figure 5.3: Oxygen and (micro)nutrient density distributions	133
Figure 5.4: Oxygen and Fe profiles at on- and off shore stations	135
Figure 5.5: Oxygen, dissolved trace metals (dFe, dCo, dMn, dCd, dNi, dCu and dZn), phosphate (PO_4) and silicic acid (Si) density profiles of the five onshore stations	137
Figure 5.6: Oxygen, dissolved trace metals (dFe, dCo, dMn, dCd, dNi, dCu and dZn), phosphate (PO_4) and silicic acid (Si) density profiles of four offshore stations	138
Figure 5.7: Depth profiles of nitrogen ($\text{NO}_3 + \text{NO}_2$) to Fe ratios along the four transects	140
Figure 6.1: Comparison of TM (Fe, Co and Mn) distribution of the two study regions	146
Figure 6.2: Density plots of redox-sensitive TMs (LpFe, dFe, dCo, dMn), macronutrients (silicic acid and phosphate) and nutrient-like TMs (dNi and dCd) for all data from the Mauritanian OMZ and the Peruvian OMZ	148

List of Tables

Table 2.1: Method settings for analysis of iodide by cathodic stripping square wave voltammetry	36
Table 3.1: Steps of the preconcentration procedure	51
Table 3.2: ICP-MS instrumentation and settings	53
Table 3.3: Recoveries obtained for Cd, Pb, Fe, Ni, Cu, Zn, Co and Mn using a WAKO resin with sample preconcentration pH 6.2 and 7.0 and a NOBIAS resin at pH 6.1	64
Table 3.4: Values for manifold and buffer blanks (± 1 standard deviation of repeated measurements) as well as combined blank with resulting detection limits (three times the standard deviation of the blank: $3 \times \text{SD}$)	70

List of Figures and Tables

Table 3.5: Analyzed reference seawater. Mean values and standard deviation in nmol L ⁻¹ for Cd, Pb, Fe, Ni, Cu, Zn, Mn and Co and available consensus values in nmol L ⁻¹ (\pm 1 standard deviation), n = number of measurements.	71
Table 4.1: Atmospheric and vertical fluxes of dFe	109
Table 4.2: Vertical fluxes of LpFe and dCo.....	109
Table 4.4: TM/Al ratios of different fractions for the repeated deployments at station 3 within the OMZ below 50 m water depth.	118

1 Introduction

Trace metals (TMs) are present in the oceans at very low concentrations of a few pmol L^{-1} to nmol L^{-1} , and some TMs are essential micronutrients for phytoplankton (Bruland and Lohan, 2006). Phytoplankton are free-floating, mostly single celled photosynthetic organisms, and contribute to approximately 50% of global primary production (Field et al., 1998) that fuels marine food webs and plays an important role in atmospheric CO_2 sequestration by the oceans (Falkowski et al., 1998). Trace metals required by phytoplankton include iron (Fe), manganese (Mn), cobalt (Co), zinc (Zn), cadmium (Cd), nickel (Ni) and copper (Cu) (Morel and Price, 2003). For example, Fe is key component in photosystems I and II (PSI and PSII) involved in photosynthetic electron transport, and nitrite and nitrate reductase, two key enzymes in the nitrogen cycle (Morel and Price, 2003). Mn is utilized in the oxygen-evolving complex of PSII, which oxidizes water to O_2 (Morel et al., 2003). Co can be a cofactor in the carbonic anhydrase enzyme catalysing the conversion of bicarbonate to carbon dioxide, and as a metal centre in cyanocobalamin (vitamin B_{12}) (Morel et al., 2003; Panzeca et al., 2008).

Low concentrations of these essential elements in seawater can result in limitation of phytoplankton growth, with Fe limitation directly demonstrated in parts of the world's oceans with elevated concentrations of the macronutrients nitrate and phosphate but depleted Fe levels; specifically the North and Equatorial Pacific, the high latitude North Atlantic, and the Southern Ocean (Boyd et al., 2007; Ryan-Keogh et al., 2013). In regions of the ocean where phytoplankton are not limited by Fe, for example in the majority of the subtropical oceans, phytoplankton appear to be limited by biologically accessible nitrogen (Moore et al., 2013). A major input of biologically accessible

Chapter 1: Introduction

nitrogen, in addition to riverine and atmospheric inputs, is the fixation of N_2 by marine nitrogen fixing bacteria—diazotrophs (Gruber and Sarmiento, 1997). Diazotrophy, in turn, requires a relatively large amount of Fe for the N_2 fixing enzyme ‘nitrogenase’ and particularly Fe-rich photosystems (Berman-Frank et al., 2001). Because of its role in directly limiting phytoplankton growth in some regions of the ocean, and indirectly regulating growth via N_2 fixation in others, Fe is a crucial factor influencing both marine carbon and nitrogen cycles (Falkowski, 1997). In addition to roles as micronutrients, some TMs, such as Cu or Cd, can be toxic to life at high concentrations (Morel and Price, 2003) or be environmental pollutants (e.g. Pb; Boyle et al., 2014).

This PhD thesis presents an investigation into the biogeochemical cycling of TMs in regions with low (suboxic to anoxic) subsurface dissolved oxygen concentrations that are referred to as ‘oxygen minimum zones’ (OMZs). Surface sediments of the continental shelves that can underlie OMZs have been demonstrated to be an important source of Fe and other TMs, such as Co and Mn, to overlying waters and adjacent ocean regions (e.g. Elrod et al., 2004; Noffke et al., 2012; Pakhomova et al., 2007; Sundby et al., 1986). OMZs have been projected to expand in the future (Schmidtko et al., 2017; Stramma et al., 2008b; Stramma et al., 2009), with potential consequences for the supply and cycling of TMs in the ocean. The major aims of this PhD project were two-fold. Firstly, a new method was developed and extensively tested for accurate and high-throughput analysis of TM concentrations in seawater. Secondly, the method was applied to seawater samples collected on two cruises in OMZs at two continental margins, Mauritania in the tropical eastern North Atlantic and Peru in the eastern tropical South Pacific, in order to better understand the sources, sinks and seawater cycling of TMs in these regions. Because of its important role in directly regulating phytoplankton productivity in the ocean, a particular focus was on the behaviour of Fe. In this introductory chapter, the current

knowledge of TM cycling in the oceans is described, with a focus on the characteristics of the two OMZ regions reported in Chapters 4 and 5.

1.1 Trace metal sources

The major TM sources to the ocean are atmospheric aerosols, sediments from continental margins, rivers, hydrothermal vents and glacial meltwater (Elrod et al., 2004; Gerringa et al., 2012; Jickells et al., 2005; Rijkenberg et al., 2014; Tagliabue et al., 2010) (Figure 1.1). Inputs can be of natural origin, as for example mineral dust (e.g. Jickells et al., 2005) or caused by anthropogenic emission from, for example, mining activities or combustion of fossil fuels (Becagli et al., 2012; Boyle et al., 2014; Sholkovitz et al., 2012). The magnitude of the different inputs varies strongly on spatial and temporal scales, and the removal of TMs from seawater is determined by a range of complex, and not yet fully understood, processes (Tagliabue et al., 2017).

Major aerosol sources to the atmosphere are soil particles, such as weathered continental crust material, which is entrained into air masses by winds, or anthropogenic emissions from fossil fuel combustion, industrial melting processes and biomass burning (Jickells et al., 2005; Sholkovitz et al., 2012). Volcanic eruptions represent an additional lower frequency but potentially strong source (Duggen et al., 2010). The aerosols can be transported far over the open ocean before deposition and are deposited directly into surface waters where phytoplankton grow. Solubilities of TMs from aerosols have been shown to vary strongly between anthropogenic and mineral dust sources, with anthropogenic aerosols typically having higher TM solubility (e.g. Aguilar-Islas et al., 2010). Also aerosol particle size, aerosol loading, and chemical weathering of dust particles in the atmosphere along their transport pathways have been found to strongly influence TM solubility (Baker and Croot, 2010). The solubility of TMs in aerosols is

critical for the impact of aerosol deposition on phytoplankton productivity, as the dissolved TM form is typically considered as the more bioavailable form (Lis and Shaked, 2009). In addition to being less directly bioavailable, the undissolved particulate phase can rapidly sink through the water column to the seafloor, representing a loss of TMs from the oceanic inventory.

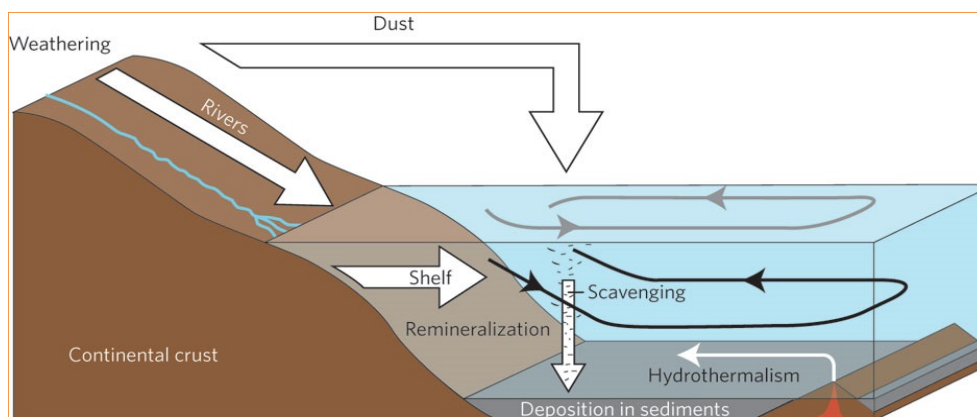


Figure 1.1: Schematic of major sources and sinks of TMs in the ocean (Frank, 2011).

Hydrothermal vents release high temperature, acidic and reducing fluids which contain high concentrations of a range of metals, such as Fe and Mn (Fitzsimmons et al., 2017; Resing et al., 2015), and contribute significantly to the oceanic Fe influx, especially close to mid-ocean ridges (Tagliabue, 2014). In the vicinity of the hydrothermal vents Fe sulphides precipitates are found, and much of the released hydrothermal Fe and Mn precipitates rapidly upon interaction with the ambient oxygenated seawater as Fe oxyhydroxides and as Mn oxides (German and Von Damm, 2006). The majority of hydrothermal inputs occur in the deep sea and consequently much of the hydrothermally released Fe and Mn is scavenged and removed before reaching the surface ocean (Bruland and Lohan, 2006), but nevertheless the Fe inputs make a significant contribution to the deep ocean Fe reservoir (Tagliabue et al., 2014).

Chapter 1: Introduction

Rivers and glacial meltwaters carry a large amount of TMs from terrestrial sources into the ocean (de Baar and de Jong, 2001). These sources can have a large local influence on TM concentrations close to their source (e.g. Rijkenberg et al., 2014), but transport further into the open ocean is often restricted, as at the freshwater-seawater interface in estuaries a large amount of TMs, and in particular Fe, flocculates due to ionic strength increases and precipitates (Boyle et al., 1977; Sholkovitz and Copland, 1981). Dissolved TMs in rivers with high organic carbon content are often present in colloids associated with humic acids (Sholkovitz and Copland, 1981). These colloids tend to flocculate during an increase in Ca^{2+} and Mg^{2+} concentrations during mixing with seawater in estuaries. Rivers with low organic carbon content can therefore comprise a stronger source of TMs to the ocean (Bruland and Lohan, 2006).

Continental shelves can form an important source of TMs to the ocean, and release from sediments dominates Fe inputs in near-coastal regions (Elrod et al., 2004). All other previously mentioned sources contribute to the sediment trace metal inventory by sedimentation of trace metal-containing particles. Release of TMs from sediments occurs by diffusion into overlying bottom waters after reductive dissolution (dissolution under reducing conditions and release in the reduced redox form) or non-reductive dissolution (dissolution and release in the oxidized redox form) (Homoky et al., 2016), or via supply following resuspension of sediments into the water column, tidal pumping and groundwater discharge (Windom et al., 2006). The release of TMs from sediments depends on a number of factors, such as bottom water oxygen concentrations, organic matter content, sediment type, and bathymetry (Homoky et al., 2016). The processes that are involved in sediment release and offshore transport are explained in more detail below.

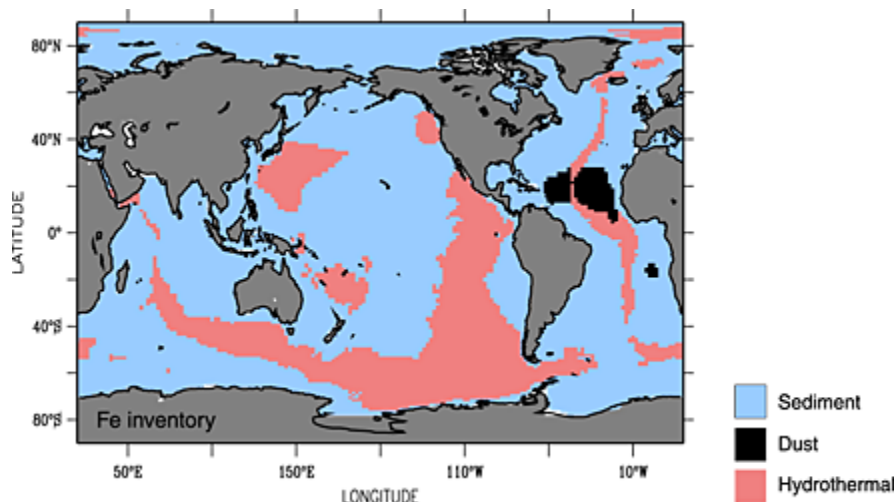


Figure 1.2: The dominant Fe sources to the integrated water column Fe budget as simulated using an ocean biogeochemical model (Tagliabue et al., 2014).

Recent modelling efforts calculate that, for integrated water column Fe inventories, about 74% of the surface area of the ocean is dominated by the influence of a sediment sources, 24% hydrothermal, and 2% by atmospheric dust deposition (Figure 1.2; Tagliabue et al., 2014). The influence of dust deposition is predicted to be particularly dominant in the tropical and subtropical North Atlantic under the North African dust plume, whereas the influence of hydrothermal venting dominates at mid-ocean ridges. Modelling TM distribution and the impacts of TM sources and sinks however currently assumes parameterization of many quantitative processes, such as input fluxes, scavenging rates and internal cycling, which are all themselves dependent on multiple factors that are poorly constrained and hence subject to high uncertainty (e.g. Tagliabue et al., 2017). Typically the input fluxes and processes used in models are parameterized according to best ability to explain observational data of local distributions observed at specific time points (e.g. Moore and Braucher, 2008): extrapolation to under-sampled areas and unmeasured temporal variability adds to uncertainty. Nevertheless, such modelling efforts are essential for projecting the effect of changes in TMs in response to a future ocean with modified anthropogenic emissions of TMs, ocean warming, ocean

acidification, and ocean deoxygenation that all potentially influence the overall TM inventory and its distribution in the ocean. These models would be much improved by better process understanding, which will allow an assessment whether all important processes influencing TMs are included in the models, and whether the processes that are included are correctly parameterized. Furthermore, increasing the number of available data aids model testing and parameterization.

1.2 Trace metal distributions

The low concentrations of many TMs in the ocean are caused by a combination of limited inputs, biological uptake, and low solubilities in seawater (Morel and Price, 2003). The distribution patterns of TMs in the ocean differ largely depending on the physical and chemical properties of the TMs and their associated interaction with oceanic life (Bruland and Lohan, 2006). Some TMs have a conservative distribution, which means they exist in nearly uniformly distributed concentrations throughout the ocean, which vary with salinity through mixing processes. Examples include molybdenum, antimony, tungsten, rubidium and uranium. This conservative nature is determined by their long residence times of more than 100,000 years, much greater than the ~1000 year mixing time of the oceans (e.g. Broecker and Peng, 1982). These long residence times are a result of limited removal that allows for accumulation in seawater, which means that any internal biogeochemical cycling acting to alter their concentration is negligible. The second group of trace metals shows a similar distribution to the major nutrients nitrate and phosphate: their distribution is characterized by low concentrations in the surface due to assimilation by phytoplankton, followed by downward transport out of the surface layer by sinking organic matter particles and remineralization in deeper waters, resulting in an increase in dissolved concentrations with depth and water age. TMs with such a distribution include Zn, Cd and Ni. The third group of TMs is characterized by a

strong decrease in concentrations with distance from their source due to strong sorption to particles ('scavenging') and hence removal from the dissolved phase. These metals have particularly short residence times of 100–1000 years in the ocean. Examples of scavenged-type TMs are Al, Pb and Mn. In addition to nutrient-like and scavenged-type distributions, some TMs, such as Fe, Cu and Co, are influenced by a combination of both biological and scavenging processes. They are referred to as hybrid-type TMs. These metals are characterized by low concentrations in the surface ocean due to biological uptake and a combination of remineralization and scavenging at greater depths. (Bruland and Lohan, 2006)

The categorization of TMs into different groups is an idealized view; actual depth profiles TMs can vary according to local sources, the productivity of surface waters, the redox state of the water column, and the amount and type of particle surfaces available for scavenging (Boyd and Ellwood, 2010).

1.2.1 Scavenging

Scavenging forms an important sink of dissolved TMs in the ocean (Boyd and Ellwood, 2010). Scavenging collectively encompasses the assimilation of TMs by marine biota and adsorption and absorption of TMs onto or into particles (e.g., particles of organic matter such as microbes or parts of microbes, faecal pellets produced by heterotrophic organisms, or inorganic particles including Fe and Mn oxides, opal, calcium carbonate, and clay minerals) followed by subsequent aggregation of particles and colloids and their removal from the water column by settling/sedimentation (Bruland and Lohan, 2006). Adsorption processes are influenced by the affinity of the free metal ion to a particle surface (different elements and different particle surfaces have different affinities), the available surface area and type of particle surface, the speciation of the metal ion in

solution and conditions of the water column, with a strong influence of pH (Balistrieri et al., 1981; Honeyman and Santschi, 1987).

1.3 Trace metal speciation

The solubility, bioavailability and surface reactivity of TMs is largely influenced by the speciation of TMs in seawater, which refers to the different chemical forms of the TM. This includes redox-speciation, the oxidation state of the TM, and the formation of inorganic and organic TM complexes. The speciation of TMs thereby also determines the cycling between soluble, colloidal and particulate fractions in seawater, which are size ranges that are operationally-defined in terms of the filter pore size they can be filtered through (Figure 1.3).

1.3.1 Redox speciation

The TM oxidation state is dependent on the redox-chemistry of the particular TM and the redox-conditions in the seawater environment. TMs are often present as mono-, di-, or trivalent cations, although some TMs can be present in a higher oxidation state as oxyanion or -cations (Bruland and Lohan, 2006). For example, Fe, Co and Mn are mainly present as trivalent cations (Fe(III), Co(III), Mn(III)) or Mn as MnO₂ in oxygenated seawater, which have a lower solubility than their reduced forms (Fe(II), Co(II), Mn (II) (Liu and Millero, 2002; Stumm and Morgan, 1995). The reduced forms are thermodynamically unstable in oxygenated seawater, and the oxidation process will render the elements less soluble. In the modern ocean, reduction of these metals is largely restricted to anoxic sediment pore waters, which may be released to overlying bottom waters by diffusion and bio-irrigation (Elrod et al., 2004; Green et al., 2002), and also photoreductive processes of Fe and Mn occur in the sunlit surface waters (Barbeau et al., 2001; Sunda and Huntsman, 1988; Voelker and Sedlak, 1995). Away from the sources of

the reduced TM forms, oxidation occurs depending on the prevailing redox conditions in the water column and by microbial oxidation processes (Bianchi et al., 2018). The half-life of the reduced form largely depends on the oxygen concentration, as well as the pH, temperature and salinity of the seawater. For example Fe(II) oxidation kinetics can be explained by Equation 1.1 (Millero et al., 1987):

$$-\frac{d[Fe(II)]}{dt} = k[Fe(II)][O_2][OH^-]^2 \quad (1.1)$$

With the dependency of the oxidation rate constant (k) on temperature (T) and ionic strength (I) according to Equation 1.2:

$$\log k = 21.56 - \frac{1545}{T} - 3.29 I^{0.5} + 1.52 I \quad (1.2)$$

After oxidation of the reduced TM form, formation of amorphous metal hydroxides occurs, which results in the formation and agglomeration of particles and loss from the water column through sedimentation. In addition to abiotic oxidation processes, biotic oxidation by manganese oxidizing bacteria is an important oxidation pathway of Mn(II) and Co(II) (by co-oxidation) in the ocean (Moffett, 1994; Moffett and Ho, 1996; Sunda and Huntsman, 1988; Tebo and Emerson, 1986).

Highest benthic Fe fluxes have been observed from sediments underlying bottom waters with low oxygen concentrations (Noffke et al., 2012; Severmann et al., 2010). Within the water column increased concentrations of Fe, Co and Mn have also been observed within oxygen depleted waters (Hatta et al., 2015; Hawco et al., 2016; Noble et al., 2012; Noble et al., 2017) that are likely influenced by both enhanced benthic fluxes and greater stability in their reduced form under low oxygen concentrations, as well as within zones of elevated remineralization (respiration) which simultaneously releases the metal from the organic particulate phase and removes oxygen (e.g. Noble et al., 2012). An

intensification and expansion of oxygen minimum zones (OMZs) has been observed during the last five decades (Schmidtko et al., 2017; Stramma et al., 2008b; Stramma et al., 2009). If this trend continues, the future sediment source strength for Fe and other redox-sensitive trace metals could be enhanced, which in turn—via its strong biological relevance in the modern ocean (Falkowski, 1997)—might have a significant feedback on the network of interconnected biogeochemical cycles (e.g. Falkowski et al., 1998). However the magnitude of such changes and their impact are not well understood yet (e.g. Moore and Doney, 2007; Watson et al., 2000; Weber and Deutsch, 2014) and urgently require further investigation.

1.3.2 Inorganic and organic complexation

The inorganic speciation of TMs in seawater largely depends on the prevalent pH and temperature conditions (e.g. Byrne et al., 1988). At seawater pH=8.2, the inorganic speciation is often determined by chloride (e.g., Cd(II), Hg(II), Ag(I)) and hydroxide (e.g. Fe(III), Al(III)) complexes, oxyanions (e.g. MoO_4^{2-}) or oxycations (e.g. UO_2^{2+}) or free hydrated divalent cations (e.g. Zn(II), Mn(II), Co(II), Ni(II)) (Turner et al., 1981). For example, at seawater pH inorganic Fe(III) is mainly present as hydroxide complexes, $\text{Fe}(\text{OH})_3$, and with more than an order of magnitude lower concentrations, $\text{Fe}(\text{OH})_2^+$ and $\text{Fe}(\text{OH})_4^-$ (Millero et al., 1995). As previously discussed, the overall solubility of Fe is very low at seawater pH. For example at pH 8, 25°C and a salinity of ~35 practical salinity units (PSU), Fe solubility was determined to be around 0.01 nmol L⁻¹ in artificial seawater in the absence of organic material (Liu and Millero, 1999). However Fe solubility in natural seawater often exceeds these concentrations. This can be explained by organic ligand complexation of the Fe ions that stabilizes them in seawater and prevents precipitation and thereby removal from solution (Gledhill and Buck, 2012). Accordingly, in the presence of organic ligands in natural seawater, Fe solubilities of

0.2–0.3 nmol L⁻¹ were observed at pH (8), temperature (25°C) and salinity (35 PSU) (Liu and Millero, 2002). In the modern ocean, more than 99% of the dissolved Fe is organically complexed (Gledhill and Buck, 2012). Organic ligands contain functional groups which interact/bind to the metal ion and thereby stabilize the metal and prevent loss by scavenging (Boyd and Ellwood, 2010). The binding strength varies according to the type of ligand. Naturally occurring Fe ligands in seawater include, for example, siderophores, humic substances, and exopolymeric substances (Gledhill and Buck, 2012). Siderophores are low molecular weight, high affinity Fe(III)-ligands produced by microorganisms to facilitate Fe uptake (Barbeau et al., 2003). Humic substances are degradation products of terrestrial or marine organic matter, predominantly consisting of polyphenols and benzoic or carboxylic acids (Buffle, 1990). In addition to Fe, organic ligand complexation has been reported to occur for Cu, Ni, Co, Zn and Cd (Achterberg and Van Den Berg, 1997; Bruland, 1989; Bruland, 1992; Gledhill and Buck, 2012; Saito and Moffett, 2001). Ligand complexation either increases bioavailability to organisms by facilitating uptake, such as for Co and Fe (Rue and Bruland, 1995; Saito and Moffett, 2001), or decreases bioavailability and thereby detoxifies elements which can be harmful for organisms at increased concentrations, such as for Cu (e.g. Coale and Bruland, 1990).

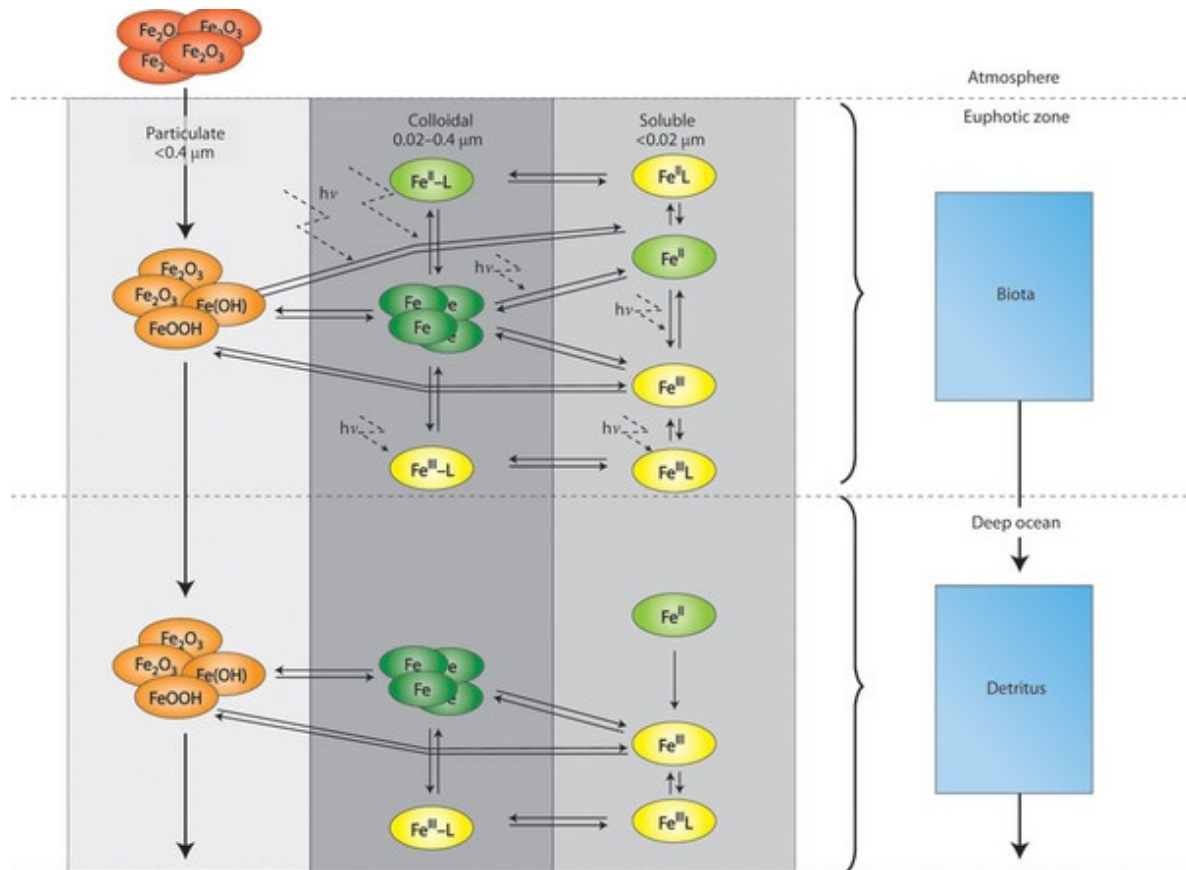


Figure 1.3: Simplified schematic of the cycling of Fe between different species and size fractions in the euphotic zone and the deep ocean after aerosol deposition (Boyd and Ellwood, 2010).

1.4 Characteristics of study areas

Three major OMZs in the modern ocean are present in the eastern tropical Atlantic, eastern tropical Pacific, and tropical Indian Ocean (Figure 1.4). Oxygen is supplied to the modern ocean from both the atmospheric inventory and by photosynthetic organisms living in the surface ocean. Consequently, oxygen concentrations are highest and often slightly over-saturated in surface waters (e.g. Brandt et al., 2015). At greater depths the oxygen distribution is controlled by a balance between oxygen consumption during organic matter remineralization and oxygen resupply by lateral advective and diapycnal fluxes from adjacent higher oxygen water masses (e.g. Brandt et al., 2015). OMZs, regions of the ocean with particularly low oxygen concentrations at intermediate depths (100–900 m), form as a result of weak ventilation coupled with high oxygen

Chapter 1: Introduction

consumption from elevated organic matter remineralization (e.g. Karstensen et al., 2008; Wyrski, 1962). High productivity of surface waters in these regions occurs due to upwelling of nutrient-rich deeper waters coupled with elevated surface water temperatures and irradiance in tropical regions. As this photosynthetically produced organic matter sinks, this leads to elevated oxygen consumption via respiration of the sinking organic matter. Weak ventilation limits oxygen resupply: in the eastern Pacific and Atlantic this is driven by the presence of so called 'shadow zones', unventilated sectors between the wind-driven circulation of the gyres, which are characterized by sluggish circulation and restricted mixing of water masses (e.g. Luyten et al., 1983).

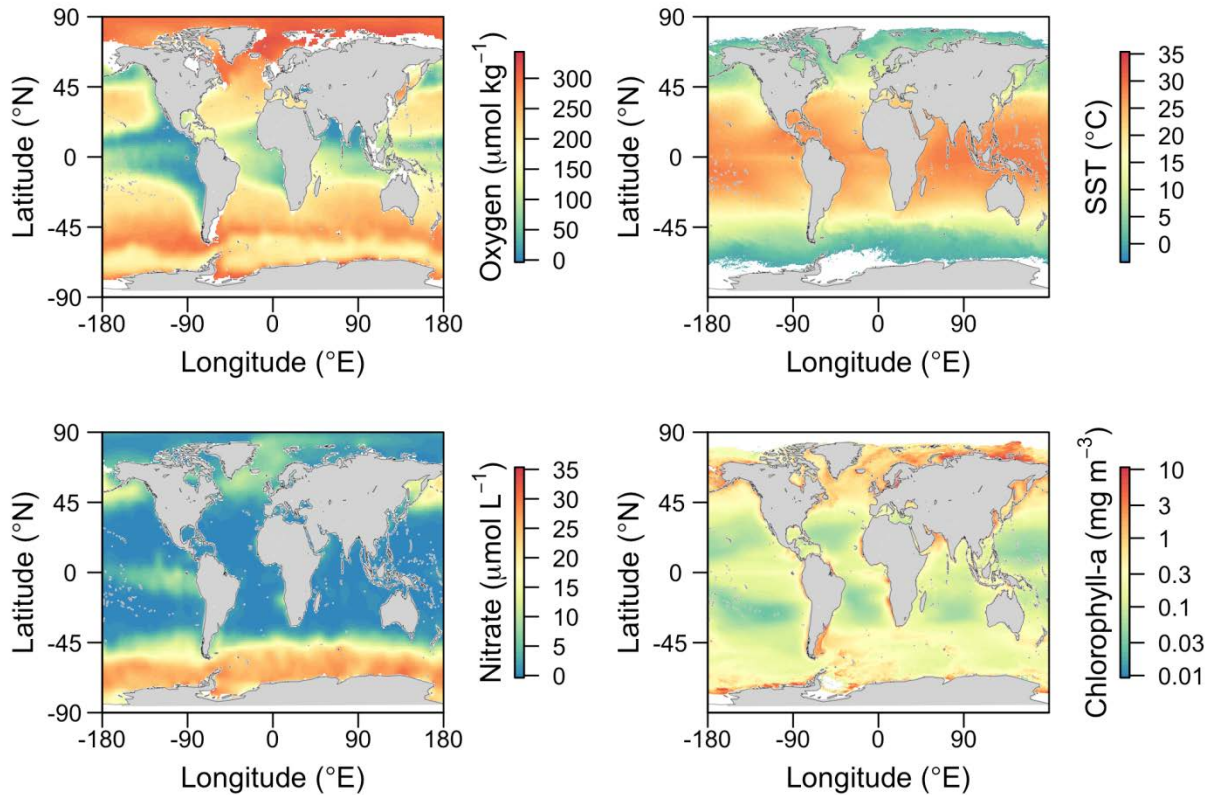


Figure 1.4: Oxygen minimum zones and their biogeochemical settings. Global distribution of oxygen at 300 m depth (annual mean, World Ocean Atlas 2009; WOA09); sea surface temperature (SST, satellite derived 2002–2016 annual climatological mean, MODIS NASA); surface nitrate concentrations (annual mean, WOA09); and surface chlorophyll a concentrations as an indicator of phytoplankton biomass (satellite derived 2002–2016 annual climatological mean, MODIS NASA).

Global warming increases the oceans' temperature and increases upper-ocean buoyancy and thereby stratification. Elevated seawater temperatures results in reduced atmospheric oxygen solubility into surface seawaters and accelerated oxygen consumption by enhanced microbial respiration. Enhanced stratification results in reduced ventilation of deeper waters (Breitburg et al., 2018). This effect has been predicted to cause a decline (1–7% by the year 2100) in the dissolved oxygen inventory of the global ocean (Keeling et al., 2010; Long et al., 2016). Observational data support this trend with a reported decline in oxygen of 2% over the past 50 years with regionally varying magnitudes (Schmidtko et al., 2017). The regional distribution of predicted and observed declines however differ largely in some regions (Stramma et al., 2012a). The latter suggests that additional mechanisms influence the decline in dissolved oxygen, such as natural climate

variability occurring on interannual to decadal timescales (Broecker et al., 1999; Schmidtko et al., 2017). Increased inputs of nutrients into coastal regions by rivers has additionally enhanced primary production in coastal areas that has led to more widespread coastal eutrophication and subsequent elevated oxygen consumption generating so called dead-zones (Diaz and Rosenberg, 2008).

Ocean deoxygenation may alter oceanic nutrient-cycles, biodiversity, foodwebs, and fisheries, as well as the oceanic source of the greenhouse gas N_2O (Breitburg et al., 2018). For example, the sedimentary source of Fe and phosphate is generally considered to be enhanced under low oxygen conditions (Ingall and Jahnke, 1994; Scholz et al., 2014), whereas bioavailable fixed nitrogen is lost through denitrification and anaerobic ammonium oxidation (anammox) under anaerobic conditions (Bristow et al., 2017). Expanding distribution of anoxic conditions causes habitat loss for strictly aerobic organisms and growth and reproduction rates are reduced in low oxygen environments (Breitburg, 2002; Diaz and Rosenberg, 2008; Thomas et al., 2015). Habitat compression, in this case the mechanism whereby aerobic organisms are constrained to a smaller depth range, may also result in an increased competition for prey and increased vulnerability to predation and fishing (Eby and Crowder, 2002; Stramma et al., 2012b). The combined effect of increased productivity by enhanced nutrient input and the negative effects through deoxygenation are however difficult to predict (Breitburg et al., 2018).

1.4.1 Upwelling

Patterns of atmospheric circulation drive downwelling of seawater in some regions of the ocean and upwelling of seawater in others. This is a result of wind stress acting upon the surface ocean, the energy of which propagates to deeper waters and in turn generates hydrostrophic pressure gradients. Regions with upwelling result from the generation of low hydrostatic pressure at the surface; for example, coastal upwelling is caused by

alongshore winds that drive offshore Ekman transport of surface seawater and its replacement by deep waters (Figure 1.5). Ekman transport is the result of the drag force created by wind stress moving surface seawater and its subsequent deflection by the Coriolis force, resulting in an integrated surface water mass transport at a right angle to the original wind direction; this is a clockwise deflection in the northern hemisphere and counter-clockwise deflection in the southern hemisphere (Figure 1.5; Williams and Follows, 2011).

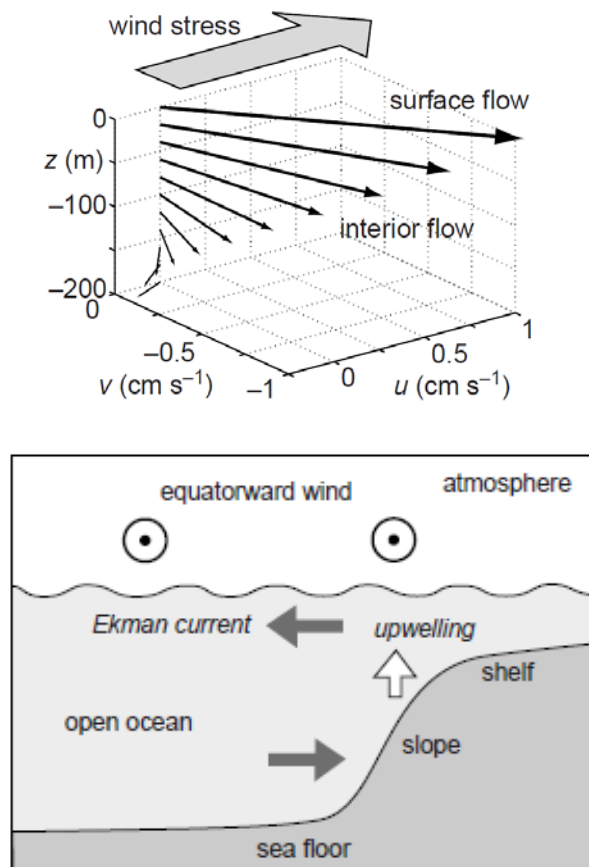


Figure 1.5: Schematic of the Ekman spiral (top) and coastal upwelling (bottom) (Williams and Follows, 2011). The wind stress in the surface-most layer is propagated to deeper depths, with decreasing velocities and at an increasing angle to the original wind direction, which is called the Ekman spiral; the net effect on the overall surface ocean layer (in this case, the upper 200 m water depth) is a motion at a right angle to that of the original wind direction. This process occurs at coastlines where alongshore winds can drive offshore transport of the integrated surface water layer, generating low hydrostatic pressure that is filled by upwelling of deeper waters flowing down the pressure gradient.

1.4.2 Study regions

This PhD thesis focuses on two OMZs, one in the Eastern Tropical North Atlantic (ETNA) and the other in the Eastern Tropical South Pacific (ETSP). In the ETNA OMZ, lowest oxygen concentrations of about $40 \mu\text{mol kg}^{-1}$ are centred at around 17°N close to the African shelf, between the equatorial current system and the north equatorial current (Stramma et al., 2005). The ETNA shows two depth layers of oxygen minima, one at shallower depths of around 100 m and one in deeper waters at around 400 m. The oxygen supply between 150 and 300 m is larger than within the deeper oxygen minimum (at 300–600 m) due to stronger water current velocities that supply oxygen-rich water (e.g. Stramma et al., 2008a). The shallower oxygen minimum (around 100 m) is maintained by higher levels of remineralization of sinking particulate organic matter produced in surface waters (e.g. Karstensen et al., 2008).

The ETSP OMZ shows a similar structure to the ETNA, but oxygen concentrations in the core of the OMZ reach suboxic ($<4.5 \mu\text{mol L}^{-1}$) to fully anoxic conditions (Karstensen et al., 2008). Lowest oxygen concentrations are found centred at around 10°S between 100–800 m ($\text{O}_2 < 30 \mu\text{mol L}^{-1}$) (e.g. Karstensen et al., 2008; Stramma et al., 2008b). The lower oxygen concentrations in the ETSP compared to the ETNA are a result of a lower ventilation in the ETSP because of lower oxygen concentrations in the eastward current bands of the Pacific OMZ compared to the Atlantic OMZ (Karstensen et al., 2008). The OMZ in the ETSP undergoes interannual variabilities related to the El Niño Southern Oscillation (ENSO) with oscillating La Niña and El Niño events every 2–7 years (McPhaden et al., 2006). Our study within the ETSP was conducted in October 2015 during a strong El Niño event (Stramma et al., 2016). During El Niño events a weakening in trade winds results in a weakening or disappearance of the Equatorial Undercurrent (EUC) (Johnson et al., 2002; Kessler and McPhaden, 1995). Effects of El Niño in the

ETSP are an increase in sea surface temperature (SST) and a deepening of the eastern thermocline, nutricline and oxycline. Consequently upwelled water over the Peruvian shelf situated within the ETSP OMZ is warmer and contains less nutrients and more oxygen (Kessler, 2006). A further positive feedback induced is an oxygen concentration increase on the shelf caused by reduced primary production driven by reduced rates of nutrient supply (Gutiérrez et al., 2008; Pennington et al., 2006). The El Niño associated changes in primary production have a drastic impact on fish populations, decreasing the anchovy harvest off the coast of Peru (Chavez et al., 1999).

1.5 Thesis objectives and outline

Chapters 3, 4 and 5 have been written as manuscripts for scientific journals, and therefore may lack some of the more detailed descriptions of the methods using in this study. In Chapter 2, therefore, a detailed description of sample collection protocols and all main analytical methods utilized throughout this study are provided in order to familiarize the reader with basic knowledge assumed in the following chapters. Chapter 3 addresses the first major aim of this study, which was to develop a reliable, high-throughput method for the simultaneous analysis of a range of TMs in seawater. Chapters 4 and 5 address the second major aim, which was to apply the new method to investigate TM cycling in OMZs in order to improve our understanding of the processes that influence sediment TM release and transport offshore. Chapter 4 presents results from a study off Mauritania, which is situated within the OMZ in the ETNA, and Chapter 5 presents results from a study off the coast of Peru, within the ETSP OMZ.

In Chapter 4, the influence of the different sources and processes on the distribution of TMs is investigated with a particular focus on the redox-sensitive TMs Fe, Co and Mn. A detailed comparison was made between the relative influences of atmospheric dust

Chapter 1: Introduction

deposition, sediment release, and remineralization processes, using supporting Al data as a tracer for atmospheric dust deposition and sediment resuspension, and Ra data as a tracer for sediment release and water mass age. A comparison between redox-sensitive elements, major nutrients and nutrient-like TMs was made in order to identify the importance of remineralization processes. Scavenging processes and interactions between dissolved and particulate phases were studied using a comparison between dissolved and leachable particulate concentrations and turbidity data, to identify differences in the scavenging behaviour between Fe, Co and Mn. Additionally, the involvement of the above mentioned processes and changes in oxygen concentrations were considered to explain the observed short-term variability in concentrations of Fe, Co and Mn at stations reoccupied over a period of several days.

Chapter 5 focuses on the distributions of Fe(II), dissolved Fe and leachable particulate Fe (fractions are defined in Chapter 2) and the influence of the oxygenation state of the shelf, which was significantly modified at the time of sample collection as a result of the 2015/16 El Niño event. Other factors influencing offshore physical transport and the removal of Fe from the water column were also investigated. The influence of oxygenation state was decoupled from biological processes, such as uptake and remineralization, using similarly redox-sensitive elements Co and Mn and non-redox-sensitive nutrient-like elements (Ni, Cd and Zn).

The two study regions, the ETNA and ETSP, are both part of large OMZs that represent enhanced benthic fluxes of Fe to the bottom boundary layer of the ocean. Nevertheless, they exhibited significantly different characteristics in the distribution of redox-sensitive TMs. Chapter 6 summarizes the main findings of Chapters 4 and 5 and discusses possible causes for the differences in TM distributions between the two study regions. At the end

Chapter 1: Introduction

of Chapter 6, suggestions for future studies are suggested in order to fill in key gaps in our current understanding of TM cycling in OMZs.

The overarching aims of this thesis were to (i) improve understanding of TM cycling in the ocean by determining the key controls on the sources, internal cycling, and removal mechanisms for redox-sensitive TMs in OMZs and (ii) to subsequently evaluate how future changes in seawater oxygenation may modify the current inventory of these. To address these aims I had two main objectives, (i) to develop a method for high throughput, accurate determination of TM concentrations in seawater, and (ii) to apply this method on samples collected in two OMZs and interpret the results within the context of a suite of ancillary chemical, physical, and biological measurements made on the same cruises.

2 Sample collection and analysis

Concentrations of trace metals (TMs) in seawater are typically very low, but abundant on land, ships, and even on new plastic surfaces. Because of this, the measurements of seawater TM concentrations are highly susceptible to contamination; detailed protocols for sampling, sample storage and sample analysis have been developed and need to be carefully followed in order to obtain high quality TM concentration data. Detailed protocols for the collection and handling of seawater TM samples were developed at the onset of the international GEOTRACES programme, an effort to map the TM concentrations of the world's oceans. A thorough description of all necessary steps in sampling and sample storage are given in the 'Sampling and Sample-handling Protocols for GEOTRACES cruises' (Cutter et al., 2014); here a brief overview is given that is relevant to the work undertaken in this PhD project.

2.1 Plastics and other materials

A high TM contamination potential derives from the material that comes into direct contact with the sample during sampling, filtration and storage. Therefore all bottles, tubing and filters need to be made of specific TM clean materials and thoroughly acid-cleaned before usage. In this study TM-free Go-Flo bottles (General Oceanics) and OTE samplers (Ocean Test Equipment) attached to a TM-free CTD rosette frame made from powder-coated aluminium or by directly attaching the bottles to a Vectran wire were used to collect seawater from specific depths under TM clean conditions. Valves, connectors and tubing were usually made out of Teflon or polyvinyl chloride (PVC), and bottles for subsampling and sample storage were made of low density polyethylene (LDPE,

Nalgene) for TM samples and opaque high density polyethylene (HDPE, Nalgene) for Fe(II) analysis and sample collection for iodide and iodate. All LDPE bottles were cleaned by (i) soaking for one day in Mucosal detergent (Sigma-Aldrich), (ii) rinsing with warm-tap water followed by three times rinsing with de-ionized water ($18.2 \text{ M}\Omega \text{ cm}^{-1}$, Milli-Q, Millipore), (iii) soaking for one week in 5 M HCl (reagent grade, Fisher), (iv) rinsing three times with de-ionized water, (v) soaking for one week in 8 M HNO₃ (reagent grade, Fisher), and finally (vi) rinsing five times with de-ionized water. Cleaned sample bottles were stored double-bagged in ziplock bags until usage. HDPE bottles (Nalgene), connectors and tubing were cleaned in the same manner using lower concentrated acids (1 M HCl, 1.6 M HNO₃).

2.2 Operationally defined trace metal fractions

As previously described, TMs are present in the ocean in different size classes: as truly dissolved cations, organically-complexed ions, within small colloids, or within particles of various sizes. In order to distinguish between these different size fractions, filtration of seawater with membrane filters of different pore sizes is conducted. The fractions, however, are operationally defined by the pore size of the filter and do not give any information in which form (inorganic or organic) the TMs are present. Commonly utilized operational fractions are: soluble TMs, usually defined as any component that passes through 0.02 μm pore sized filters; dissolved trace metals, anything passing through a 0.2 or 0.45 μm pore sized filter; and particulate samples ($>0.2 \mu\text{m}$). An unfiltered sample, referred to as the 'total dissolvable' (TD) TM fraction, is defined as the total amount of TMs present that are dissolvable following acidification and storage for a minimum of six months prior to analysis. Additionally, a 'colloidal fraction' is defined as the difference between dissolved (i.e., <0.2 or $0.45 \mu\text{m}$) and soluble concentrations (i.e., $<0.02 \mu\text{m}$), and a 'leachable particulate fraction' as the difference

between total dissolvable (i.e., no filtration) and dissolved (i.e., <0.2–0.45 μm) concentrations. Particulate TM concentrations are defined as the concentration measured following full digestion of samples collected onto filters (0.2 or 0.4 μm pore size).

2.3 Sampling

TM clean OTE-samplers were prepared for sampling by opening them and activating the closing mechanism. This was performed wearing plastic gloves within a laboratory container over-pressurized by filtered air. Before transferring the bottles onto the ship's deck, the top and bottom opening and subsampling valve were covered using plastic covers. Plastic covers were only removed shortly before deployment in order to avoid any exposure to contamination on deck. The procedure for sample collection using OTE samplers on a non-conducting Kevlar wire was as follows: all samplers are attached separately as the wire is lowered over the ship's side, representing the final desired sampling depths. Closure of the samplers was triggered via sending a 'messenger' (non-contaminating weight (Teflon coated)) down the wire. A depth sensor (DST centi, STAR:ODDI) was attached to the bottom bottle. For collecting samples using a rosette frame the attached samplers were closed at required depths using an electrical trigger controlled from the deck. Samplers were closed during the upcast to allow all bottles to be flushed with seawater on the downcast prior to sampling. Back on deck, the closed samplers were transferred back to the clean laboratory container where subsampling of the bottles occurred. Before subsampling, the OTE samplers were pressurized using a low overpressure (<2 bar) with filtered (0.2 μm , PTFE filter) N_2 gas and the valve for subsampling was thoroughly rinsed with de-ionized water before attaching the tubing. The other end of the tubing was placed under a laminar flow bench within the clean laboratory container, where subsamples were collected. Surface samples were collected using a towed water sampling device (often referred to as a towed-fish) at 1–3 m depth

with water pumped through acid-cleaned PVC tubing into the clean laboratory container using a Teflon bellows pump (Almatec A15).

TM samples were sub-sampled into different size classes via filtration. Samples were collected either unfiltered or filtered with 0.2 μm pore sized filters (Acropack 500, Pall) into LDPE bottles. The Acropack filters were re-used between samples with the filters stored in the fridge between usage. New filters were flushed with at least 10 L of surface seawater, and always with at least 500 mL of the sample prior to sample collection. Additionally, samples were filtered with a smaller pore size for soluble TMs (0.02 μm , diameter 47 mm, Anodisc membrane filters) from prefiltered (0.2 μm) samples that were collected within a plastic bag which was flushed with N_2 gas before sample collection. The Anodisc filters were placed in acid-cleaned filter holders (Swinex) and attached to acid-cleaned 60 mL syringes with luer-lock tip. The filters were then rinsed with 60 mL de-ionized water and 30 mL of the sample prior to sample collection. The sub-samples were acidified to pH 1.9 using ultra-pure HCl (OPTIMA grade, Fisher Scientific) and stored double-bagged until analysis. In the following, the samples are referred to as soluble (0.02 μm filtered), total dissolved (0.2 μm) and total dissolvable (unfiltered) trace metals. Additional samples were collected for iodide/iodate measurements and Fe(II) measurements. Samples for iodide/iodate were collected filtered (Acropack 500) and samples for Fe(II) unfiltered, both were stored in opaque amber acid-cleaned high-density polyethylene (HDPE) bottles. For Fe(II), sample bottles were filled entirely, leaving no head-space, in order to minimize the intrusion of O_2 . Fe(II) samples were analyzed as soon as possible, latest within one hour after subsampling. Iodine samples were stored frozen at -20°C until analysis. All sample handling, including acidification and analysis, was performed in a clean container or clean laboratory and under a laminar flow hood in order to prevent sample contamination.

2.4 Trace metal analysis

2.4.1 Multielement analysis by ICP-MS after sample preconcentration

Most methods for TM analysis are based on the separation of the TMs from the seawater matrix and preconcentration in order to reduce analytical interferences and increase detection limits. Soluble, dissolved and total dissolvable TM samples in this study were analyzed using an automated preconcentration device (*SeaFAST*, Elemental Scientific Inc) with a similar set-up to Lagerstrom et al. (2013), separating the TMs from the matrix using a cation-exchange resin and analysis by inductively-coupled plasma mass spectrometry (ICP-MS) (Rapp et al., 2017). The matrix separation occurs in four steps: 1) buffering of the seawater sample to required pH; 2) loading of the seawater sample onto the resin; 3) rinsing of the seawater matrix with de-ionized water; and 4) elution of the trace metals using a diluted acid (here 1 M HNO₃). Full details of the method are given in Chapter 3 and are therefore not further discussed at this point. Here, the basic mechanisms of the cation-exchange resin and ICP-MS detection are described, which are not detailed in Chapter 3.

The utilized resin consists of immobilized carboxymethylated pentaethylenehexamine (CM-PEHA) as functional groups (Figure 2.1; Kagaya et al., 2009). TMs in the seawater are retained by interaction with the negatively charged/deprotonated functional groups of the resin over a certain pH range. Elution is performed by diluted acids, as the H⁺ ions in the acid compete with the binding sites of the functional groups of the resin and thereby replace the TMs.

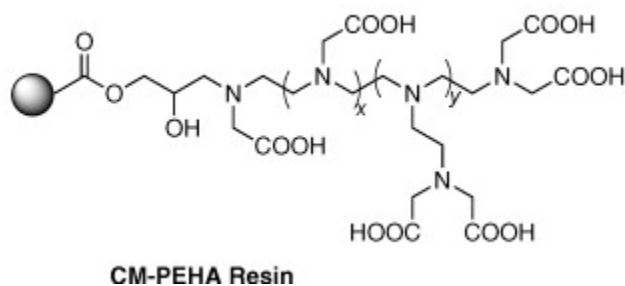


Figure 2.1: Structure of the CM-PEHA resin (Kagaya et al., 2009). TMs bind to the carboxyl groups and the tertiary nitrogen atom and are replaced by H^+ ions upon elution.

After preconcentration, the eluted metals can be directly analyzed by sector-field ICP-MS (Element-XR, Thermo Fisher Scientific) (Figure 2.2) with analysis of a wide range of metals on the same sample. The limiting factor for the number of metals that can be preconcentrated simultaneously is predominantly the requirement that all metals need to be retained on the resin at the same pH and eluted off the resin with a similar acid strength.

During ICP-MS analysis, liquid samples are vaporized and introduced as aerosols into an argon (Ar) plasma by a nebulizer (Figure 2.2). The plasma is created by an Ar gas flow inside the ICP-MS torch. A radio-frequency (RF) generator supplies power to the load coil, creating oscillating electric and magnetic fields at the end of the torch. During ignition of the plasma, a spark is applied, forming Ar ions that collide with each other and establish a plasma in the oscillating fields. The plasma ionizes the analytes at $\sim 6000^\circ\text{C}$. The next step is the transmission of the analyte ions, carried in the Ar stream, from atmospheric pressure into the high-vacuum of the mass spectrometer ($\sim 1 \times 10^{-7}$ mbar). This is done via an interface consisting of two cones, the sampler and the skimmer cones, with an intermediate vacuum in between them. The cones extract the centre of the ion beam coming from the torch. After passing the skimmer cone, the ion beam is focused by electrostatic lenses into the slit of the mass spectrometer. During sector-field ICP-MS, the ions are separated by their differing mass-to-charge ratios

within a magnetic sector and an electric sector. After separation, the ions are detected by a Faraday detector combined with a dual mode Secondary Electron Multiplier (SEM) detector, and converted into an electric signal, which itself is proportional to the number of ions hitting the detector surface. (Prohaska et al., 2014)

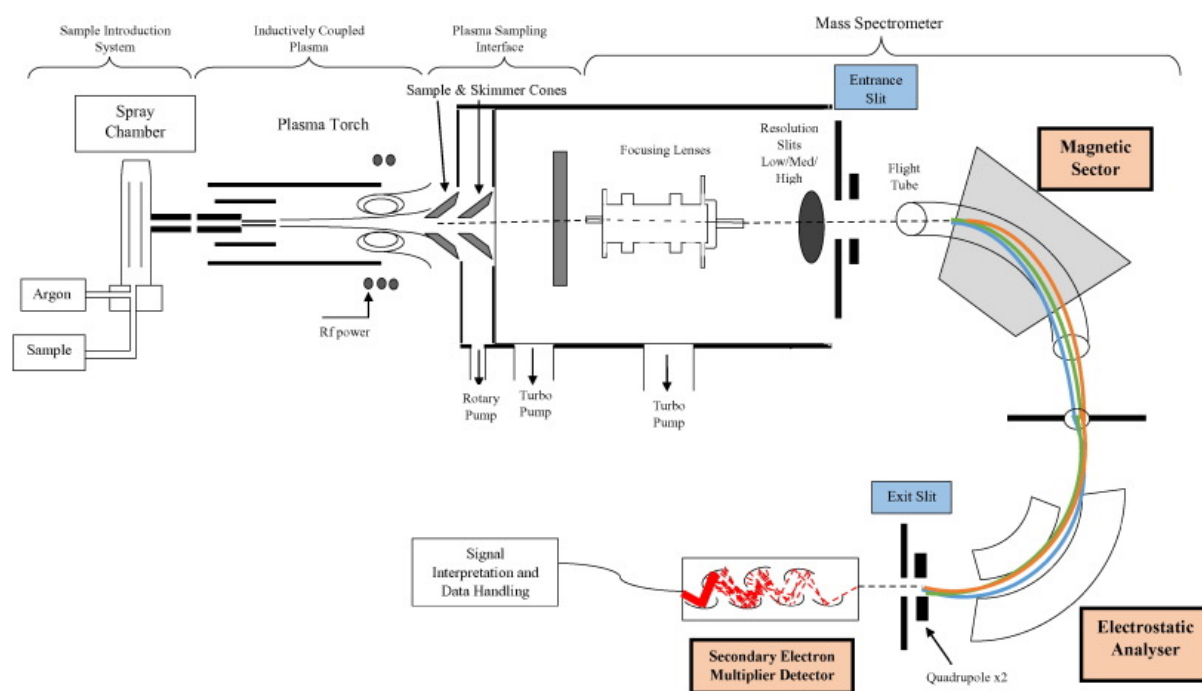


Figure 2.2: Schematic diagram of a sector-field ICP-MS (Ring et al., 2016).

2.4.2 Chemiluminescence flow injection analysis of Fe(II) and H₂O₂

Whereas total size fractionated TMs can be stored acidified for a long time prior to analysis, measurement of redox species, such as Fe(II), require immediate analysis after sampling as every changes in initial conditions, such as light exposure, oxygen or pH changes, or biological activity will result in changes in redox-speciation (i.e., interconversion of Fe(II) and Fe(III)). Samples for Fe(II) were therefore analyzed onboard within 1 hour after subsampling using a luminol chemiluminescence flow injection system without sample preconcentration (Figure 2.3). The system was equipped with two separate reagent lines and loops allowing the alternating analysis of Fe(II) and

Chapter 2: Sample collection and analysis

H₂O₂ on the same sample (Hopwood et al., 2017b). The system consisted of a 10-port valve (Valco, Vici), switching between reagents and sample loading, a second 10-port valve changing between samples, a peristaltic pump (MiniPuls3, Gilson), a glass flow cell with a mirrored base (Waterville Analytical Products) and a photomultiplier tube (H9319-11, Hamamatsu). The reagent flow rates were set to 2.5 mL min⁻¹ for the sample and 1.4 mL min⁻¹ for both reagents. The ratio of reagent and sample flow rate was set by using pump tubing (PVC, Tygon) with different inner diameters (sample: 1.85 mm, reagent: 1.42 mm). All other tubing was black polytetrafluorethylene (PTFE) tubing (0.8 mm inner diameter, Eydam).

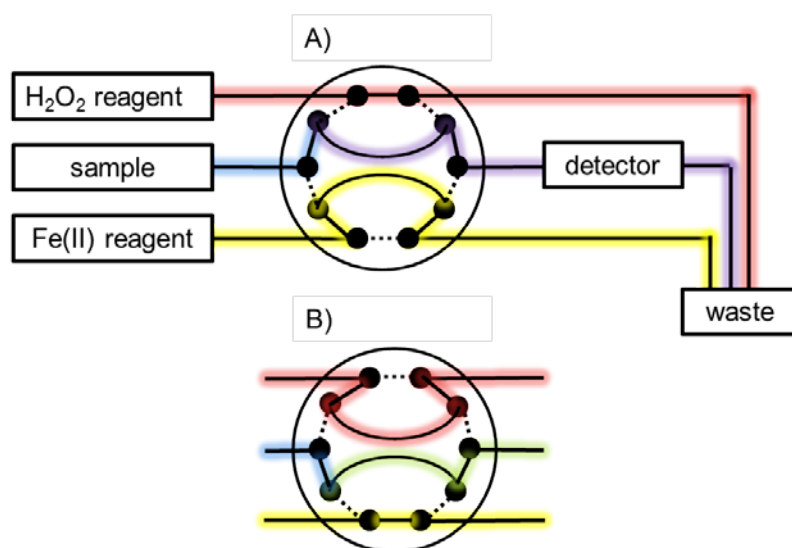


Figure 2.3: Simplified Fe(II) system scheme showing the reagent flow path and alternating valve positions, A) loading of sample loop 2 with Fe(II) reagent, unloading of sample loop 1 and detection of H₂O₂ signal and B) loading of sample loop 1 with H₂O₂ reagent, unloading of sample loop 1 and detection of Fe(II) signal.

The reagents were prepared in 2 L batches. For the Fe(II) reagent, 0.26 g Luminol (98%, Carl Roth) and 1.06 g K₂CO₃ (reagent grade, Roth) were mixed in 10 mL de-ionized water and fully dissolved using an ultrasonic bath. This pre-mix was added to de-ionized water containing 80 mL NH₄OH solution (trace metal grade, Fisher), and approximately 22 mL concentrated HCl (trace metal grade, Fisher) to adjust the pH to 10.1 with a final volume of 2 L. For the H₂O₂ reagent 0.54 g luminol, 44 g potassium carbonate (reagent 30

grade, Roth), 7.8 mL Co(II) solution (1000 ppm in 2% HNO₃, Roth) and approximately 15 mL HCl (trace metal grade) were mixed in aged de-ionized water and the solution was adjusted to pH 10.2 using HCl. Reagents were stored for >24 h in the dark before usage to increase the Luminol response (King et al., 1995).

Analysis of Fe(II) and H₂O₂ was performed on the same sample by loading one of two alternating reagent loops with Fe(II) reagent, while the other one was flushed with sample that flows through the detector. Switching of the valve position results in mixing of the sample with Fe(II) reagent and transport to the detector, while the other loop is loaded with H₂O₂ reagent. The two compounds were analyzed with at least four replicates. Standard additions were performed for each analytical run by spiking aged seawater with increasing amounts of an Fe(II) or H₂O₂ solution. An Fe(II) stock solution was prepared from ammonium Fe(II) sulphate hexahydrate (99.997% purity, Sigma Aldrich) in de-ionized water and acidified using 1 µL concentrated HCl (trace metal grade, Fisher) per mL. This stock solution was diluted daily freshly in de-ionized water to be used for standard addition. The H₂O₂ spike solution was prepared by diluting H₂O₂ (TraceSelect, Fluka) in aged de-ionized water. For H₂O₂ quantification, the mean peak height was determined of repeated injections for samples and standard additions. The standard deviation of the peak heights was utilized to determine the standard deviation of the sample concentration. The same was applied for Fe(II) quantification, provided the Fe(II) was considered stable over the time duration of the measurements. When the Fe(II) signal decreased with time, which is commonly the case for standard additions, the decrease in signal with time was utilized to calculate the expected Fe(II) signal at time=0 of spiking of the sample with Fe(II) stock solution for calibration curve samples or the time were samples were subsampled from OTE samplers. The signal at time=0 was then utilized to calculate the sample concentration.

Luminol chemiluminescence is based on the oxidation of the luminol molecule, which results in the emission of light with a wavelength of ca. 425 nm (Rose and Waite, 2001). In the case of the H₂O₂ measurements in this study, the luminol molecules are oxidized by H₂O₂ in the presence of Co²⁺ as a catalyst (Yuan and Shiller, 1999). During Fe(II) analysis, Fe(II) is oxidized by oxygen, whereby hydroxyl and superoxide radicals (OH[•] and O₂^{•-}) are formed and then oxidize luminol (Rose and Waite, 2001). The light emission is detected by a photomultiplier tube (PMT), which converts photons into electrons and amplifies the signal.

Measured Fe(II) concentrations in surface waters can be high, despite the presence of enhanced oxygen concentrations, due to photoreductive processes (Barbeau et al., 2001; Voelker and Sedlak, 1995). Reported surface water Fe(II) concentrations are often higher than the dFe concentration of the same sample (e.g. Vedamati et al., 2014). This artefact has been attributed to interference by other compounds that are likely produced by photoreduction. Interferences have been determined to occur for example for Co(II) and V(IV) (Hopwood et al., 2017a). Therefore in this thesis no Fe(II) data from shallower depths than 40 m was used in data interpretation. The analysis of H₂O₂ interferences is also subject to interferences such as by Fe(II) and V(IV) (Hopwood et al., 2017b). Therefore, all H₂O₂ data where Fe(II) was >0.5 nmol L⁻¹ was excluded. The concentrations of V(IV) in the samples, however, is unknown, cannot be corrected for, and might result in an overestimation of the H₂O₂ and Fe(II) concentrations.

2.5 Stability of the soluble trace metal fraction

The soluble fraction (<0.02 μm) of TMs mainly exists as free cations and inorganic and organic metal complexes, and may include some small particles (nanoparticles) (Gledhill and Buck, 2012). A large fraction of soluble Fe is often present as Fe(II) especially in

sunlit surface waters and oxygen minimum zones (OMZs) (e.g. Barbeau et al., 2001; Lohan and Bruland, 2008; Vedamati et al., 2014). Therefore, if the sample is exposed to oxygen, for example during subsampling from OTE samplers, oxidation of Fe(II) to Fe(III) occurs and results in the formation of particles potentially larger than 0.02 μm on time-scales that may be shorter than the time between subsampling and filtration of soluble samples. This process might therefore bias the fractionation between soluble and dissolved phase. To avoid a large intrusion of oxygen into the samples, samples for further filtration of soluble samples were collected under an environment overpressurized with N_2 gas. In order to test the stability of the soluble TM fraction in the pre-filtered samples, filtration of soluble samples was performed for one coastal station in the Peruvian OMZ as soon as possible within 1 hour after subsampling from OTE-samplers, and approximately after 12 hours storage refrigerated on two different sets of pre-filtered (0.2 μm) subsamples.

We observed a drastic decrease in the soluble fraction of Fe with duration of storage of the samples before filtration, with the most pronounced concentration decrease in samples with low oxygen concentrations (Figure 2.4). This indicated that immediate filtration of the soluble samples after sampling was required in order to obtain realistic results, particularly in OMZ samples where the intrusion of traces of oxygen can result in oxidation and subsequent transformation of soluble Fe into the colloidal or particulate phase. Samples filtered within 1 hour (sFe1) revealed higher concentrations than Fe(II) within the oxycline, indicating that soluble Fe was also present as oxidized Fe(III), likely stabilized by organic ligand complexation (Gledhill and Buck, 2012). In contrast for the sample closest to the seafloor under anoxic conditions, concentrations of Fe(II) and sFe1 are very similar (within standard error). Due to the long time-requirement of soluble filtration using the method we employed (syringe filtration) it was usually not possible to

filter the soluble samples immediately. Therefore the results of soluble samples are not discussed in Chapters 4 and 5.

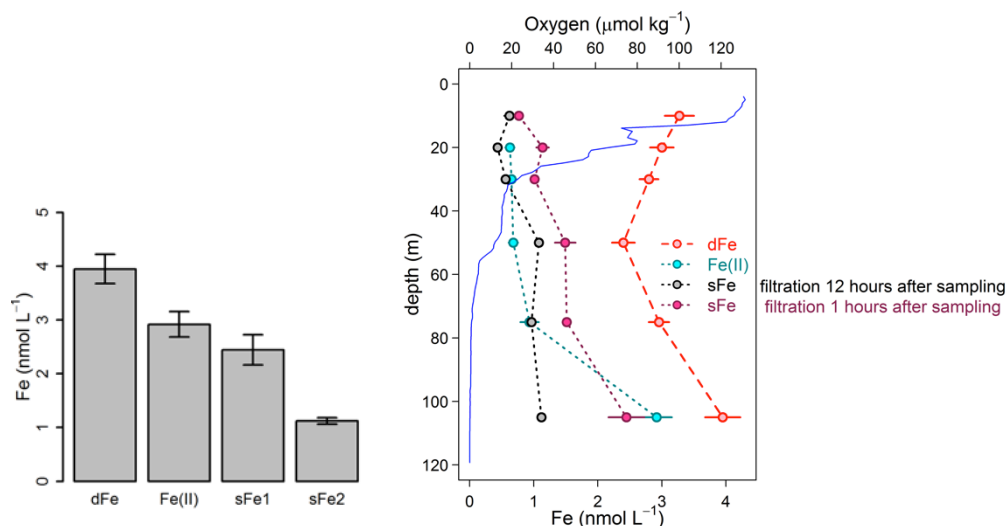


Figure 2.4: Test for soluble Fe (sFe) filtration. A) Fe concentrations of deepest sample (105 m) of a coastal station in the Peruvian OMZ (75.274 °W, 15.318 °S, Oct 2015). The filtration of soluble samples was performed either 1 hour after sampling of Niskin bottles for dFe (sFe1) or after 12 hours refrigerated storage of samples (sFe2). B) Depth profile of Fe(II), dFe, sFe1 (filtration 1 hour after sampling) and sFe2 (filtration ~12 hours after sampling) at the same station with oxygen plotted as blue line.

2.6 Iodide and Iodate analysis

Samples for iodide (I^-) and iodate (IO_3^-) were collected in combination with TM samples, as the redox couple is a sensitive indicator for suboxic conditions (Rue et al., 1997). In oxygenated waters, the oxidized form (IO_3^-) is the thermodynamically stable form, however, under reducing conditions a transition to the reduced form I^- occurs (pE ~10, in comparison the reduction potential of the redox couple Fe(II)/Fe(III) is ~ 0.8) (Stumm and Morgan, 1995). The distribution of I^- and IO_3^- in surface waters is influenced by photochemically-induced reduction, resulting in the presence of an increased fraction of iodine as I^- (Spokes and Liss, 1996). Additionally a slight surface depletion of total inorganic iodine ($I^-+IO_3^-$) is commonly observed due to microbial uptake or the microbial production of other iodine species (e.g. Chance et al., 2007). At greater depths the total concentration of $I^-+IO_3^-$ is typically constant at around 500 nmol L⁻¹ (Elderfield and

Truesdale, 1980), and under low oxygen conditions a large amount is present as I⁻ (Rue et al., 1997).

Iodide and iodate analysis was undertaken from the same sample bottle. Frozen samples were defrosted overnight at room temperature. Afterwards samples were stored refrigerated for a maximum of 5 days until iodate analysis. Iodide was analyzed by cathodic stripping square wave voltammetry after Luther et al. (1988). During voltammetry, the analyte is deposited on a hanging mercury drop electrode at a specific potential (here, -0.0488 V). In the next step, a voltage scan (mode: square wave, for scan details see Table 1.1) is applied to the electrode, resulting in the dissolution of the analyte back into solution (stripping) at a certain potential (-0.29 ± 0.05 V). This process is measured by changes in the current-potential behaviour at the electrode surface. The resultant current is proportional to the concentrations of the analyte (Scholz, 2015). The voltammetry unit consisted of a voltammeter stand (663 VA, Metrohm), an autosampler (863 Compact Autosampler, Metrohm) and a burette (843 Pump Station, Metrohm) for automated spike addition. The system was controlled by the 797 VA Computrance software (Metrohm). The method settings are given in Table 2.1.

Chapter 2: Sample collection and analysis

Table 2.1: Method settings for analysis of iodide by cathodic stripping square wave voltammetry

Electrode	Hanging mercury drop electrode (HMDE)
Drop size	Medium
Purge time	230s (with nitrogen)
Start potential	-0.09995 V
End potential	-0.9998 V
Deposition potential	-0.0499
Deposition time	15–180 s *
Scan rate	200 mV/s
Amplitude	0.02 V
Frequency	100 Hz

* adjusted according to expected concentration range

A maximum of 10 samples were analyzed per analytical run. An aliquot of 10 mL of each sample was transferred into a 12 mL autosampler vials and 100 μ L of 0.2% Triton X-100 were added to each sample. The burette was filled with an iodide standard solution made from potassium iodide (purity $\geq 99.5\%$, Sigma Aldrich) in de-ionized water prepared daily. Samples were automatically transferred into the voltammetry cell and analyzed in triplicates. Before deposition, samples were purged for 230 seconds with N_2 gas in order to remove oxygen from the sample solution, which would interfere with the analysis. The solution was stirred during deposition in order to maximize the amount of analyte in contact with the electrode. An equilibration period (5 s) without stirring was applied before stripping. Increasing the deposition time increases the sensitivity and is therefore adjusted according to the expected concentration range.

Four standard additions are automatically performed on the sample and measured in triplicates after each addition. Added concentration ranges varied largely according to cover the expected range of iodide concentrations in the sample. The applied standard addition should produce a linear regression line. If the calibration curve flattened at

higher concentrated standard additions, a reduction of the deposition time was required. After each sample the cell was automatically emptied and rinsed with de-ionized water prior to loading of the next sample.

Iodate samples were analyzed spectrophotometrically as described in Chapman and Liss (1977). In this method, sulphamic acid is used to reduce iodate to iodine. The reaction of iodine with excess iodide forms a coloured I_3^- ion, which was measured with a USB 4000 detector (Ocean Optics) and a light source (DT-Mini-2-GS, Ocean Optics), and using the spectra suite (Ocean optics) software. After equilibration of samples to room temperature, an aliquot of 10 mL sample was transferred into a glass cylinder and 250 μ L of 1.5 M sulphamic acid was added and mixed. After an incubation period of exactly 2.5 min, 750 μ L of 10% (w/v) KI solution was added and mixed. After another incubation period of 2 min, the sample was transferred into a 10 mL quartz glass cuvette and the absorbance was measured three times at 350 nm and at 700 nm. The de-ionized water blank spectrum was subtracted. A reagent blank was measured by adding all reagents to 10 mL of de-ionized water. Calibration was performed by standard additions, spiking 10 mL seawater with a KIO_3^- solution ($100 \mu\text{mol L}^{-1}$) to final added concentrations of 200, 400 and 600 nmol L^{-1} . An additional quantification of the reagent blank was performed with a double reagent standard addition, adding double the concentration of KIO_3 and double the amount of reagents.

3 Automated preconcentration of Fe, Zn, Cu, Ni, Cd, Pb, Co, and Mn in seawater with analysis using high- resolution sector field inductively-coupled plasma mass spectrometry

Insa Rapp¹, Christian Schlosser¹, Dagmara Rusiecka^{1,2}, Martha Gledhill¹ and Eric P.
Achterberg¹

Published in *Analytica Chimica Acta*

¹Marine Biogeochemistry Division, GEOMAR Helmholtz Centre for Ocean Research
Kiel, Kiel 24148, Germany

²Ocean and Earth Sciences, University of Southampton, National Oceanography Centre
Southampton, SO14 3ZH, UK

Abstract

A rapid, automated, high-throughput analytical method capable of simultaneous analysis of multiple elements at trace and ultratrace levels is required to investigate the biogeochemical cycle of trace metals in the ocean. Here we present an analytical approach which uses a commercially available automated preconcentration device (*SeaFAST*) with accurate volume loading and in-line pH buffering of the sample prior to loading onto a chelating resin (*WAKO*) and subsequent simultaneous analysis of iron (Fe), zinc (Zn), copper (Cu), nickel (Ni), cadmium (Cd), lead (Pb), cobalt (Co) and manganese (Mn) by high-resolution inductively-coupled plasma mass spectrometry (*HR-ICP-MS*). Quantification of sample concentration was undertaken using isotope dilution for Fe, Zn, Cu, Ni, Cd and Pb, and standard addition for Co and Mn. The chelating resin is shown to have a high affinity for all analyzed elements, with recoveries between 83 and 100% for all elements, except Mn (60%) and Ni (48%), and showed higher recoveries for Ni, Cd, Pb, Co and Mn in direct comparison to an alternative resin (*NOBIAS Chelate-PA1*). The reduced recoveries for Ni and Mn using the *WAKO* resin did not affect the quantification accuracy. A relatively constant retention efficiency on the resin over a broad pH range (pH 5–8) was observed for the trace metals, except for Mn. Mn quantification using standard addition required accurate sample pH adjustment with optimal recoveries at $\text{pH } 7.5 \pm 0.3$. UV digestion was necessary to increase recovery of Co and Cu in seawater by 15.6% and 11.4%, respectively, and achieved full breakdown of spiked Co-containing vitamin B₁₂ complexes. Low blank levels and detection limits could be achieved (e.g., $0.029 \text{ nmol L}^{-1}$ for Fe and $0.028 \text{ nmol L}^{-1}$ for Zn) with the use of high purity reagents. Precision and accuracy were assessed using *SAFe S*, *D1*, and *D2* reference seawaters, and results were in good agreement with available consensus values. The presented method is ideal for high throughput simultaneous analysis of trace

elements in coastal and oceanic seawaters. We present a successful application of the analytical method to samples collected in June 2014 in the Northeast Atlantic Ocean.

3.1 Introduction

A number of trace metals are essential micronutrients for phytoplankton growth and play important roles in ocean biogeochemical cycles (Boyd et al., 2007; Morel and Price, 2003). In particular iron (Fe) has been identified as a micronutrient that directly limits phytoplankton growth in high nitrate low chlorophyll regions, which constitute ~30% of the oceans surface (Boyd et al., 2007), and also controlling di-nitrogen fixation in oligotrophic gyres (Moore et al., 2009). Other trace metals such as cobalt (Co), zinc (Zn), cadmium (Cd), manganese (Mn) and copper (Cu) may also be (co-)limiting for phytoplankton growth and/or influence phytoplankton community composition (Moore et al., 2013; Morel and Price, 2003; Saito et al., 2008). Major sources of trace metals to the ocean include continental shelf sediments, mineral dust, river discharge, submarine hydrothermal activity, and glacial melt waters (Bruland and Lohan, 2006). Trace metal distributions are modulated by advection and diffusion, biological uptake, solubility, scavenging, organic ligand complexation and remineralization (Bruland and Lohan, 2006). In addition, some trace metals can be used as tracers for source inputs (e.g. Mn for lateral transport from continental margins; (Aguilar-Islas and Bruland, 2006; Landing and Bruland, 1980), and Pb for anthropogenic inputs (Boyle et al., 1986; Schaule and Patterson, 1981)).

Due to the complexity of these processes, and a paucity of data, our understanding of the distributions and dynamics of trace metals in the ocean remains limited. In response, the international GEOTRACES program was launched to sample and measure trace metal distributions throughout all of the major ocean basins in order to resolve controls on sources, sinks, and oceanic cycling of trace elements (Henderson et al., 2007). These sampling campaigns generate large numbers of seawater samples (often >1000) that

require reliable, high throughput analytical methods to determine the concentrations of a range of trace metals.

Trace metals occur typically at very low concentrations in seawater, ranging from a few pmol L^{-1} to nmol L^{-1} which are challenging to measure. In addition, alkali and alkaline earth elements are present at relatively high concentrations of up to several hundred mmol L^{-1} , and may cause challenges during ICP-MS analysis as a result of salt precipitation in parts of the instrument and isobaric interferences with the analyte of interest. Consequently, for most seawater samples preconcentration of the analytes and removal of the salt matrix is required prior to analysis. A range of preconcentration and extraction methods have been developed, including organic solvent extraction (Bruland et al., 1979; Danielsson et al., 1978), co-precipitation with magnesium hydroxide (Wu, 2007; Wu and Boyle, 1997), and solid phase extraction using chelating resins in columns or as a batch extraction onto suspended resin beads (Biller and Bruland, 2012; Lagerstrom et al., 2013; Lee et al., 2011; Milne et al., 2010; Sohrin et al., 2008).

A variety of resins have been developed with different functional groups that retain trace metals over a wide range of pH conditions, with recovery using diluted acids. For example, Toyopearl AF-Chelate-650M with iminodiacetic acid (IDA) functional groups has been used in conjunction with ICP-MS detection for determination of seawater Fe, Mn, Co, Ni, Cu, Zn, Cd and Pb (Milne et al., 2010). A nitrilotriacetic acid (NTA)-type Superflow resin has been employed with a single batch extraction and ICP-MS detection for Fe, Pb, Cd and Cu (Lee et al., 2011). NOBIAS Chelate-PA1, containing ethylenediaminetriacetic acid and IDA functional groups on a hydrophilic methacrylate resin, has been applied for the analysis of Al, Mn, Fe, Co, Ni, Cu, Zn, Cd and Pb with ICP-MS detection (Biller and Bruland, 2012; Sohrin et al., 2008).

Here we present a new method for simultaneous, accurate, and precise determination of dissolved Cd, Pb, Fe, Cu, Ni, Zn, Co and Mn in seawaters using a commercially available automated preconcentration device with subsequent analysis by ICP-MS. We applied a resin with immobilized carboxymethylated pentaethylenehexamine (CM-PEHA) functional groups (WAKO; Kagaya et al., 2009). Sample quantification was undertaken using isotope dilution for all elements apart from the monoisotopic elements, Co and Mn. Accuracy and precision were examined using standard reference seawater and resin performance was extensively tested over pH ranges between 1.9 and 8.1 to assess whether this newly tested resin can achieve constant recoveries over a wider pH range than previously studied resins. Resin performance was also directly compared to an alternative resin (NOBIAS Chelate-PA1) using the same preconcentration set-up.

3.2 Experimental

3.2.1 Reagents for sample pre-concentration

All reagents were prepared in de-ionized water ($> 18.2 \text{ M}\Omega \text{ cm}$; Milli-Q, Millipore). Nitric acid (SpA, Romil) was purified by single distillation in a sub-boiling perfluoroalkoxy-polymer (PFA) distillation unit (DST-1000, Savillex). Glacial acetic acid and ammonium hydroxide (20–22%) were of the highest purity (Optima, Fisher Scientific). Ammonium acetate (NH_4Ac) buffer (1.5 M) was prepared in de-ionized water using 140 mL ammonium hydroxide solution and 90 mL acetic acid for 1 L buffer, and adjusted to $\text{pH } 8.5 \pm 0.05$ using ammonium hydroxide or acetic acid. 1 M nitric acid was prepared using subboiled distilled nitric acid (d-HNO_3) diluted with de-ionized water. For preparation of the elution acid, 1 M d-HNO_3 was spiked with 250 ng L^{-1} indium (In) for drift correction during ICP-MS analysis. All reagents were stored in cleaned polypropylene (PP) containers provided by Elemental Scientific Inc. (ESI). All

containers and sample bottles were cleaned by soaking in 2% Decon for 1 day, 1.2 M HCl (reagent grade) for 5 days, 1.5 M HNO₃ (reagent grade) for 5 days and a final rinse with de-ionized water and in between the soaking steps. The buffer and diluted acid were prepared inside a fume hood within a clean laboratory (ISO 5). Further reagent handling was carried out in an ISO 3 laminar flow bench with a HEPA filter unit.

3.2.2 Spike solutions

Quantification of samples and reference seawater was performed for Fe, Zn, Cu, Ni, Cd and Pb using isotope dilution, and for the monoisotopic elements Mn and Co using standard addition. To assess changes in recovery following resin preconcentration, which affects both naturally occurring and spiked isotope, quantification using standard addition is necessary for all elements. Therefore, we distinguished between three different spikes used during sample preparation: (1) Isotope spike, (2) multi-element spike (for standard additions) and (3) Co-Mn spike.

The employed isotope spike solution contained artificially enriched ⁵⁷Fe, ⁶²Ni, ⁶⁵Cu, ⁶⁸Zn, ¹¹¹Cd and ²⁰⁷Pb. The isotopes were received in solid form (ISOFLEX USA) and were dissolved in concentrated d-HNO₃. After mixing in 2% HNO₃, concentrations were verified by ICP-optical emission spectroscopy (ICP-OES; 7500 Agilent) and by reverse isotope dilution using a multicollector ICP-MS (MC-ICP-MS; ThermoFisher Neptune). Spike ratios for ⁵⁶Fe/⁵⁷Fe, ⁶⁰Ni/⁶²Ni, ⁶³Cu/⁶⁵Cu, ⁶⁶Zn/⁶⁸Zn, ¹¹⁰Cd/¹¹¹Cd and ²⁰⁷Pb/²⁰⁸Pb were determined by MC-ICP-MS. A multi-element spike for standard additions containing Cd, Pb, Mn, Co, Fe, Ni, Zn, and Cu was prepared by serial dilution of individual stock standards (CertiPur, Merck) in 0.45 M d-HNO₃. For lower concentrated standard additions, further dilutions were prepared in 0.045 M d-HNO₃. A Co-Mn spike was prepared in a similar way as the multi-element spike by serial dilution of Co and Mn stock standards in 0.045 M d-HNO₃.

3.2.3 Seawater sample preparation

Sample preparation was performed in a laminar flow bench. All low-density polyethylene (LDPE) and fluorinated ethylene propylene (FEP) bottles used for sample preparation and standard solutions, were acid washed according to protocols for washing of sample bottles described above (Achterberg et al., 2001b). After each use the FEP bottles were rinsed with de-ionized water, filled with 0.35 M hydrochloric acid (HCl), and stored for a minimum of 4 days before next usage. Prior to use, the FEP-bottles were rinsed 5 times with de-ionized water and once with a few mL of the sample. Pipette tips were rinsed three times with 3 M HCl (Trace Metal Grade, Fisher) and 3 times with de-ionized water.

Method tests were made using filtered (0.2 μm Sartobran capsule filter, Sartorius) North Pacific (Cruise NH1417, 2014, 25 m depth) and Southern Ocean seawater (Cruise JR271, 2012, surface water), as specified. Seawater was sub-sampled from 25 L carboys into 1 L LDPE bottles (Nalgene) and acidified to pH 1.9 using concentrated HCl (UpA, Romil). 15 mL aliquots of acidified seawater were transferred into 30 mL FEP bottles (Nalgene). Seawater and reference seawater samples (SAFe S1, D1 and D2) were spiked with 125 μL of diluted isotope-spike. To determine Co and Mn concentrations in these samples, standard additions using the Co-Mn spike were performed on several ($n = 4-7$) 15 mL aliquots of North Pacific seawater covering a concentration range of 0.005–0.4 nmol L^{-1} for Co and 0.25–20 nmol L^{-1} for Mn. Prior to preconcentration, samples were UV-digested by placing the filled FEP-bottles into a homemade UV light box equipped with four low pressure mercury vapor lamps (25 Watt, Philips) (Milne et al., 2010). Sample bottles were UV irradiated for 4 hours (unless stated differently). For tests on efficiency of UV digestion and recovery, no isotope-spike was added to the seawater

and standard addition (n=7) was performed for all elements using the multi-element spike.

3.2.4 Preconcentration set-up

An automated system (SC-4 DX SeaFAST pico; ESI) with online pH buffering was used for sample preconcentration and seawater matrix removal. The preconcentration device (Figure 3.1) was equipped as recommended by the manufacturer. The autosampler (4DX FASTready) was equipped with a sample probe with 1.0 mm inner diameter (ID), a vacuum pump for sample aspiration and two independent rinse pumps supplying the rinsing station with 1 M d-HNO₃ from 4 L reservoirs. The reagents were distributed by a syringe system (S400V) consisting of an ethylene chlorotrifluoroethylene (CTFE) valve with PFA rotor and four syringes: one 12 mL CTFE/polytetrafluoroethylene (PTFE) syringe (S1), and three 3 mL quartz/PFA syringes (S2, 3 and 4). The reagent flow paths were controlled by a valve module (FAST DX 3) with two 11-port CTFE valves (V1 and V2) and one 5-port CTFE valve (V3), all three with a PFA rotor. The sample coil utilized in this study had a volume of 10 mL. All tubing connecting the valves was made of PFA. Valve 3 was connected to pressurized air for sample elution. The pressurized air was pre-filtered (ReZist Syringe Filter, PTFE, 5.0 μm, Whatman) in order to minimize any particle introduction. The buffer was cleaned in-line before mixing with the sample by a clean-up column (Nobias, ESI). Samples were eluted into 4 mL PP scintillation vials (Novodirect). The PP scintillation vials were cleaned in 2% Decon for 1 day, rinsed with tap water followed by de-ionized water, soaked 1 day in 1 M HCl heated to 45 °C, rinsed with de-ionized water, soaked 1 day in 1.5 M HNO₃ heated to 45 °C, rinsed 5 times with de-ionized water, and dried in a laminar flow bench.

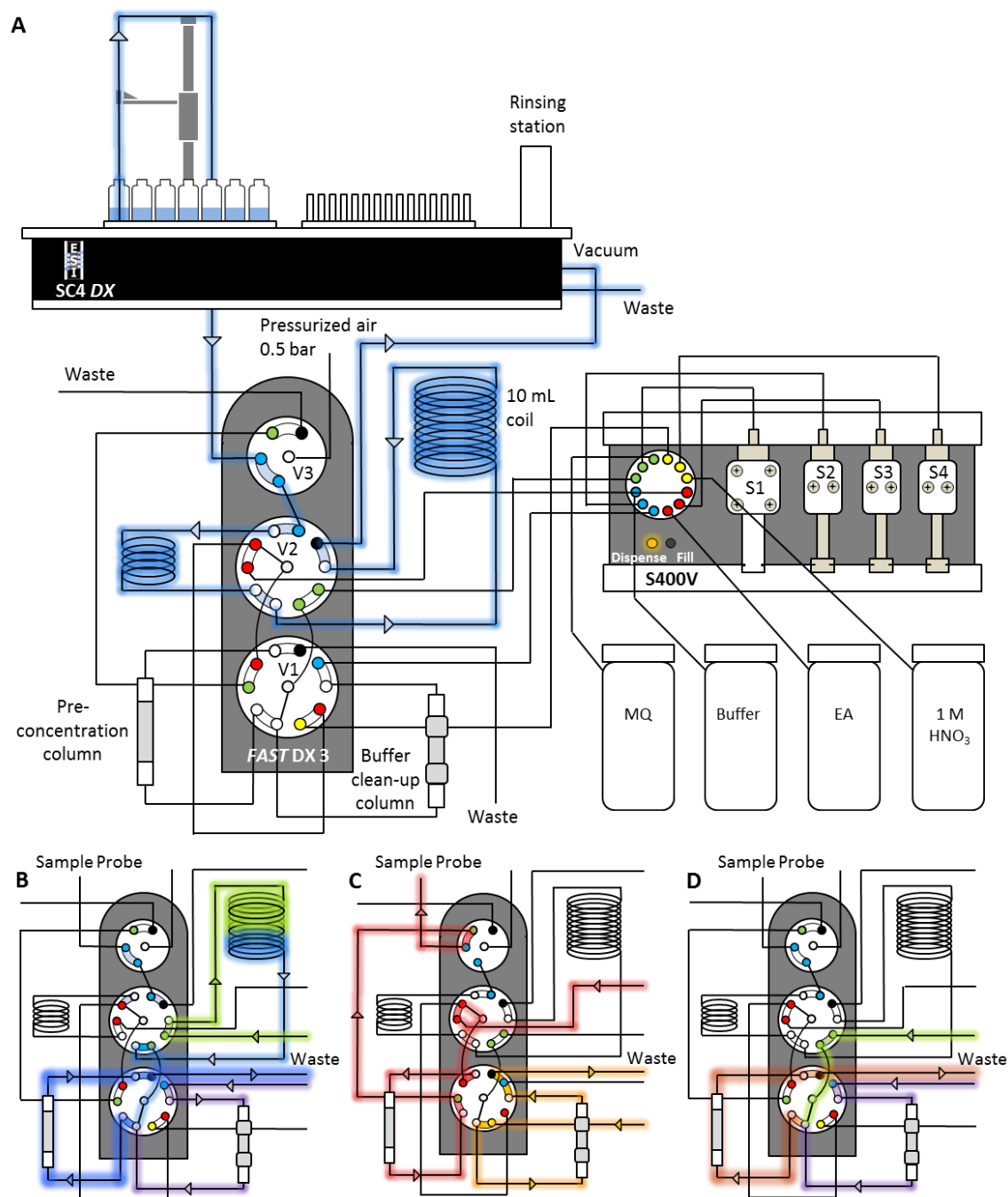


Figure 3.1: Schematic set-up of SeaFAST system and valve positions. A) Entire set-up including autosampler unit (SC4 DX), syringe system (S400V) and valve module (FAST DX 3) with the three valves in position for sample loading on coil (V1: Valve 1, V2: Valve 2, V3: Valve 3), blue line contours indicate sample flow path. B) Valve module in position for sample loading on resin and matrix rinsing. Line contours indicate sample and reagent flow (blue: sample, green: de-ionized water, purple: buffer, dark blue: sample-buffer mix). C) Valve module in position for elution. Line contours (red: elution acid (EA), orange: 1 M HNO₃). D) Valve module in position for column conditioning. Line contours (green: de-ionized water, purple: buffer, brown: de-ionized water-buffer mix).

3.2.5 Resins for preconcentration

Trace elements were preconcentrated with a WAKO chelate resin (similar to Presep® PolyChelate, Wako Pure Chemical Industries, Japan) with immobilized carboxymethylated pentaethylenhexamine (CM-PEHA) functional groups (Kagaya et al., 2009). The resin material was obtained from Wako Pure Chemical Industries via S. Kagaya (University of Toyama, Japan) and showed the same characteristics for trace metal recovery as Presep® PolyChelate which is commercially available as a packed resin (Kagaya et al., 2009; Kagaya et al., 2013). The performance of the WAKO resin was compared to the NOBIAS Chelate-PA1 chelating resin (Sigma Aldrich) in tests on recovery and sample carry-over. Both resin columns were prepared in 2 cm tapered mini columns with an internal volume of 27 μL (Global FIA) by filling approximately half the column with resin material (10–15 μL). The packed resins were cleaned by flushing for at least 4 h with 1 M d- HNO_3 .

3.2.6 Preconcentration and extraction

The ESI SC-Autosampler and preconcentration device was controlled using a modified protocol of the ESI Software Version 2.9.0.82c. The preconcentration procedure (Table 3.1) includes loading of the sample into a coil (Figure 3.1A), loading the sample onto the resin and rinsing off the seawater matrix using de-ionized water (Figure 3.1B), rinsing the sample introduction parts with 1 M d- HNO_3 , eluting the sample using elution acid (Figure 3.1C), cleaning the sample and buffer clean-up resins using elution acid and 1 M d- HNO_3 (Figure 3.1C, with change in position of valve 3), final rinsing of sample introduction/elution parts using 1 M d- HNO_3 and pre-conditioning of the preconcentration resin using the 1.5 M NH_4Ac buffer and de-ionized water (Figure 3.1D). In the utilized set-up, up to 63 samples (including samples for standard addition and reference samples) can be preconcentrated in one batch with a throughput of ca. 50

4 samples h⁻¹ which is similar to less automated methods (Biller and Bruland, 2012; Milne et al., 2010) but in the absence of an analyst.

Table 3.1: Steps of the preconcentration procedure

Step	Valve (V) positions	Syringe (S) action (flow rate – total volume)	Action
(1) Load sample on coil	V1: Load V2: Load V3: Load		Probe moves into sample, integrated vacuum pump turns on (28 s) and aspirates sample into 10 mL sample coil
(2) Load sample on resin	V1: Load V2: Inject V3: Load	S1: 2500 µL min ⁻¹ – 11000 µL S2: Adjusted for each sample set *	The 10 mL sample is pushed over preconcentration resin at same time as pH buffer
(3) Rinse matrix	V1: Load V2: Inject V3: Load	S1: 2500 µL min ⁻¹ – 7500 µL	Salt matrix is removed from the resin using de-ionized water
			Probe moves to rinsing station and sample loop and sample introduction system are flushed with 1 M d-HNO ₃
(4) Elution	V1: Inject V2: Load V3: Inject	S2: 1000 µL min ⁻¹ – 1050 µL	Preconcentrated metals are eluted using elution acid into 4 mL vials using pressurized air (0.3–0.5 bar)
(5) Clean Columns	V1: Inject V2: Load V3: Load	S3: 2000 µL min ⁻¹ – 3000 µL S4: 2000 µL min ⁻¹ – 3000 µL	Cleaning of preconcentration resin and buffer clean-up resin with elution acid and 1 M d-HNO ₃
(6) Condition Columns	V1: Load V2: Load V3: Load	S1: 2500 µL min ⁻¹ – 4500 µL S2: 550 µL min ⁻¹ – 1000 µL	Buffer and de-ionized water are pushed over the preconcentration resin in order to condition it for the next sample.
			Probe moves back to rinsing station and sample loop and sample introduction system are flushed with 1 M d-HNO ₃

* Depending on the sample pH and the desired pH for sample loading. For a sample acidified to pH 1.9 and a desired pH of 6.4 the required amount of buffer added was typically between 1188 µL (270 µL min⁻¹) and 1320 µL (300 µL min⁻¹).

3.2.7 Blanks

Blank contributions were determined as two separate parts, the manifold blank and the NH_4Ac buffer blank. The manifold blank accounted for contributions from the elution acid, any component of the preconcentration procedure (except buffer contributions) and manifold, as well as from the analysis on ICP-MS. The manifold blank was determined using the preconcentration method on the preconcentration device with modifications to the first three steps. Step 1 (Loading of sample on coil) and step 2 (Loading sample onto resin) were omitted and in step 3, a smaller amount (2500 μL) of de-ionized water was used for matrix removal. Elution, column cleaning and pre-conditioning steps remained the same as during seawater sample preconcentration. The NH_4Ac buffer blank was determined using two batches of diluted North Pacific seawater (1:10 dilution with de-ionized water), one batch acidified with 1200 $\mu\text{L HCl L}^{-1}$ and the other batch acidified with 2400 $\mu\text{L HCl L}^{-1}$. The seawater was diluted in order to reduce the concentrations of trace metals in the solutions. Fe concentrations in undiluted North Pacific seawater were $0.747 \pm 0.060 \text{ nmol L}^{-1}$ with analytical standard deviations exceeding buffer blank values. Both dilutions were treated the same as regular samples and analyzed in replicates ($n=5$) for each set of buffer. The buffer added in an automated manner during preconcentration was adjusted to obtain a similar pH (6.4 ± 0.2) for both dilutions. Buffer contributions were then calculated as the difference between the mean metal concentrations for the two buffer and acid volumes. This approach will also account for any contribution from the acid used for acidification. However the contribution of the high purity acid should be minimal in comparison to the buffer. The buffer contributions were also determined as the difference between obtained concentrations in the acidified (1200 $\mu\text{L HCl L}^{-1}$) diluted seawater and the concentration calculated using the mean value of repeated

measurements of the undiluted North Pacific seawater divided by 10 (dilution factor). As final buffer blank, the mean value of the two different approaches was applied.

3.2.8 ICP-MS

Preconcentrated samples were analyzed using an Element-XR high resolution sector field inductively coupled plasma mass spectrometer (Thermo Fisher Scientific) in low resolution (R=300) for ^{110}Cd , ^{111}Cd , ^{207}Pb , ^{208}Pb , ^{95}Mo , ^{96}Mo and ^{115}In and in medium resolution (R=4000) for ^{56}Fe , ^{57}Fe , ^{60}Ni , ^{62}Ni , ^{63}Cu , ^{65}Cu , ^{66}Zn , ^{68}Zn , ^{59}Co and ^{55}Mn allowing isobaric interferences (e.g. $^{40}\text{Ar}^{16}\text{O}$ on ^{56}Fe) to be resolved. Specification of autosampler, sample introduction system, gas flow rates and RF Power are listed in Table 3.2.

Table 3.2: ICP-MS instrumentation and settings

Instrument	Element XR, Thermo Fisher Scientific
Autosampler	4DX FASTready , ESI
Nebulizer	200 μL PFA nebulizer, AHF
Nebulizer uptake rate	180 $\mu\text{L min}^{-1}$
Sampler Cone	Ni, ICP-MS Cones LTD
Skimmer Cone	Ni 'H', ICP-MS Cones LTD
Spray Chamber	PFA Scott-Spray Chamber, AHF
Injector	Sapphire injector, AHF
Cool gas flow (L min^{-1})	14.5–15.32
Sample gas flow (L min^{-1})	1.174–1.210
Auxiliary gas flow (L min^{-1})	0.70–0.73
RF Power (W)	1110–1117

The instrument was tuned before each run to obtain maximum sensitivity and stability. For tuning, a solution of In and Uranium (U) was used and standard deviations of both

elements were below 1.5%. As a result of the use of Ni cones, a relatively high Ni background signal was obtained. The Ni background signal could be reduced by running the instrument with diluted tap water (1:10 in de-ionized water) for 2–4 h in order to plate the cones. Afterwards, the instrument was run with 1 M d-HNO₃ to clean the tubing and instrument from remaining metals from the diluted tap water. Interferences of MoO⁺ on ¹¹⁰Cd and ¹¹¹Cd were corrected as described by Wu and Boyle (Wu and Boyle, 1997). Briefly, Mo standards were prepared by serial dilution of a Mo stock solution (Inorganic Ventures) in 1 M d-HNO₃ with concentrations between 2 and 200 nmol L⁻¹ and were measured at the beginning and end of each analytical run. The isotope ⁹⁵Mo was measured on all samples and the slopes from the linear regression of ⁹⁵Mo/¹¹⁰Cd and ⁹⁵Mo/¹¹¹Cd obtained from the Mo standards was used to correct for MoO⁺ interference on ¹¹⁰Cd and ¹¹¹Cd counts of the samples.

A diluted multi-element solution, diluted isotope spike solution, and 1 M d-HNO₃ were analyzed after every 10th sample during each ICP-MS run. This was done in order to correct for an instrumental mass bias producing slightly different isotopic ratios than the true naturally occurring isotope ratios in the multi-element solution and the artificial isotope ratios of the isotope spike solution used during sample preparation. The multi-element solution was prepared from individual stock standards (CertiPur, Merck) in 1 M d-HNO₃. The isotope spike solution was also diluted in 1 M d-HNO₃. The 1 M d-HNO₃ used for preparation of the dilutions was from the same batch as the acid analyzed on the ICP-MS in order to allow correction of the count rates for contribution from the 1 M d-HNO₃.

3.2.9 Calculation of elemental concentration and uncertainties

Isotope ratios of Cd, Pb, Fe, Ni, Cu and Zn of the samples were calculated after subtracting mean counts of three manifold blanks. The concentrations of these elements

were then calculated as described by de Jong et al. (2008). Isotope ratios of the multi-element and isotope spike solutions obtained using the ICP-MS analyses were used instead of the stated isotope ratios of these solutions. Concentrations of Co and Mn calculated using standard addition were based on linear regressions of the sequentially-spiked sample. Standard additions were performed after every 10th sample and the mean slope from one standard addition run before and one after the sample was used for sample concentration calculation. Sensitivity changes of the mass spectrometer were corrected for using ratios of Co and Mn count rates to indium count rates for standard additions and samples.

Measurement uncertainties were calculated after the Nordtest approach (Magnusson et al., 2012) incorporating uncertainties of within-lab reproducibility and uncertainties derived from the bias of determined reference materials to the certified or nominal values of the reference materials. This approach creates higher uncertainties (between 13% and 25% in our study) than previously published uncertainties for oceanic trace metal measurements but is accounting for random as well as systematic effects and consequently provides a more reliable and realistic estimation of uncertainties. Uncertainties of the measurement itself using only standard deviations in count rates and isotope ratios or standard addition slopes typically revealed uncertainties between 1% and 10%.

We applied the square root of the square sum of two separately determined uncertainties to obtain the combined uncertainty u_c (Eq. 3.1).

$$u_c = \sqrt{u(R_w)^2 + u(bias)^2} \quad (3.1)$$

With $u(R_w)$ being the within lab reproducibility and $u(bias)$ being the method and laboratory bias.

The within lab reproducibility was accounted for as the uncertainty obtained for multiple measurements of the same sample or reference material over a time period of several months. Here the pooled relative standard deviation of repeated measurements of the reference seawaters SAFe S, D1 and D2, and North Pacific seawater was applied. $U(bias)$ was calculated as described in (Magnusson et al., 2012) after Equation 3.2.

$$u(bias) = \sqrt{RMS_{bias}^2 + u(Cref)^2} \quad (3.2)$$

Where RMS_{bias} is the root mean square of the bias value (as % difference from the consensus value) (Eq. 3.3) and $u(Cref)$ is the uncertainty of the consensus value (Eq. 3.4).

$$RMS_{bias} = \sqrt{\frac{\sum(bias_i)^2}{n}} \quad (3.3)$$

$$u(Cref) = \sqrt{\frac{\sum u(Cref_i)^2}{n}} \quad (3.4)$$

With $bias_i$ being the difference between determined mean concentration of reference materials and the reported consensus values, n being the number of different reference materials used and $u(Cref)_i$ being the reported uncertainties in consensus values. Final uncertainties (U) were determined as $u_c \times 2$.

3.2.10 Reference Material

To assess the accuracy of our analytical procedure, we analyzed reference seawater and compared our results to the available consensus values. Reference seawater standards collected as part of the SAFe inter-comparison projects S (surface, ~10 m), D1 and D2 (deep, 1000 m) were used (Bruland, 2009).

3.3 Results and Discussion

3.3.1 UV-digestion

Previous studies using chelating resins for trace element preconcentration in seawater samples have shown that trace element recovery, particularly for Co and Cu, can be reduced by the presence of strong, metal-binding ligands that prevent full preconcentration by the resin (Achterberg et al., 2001a; Biller and Bruland, 2012; Milne et al., 2010). UV-digestion of the samples has been shown to be effective in breaking down organic complexes and achieving full recovery for Co and Cu (Achterberg et al., 2001a; Biller and Bruland, 2012; Milne et al., 2010; Vega and van den Berg, 1997). The acidification of the seawater samples to pH 1.9 following collection, with consequent dissociation of organic-metal complexes, appears to facilitate efficient preconcentration of other trace metals (Biller and Bruland, 2012; Milne et al., 2010).

Efficiency of UV-digestion was tested by determination of Cu and Co concentrations after different time periods of UV exposure (10 min to 4 h) of acidified (pH 1.9) Southern Ocean seawater in FEP bottles (Figure 3.2). The strength and concentrations of Co and Cu binding ligands in the Southern Ocean seawater were unknown and may have influenced the outcome of this experiment. In order to better constrain the efficiency of the UV-treatment, we also performed this test using the same seawater, spiked with a known amount (0.1 nmol L^{-1}) of vitamin B₁₂ (added Co concentration determined separately by ICP-MS = $0.086 \pm 0.001 \text{ nmol L}^{-1}$). Vitamin B₁₂ is a Co complex known to be present at concentrations up to a few pmol L^{-1} in open ocean seawater and a few tens pmol L^{-1} in coastal seawater (Bonnet et al., 2013; Zhu et al., 2011). In addition, a UV digestion was performed for 250 min using quartz glass cuvettes rather than FEP bottles to investigate whether UV light transparency was sufficient for the FEP bottles.

Efficiency of lamps was tested with old lamps (>4000 h operation; recommended lifetime of lamps is 9000 h) and with new lamps (<100 h operation). The tests using old and new lamps have been performed on the same sample of seawater but have been carried out after different durations samples have been acidified, with 5 days for tests using old lamps and 4 weeks for tests using new lamps.

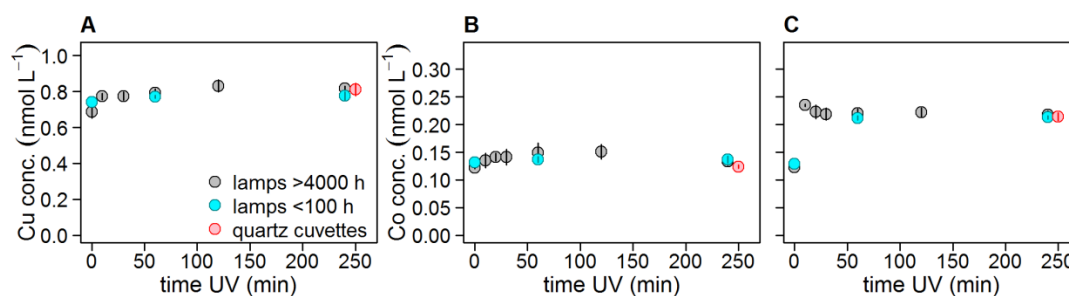


Figure 3.2: UV digestion efficiency experiment for Co and Cu with Southern Ocean water. A) Cu concentrations (in nmol L⁻¹) determined after UV exposure of up to 240 min with old UV lamps >4000 h and new UV lamps <100 h, and using quartz glass cuvettes rather than FEP bottles. Error bars show the standard deviation of three repeated samples. B) The same as A for Co. C) The same as B after spiking the seawater with vitamin B₁₂. The Co concentration after 10 min of UV treatment was higher than at any other time points, indicating possible contamination.

Co and Cu concentrations increased by 15.6% and 11.4%, respectively, between non UV-treated Southern Ocean seawater samples (Co: 0.117 ± 0.003 nmol L⁻¹, Cu: 0.678 ± 0.034 nmol L⁻¹) and samples UV treated for 30 min. After 30 min, no further significant increase was observed (t-test, $p > 0.05$). The Co concentration in vitamin B₁₂ spiked seawater with no UV treatment was only slightly higher by 0.006 nmol L⁻¹ (0.123 ± 0.003 nmol L⁻¹) to the original seawater concentration. After 20 min of UV exposure, Co added as the B₁₂ complex was quantitatively recovered. Total measured Co concentration was 0.223 ± 0.012 nmol L⁻¹. This demonstrates that Co in the vitamin B₁₂ molecule was not retained on the resin, and after about 10–20 minutes of UV exposure, all Co was released from the vitamin B₁₂ and quantitatively recovered on the resin. We did not observe any significant difference between used and new UV lamps (t-test, $p > 0.05$), indicating that after >4000 h operation, the UV lamps were still efficiently degrading

organic compounds that complexed Co and Cu. In all tests, Cu and Co concentrations obtained after 250 min of UV exposure in quartz cuvettes were indistinguishable (t-test, $p > 0.05$) from those in FEP bottles, indicating the FEP bottles are as suitable as quartz cuvettes for UV treatment. Cu and Co concentrations in seawater without UV treatment increased by 7.3% and 8.2%, respectively, with increased duration of storage from 5 days to 4 weeks of the acidified samples prior to preconcentration. Hence, it is possible that after 4 weeks of storage a fraction of the Cu and Co-complexes was broken down under acidic conditions, increasing the recovery. Co concentrations in vitamin B₁₂ spiked seawater increased only slightly in comparison to the concentration obtained after UV digestion. This indicates Co-vitamin B₁₂ complexes, do not significantly dissociate by acidification to pH 1.9 for a period of less than 4 weeks.

3.3.2 Recovery and pH

The chelation of metals by the functional groups on the resin is influenced by pH, and consequently the recovery of the trace metal depends on the pH of the sample. Therefore it is necessary to buffer the acidified sample to a pH where best recoveries are achieved. However, trace metal colloids can be formed after acidified samples are buffered to a pH higher than 2 and may alter the retention of trace metal on the resin (Kremling et al., 2007; Schlosser et al., 2011). In this study, pH is adjusted online prior to loading onto the resin, minimizing the time trace metal colloids can be formed and increasing the reproducibility by eliminating changes in time periods samples have been buffered before loading on the resin. To assess the optimal pH for the chelating resin used in this study, we tested the recoveries for Fe, Zn, Cu, Ni, Cd, Pb, Co, and Mn in the range of pH 1.9 and 8.1. To reduce analytical variability at low concentrations we spiked North Pacific seawater with the multi-element spike (final concentrations: 5.35 nmol Fe L⁻¹, 5.76 nmol Zn L⁻¹, 7.14 nmol Ni L⁻¹, 4.77 nmol Cu L⁻¹, 0.98 nmol Co L⁻¹, 2.45 nmol Cd L⁻¹,

0.68 nmol Pb L⁻¹, 6.14 nmol Mn L⁻¹). Modifications to seawater pH were achieved by addition of different amounts of buffer to the sample prior to loading onto the WAKO resin. Figure 3.3 displays the count rates (exact recoveries were only quantified at pH 6.2 and 7.0; see Table 3.3) obtained for the different elements and isotopes from the same seawater sample buffered to different pH values. Count rates were not corrected for blank contributions and isobaric interferences. Hence, a slight increase in count rates for some metals could have been achieved by an increased buffer contribution with increasing amounts of buffer added. But these contributions were very low (<1% at pH 6.4) compared to the concentrations in the utilized seawater (see section '3.3.5 Procedural blanks and detection limits').

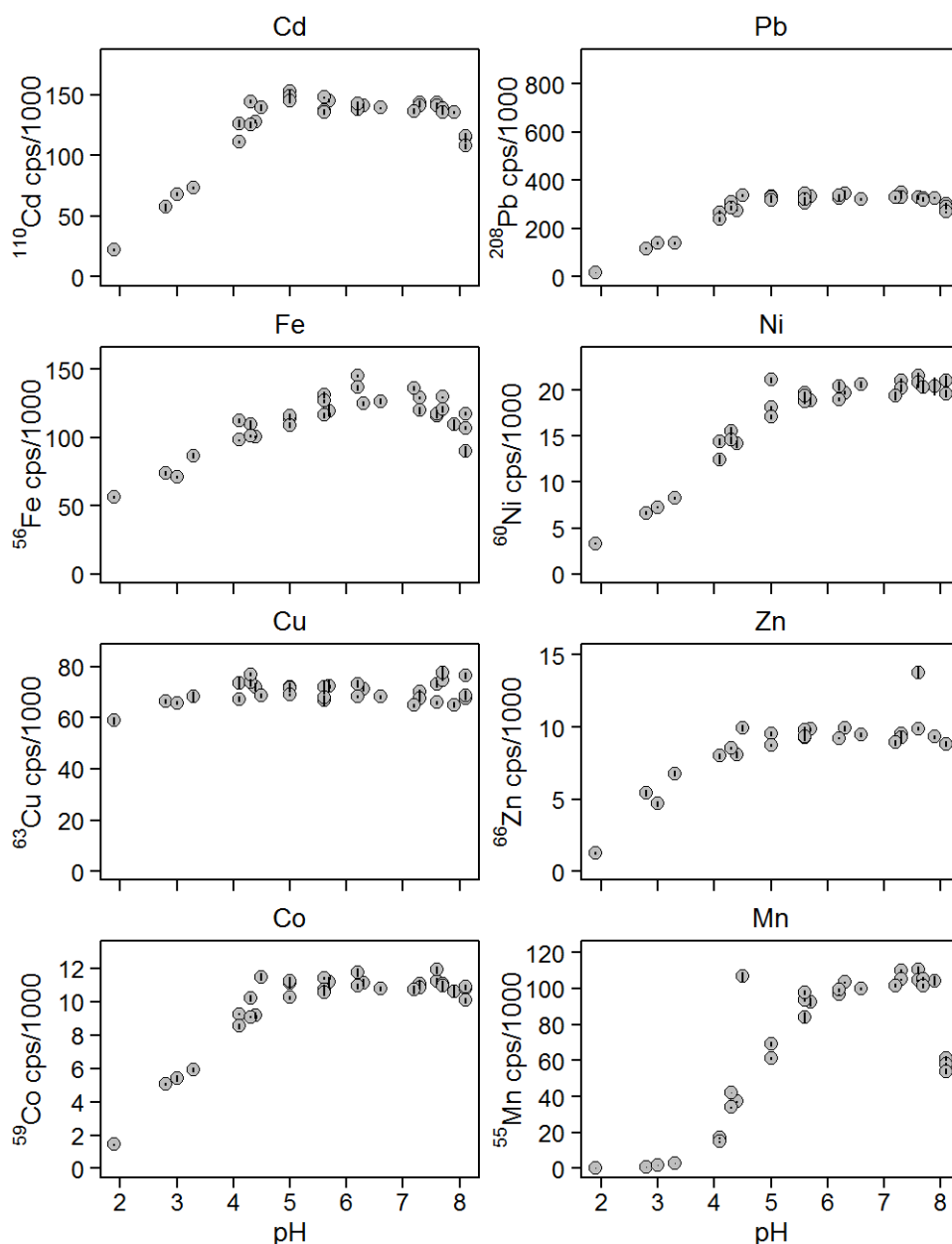


Figure 3.3: Count rates (cps) for the most abundant isotope of Cd, Pb, Fe, Ni, Cu, Zn, Co and Mn in North Pacific seawater with added spikes of trace metals over a pH range between 1.9 and 8.1. Displayed count rates are not corrected for blank contributions and isobaric interferences and were obtained in one analytical session.

All elements apart from Cu showed significantly lower recoveries at the lowest pH of 1.9 and recovery typically increased with increasing pH. Cu recoveries were remarkably constant over the entire pH range tested with slightly lower recoveries at pH 1.9. Recoveries of Cd, Pb, Fe, Zn and Mn showed a decrease at the highest pH of 8.1. Between pH 5 and 7.9 most elements (Cd, Pb, Cu, Zn and Co) showed a relatively

constant recovery, whereas Mn and Ni showed an increase in count rates up to pH 7.1. The recovery of Fe showed a maximum between pH 5.6 and 7.4. Good recoveries for all elements apart from Mn at pH 5–8 are very similar to previously observed pH ranges for Toyopearl (Milne et al., 2010) and NOBIAS (Biller and Bruland, 2012) resins. Mn recoveries at pH 5 were about 50% of the maximum recovery achieved at $\text{pH } 7.5 \pm 0.3$ (Figure 3.3), whereas a low retention of Mn (less than 10% of maximum recovery) was obtained at pH 5.0 for the Toyopearl resin (Milne et al., 2010). Nevertheless, Mn recoveries still increased significantly up to pH 6.2.

Isotopic ratios for Pb, Fe, Ni, Cu and Zn were constant over the entire range of pH investigated (Figure 3.4), which shows that calculations of concentrations of these elements by isotope dilution is possible over a wide range of pH without any significant bias to one isotope, provided recovery does not drop sufficiently to alter quantification accuracy. However, Cd showed a decrease of $^{110}\text{Cd}/^{111}\text{Cd}$ ratio with decreasing pH, which can be contributed to MoO^+ interferences for both ^{111}Cd and ^{110}Cd , with stronger interference for ^{111}Cd due to the natural isotope ratio of $^{96}\text{Mo}/^{95}\text{Mo}$ of 1.73 (we observed 1.7 times larger interference for ^{111}Cd than for ^{110}Cd). The significance of MoO^+ interferences increases with decreasing pH due to the decrease in Cd recovery, whereas best recovery for Mo on the WAKO resin was between pH 2 and 4.5 (Kagaya et al., 2009). Thus, for Cd analysis it is important to operate at a buffered pH higher than pH 5 in order to minimize potential MoO^+ interferences. During a typical analytical run with Cd concentrations ranging from 0.011 to 1.089 nmol L^{-1} , observed MoO^+ interferences resulted in an overestimation of Cd concentrations of 3–9 pmol L^{-1} , compared to MoO^+ corrected concentrations. This level of interference is negligible at deep water Cd concentrations, but contributes a large fraction to surface seawater Cd concentrations, which are typically below 10 pmol L^{-1} (Xie et al., 2015).

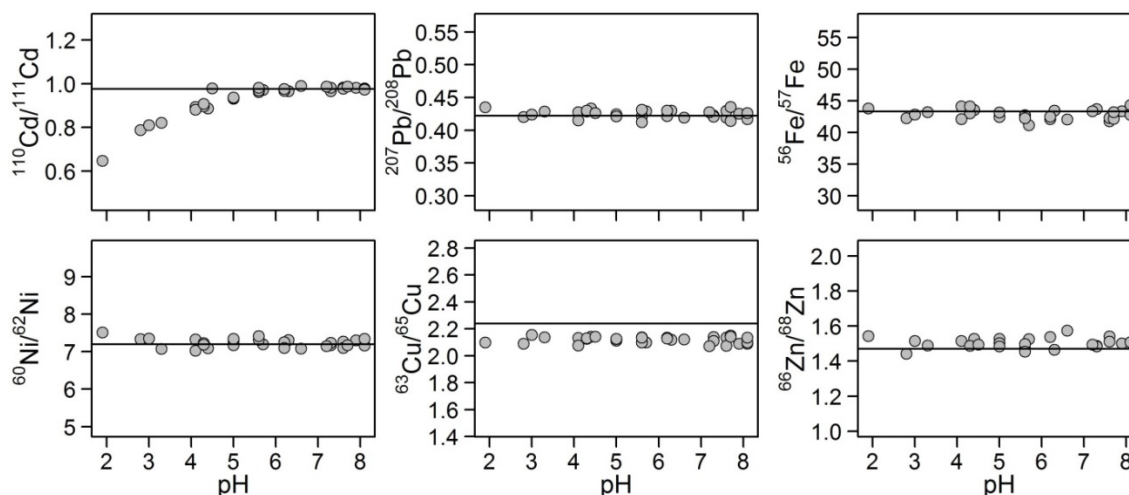


Figure 3.4: Isotope ratios obtained for Cd, Pb, Fe, Ni, Cu and Zn (natural isotopic composition) over a pH range employed during preconcentration of between 1.9 and 8.1 in North Pacific seawater. Ratios were not corrected for MoO^+ interferences and instrumental mass bias. Horizontal lines indicate the natural isotopic ratios.

For optimal recovery for all eight trace metals using the WAKO resin, a pH range between 6 and 7.5 appears suitable. Preconcentration at the lower end of this pH range is preferential to keep the volume addition of buffer, and consequently the buffer trace element contribution, to a minimum. Recoveries were quantified for all elements using the WAKO resin at pH 6.2 and 7.0, and compared to the NOBIAS resin at pH 6.1 (optimal pH range: 6.2 ± 0.3 ; Biller and Bruland, 2012). To quantify trace metal recovery from the chelating resin, standard additions using multi-element spike were performed in triplicate (duplicate for WAKO at pH 7.0) in North Pacific seawater. Exact preconcentration factors (loaded sample volume divided by volume of eluate) were determined by mass in the preconcentrated samples and used to determine the added concentrations in the eluate. Recoveries were determined as the ratio of the slopes obtained from the preconcentrated standard additions in seawater to the slopes of calibration curves prepared directly in the elution acid. Table 3.3 summarizes the obtained recoveries for the most abundant isotope for each element.

Table 3.3: Recoveries obtained for Cd, Pb, Fe, Ni, Cu, Zn, Co and Mn using a WAKO resin with sample preconcentration pH 6.2 and 7.0 and a NOBIAS resin at pH 6.1.

	¹¹⁰ Cd (%)	²⁰⁸ Pb (%)	⁵⁶ Fe (%)	⁶⁰ Ni (%)	⁶³ Cu (%)	⁶⁶ Zn (%)	⁵⁹ Co (%)	⁵⁵ Mn (%)
WAKO pH 6.2	97.1 ± 2.6	96.4 ± 2.8	80.3 ± 2.6	46.2 ± 1.1	99.3 ± 2.7	99.0 ± 2.8	87.8 ± 3.1	41.0 ± 0.9
WAKO pH 7.0	98.4 ± 0.5	96.5 ± 2.5	83.2 ± 0.9	48.0 ± 0.4	100.8 ± 1.2	99.9 ± 1.4	83.3 ± 1.2	59.6 ± 2.4
NOBIAS pH 6.1	85.5 ± 3.1	88.5 ± 1.6	83.1 ± 2.6	38.5 ± 1.4	102.7 ± 3.4	95.0 ± 3.4	73.1 ± 3.2	24.1 ± 0.2

Excellent recoveries of >95%, for pH 6.2 and 7.0 using the WAKO resin were obtained for Cd, Pb, Cu and Zn. Recoveries for Fe and Co were slightly lower, between 80 and 90%, but were very similar for pH 6.2 and 7.0. For Ni and Mn, however, recoveries at pH 6.2 were below 50%. Increasing the pH to pH 7.0 improved the recovery for Mn from 41 to 60%, but no significant increase of the recovery for Ni was observed. Highest count rates for Mn and Ni were observed around pH 7, which implies that the curves in Figure 3.3 do not reach 100% recovery for all elements. Previous reports using a WAKO resin found Ni recovery of 100% (Mn was not analyzed) at pH 4.0 using surface seawater and 3 M HNO₃ elution acid (Kagaya et al., 2009). Our observed recovery of 60% for Mn was similar to Mn recovery obtained using a Toyopearl resin at pH 6.3–6.8 (Milne et al., 2010). Recoveries of Fe, Cu and Zn using the NOBIAS resin at pH 6.1 were similar to the WAKO resin at both pH tested. All other elements showed lower recoveries, especially Ni (below 38.5%) and Mn (24.1%). The recoveries for Ni and Mn are again lower than previous studies which indicated recoveries of >96% for all elements using a NOBIAS resin and 1 M HNO₃ elution acid (Biller and Bruland, 2012; Sohrin et al., 2008). In a direct comparison between Nobias and the Presep® PolyChelate resin using artificial seawater, recovery characteristics were very similar for both resins apart from highest Mn recovery for Nobias being observed at pH 8, suggesting that the here tested

pH of 6.1 was not sufficiently high to achieve best recoveries (Kagaya et al., 2013). Recoveries can vary for the same resin as individual laboratory practices (such as length of storage time of resins, flow rates for sample loading, and resin volume) may have an impact on resin performance. It is thus important to assess recoveries for each approach. Here, we utilized a smaller resin volume (15 μL) than Kagaya et al. (2009) (their resin volume was 6 mL) with similar flow rates (3 mL min^{-1}) which might have impacted the recovery of Mn and Ni. The level of recovery does not affect the final quantified sample concentration, as this is accounted for in the isotope dilution and standard addition approaches. However, low recoveries may increase detection limits, since these will reduce overall element concentrations in eluted samples and therefore reduce total count rates. Here, despite the reduced recoveries for Ni and Mn, a strong correlation (R^2 typically >0.99) was obtained for standard additions for all elements over a broad range of naturally occurring concentrations in coastal and open-ocean seawater. However, due to the differing recoveries of Mn with changing pH, it is crucial to perform standard addition in seawater with the same pH as sample pH and to assure that samples are buffered to the same pH to guarantee accurate Mn determination.

3.3.3 Sample carry-over

The recovery experiments showed that we often do not obtain 100% recovery. Whereas this does not seem to cause a problem for metal quantification of single samples, problems could occur for the analysis of the following sample if metals were not fully eluted from the resin (during elution and cleaning step) and carried over to the next sample. To assess this risk, we measured five manifold blanks after the preconcentration of North Pacific seawater which was spiked to increase concentrations of trace metals (Fe: 51 nmol L^{-1} , Zn: 43 nmol L^{-1} , Ni: 48 nmol L^{-1} , Cu: 45 nmol L^{-1} , Co: 5 nmol L^{-1} , Cd: 25 nmol L^{-1} , Pb: 7 nmol L^{-1} , Mn: 51 nmol L^{-1}). This has been performed for both,

WAKO and NOBIAS resin. The obtained carry-over was negligible for all elements except Fe and Ni (Figure 3.5). Carry-over of Fe was 0.5% for both resins and was entirely washed out after the third manifold blank. Carry-over of Ni was 0.3% using the NOBIAS resin and dropped to background level at the second manifold blank. Carry-over of Ni using the WAKO resin was 1.3% and needed two manifold blanks before decreasing to less than 0.5%. Sample carry-over of 0.5–1.3% for Fe and Ni should not cause a problem if the concentration of preconcentrated samples are within the same order of magnitude, but caution needs to be applied if samples with very low concentrations are preconcentrated directly after samples containing Fe or Ni concentrations that are an order of magnitude or higher. To monitor the sample carry-over during preconcentration of a batch of samples, we recommend running two manifold blanks after every 10th sample.

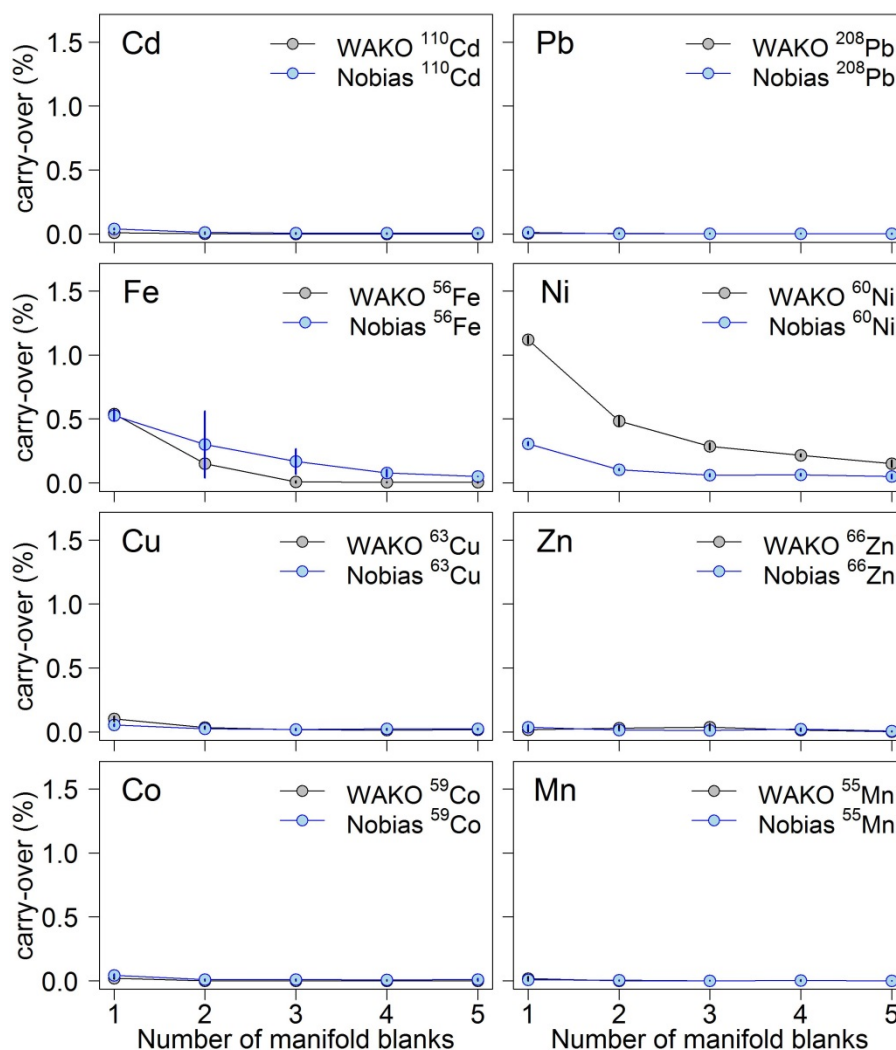


Figure 3.5: Carry-over of metals from an enriched North Pacific seawater sample to five following manifold blanks using a WAKO and a NOBIAS resin for preconcentration. The carry-over is given as percentage of counts of the blank to counts of the sample. This test was performed three times and error bars show standard deviations of triplicates.

3.3.4 Linearity

To verify the concentration range over which the recovery from the resin is linear and to investigate whether there is a potential of full saturation of the resin (with the used resin volume of approximately 15 μL) at certain threshold concentrations, standard additions were made to seawater solutions. For Ni, Cu, Zn and Co no decrease in recovery was observed over the entire concentration range tested in this experiment as shown in Figure 3.6. All data points lie in close proximity to the regression line obtained excluding the two highest concentrations of the standard additions. R^2 values for the regression lines

were >0.997 for all standard additions. For Cd, Pb, and Fe a slight decrease in recovery could be observed at concentrations higher than $100 \text{ nmol Cd L}^{-1}$, $30 \text{ nmol Pb L}^{-1}$ and $200 \text{ nmol Fe L}^{-1}$. Data points at higher concentrations lie below the regression line obtained excluding those data points. As these concentrations are much higher than typically observed natural seawater concentrations, the resin volume and sample volume used in this study can be applied over a wide range of seawater environments (coastal, deep sea). However in anoxic near sediment samples these concentrations can be exceeded for Fe (Scholz et al., 2016), in which case adjustment of sample or resin volume should be considered.

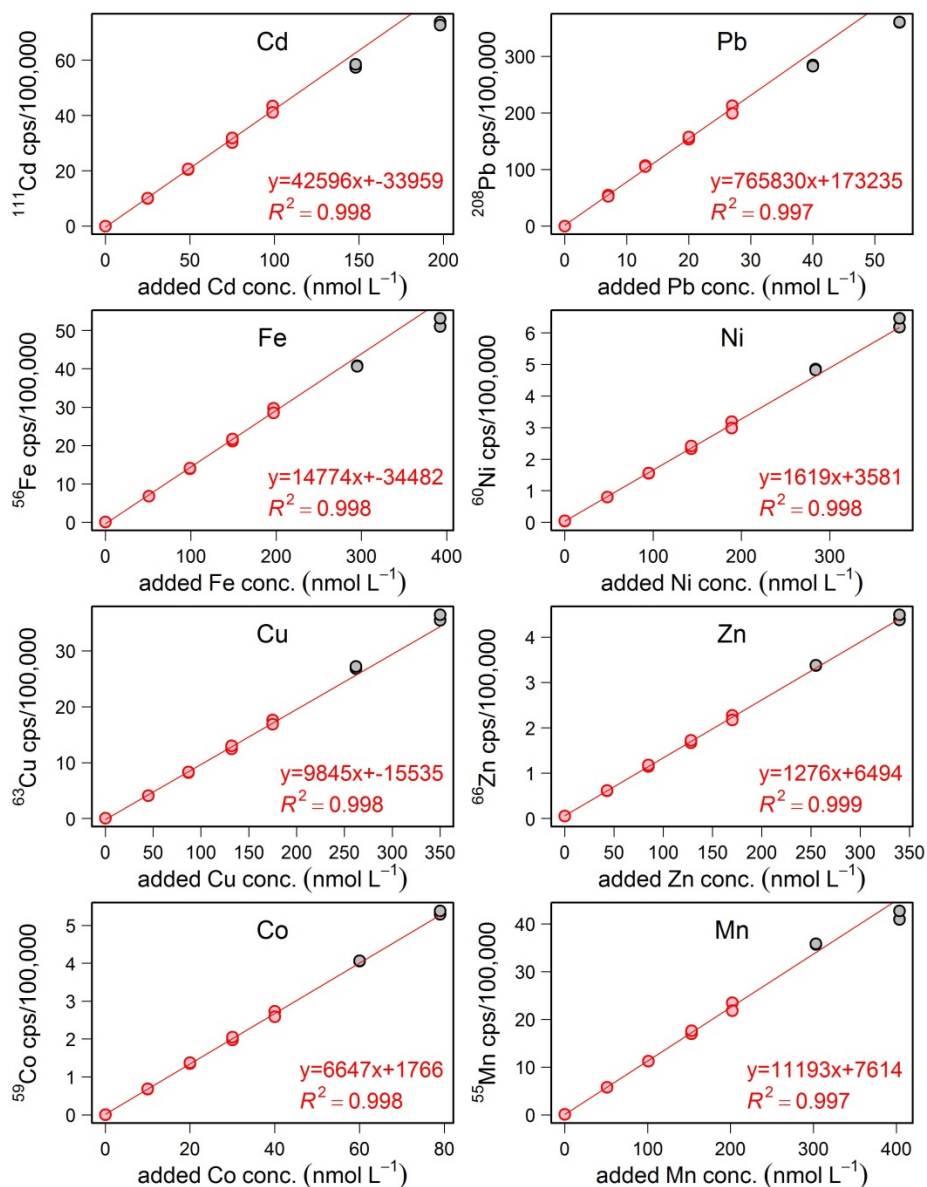


Figure 3.6: Linear regressions for high concentrated standard additions. Red line: regressions obtained by excluding the highest two concentrations. Red circles: data points included to calculate the linear regression. Standard deviations in count rates for each measurement were typically below 3%.

3.3.5 Procedural blanks and detection limits

At very low concentrations of trace metals in seawater it is crucial to accurately determine the contributions of reagents, the preconcentration device (i.e. resin, tubing) and ICP-MS to the observed sample concentration. We separately analyzed the contributions of the buffer (NH_4Ac buffer blank) and combined background counts of the preconcentration procedure, including the elution acid, chelating resin, manifold, PP-

vials and the analysis by ICP-MS (manifold blank). Buffer blanks were minimized by an additional buffer clean-up column, and especially for Zn buffer blanks were much lower than previously reported (Lagerstrom et al., 2013; Milne et al., 2010). The obtained values for manifold and buffer blank, the combined (procedural) blank, and the resulting detection limits are summarized in Table 3.4, and reveal similar values to previously reported detection limits of comparable methods (Biller and Bruland, 2012; Lagerstrom et al., 2013; Lee et al., 2011; Milne et al., 2010).

Table 3.4: Values for manifold and buffer blanks (± 1 standard deviation of repeated measurements) as well as combined blank with resulting detection limits (three times the standard deviation of the blank: $3 \times \text{SD}$)

	Manifold blank (pmol L^{-1})	Buffer blank (pmol L^{-1})	Procedural blank (pmol L^{-1})	Detection limit ($3 \times \text{SD}$) (pmol L^{-1})
Cd	0.7 ± 0.2	1.5 ± 0.2	2.2 ± 0.3	0.8
Fe	33.4 ± 4.4	34.0 ± 8.6	67.6 ± 9.6	28.8
Ni	111.6 ± 19.5	0.1 ± 0.2	111.7 ± 19.5	58.5
Cu	11.1 ± 2.3	3.1 ± 2.1	14.2 ± 3.1	9.3
Zn	4.7 ± 1.6	25.3 ± 9.2	30.0 ± 9.4	28.1
Mn	2.3 ± 1.6	11.2 ± 5.4	13.5 ± 5.6	16.9
Co	2.1 ± 0.7	0.6 ± 0.3	2.7 ± 0.8	2.5
Pb	0.084 ± 0.003	0.3 ± 0.2	0.4 ± 0.2	0.6

3.3.6 Precision and accuracy

The precision and accuracy of the method was evaluated by analysis of SAFe reference seawater S, D1 and D2. The results from multiple measurements of different analytical runs and the available consensus values for all measured elements are listed in Table 3.5. The calculated mean values include several measurements from the same bottle of D2, two different bottles of S1 and three different bottles of D1. Relative standard deviations were between 1.8% and 7.3% for concentrations $>0.1 \text{ nmol L}^{-1}$, between 4.7% and 9.7% for concentrations of $25\text{--}100 \text{ pmol L}^{-1}$ and increased at very low concentrations to 62.6%

for 3 pmol L⁻¹ of Cd. Precisions vary largely for different elements and between different concentration ranges and may also be affected by the use of different bottles of reference seawater. However, observed relative standard deviations did not differ significantly from previously reported precisions for S and D2 obtained using similar methods (Biller and Bruland, 2012; Lagerstrom et al., 2013; Milne et al., 2010; Sohrin et al., 2008). The results for S and D1 were in good agreement with the consensus values. We note that concentrations of the reference seawater D2 for Cd, Fe, Mn and Ni are slightly (<10%) higher than the reported consensus values. As measurements of S and D1 for these elements were in good agreement, we assume that our measurements were accurate, but that the bottle of SAFe D2 utilized here, likely contained somewhat higher concentrations of those elements.

Table 3.5: Analyzed reference seawater. Mean values and standard deviation in nmol L⁻¹ for Cd, Pb, Fe, Ni, Cu, Zn, Mn and Co and available consensus values in nmol L⁻¹ (± 1 standard deviation), n = number of measurements.

	SAFe S n=11	SAFe S consensus value	SAFe D1 n=13	SAFe D1 consensus value	SAFe D2 n=7	SAFe D2 consensus value
Cd	0.003 \pm 0.002	0.001	1.015 \pm 0.020	1.016 \pm 0.032	1.089 \pm 0.043	1.011 \pm 0.024
Pb	0.050 \pm 0.003	0.049 \pm 0.002	0.025 \pm 0.003	0.029 \pm 0.003	0.028 \pm 0.001	0.029 \pm 0.002
Fe	0.091 \pm 0.009	0.095 \pm 0.008	0.645 \pm 0.037	0.69 \pm 0.04	1.029 \pm 0.038	0.956 \pm 0.024
Ni	2.415 \pm 0.086	2.34 \pm 0.09	8.693 \pm 0.197	8.79 \pm 0.27	9.625 \pm 0.175	8.85 \pm 0.26
Cu	0.514 \pm 0.037	0.53 \pm 0.05	2.216 \pm 0.087	2.33 \pm 0.11	2.176 \pm 0.152	2.34 \pm 0.15
Zn	0.070 \pm 0.005	0.071 \pm 0.010	7.327 \pm 0.277	7.59 \pm 0.36	7.433 \pm 0.216	7.62 \pm 0.26
Co	0.005 \pm 0.001	0.005 \pm 0.001	0.048 \pm 0.003	0.046 \pm 0.005	0.048 \pm 0.003	0.047 \pm 0.003
Mn	0.814 \pm 0.033	0.810 \pm 0.062	0.365 \pm 0.017	-	0.437 \pm 0.029	0.36 \pm 0.05

3.3.7 Environmental Application—vertical oceanic profiles

Vertical profiles of seawater samples were collected using trace metal clean GEOTRACES protocols in June 2014 in the tropical Northeast Atlantic as part of the cruise Meteor 107. The samples were filtered on board using 0.2 μ m pore size cartridge

filters (Acropak 500, Pall) and acidified to pH 1.9 and subsequently analyzed in our laboratory for eight trace metals. The sampling location (18°15'N, 16°75'W) was 76 km (41 nm) off the Mauritanian coast and within an oxygen minimum zone with oxygen levels reduced to below 50 $\mu\text{mol kg}^{-1}$ at depths between 50 and 70 m, and between 420 and 450 m. Dissolved Cd, Ni, Cu and Zn (Figure 3.7) showed a nutrient-like profile with lowest concentrations in the surface waters and increasing concentrations with depth due to remineralization of sinking organic matter (Bruland, 1980). In contrast, dissolved Mn concentrations were enhanced in the surface waters and decreased with depth. The high dissolved Mn concentrations in the surface waters are maintained by photo-reduction of Mn(IV)-oxides to the soluble Mn(II) (Sunda and Huntsman, 1994), whereas Mn in subsurface waters is affected by particle scavenging (Landing and Bruland, 1980). Dissolved Pb profiles showed very low concentrations in surface waters, with a slight increase with depth, and were consistent with other observations in this area (Noble et al., 2015). Dissolved Fe and Co showed typical hybrid-type depth distributions, with low concentrations in the surface waters due to microbial uptake. At depth, Fe and Co showed increases in the low oxygen regions as a result of release from organic matter during remineralization, with lower concentration at other depths as a result of scavenging processes of the elements onto sinking particles (Boyd and Ellwood, 2010; Saito and Moffett, 2002).

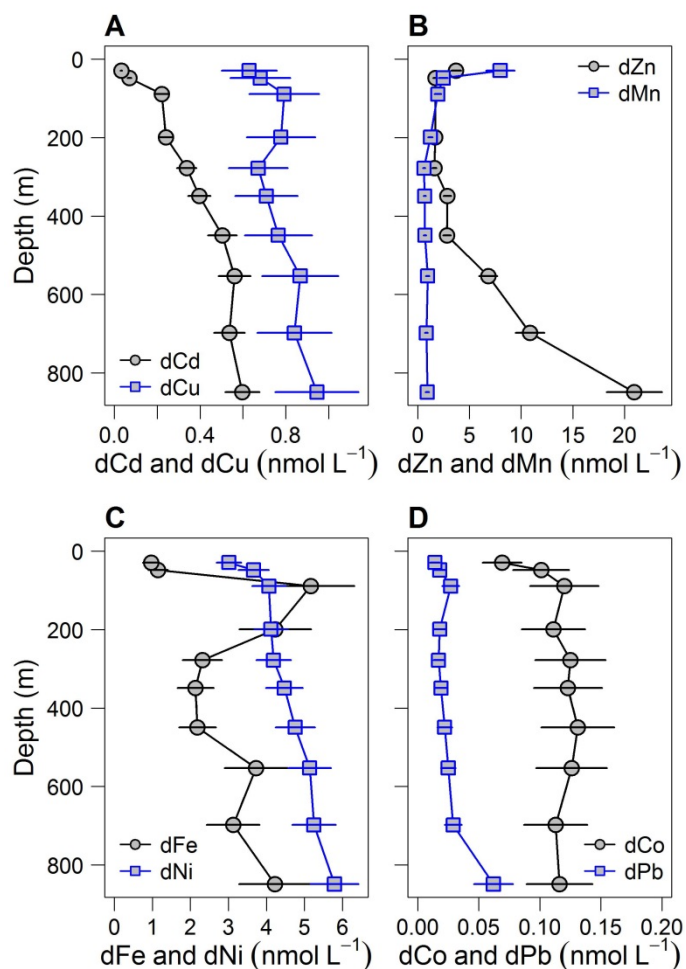


Figure 3.7: Depth profiles of eight trace metals. Samples were collected during cruise M107 using trace metal clean water sampler on June 12, 2014 (18°15'N, 16°75'W). Error bars indicate uncertainties calculated after the Nordtest approach.

3.4 Conclusion

Here we present a method for the simultaneous analysis of Cd, Pb, Fe, Cu, Ni, Zn, Mn and Co concentrations in seawater using an automated preconcentration device. The approach uses a sample volume of only 10 mL for preconcentration using syringe injection, thereby avoiding the need for large sample volumes. Samples are pH buffered inline reducing the sample preparation time and analytical artefacts by colloid forming trace metals at pH higher than 2. The blank contribution of the buffer is minimized via a separate additional buffer clean-up column. Isotope-dilution is used for determination of all elements except Mn and Co, eliminating sensitivity to variations in recovery and

preconcentration factor. However, minimal variability in automated sample loading or elution volumes allows accurate quantification via standard addition which is particularly important for the monoisotopic elements Co and Mn. Observed concentrations of reference seawater are in good agreement with available consensus values, confirming the high levels of accuracy. Full recovery of Co and Cu were achieved only after UV digestion of samples. Collectively, best recoveries for the suite of elements studied here were between pH 6–7.5 for the WAKO resin. This was mainly determined by low recoveries of Mn and increased MoO^+ interferences on Cd at lower pH. In direct comparison, of the WAKO to the NOBIAS resin, we could achieve better recoveries for most elements using the WAKO resin which is particularly important at very low concentrations of trace metals such as $<10 \text{ pmol L}^{-1}$ for Cd and Co in surface waters. Further improvement in time efficiency and sensitivity might be achieved by on-line coupling of the preconcentration system directly to ICP-MS.

Acknowledgements

The authors would like to thank Shigehiro Kagaya for facilitating the supply of the WAKO resin and the Captain and crew of the R/V Meteor. We also thank two anonymous reviewers for their constructive comments on this manuscript. This work was supported by The Deutsche Forschungsgemeinschaft as part of Sonderforschungsbereich 754: 'Climate-Biogeochemistry Interactions in the Tropical Ocean'.

4 Controls on redox-sensitive trace metals in the Mauritanian oxygen minimum zone

Insa Rapp¹, Christian Schlosser¹, Jan-Lukas Menzel Barraqueta¹, Bernhard Wenzel¹, Jan Lüdke¹, Jan Scholten², Beat Gasser³, Patrick Reichert², Martha Gledhill¹, Marcus Dengler⁴, and Eric P. Achterberg¹

to be submitted

¹Marine Biogeochemistry Division, GEOMAR Helmholtz Centre for Ocean Research Kiel, Kiel 24148, Germany

²Institute of Geosciences, Christian-Albrecht University Kiel, Kiel 24118, Germany

³IAEA-Environment Laboratories, Monaco

⁴Ocean Circulation and Climate Dynamics, GEOMAR Helmholtz Centre for Ocean Research Kiel, Kiel 24148, Germany

Abstract

The availability of the micronutrient iron (Fe) in surface waters determines primary production, N₂ fixation and microbial community structure in large parts of the world's ocean, and thus plays an important role in ocean carbon and nitrogen cycles. Eastern boundary upwelling systems and the connected oxygen minimum zones (OMZs) are typically associated with elevated concentrations of redox-sensitive trace metals (e.g. Fe, manganese (Mn) and cobalt (Co)), with shelf sediments likely forming a key source. Over the last five decades, an expansion and intensification of OMZs has been observed and this trend is likely to proceed. However, it is unclear how trace metal (TM) distributions and transport are influenced by decreasing oxygen levels. Here we present dissolved (<0.2 µm) and leachable particulate (>0.2 µm) TM data collected at 7 stations along a 50 km transect in the Mauritanian shelf region. We observed enhanced concentrations of Fe, Co and Mn corresponding with low oxygen concentrations (<50 µmol kg⁻¹), which were decoupled from major nutrients and nutrient-like and scavenged TMs (cadmium (Cd), lead (Pb), nickel (Ni) and copper (Cu)). Additionally, repeated station data suggest a direct link between dissolved Fe, Co, Mn and oxygen. An observed Fe decrease from 10 to 5 nmol L⁻¹ coincided with an oxygen increase from 30 to 50 µmol kg⁻¹ and a decrease in turbidity. The changes in Fe (Co and Mn) were likely driven by variations in their sediment fluxes, facilitated by lower oxygen concentrations and longer residence time of the water mass on the shelf. Variations in organic matter remineralization and lithogenic inputs (atmospheric deposition or sediment resuspension) only played a minor role in redox-sensitive TM variability. Vertical Fe fluxes from oxygen depleted subsurface to surface waters (0.08–13.5 µmol m⁻² d⁻¹) were driven by turbulent mixing and vertical advection, and were an order of magnitude larger than fluxes due to atmospheric deposition on the shelf. Benthic fluxes are therefore the

dominant dissolved Fe (dFe) supply to surface waters at the continental margins of upwelling regions. Overall, our results indicate that the projected future decrease in oxygen concentrations in OMZs may result in an increase in dFe concentrations.

4.1 Introduction

The micronutrient iron (Fe) is essential for phytoplankton growth, but due to its low solubility, biological uptake and supply rates, the availability of Fe is often low in open ocean surface waters (Bruland and Lohan, 2006). As a result, Fe limits primary production in high nitrate low chlorophyll regions (Boyd, 2007) and regulates dinitrogen (N₂) fixation in the low latitude regions (Moore et al., 2009). Alongside Fe, other TMs (TMs) such as cobalt (Co), manganese (Mn), zinc (Zn), cadmium (Cd) and copper (Cu) may (co-)limit phytoplankton growth and influence community composition (Browning et al., 2017; Moore et al., 2013; Morel and Price, 2003; Saito et al., 2008).

Oxygen minimum zones (OMZs) are characterized by stable subsurface oxygen minima, which are maintained by a combination of enhanced oxygen consumption in the thermocline and limited supply of ventilated water masses from the subtropics (e.g. Brandt et al., 2015; Karstensen et al., 2008; Wyrski, 1962). Enhanced oxygen consumption is a result of elevated surface productivity caused by upwelling of nutrient rich subsurface waters at eastern boundaries in the oceans through Ekman divergence, and intense remineralization of sinking particles. Elevated organic matter supply and water column oxygen depletion lead to enhanced benthic release of redox-sensitive elements by influencing sediment diagenetic processes (Noffke et al., 2012; Severmann et al., 2010). Elevated concentrations of sediment derived dissolved Fe, Co and Mn have been associated with lateral offshore advection in oxygen depleted waters in the Arabian Sea, Pacific and Atlantic Ocean (Biller and Bruland, 2013; Hatta et al., 2015; Hawco et al., 2016; Moffett et al., 2015; Noble et al., 2012).

Oxygen concentrations affect the distribution of redox-sensitive TMs by controlling oxidation rates and influencing microbially mediated redox transformations. The reduced

form of redox-sensitive TMs, such as cobalt (Co(II)), iron (Fe(II)) and manganese (Mn(II)), have a higher solubility in aqueous solutions, than their oxidized forms (Fe(III), Co(III), Mn(III/IV)) (Liu and Millero, 2002; Stumm and Morgan, 1995). Reduction of these metals occurs to a large extent in anoxic sediment pore waters by microbial induced dissolution of particulate Fe(III) and Mn(III/IV) oxides and hydroxides or reactions with hydrogen sulfide (H₂S) (Burdige, 1993; Chaillou et al., 2002; Froelich et al., 1979; Jensen et al., 1995). Sediment pore waters are released to overlying bottom waters by diffusion and bio-irrigation (Elrod et al., 2004; Green et al., 2002). In contact with oxygen, Fe(II) oxidizes to the poorly soluble Fe(III) species, that are rapidly transformed into amorphous Fe oxyhydroxides or scavenged onto particle surfaces (Wu and Luther, 1994). Mn(II) also oxidizes to insoluble Mn(III/IV) oxides, but due to the slow abiotic oxidation kinetics, especially under low oxygen conditions (e.g. von Langen et al., 1997), biotic oxidation by manganese oxidizing bacteria is the main oxidation mechanism for Mn (Moffett, 1994; Sunda and Huntsman, 1988; Tebo and Emerson, 1986). Co removal is mainly associated with the incorporation of Co into Mn oxides formed by biotic or abiotic Mn oxidation with Co co-oxidation (Moffett and Ho, 1996).

Stabilizing mechanisms that prevent removal by scavenging and precipitation of Fe, Co and Mn are organic ligand complexation (Elrod et al., 2004; Liu and Millero, 2002; Oldham et al., 2017; Parker et al., 2007) and adsorption onto small slow sinking particles (Lam et al., 2012). Recent studies suggest a potentially important role for dynamic exchange processes between dissolved and particulate phase of Fe, thereby influencing cycling and transport (Fitzsimmons et al., 2017; Labatut et al., 2014; Milne et al., 2017). This was indicated by iron isotope studies suggesting an equilibrium isotopic fractionation in deep waters (Labatut et al., 2014) and the concomitant deepening of the

dissolved and particulate iron plume that originated from a hydrothermal vent (Fitzsimmons et al., 2017).

A recent study using modelling approaches proposed an underestimated influence of shelf derived Fe on the global oceanic Fe budget (Dale et al., 2015). Spatial and seasonal variations in sediment derived TMs, as well as ex-situ sediment incubation experiments suggest a direct influence of bottom water and water column oxygen concentrations on the distribution of Fe, Co and Mn (e.g. Biller and Bruland, 2013; Homoky et al., 2012). Differences in benthic TM supply in field studies however are also influenced by a range of other processes as for example sediment type, organic matter supply etc. (Homoky et al., 2016). Ex-situ sediment incubation experiments offer a potential means to disentangle the influence of oxygen concentrations relative to these controls (Homoky et al., 2012); however, these experiments need to be interpreted within the context of the confined conditions that eliminate potentially important interactions in open systems, such as seawater exchange and mixing. Furthermore, they offer no means to confidently evaluate controls higher in the water column.

In an attempt to resolve the controls on TM release and stabilization in OMZs we measured the concentration of a suite of trace elements along a transect on the Mauritanian shelf in the Eastern Tropical North Atlantic (ETNA). The Mauritanian shelf is associated with a major OMZ (minimum O₂ concentrations below 40 µmol kg⁻¹; Brandt et al., 2015) and is an important Fe source to the North Atlantic Ocean (Milne et al., 2017). Furthermore, atmospheric dust deposition from the Saharan desert can markedly elevate surface water Fe concentrations in the ETNA (Conway and John, 2014; Rijkenberg et al., 2012). Recent observations suggest a decline in oxygen content of the oceans, particularly in the northern and southern eastern Atlantic, and an expansion of OMZs, modulated by the variability of our climate system (Hahn et al., 2017; Schmidtko

et al., 2017; Stramma et al., 2008b). These changes may result in changes in TM supply and mechanistic understanding of the factors regulating metal release and stabilization in OMZs is therefore urgently needed. This study was conducted to assess the direct influence of variability in water column oxygen concentrations on the distribution of redox-sensitive TMs and to crystalize responsible control mechanisms. Firstly, we assessed the significance of dFe from the OMZ to surface waters by turbulent mixing and compare estimated diffusive fluxes to the atmospheric deposition flux of Fe. Secondly, by focusing on the influence of oxygen and particles on the distribution of dissolved and leachable particulate TMs, including redox-sensitive (Fe, Co and Mn) and nutrient-type and scavenged elements (aluminum (Al), lead (Pb), nickel (Ni), Cd and Cu), we evaluate the importance of redox and non-redox controls on Fe, Co and Mn. Thirdly, we determine the influence of rapid variability in shelf current strength and O₂ concentration in regulating TMs.

4.2 Methods

4.2.1 Sampling

Samples were collected on RV Meteor cruise M107 in June 2014 at 7 stations along a cross-shelf transect at 18°20'N on the Mauritanian shelf in the Northeast Atlantic Ocean. The bottom depths of stations varied between 50 m on the shelf to 1136 m furthest off shore. Seawater sampling was carried out using a trace metal clean CTD (TM-CTD) rosette frame equipped with 24 trace metal clean samplers (12 L, Ocean Test Equipment (OTE)). The CTD frame was attached to plastic coated nonconductive steel cable and deployed using an auto fire module (AFM, Seabird) that closed the bottles at predefined depths. After recovery, the bottles were transferred to a clean-laboratory container and pressurized to 0.2 bar overpressure using filtered nitrogen gas. Samples were collected

unfiltered for total dissolvable (TD) TM measurements and filtered using a 0.2 μm cartridge filter (Acropack 500, Pall) for dissolved (d) TMs and iodide. Trace metal samples were collected in acid clean 125 mL low density polyethylene (LDPE) bottles (Nalgene), and iodide samples in opaque 60 mL high density polyethylene (HDPE) bottles (Nalgene). Trace metal samples were acidified to pH 1.9 using ultra clean HCl (UpA, Romil) and stored double-bagged for >6 months before preconcentration and analysis. Samples for iodide measurements were stored frozen at -20°C until analysis.

Samples for the determination of radium isotopes (^{223}Ra ; $T_{1/2} = 11.4$ d; ^{224}Ra $T_{1/2} = 3.7$ d) were obtained using in-situ filtration pumps (Challenger Oceanic) following the procedures described in Charette et al. (2015) and Henderson et al. (2013), Briefly, each in-situ filtration pump was equipped with two particle filters (70 μm ; 1 μm) and two MnO_2 impregnated cartridges (MnO_2 impregnated cartridges CUNO Micro Klean III acrylic) on which dissolved radium adsorbs. The pumped water volumes varied between 1000 L and 1700 L. For the determination of Ra in surface waters (~ 5 m water depth) about 200-300 L of seawater was pumped into barrels followed by filtration over MnO_2 coated acrylic fibers (Mn-fibers).

4.2.2 Trace metal analysis

Determination of Co, Mn, Fe, Cd, Pb, Ni and Cu was carried out as described in Rapp et al. (2017). Briefly, samples were preconcentrated using an automated preconcentration device (SeaFAST, Elemental Scientific Inc.) equipped with a cation chelating resin (WAKO; Kagaya et al., 2009). Samples were UV-digested prior to preconcentration to breakdown organic-metal complexes. Samples were buffered inline to $\text{pH } 6.4 \pm 0.2$ using 1.5 M ammonium acetate buffer, before loading onto the resin. The pH buffer was prepared using an ammonium hydroxide solution (22%, Optima grade, Fisher) and acetic acid (glacial, OPTIMA grade, Fisher) in de-ionized water (MilliQ, Millipore), adjusted to

pH 8.5. Retained TMs were eluted from the resin using 1 M distilled HNO₃ and collected in 4 mL polypropylene scintillation vials (Wheaton). The acid was distilled from supra-pure HNO₃ (SpA grade, Romil) using a sub-boiling PFA distillation system (DST-1000, Savillex). Preconcentration was performed within a clean laboratory (ISO 5) and all sample and reagent handling was performed within the same laboratory in an ISO 3 laminar flow bench with a HEPA filter unit. Preconcentrated samples were analyzed by high resolution inductively coupled plasma-mass spectrometry (HR-ICP-MS, ELEMENT XR, ThermoFisher Scientific) using isotope dilution for Fe, Cd, Pb, Cu and Ni and standard additions for Co and Mn. SAFe reference seawater S and D2 were analyzed with each analytical run and concentrations produced were in good agreement with consensus values (Table 3.5).

Leachable particulate (Lp) concentrations were calculated as the difference between TD and dissolved concentration. The limit of quantification (LOQ) for the Lp concentrations was determined as the sum of the analytical standard deviations of TD and dissolved concentrations. Extended uncertainty calculations were performed after the Nordtest approach (Naykki et al., 2015) accounting for random as well as systematic errors (Rapp et al., 2017). The Lp fraction only represents the particulate fraction which is readily dissolvable in the acidified samples during storage at pH 1.9 for 6 months and therefore does not contain any refractory particle components. The more labile fraction of particulate TMs mainly includes TMs in organic/biogenic particles and adsorbed to particle surfaces and oxides (Hurst et al., 2010).

4.2.3 Aluminum measurements

Aluminum concentrations were determined in surface water samples for all stations along the transect and at two stations (3 and 8) for the entire water column. Samples were analyzed for Al according to Hydes and Liss (1976). All the samples were analyzed in

the clean laboratory (ISO 5). Acidified samples were buffered offline with a 2 M ammonium acetate buffer (Romil, UpA) to a pH between 5.1 and 5.2. Buffered samples were spiked with a 2 mg L⁻¹ lumogallium (TCI) solution. The lumogallium solution was prepared in 2 M ammonium acetate buffer (Romil, UpA). After spiking, samples were heated up for 1.5 h at 80°C in an oven (Heratherm, Thermo Scientific) and left to cool down overnight at room temperature to allow the formation of a fluorescence Al complex. Samples were measured using a fluorescence spectrophotometer (Cary Eclipse, Agilent). The samples were measured with an excitation and emission wavelength of 465 and 555 nm, respectively. All samples were analyzed in duplicate and the concentrations calculated from the peak heights via standard addition. GEOTRACES reference sweater (GS) was run with a mean average value of 27.76 ± 0.17 nM (n=4).

4.2.4 Iodide measurements

Frozen samples were defrosted overnight at room temperature prior to analysis for iodide by cathodic stripping square wave voltammetry after Luther et al. (1988). The voltammetry unit consisted of a voltammeter stand (663 VA, Metrohm), an autosampler and an automatic burette (Dosino, Metrohm) for automated spike addition. The system was controlled by a 797 VA Computrace (Metrohm).

4.2.5 Oxygen and nutrient analysis

Oxygen was measured at 63 CTD stations along the 18°20`N transect using a Seabird SBE 9 CTD rosette system equipped with double sensor packages for oxygen, salinity and temperature and 24 OTE samplers (10 L). Oxygen sensor data were calibrated by Winkler titration (Hansen, 2007; Winkler, 1988) on 348 discrete water samples that were taken from the OTE samplers. The oxygen calibration was done using a linear fit with respect to oxygen concentration, temperature, and pressure. An uncertainty of

1.5 $\mu\text{mol kg}^{-1}$ was determined. On-board nutrient measurements of nitrite (NO_2^-), nitrate (NO_3^-), phosphate (PO_4^{3-}) and silicic acid (Si(OH)_4) of the discrete water samples were conducted using a QuAatro autoanalyzer (Seal Analytical) according to Grasshoff et al. (1983).

Apparent Oxygen Utilization (AOU) was calculated as the difference between saturation concentrations of oxygen and measured oxygen concentrations. The saturation concentration of oxygen was calculated after the Weiss methods (Weiss, 1970) using the R package marelac (Soataert et al., 2016) taking into account salinity and temperature.

4.2.6 Radium analysis

On-board the ship the Mn-cartridges and Mn-fibers were washed with Ra-free fresh water and afterwards partially dried with filtered compressed air to remove excess water. The samples were analyzed for ^{223}Ra , ^{224}Ra and ^{228}Th using a Radium Delayed Coincidence Counting System (RaDeCC) (Moore and Arnold, 1996). For the efficiency calibration of the RaDeCC, ^{227}Ac and ^{232}Th standard solutions were used, and the calibration followed the procedure described in Scholten et al. (2010) and Moore and Cai (2013). Counting errors were propagated following Garcia-Solsona et al. (2008). As the Mn-cartridges do not adsorb radium quantitatively we report here only $^{224}\text{Ra}_{\text{ex}}/^{223}\text{Ra}$.

4.2.7 Turbulence measurements and vertical flux calculations

In order to advance understanding of the role of benthic Fe supply to the high productive surface in the upwelling region, diffusive fluxes and upwelling induced vertical advective fluxes were estimated. At depth in the water on a continental margin, solutes are transferred vertically toward the surface waters by turbulent mixing processes and by vertical advection forced by Ekman divergence (e.g. Steinfeldt et al., 2015):

$$J_z = K_z \frac{\partial[TM]}{\partial z} + w \cdot \Delta[TM] \quad (4.1)$$

Here, K_z is the turbulent eddy diffusivity, $\partial[TM]/\partial z$ the vertical gradient with depth of the trace metal concentration [TM], $\Delta[TM]$ a TM concentration difference and w represents vertical velocity. The equation is solved vertically integrating the tracer transport budget equation between two vertical layers while ignoring lateral fluxes, changes of w with depth and assuming steady state. However, vertical advective fluxes resulting from meso- and submesoscale processes along sloping isopycnals were not considered. TM-fluxes were calculated for the depth interval from the upper boundary of the shallow oxygen depleted waters to a depth of increased chlorophyll a concentrations (8–29 m depth).

Diffusive Fe fluxes were determined by combining concurrently measured microstructure profiles with TM concentration measurements from the TM-CTD stations. The microstructure measurements were performed with an MSS90-D profiler (S/N 32, Sea & Sun Technology). The loosely-tethered profiler was optimized to sink at a rate of 0.55 m s^{-1} and was equipped with three shear sensors, a fast-response temperature sensor, and an acceleration sensor, two tilt sensors and conductivity, temperature, depth sensors sampling with a lower response time. At TM-CTD stations with bottom depths less than 400 m, 18 to 65 microstructure profiles were available at each station. At greater depths, the number reduced to 5 to 12 profiles. Standard processing procedures were used to determine the rate of kinetic energy dissipation (ϵ) of turbulence in the water column (see Schafstall et al. (2010) for a detail description). Subsequently, eddy diffusivities were determined from $K_\rho = \Gamma \epsilon N^{-2}$ (Osborn, 1980), where N is stratification and Γ is mixing efficiency for which a value of 0.2 was used. The use of this value has recently shown to yield good agreement between turbulent eddy diffusivities determined from

microstructure measurements and from tracer release experiments performed in our study region (Köllner et al., 2016). 95% confidence intervals for station-averaged K_p values were determined from Gaussian error propagation following Schafstall et al. (2010). Finally, diffusive fluxes were calculated by multiplying station-averaged K_p with the vertical gradient of the respective TM solute, implicitly assuming $K_z=K_p$.

The vertical advective flux by Ekman divergence requires determination of vertical velocity in the water column that varies with depth and distance from the coast line. Recent studies found good agreement between vertical velocities derived from Ekman divergence and from helium isotope equilibrium within the Mauritanian and Peruvian coastal upwelling regions (Steinfeldt et al., 2015) when parameterizing vertical velocities as (Gill, 1982):

$$w = \frac{\tau_y}{\rho f a} e^{-x/a} \quad (4.2)$$

where τ_y represents the alongshore wind stress, ρ the density of sea water, x the distance from maximum Ekman divergence taken here as the position at 50 m bottom depth on the shelf and a the first baroclinic Rossby radius. The parameterization results from considering the baroclinic response of winds parallel to a coastline in a two-layer ocean (Gill, 1982). The baroclinic Rossby radius $a = f^{-1} \sqrt{g \frac{\rho_2 - \rho_1}{\rho} \frac{H_1 H_2}{H_1 + H_2}}$ ($\rho_{1/2}$ and $H_{1/2}$ is density and thickness of the surface and lower layer, respectively) was found to be 15 km during the experiment, similar to the values determined by Steinfeldt et al. (2015) in the same region. Using average alongshore wind stress according to satellite data (0.025 Nm^{-2}), maximum vertical velocities of $3.7 \times 10^{-5} \text{ m s}^{-1}$ were determined, which decayed offshore to $1.7 \times 10^{-6} \text{ ms}^{-1}$ at the position of the 1000 m isobath at 18°N . As these vertical velocities describe the magnitude of upwelling at the base of the mixed-layer,

additional corrections need to be considered for deeper depths. Here, we approximated the vertical decay of w as a linear function with diminishing at the ocean floor. Additionally, the calculation of the vertical advective flux supplying solutes from the shallow oxygen depleted waters to the chlorophyll a maximum requires knowledge of a concentration difference $\Delta[\text{TM}]$ associated with the upwelling flux. Ideally, the vertical scale of the concentration difference is determined by correlation analysis of vertical velocity fluctuations and concentration variability at different depth ($w' \cdot [\text{TM}]'$). As these data are not available, we chose to use the mean vertical concentration differences over a vertical distance of 10 m. Thus, the vertical advective flux F_{az} at each station was estimated from $F_{az} = w(x, z) \cdot \frac{\partial[\text{TM}]}{\partial z} 10m$.

4.3 Results & Discussion

4.3.1 Oceanographic settings of the study area

The cruise was conducted along a narrow cross-shelf transect off the Mauritanian coast at 18°20'N. The vertical structure of the OMZ in this region is characterized by a deep OMZ at about 400 m depth, and a shallow OMZ at about 100 m depth (Brandt et al., 2015). Coastal upwelling of nutrient-rich deep water occurs as a result of offshore transport of surface waters caused by a Northeast Trade wind component parallel to the coast. While north of 20°N upwelling persists throughout the year, upwelling south of 20°N, including the Mauritanian upwelling region, undergoes seasonal changes in upwelling strength (Barton et al., 1998), with strongest upwelling occurring between December and April. The seasonal variability is mainly driven by changes in wind forcing associated with the migration of the Intertropical Convergence (Schafstall et al., 2010).

The eastern boundary circulation consists of the Mauritania Current (MC, Figure 4.1) flowing poleward against the equatorward winds at the surface and the Poleward Undercurrent (PUC) flowing in the same direction between depths of 50 and 300 m (Barton, 1989; Klenz et al., submitted; Mittelstaedt, 1983; Peña-Izquierdo et al., 2015). Both currents supply cold, oxygen and nutrient-rich waters of predominantly South Atlantic origin (South Atlantic Central Water, SACW) to the coastal upwelling region (e.g. Mittelstaedt, 1983; Mittelstaedt, 1991; Peña-Izquierdo et al., 2015). In response to the changing winds, the eastern boundary circulation likewise exhibits pronounced seasonal variability (Klenz et al., submitted; Stramma et al., 2008a). The strongest poleward flow is observed during the relaxation period between May and July when alongshore, upwelling-favorable winds weaken but wind stress curl is at its maximum (Klenz et al., submitted). During the upwelling season in boreal winter, the circulation more closely resembles the classical eastern boundary circulation structure, with a weak poleward undercurrent flowing beneath an equatorward coastal jet. The boundary circulations turn offshore at the southern flank of the Cape Verde frontal zone (CVFZ) (e.g. Tomczak, 1981; Zenk et al., 1991) at about 20°N separating SACW from more saline and oxygen-rich Central Waters formed in the North Atlantic (NACW).

Meridional sections of water mass properties and oxygen concentrations from around 18°N showed that waters with enhanced SACW proportion advected from the south as well as NACW coming from the north, have higher oxygen concentrations than the ambient waters (Klenz et al., submitted). The mixture of SACW and NACW waters found in the thermocline particularly during boreal winter, previously identified as a regional water mass and termed the Cape Verde SACW (SACW_{cv}) by Peña-Izquierdo et al. (2015), is a signature of an older water mass with lower oxygen concentrations than those of SACW or NACW concentrations due to a longer residence time and oxygen

consumption through remineralization. During the transition period in May through July the highest proportions of SACW in the boundary current region around 18°N are observed (Klenz et al., submitted).

The SACW transported poleward within the boundary circulation is supplied by the zonal North Equatorial Counter Current (NECC) and North Equatorial Under Current (NEUC), which flow eastward at about 5°N (Brandt et al., 2015) before diverging into a northward and a southward flowing branch in front of the African coast.

As a result of interactions between tidal currents and topography and critically sloping upper continental slope topography (e.g. Eriksen, 1982), the Mauritanian upwelling region is known for elevated nonlinear internal wave activity resulting in enhanced mixing in the water column of the upper slope and shelf region (Schafstall et al., 2010). Vertical fluxes of nutrients driven by mixing processes are amongst the largest reported in literature (Cyr et al., 2015).

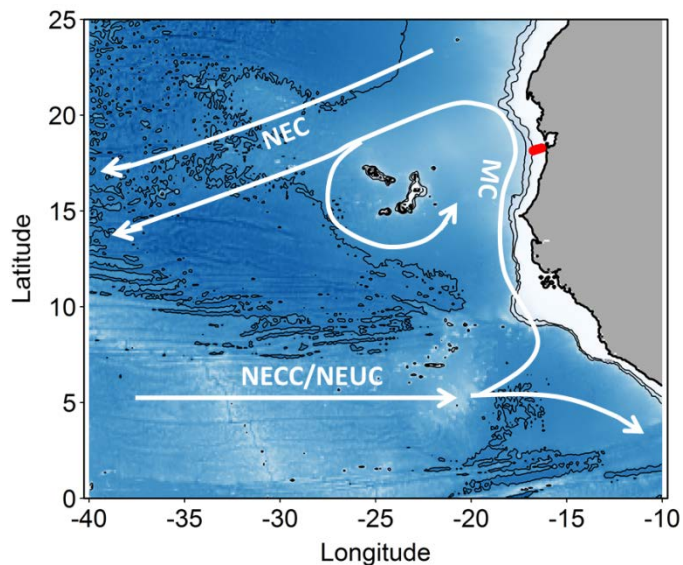


Figure 4.1: Map of the study area. Stations along the transect during M107 (June 2014) are displayed in red and major currents in white (adapted from Brandt et al. 2015). MC = Mauritania Current; NEC = North Equatorial Current; NECC = North Equatorial Countercurrent; NEUC = North Equatorial Undercurrent.

CTD and microstructure deployments were performed along the east-west transect in the period June 8 to June 27 (2014). Oxygen concentrations reached a deep minimum of 40–50 $\mu\text{mol kg}^{-1}$ at about 400 m and a shallow minimum of 30–50 $\mu\text{mol kg}^{-1}$ at about 50–100 m (Figure 4.2), which is in agreement with previous studies (Brandt et al., 2015). Mixed layer depths ranged between 10 and 22 m during the cruise. Salinity was highest at the surface (ca. 36.02) and generally decreased with depth to a minimum of 34.71 at around 1000 m. Nitrate (NO_3^-) concentrations in the surface mixed layer varied between 0.1 and 11.3 $\mu\text{mol L}^{-1}$ and phosphate (PO_4^{2-}) between 0.15 and 0.91 $\mu\text{mol L}^{-1}$. NO_3^- and PO_4^{2-} concentrations increased with depth to a maximum of 47.6 and 3.2 $\mu\text{mol L}^{-1}$, respectively (Figure 4.2).

Over a time period of 19 days, two stations were reoccupied along the transect at water depth of 170 m (18.23 °N, 16.52 °W, 1st deployment: June 12, 2nd deployment: June 21) and 189–238 m (18.22°N, 16.55°N, 1st deployment: June 24, 2nd deployment: June 26). Minimum oxygen concentrations of 30 $\mu\text{mol kg}^{-1}$ observed before June 15 increased to 50 $\mu\text{mol kg}^{-1}$ after June 19 or June 24, depending on the location. This change was attributed to an observed increase in current speed of the MC flowing northward parallel to the coast line transporting relatively oxygen-rich water and decreasing the residence time of the water mass on the shelf.

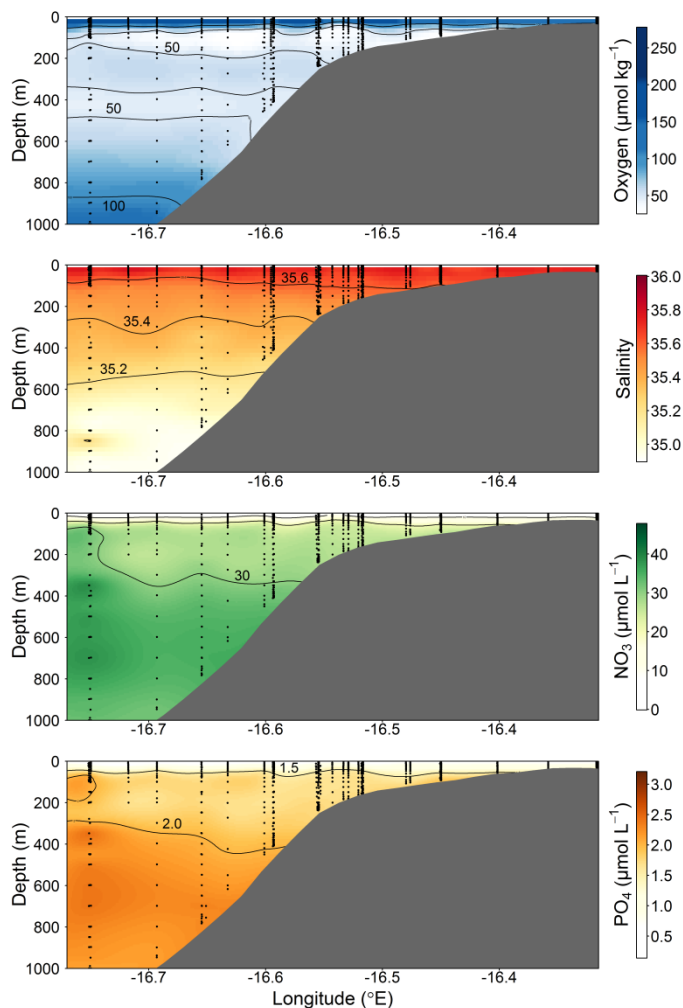


Figure 4.2: Section plots of oxygen ($\mu\text{mol kg}^{-1}$), salinity (PSU), NO_3 ($\mu\text{mol L}^{-1}$) and PO_4 ($\mu\text{mol L}^{-1}$) along the transect off the Mauritanian coast in June 2014.

4.3.2 Spatial distribution of dissolved and leachable particulate trace metals

Dissolved and LpFe concentrations ranged between $0.97\text{--}18.5 \text{ nmol L}^{-1}$ and $1.6\text{--}351 \text{ nmol L}^{-1}$, respectively (Figure 4.3A,B). Surface waters had lowest dFe ($0.97\text{--}4.7 \text{ nmol L}^{-1}$) and LpFe ($1.6\text{--}35.9 \text{ nmol L}^{-1}$) concentrations, whereas highest concentrations were present on the shelf close to the seafloor (up to 18.5 and 351 nmol L^{-1} for dFe and LpFe respectively). Enhanced concentrations of both Fe fractions at any given station were observed at the depths with low oxygen concentrations ($30\text{--}60 \mu\text{mol O}_2 \text{ kg}^{-1}$). A similar distribution pattern was found for dCo, with concentrations between 0.069 and $0.185 \text{ nmol L}^{-1}$ (Figure 4.3C). In contrast, LpCo

concentrations varied between below LOQ and $0.179 \text{ nmol L}^{-1}$ and were generally highest in surface waters and close to the coast (Figure 4.3D). In comparison to dFe the concentration range of dCo was much narrower and enhanced concentrations were observed over a broader depth range and further offshore.

Surface dFe and dCo concentrations were low, presumably due to high biological uptake. No clear increasing trend in dFe and dCo with depth was observed, indicating that processes other than, or in addition to, remineralization influenced their distributions. Elevated concentrations were found close to the sediments and within low oxygen waters. This suggested a benthic source of Fe and Co under oxygen-depleted conditions, and offshore transport along oxygen-depleted water filaments. This is in agreement with previous studies (e.g. Hatta et al., 2015; Hawco et al., 2016; Noble et al., 2012). A sharper onshore-offshore gradient of dFe concentrations compared to dCo shows that oxidation and removal mechanisms/scavenging rates were faster for Fe than Co (Noble et al., 2012). Previously reported dFe concentrations in coastal regions of the tropical North Atlantic were lower than we observed, between $0.5\text{--}6.3 \text{ nmol L}^{-1}$ (Hatta et al., 2015; Milne et al., 2017), but all these samples were collected at a greater distance from the coast than in this study. In the near-coastal Oregon and Washington shelf bottom water dFe concentrations were similar to this study under equivalent O_2 concentrations ($18.7\text{--}42.4 \text{ nmol L}^{-1}$ dFe; Lohan and Bruland 2008), whereas in the anoxic Peruvian shelf, dFe concentrations were more than an order of magnitude higher, exceeding 300 nmol L^{-1} (Scholz et al., 2016). Similar dCo concentrations to our study were previously observed in the North and South Atlantic, with highest concentrations of $\sim 0.16 \text{ nmol L}^{-1}$ present within oxygen-depleted waters (Noble et al., 2012; Noble et al., 2017).

Dissolved Mn concentrations ranged between $0.46\text{--}13.8 \text{ nmol L}^{-1}$ and LpMn between below LOQ– 4.4 nmol L^{-1} (Figure 4.3E,F). Highest observed dMn and LpMn

concentrations were observed in surface waters, generally decreasing with depth. Additionally, concentrations were highest on the shelf and decreased offshore. The dMn concentrations were generally elevated within and below the deeper oxygen-depleted waters with 0.70–1.34 nmol L⁻¹ compared to 0.46–0.91 nmol L⁻¹ just above. The increased dMn concentrations within the deeper oxygen-depleted waters indicate a benthic source, similar to Fe and Co, which is in accordance with previous studies (Noble et al., 2012). However in the shallow oxygen-depleted waters this effect is not resolvable due to high surface concentrations, which were maintained by photo-reduction of Mn oxides to soluble Mn(II) that prevents loss of Mn from solution (Sunda and Huntsman, 1994). Reported dMn concentrations in the North and South Atlantic were lower than in our study, with concentrations <3.5 nmol L⁻¹ in surface waters and around 0.5–1 nmol L⁻¹ dMn within the OMZ (Hatta et al., 2015; Noble et al., 2012). As for dFe, these lower previously reported values can also be explained by sampling stations positioned at further distance from the coast and removal of dMn via biological oxidation processes with distance from the source (Moffett and Ho, 1996).

Dissolved Cd and Ni concentrations were lowest in surface waters with 0.022–0.032 nmol Cd L⁻¹ and 2.6–2.8 nmol Ni L⁻¹ and showed an increasing trend with depth to maximum values of 0.60 nmol L⁻¹ and 5.8 nmol L⁻¹, respectively (Figure 4.3G,M). Leachable particulate Cd concentrations were between below LOQ and 0.20 nmol L⁻¹ and LpNi concentrations between below LOQ and 1.7 nmol L⁻¹. A large fraction of Ni (72–100%) was present in the dissolved form. The majority of LpNi was below LOQ (>70% of the data) and LpNi is therefore not included in Figure 4.3. LpCd concentrations were highest close to the coast and decreased offshore (Figure 4.3H). In surface waters close to the coast the LpCd fraction was dominant with up to 84.3%. The fraction of LpCd in surface water beyond the shelf break (including stations 2, 1 and 9) was still up

to 54.3%, whereas below 50 m only 0–12.8% of TDCd was in the Lp phase. In contrast to Fe, Co and Mn, no increases in Cd and Ni were observed near the seafloor and within the oxygen depleted waters indicating that Cd and Ni concentrations are mainly controlled by remineralization of sinking organic matter, which is typical for these two nutrient-like TMs (Biller and Bruland, 2013). A very similar distribution with concentrations between 0 and 1000 m water depth ranging from ~2–5.5 and ~0–0.55 nmol L⁻¹ for dNi and dCd, respectively, was observed during the GEOTRACES transect GA03_w in the tropical North Atlantic (Mawji et al., 2015).

Dissolved Cu concentrations in surface waters ranged between 0.625–0.81 nmol L⁻¹ (Figure 4.3I). Concentrations increased with depth to around 1.37 nmol L⁻¹ at 700 m depth close to the seafloor, whereas away from this seafloor maximum the observed concentrations were 0.945 nmol L⁻¹ at the greatest sampled depth of 850 m. These results indicate that in addition to remineralization processes of sinking biogenic particles, the distribution of Cu is influenced by inputs from the seafloor. Cu also undergoes redox chemistry and is released from continental shelf sediments under moderately reducing conditions (Heggie, 1982). In strongly reducing sediments, Cu forms inorganic sulfide compounds and precipitates, and a decrease in sediment source of Cu was reported with a seasonal decrease in oxygen (Biller and Bruland, 2013). Therefore, the sediment source of dCu might show a different dependency on bottom water oxygen concentrations explaining the distinct distribution of dCu compared to dFe, dCo and dMn. Concentrations of LpCu were between below LOQ to 0.61 nmol L⁻¹ with enhanced levels at station 4 close to the coast and at mid depths of the three stations furthest offshore (9, 5 and 2) (Figure 4.3J).

Observed dPb concentrations were lowest in the surface with 9–14 pmol L⁻¹ and increased with depth to 29–86 pmol L⁻¹ below 600 m depth (Figure 4.3K). Pb is not

considered a nutrient-like TM (e.g. Boyle et al., 2014), but our observations indicate a release of Pb sinking particles following remineralization. The concentration range and depth distribution is very similar to previously observed distributions further offshore at about 21°W (Noble et al., 2015). These authors suggested that increased concentrations of up to 70 pmol L⁻¹ between 600 and 800 m depth were related to the influence of Mediterranean Outflow Waters (MOW). Additionally, increased Pb concentrations in proximity to sediments have been attributed to the benthic release of historic Pb through reversible scavenging from particles and the release of dPb associated with Fe/Mn oxyhydroxides during reductive dissolution of those oxides in anoxic sediments (Rusiecka et al., 2018). The major source of Pb to the ocean is atmospheric dust deposition from anthropogenic emissions (Nriagu and Pacyna, 1988; Veron et al., 1994) with recent indications of strongly reduced anthropogenic Pb inputs to the study region (Bridgestock et al., 2016). Low surface water concentrations on the Mauritanian shelf indicate a low atmospheric input of Pb in this region. LpPb was below LOQ–27 pmol L⁻¹, and the distribution of LpPb was similar to that of LpFe, with subsurface maxima within oxygen depleted waters (Figure 4.3L) and may indicate increased scavenging of Pb in these layers which might be associated with Fe containing particles.

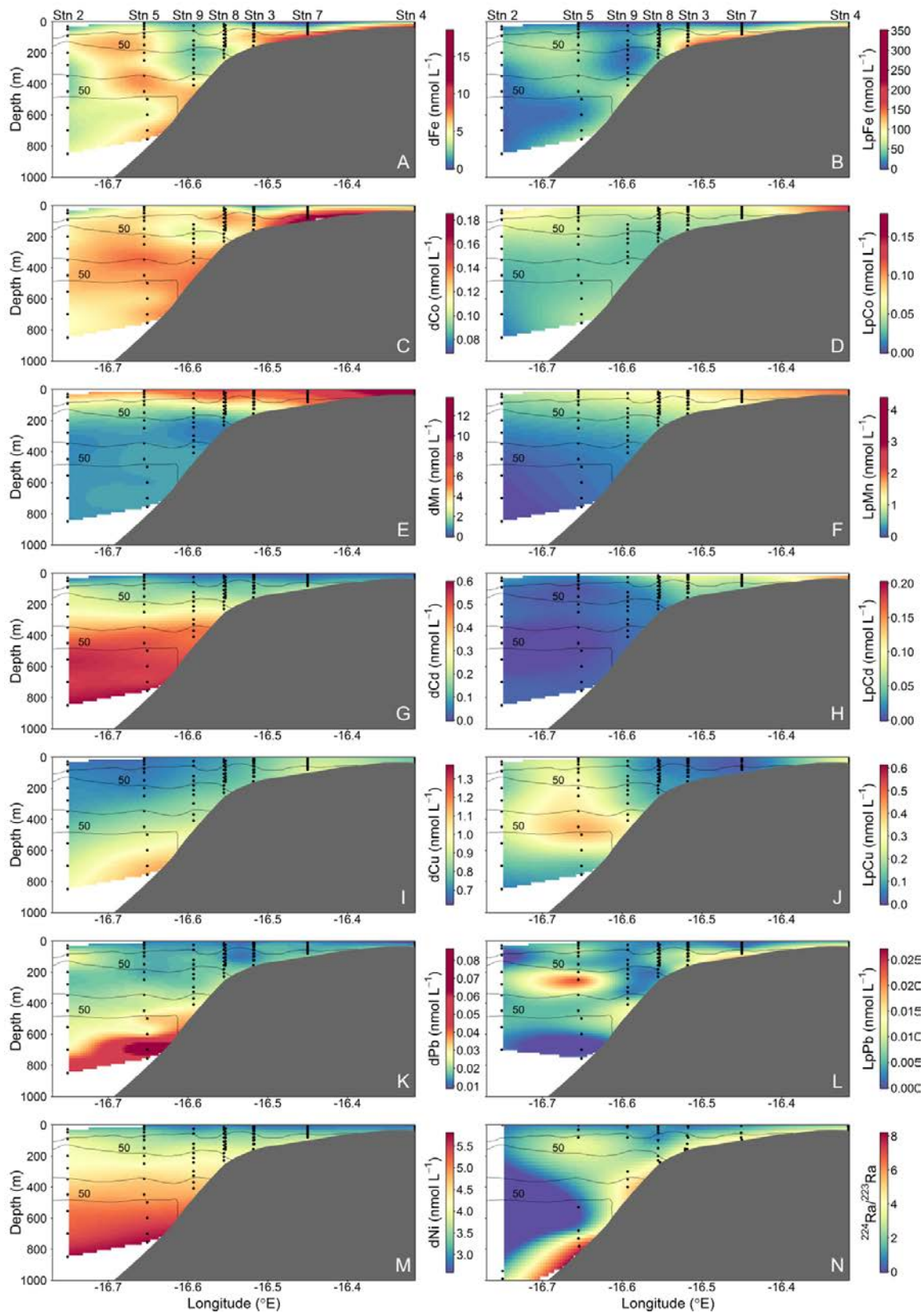


Figure 4.3: Spatial distributions of dissolved and leachable particulate trace metals and $^{224}\text{Ra}/^{223}\text{Ra}$ across the Mauritanian shelf at $18^{\circ}20'\text{N}$ in June 2014. Each sample location is indicated as black dot and oxygen contours at $50 \mu\text{mol kg}^{-1}$ are displayed as black lines.

Sediment derived TM concentrations decrease with distance from the shelf and with time that passed since the water mass has been in contact with the sediment due to water mass mixing and removal processes such as precipitation and scavenging (Bruland and Lohan, 2006). Radium (Ra) isotopes can be used as a tracer for benthic sources. The major source of Ra to the ocean is input from sediments through the efflux of pore water and desorption from sediment particles after production from the decay of thorium isotopes (Moore, 1987; Moore and Arnold, 1996; Rama and Moore, 1996). Due to the distinctive half-lives of the different Ra isotopes (e.g. ^{224}Ra ($t_{1/2} = 3.66$ d) and ^{223}Ra ($t_{1/2} = 11.4$ d)) and their conservative behavior in seawater, it is possible to determine mixing rates and the time that has passed since the water was in contact with the sediment (Moore, 2000a; Moore, 2000b).

The highest $^{224}\text{Ra}_{\text{ex}}/^{223}\text{Ra}$ activity ratios were observed close to the seafloor (Figure 4.3N). The average $^{224}\text{Ra}_{\text{ex}}/^{223}\text{Ra}$ ratio in proximity to the sediment source (< 20 m above seafloor) was 4.1 ± 0.7 and was similar to previous reported ratios for shelf waters off South Carolina ($^{224}\text{Ra}_{\text{ex}}/^{223}\text{Ra} = 4.1 \pm 0.7$; Moore, 2000a). $^{224}\text{Ra}/^{223}\text{Ra}$ ratios decreased away from their benthic source due to mixing and decay ($^{224}\text{Ra}_{\text{ex}}/^{223}\text{Ra} = 0\text{--}0.5$ in surface waters). Ratios close to the sediments were relatively constant along the transect at bottom depths <600 m, whereas dFe, dCo and dMn concentrations varied largely in the bottom samples. This suggests that factors, which are not influencing the Ra distribution, impact the distribution of dFe, dCo and dMn, with a likely influence of enhanced oxygen concentrations reducing sediment release or increasing removal rates of these metals between 200 and 400 m water depth. At around 800 m bottom depth, $^{224}\text{Ra}_{\text{ex}}/^{223}\text{Ra}$ ratios were slightly elevated and were accompanied with increased dCo, dFe, dMn and dCu concentrations despite oxygen concentrations $>70 \mu\text{mol kg}^{-1}$. This suggests that the high TM concentrations at this location were influenced by an increased sediment source

which was related to the presence of a benthic nepheloid layer, which is supported by an increase in turbidity in proximity to the sediment surface. An elevated $^{224}\text{Ra}_{\text{ex}}/^{223}\text{Ra}$ ratio of 3.5 ± 0.6 was observed at about 16.65°N and 80 m water depth (bottom depth 782 m) during the same cruise which coincided with a local maximum of dFe, dMn and dCo and reduced O_2 concentrations. These observations indicate that the waters have been in recent contact (12–20 days assuming initial pore water $^{224}\text{Ra}_{\text{ex}}/^{223}\text{Ra}$ ratios between 18–38; Moore, 2007) with sediments and that the dynamic current system in this region can cause local and short-term variability in the offshore transport of sediment derived TMs.

4.3.3 Classification of different groups of trace metals based on principle component analysis

Principle Component Analysis (PCA) was performed (using the RDA function within the vegan package in R; Oksanen et al., 2017) to investigate different groups and correlations in the data set. Dissolved TMs (Fe, Mn, Co, Ni, Pb, Cu and Cd), nutrients (silicic acid, nitrate and phosphate), dissolved O_2 , Apparent Oxygen Utilization (AOU), depth and iodide concentrations were utilized in the PCA. Radium data were not included in the PCA, as the number of available data points for $^{224}\text{Ra}_{\text{ex}}/^{223}\text{Ra}$ was much lower than for the other parameters. Surface waters shallower than 50 m were excluded from the PCA to remove the influence of local processes in surface waters, such as localized atmospheric deposition and photochemical processes, which in particular influence Mn and iodide distributions. The PCA generated three principle components (PC) with eigenvalues larger than 1, with PC1 explaining 53.6% and PC2 25.5% of the total variance in the dataset (together 79.1%). Inclusion of PC3 in the analysis explained only 6.8% more of the variance.

The first PC group is formed by Cd, Cu, Ni and Pb (Figure 4.4), which are associated with depth, AOU, nitrate and phosphate. This indicates that the distribution of Cd, Cu,

Ni, and potentially Pb, are controlled by organic matter remineralization processes. This is in agreement with strong Pearson correlations $R > 0.9$ for the relationships of dCd and dNi with depth, nitrate, and silicate (Appendix Table A1). Weaker correlations with major nutrients were observed for dPb ($R > 0.6$) and dCu ($R > 0.4$), potentially due to additional remineralization or removal mechanisms for these elements (e.g. prior atmospheric inputs and water mass transport, Pb; sediments, Cu and Pb, and scavenging). The second group of TMs is composed of dFe, dCo and dMn that are associated with elevated iodide and turbidity, and low dissolved O_2 . Iodide (I) is the reduced form of iodine (I), which is typically present as iodate (IO_3^-) in oxygenated subsurface water. Both I forms are present as soluble anions in seawater. Due to a relatively high redox potential (pE ~ 10), iodine is one of the first redox-sensitive elements to undergo reduction under suboxic conditions and is therefore a useful indicator for active reductive processes (Rue et al., 1997). Despite their role as micronutrients, Fe, Mn and Co do not correlate with nutrients indicating that processes other than remineralization control their distribution.

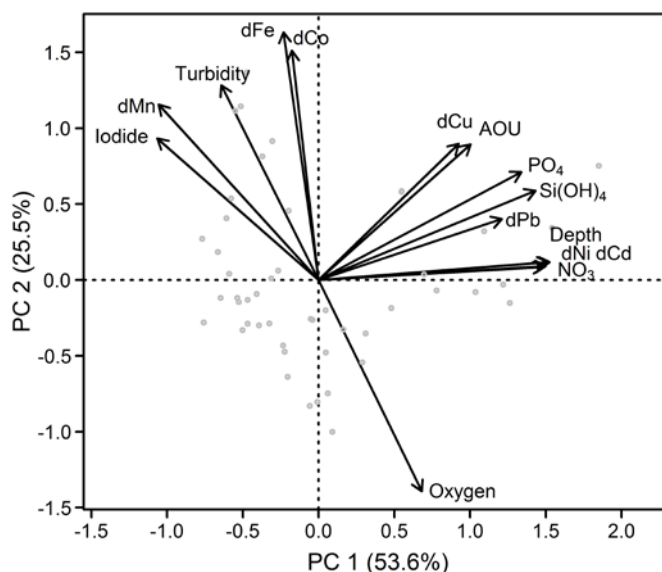


Figure 4.4: Principle component analysis of the Mauritanian shelf data set. Principle component loadings for each variable are indicated by black vectors. Component scores of each sample are indicated as grey circles. Loadings/scores have been scaled symmetrically by square root of the eigenvalues.

The anti-correlation with oxygen (also shown in Figure 4.6) and correlation with iodide support the notion that Fe, Co and Mn distributions are strongly influenced by water column oxygen concentrations, presumably by: (i) enhanced benthic metal fluxes from anoxic sediments, and (ii) decreased oxidation rates in the overlying water column under oxygen depleted conditions. This is also supported by elevated benthic Fe(II) fluxes observed at the seafloor within the shallow OMZ, with benthic fluxes of 15–27 $\mu\text{mol m}^{-2} \text{d}^{-1}$ (Lomnitz et al., in review).

Variability in the redox-sensitive metals, Fe, Mn and Co, were not fully explained by either oxygen or iodide concentrations; Pearson correlations with oxygen were -0.55, -0.61 and -0.58, respectively (Appendix Table A1). As shown before, other factors such as, for example, water mass mixing and age, the amount and type of particles present, and remineralization all likely impact their dissolved concentrations. Consequently, such a complex chain of factors and processes means that one variable alone is unlikely to explain the behaviour of these elements.

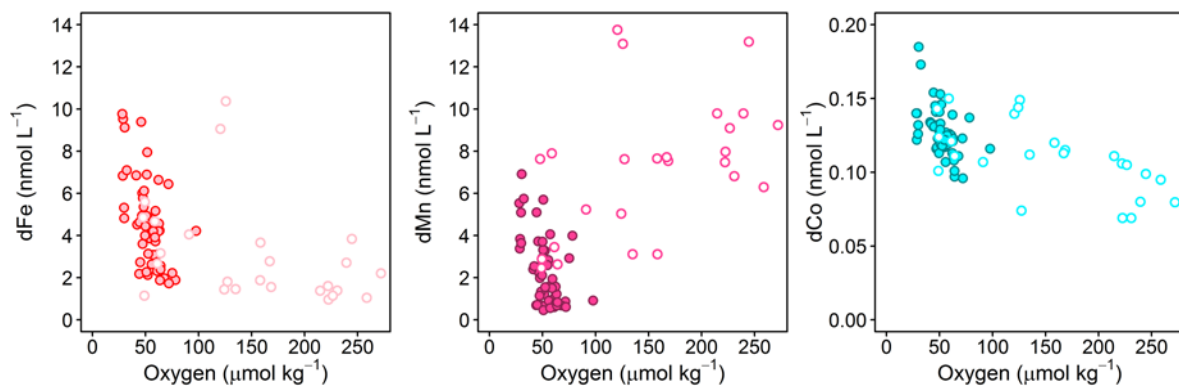


Figure 4.5: Dissolved TM concentrations against oxygen for Fe (left), Mn (middle) and Co (right). Filled circles display all data points below 50 m depth, open circles at depths shallower than 50 m.

4.3.4 Influence of the different sources of Fe, Mn and Co

The potential main sources of TMs in this region are sediment release and atmospheric dust deposition (e.g. Rijkenberg et al., 2012). Also release of TMs during organic matter

rem mineralization may have an important influence on the distribution of TMs. In the following, we evaluate the influence of water column rem mineralization and atmospheric dust deposition to surface waters in comparison to sediment release on the distribution of Fe, Co and Mn in our study.

1) Remineralization

To quantify the influence of rem mineralization for dFe, we employed Fe to carbon ratios (carbon was calculated using AOU, with an AOU/Carbon ratio of 1.6; Martin et al., 1989). Dissolved Fe/C ratios for the entire transect varied between 15 and 74 $\mu\text{mol mol}^{-1}$. These results agree with those for shelf-influenced waters with Fe/C ratios of 13.3–40.6 $\mu\text{mol mol}^{-1}$ further south at 12°N (Milne et al., 2017). Observed ratios for the North Atlantic, further away from a strong influence of the shelf, ranged between 4 and 12.4 $\mu\text{mol mol}^{-1}$ (Fitzsimmons et al., 2013; Milne et al., 2017; Rijkenberg et al., 2014). To calculate the amount of dFe being derived by rem mineralization, we assume a dFe/C ratio of 12 from organic matter rem mineralization, as this is at the upper range of observed dFe/C ratios in the open ocean close to our study area without a strong shelf influence. We obtain a range between 8 and 81% of dFe being derived from rem mineralization processes with lowest values observed on the shelf (8%) and highest values observed beyond the shelf break at Stn 9 (81%) and Stn 2 (78%). These results indicate that rem mineralization controlled dFe concentrations with increasing distance from the coast. Close to the shelf, benthic inputs of dFe were important sources.

Similar analysis for dCo/C ratios revealed an increased importance of an additional source close to the shelf. Observed dCo/C ratios ranged between 0.81 and 2.2 $\mu\text{mol mol}^{-1}$. The larger ratios were observed close to the coast and decreased further offshore. Overall, the observed ratios were somewhat higher than reported cellular ratios of phytoplankton in the North Atlantic of 0.5–1.4 $\mu\text{mol mol}^{-1}$ (Twining et al., 2015). Due

to the lack of comparable data and the multiple processes influencing this ratio (varying phytoplankton nutrient stoichiometry and scavenging), we did not use these values to calculate a remineralized fraction.

The distribution of Mn was not predominantly determined by biological uptake and remineralization in our study region. In contrast, dMn/C ratios were largely influenced by photoreduction in the surface (Sunda and Huntsman, 1994) and removal via biotic oxidation and formation of Mn oxides at depth (Tebo et al., 2004). Therefore, we did not assess remineralization processes for Mn using dMn/C ratios.

2) Atmospheric deposition

Aluminum is present as a relatively constant fraction of ~8.15 wt% in the continental crust (Rudnick and Gao, 2006) and reaches the open ocean mainly by atmospheric dust deposition (Orlans and Bruland, 1986). Therefore it is used as a tracer for dust supply to the surface ocean (Measures and Vink, 2000). The dust input in the study region is mainly influenced by North African/Saharan mineral dust with only a small contribution of anthropogenic sources which differ in TM composition and solubilities from continental crust material (Conway and John, 2014; Patey et al., 2015; Shelley et al., 2015). Close to continental shelves, in addition to atmospheric input, Al can also be supplied by sediment resuspension (Middag et al., 2012; Moran and Moore, 1991). Dissolved surface water Al concentrations ranged between 30 and 49 nmol L⁻¹ and LpAl 3.4–18.2 nmol L⁻¹. Al concentrations decreased with depth, indicating that Al was released by aeolian dust deposition to surface waters and removed through scavenging with depth (Orlans and Bruland, 1985).

Trace metal (Fe, Co, and Mn) to Al ratios were utilized to investigate the influence of atmospheric dust deposition. We present molar ratios for dissolved, total dissolvable and leachable particulate (Lp) concentrations. Similar to higher Al than Fe solubilities from

aerosol leach experiments in ultra-high purity water (UHP) and 25% acetic acid were reported (Baker et al., 2006; Buck et al., 2010; Shelley et al., 2018), indicating that Lp Fe/Al ratios might be similar or lower than total particulate ratios from dust deposition. Therefore it seems reasonable to assume an additional source of LpFe if LpFe/LpAl ratios are higher than total ratios in aerosol samples.

In the surface mixed layer, dFe/dAl molar ratios ranged between 0.019 and 0.114, TDFe/TDAI 0.236 and 0.826 and LpFe/LpAl ratios ranged between 1.04 and 9.50. In comparison, the total Fe/Al ratio in dust samples collected in the remote North Atlantic between 8.7°N and 23°N was 0.31 ± 0.06 (Buck et al., 2010; Patey et al., 2015) and 0.37 ± 0.02 in the North East Atlantic ~18°N under the Saharan dust plume (Shelley et al., 2015), which is higher than upper crustal ratios of 0.19–0.23 (McLennan, 2001; Rudnick and Gao, 2006; Wedepohl, 1995). However, soluble Fe/Al ratios varied dependant on the leach medium and were lower than total dust ratios (UHP: 0.21 ± 0.04 , 25% HAC: 0.25 ± 0.04 , seawater: 0.051 ± 0.009 ; Shelley et al., 2018). Apart from the seawater soluble ratios in dust samples, all dust ratios are higher than the dFe/dAl but lower than the LpFe/LpAl ratios in the surface seawater samples in this study. This indicates an additional source of LpFe to surface waters other than dust. Soluble ratios of aerosol leaches in seawater are within the range of dFe/dAl ratios observed and indicate a potential additional input of dFe at the upper range (dFe/dAl: 0.114). The lower end of total dissolvable ratios (0.236) comprising dissolved and leachable particulate phases were close to total ratios in aerosol samples, suggesting that dust represented an important source of Fe and Al to the surface ocean. At the upper end, ratios were much larger (0.826) than aerosol ratios and indicate an additional source of benthic Fe. This interpretation however only applies if residence times of dust supplied TDFe and TDAI are similar. This is difficult to assess, as estimated residence times for both elements vary

largely depending on the location and the amount of dust input. For example, short residence times of 1–62 days were observed for TDFe under the Saharan dust plume (Buck et al., 2010; Croot et al., 2004). Overall, Fe/Al ratios suggest that atmospheric deposition is an important of Fe to surface waters with an additional contribution of benthic inputs. However, uncertainties in solubilities and residence times cause a high uncertainty in the interpretation of the data.

Atmospheric dFe fluxes were calculated using the dAl inventory in the surface mixed layer, a residence time of dAl of 0.65 ± 0.45 years as reported for the Canary Current System (Dammshäuser et al., 2011), and a ratio of 0.31 for dust derived dissolved Fe/Al (Buck et al., 2010). The estimated atmospheric dFe fluxes ranged between 0.37 and 4.65 $\mu\text{mol m}^{-2} \text{d}^{-1}$. Mean atmospheric dFe fluxes of the individual stations were 0.63–1.43 $\mu\text{mol m}^{-2} \text{d}^{-1}$ and lie within previously observed fluxes close to our study region of 2.12 $\mu\text{mol m}^{-2} \text{d}^{-1}$ (Rijkenberg et al., 2012) and 0.120 $\text{nmol m}^{-2} \text{d}^{-1}$ (Ussher et al., 2013). The large range of the estimated fluxes is mainly driven by the uncertainty in the residence time of dAl rather than the location of the station. The utilized approach assumes that dAl is only supplied to the surface via atmospheric deposition. A potential supply by vertical fluxes from sediment derived Al would consequently result in an overestimation of atmospheric fluxes.

Co and Mn are present in the upper continental crust in a much smaller molar fraction (Mn/Al: 0.0032–0.0037, Co/Al: 0.000071–0.000097; McLennan, 2001; Rudnick and Gao, 2006; Wedepohl, 1995). However, ratios in dust samples under the North African dust plume were slightly higher than crustal ratios (Mn/Al: 0.0061 ± 0.0002 , Co/Al: 0.00016 ± 0.00002 ; Shelley et al., 2015) and solubilities of Co and Mn from these dust samples were much higher than Al solubility resulting in soluble Mn/Al of 0.24 ± 0.09 and Co/Al of 0.0021 ± 0.0009 in UHP (Shelley et al., 2018). The soluble ratios also

varied largely depending on the leach medium and might therefore also vary from the actual dust solubility in seawater at our study site. Here observed $d\text{Co}/d\text{Al}$ ratios in the upper 50 m were 0.001–0.004, TDCo/TDAI ratios were slightly higher with 0.003–0.005 and LpCo/LpAl ratios were 0.006–0.020. Consequently the ratios of all fractions were larger than aerosol ratios and mostly higher than soluble ratios. This indicates that an additional benthic source of Co likely contributed to the Co present in surface waters, but similar dissolved ratios to soluble dust ratios might support the importance of a dust component.

Dissolved $\text{Mn}/d\text{Al}$ ratios in the upper 50 m ranged between 0.082–0.347 and TDMn/TDAI 0.083–0.256. The ratios are much larger than upper crustal ratios but similar to the soluble ratios of Mn/Al from dust. Therefore a large amount of Mn might be from atmospheric depositions. However, these ratios may also be influenced by the long residence time of Mn in surface water due to photoreduction. Therefore it is not possible to estimate the contribution of atmospheric dust deposition.

3) Vertical trace element fluxes to surface waters

The vertical fluxes (diffusive and advective) of $d\text{Fe}$ and LpFe from the top of the shallow oxygen depleted waters (23–89 m) into surface waters was determined to assess the potential Fe contribution to phytoplankton growth. Closest to the shelf (bottom depth: 50 m) mean $d\text{Fe}$ fluxes were $13.5 \mu\text{mol m}^{-2} \text{d}^{-1}$. Further offshore, fluxes decreased to $0.16 \mu\text{mol m}^{-2} \text{d}^{-1}$ (bottom depth: 1136 m, 77 km offshore). Between repeat stations 3A and 3B, mean fluxes decreased from 2.3 (stn 3A) to $1.35 \mu\text{mol m}^{-2} \text{d}^{-1}$ (stn 3B). Leachable particulate Fe fluxes were also highest closest to the coast with a mean flux of $166 \mu\text{mol m}^{-2} \text{d}^{-1}$ and decreased to $0.30 \mu\text{mol m}^{-2} \text{d}^{-1}$ further offshore. However at station 5 high $d\text{Fe}$ and LpFe fluxes were observed ($d\text{Fe}$: $1.3 \mu\text{mol m}^{-2} \text{d}^{-1}$, LpFe : $20 \mu\text{mol m}^{-2} \text{d}^{-1}$) compared to station 9 (closer to the shelf) and station 2 (further

offshore). Diffusivity was determined over 5 profiles only and was unusual high at this station. Therefore the high vertical fluxes may be caused by an atypical mixing event. On the shelf (45 m bottom depth), Fe fluxes were dominated by advective rather than diffusive fluxes due to the strongest upwelling velocity on the shelf (detailed in Tables 4.2 and 4.3). At continental slope stations (90–400 m bottom depth), fluxes were dominated by high diffusive fluxes which were around 3 times larger than the advective fluxes. Further offshore (>400 m bottom depth, except stn 5 with particularly strong vertical mixing) the contribution of advective and diffusive fluxes were similarly low. Similar dFe ($16 \mu\text{mol m}^{-2} \text{d}^{-1}$) and LpFe ($222 \mu\text{mol m}^{-2} \text{d}^{-1}$) fluxes were observed on the shelf at 12°N (Milne et al., 2017). Although, the atmospheric fluxes of dFe are enhanced with mean fluxes of $0.63\text{--}1.43 \mu\text{mol m}^{-2} \text{d}^{-1}$, vertical dissolved Fe fluxes from the shallow oxygen depleted waters exceed atmospheric fluxes at all stations apart from station 2 furthest offshore and potentially station 9, where no atmospheric fluxes were determined. The weaker influence of atmospheric dust in this region is in accordance with previous studies that demonstrated sediments form the major contributor to the Fe inventory in the coastal region of the eastern tropical Atlantic, whereas the importance of dust input increases further offshore (Milne et al., 2017).

Dissolved Co fluxes ranged between 2 and $113 \text{ nmol m}^{-2} \text{d}^{-1}$. These values are lower than reported upwelling fluxes of dCo of $250 \text{ nmol m}^{-2} \text{d}^{-1}$ in this region (Noble et al., 2017), but are much larger than atmospheric deposition fluxes of $1.7 \text{ nmol m}^{-2} \text{d}^{-1}$ (Shelley et al., 2015). Fluxes of LpCo, dMn and LpMn resulted in downward fluxes due to increased surface water concentrations compared to below. A detailed summary of calculated fluxes, the contribution of diffusive and advective term and uncertainties for dFe, LpFe and dCo for all stations is given in Tables 4.1 and 4.2.

Table 4.1: Atmospheric and vertical fluxes of dFe. Atmospheric fluxes are obtained from dAl inventory in the mixed layer. Vertical fluxes are combined diffusive (Diff.) and upwelling (Adv.) fluxes. Minimum and maximum vertical fluxes were calculated using the upper and lower 95% confidence interval of diffusivity measurements and an error of 50% for the upwelling velocity.

Station	Atmospheric dFe flux ($\mu\text{mol m}^{-2} \text{d}^{-1}$)	Vertical dFe flux ($\mu\text{mol m}^{-2} \text{d}^{-1}$)		
	Mean (min–max)	Mean (min–max)	Diff.	Adv.
4	0.66 (0.39–2.14)	13.5 (7.13–22.15)	1.56	11.98
7	0.74 (0.44–2.41)	2.31 (1.52–3.25)	1.75	0.56
3A	0.77 (0.46–2.52)	2.31 (1.28–3.74)	1.63	0.68
3B	0.63 (0.37–2.06)	1.35 (0.75–2.18)	0.79	0.57
8A	0.68 (0.40–2.20)	0.95 (0.58–1.42)	0.72	0.22
8B	1.18 (0.70–3.84)	-	-	-
9	-	0.08 (0.05–0.12)	0.04	0.04
5	0.87 (0.51–2.83)	1.27 (0.60–2.42)	1.03	0.25
2	1.43 (0.85–4.65)	0.16 (0.09–0.23)	0.05	0.10

Table 4.2: Vertical fluxes of LpFe and dCo. Vertical fluxes are combined diffusive (Diff.) and upwelling (Adv.) fluxes. Minimum and maximum vertical fluxes were calculated using the upper and lower 95% confidence interval of diffusivity measurements and an error of 50% for the upwelling velocity.

Station	Vertical LpFe flux ($\mu\text{mol m}^{-2} \text{d}^{-1}$)			Vertical dCo flux ($\text{nmol m}^{-2} \text{d}^{-1}$)		
	Mean (min–max)	Diff.	Adv.	Mean (min–max)	Diff.	Adv.
4	166.7 (87.7–272.8)	19.2	147.5	113 (59.5–185)	13.0	100
7	20.2 (13.3–28.4)	15.3	4.91	28.4 (18.6–39.9)	21.5	6.9
3A	24.4 (13.6–39.62)	17.3	7.16	33.6 (18.7–54.5)	23.8	9.9
3B	3.24 (1.79–5.22)	1.88	1.36	10.3 (5.7–16.5)	6.0	4.3
8A	13.3 (8.10–19.9)	10.1	3.15	14.6 (8.9–21.9)	11.1	3.5
8B	-	-	-	-	-	-
9	-1.24 (-0.71– (-1.80))	-0.60	-0.65	-	-	-
5	20.0 (9.49–38.0)	16.1	3.85	3.6 (1.7–6.8)	2.9	0.7
2	0.30 (0.17–0.44)	0.11	0.20	1.9 (1.1–2.8)	0.7	1.2

4.3.5 Removal mechanisms and particle interactions

In the top 50 m of the water column a large part of the LpTMs may be part of living biological cells or detritus. Additionally, LpTM may be part of lithogenic phases from Saharan dust or authigenic phases. Authigenic phases are formed in situ by TM adsorption onto particles or the in situ formation of amorphous TM oxides and hydroxides (Sherrell and Boyle, 1992).

Iron is mainly present in the size fraction $>0.2 \mu\text{m}$ with TD concentrations being 0.44–44.5 times (84% of the data >4) higher than dFe ($<0.2 \mu\text{m}$) (Figure 4.6A). To investigate the influence of particle load on distribution between dissolved and particulate phase, the fraction of Lp (Lp/TD) TMs is plotted against turbidity (Figure 4.6B) and the Lp concentrations against turbidity (Figure 4.6C). Lowest fractions of LpFe of around 0.6 are observed at lowest turbidity. As turbidity increases from 0.1 to 0.2, the Lp fraction increases to over 0.9. This suggests that the fraction of LpFe is tightly coupled to the particle load. Fe adsorption onto particles has been demonstrated to be reversible with a constant exchange between dissolved and particulate fractions (Abadie et al., 2017; Fitzsimmons et al., 2017; John and Adkins, 2012; Labatut et al., 2014). Furthermore, offshore transport of acid-labile Fe particles originating from reductive dissolution from continental shelf sources was observed in the North Pacific (Lam and Bishop, 2008) and may contribute partly to the bioavailable pool. Therefore an important fraction of Fe may be transported offshore adsorbed to particles and can enter the dissolved pool by cycling between dissolved and particulate phases.

Manganese and Co mainly occurred in the dissolved form. The fraction of LpMn varied between 0.03 and 0.4 and did not show a correlation with turbidity, whereas the Lp concentration showed an increase with turbidity. This indicates that an increased presence of particles yielded enhanced LpMn levels, but that the particle load did not substantially influence the distribution between dissolved and Lp phases and did not comprise a large source of dMn. This suggests that particles did not play a major role in transport of dMn, which agrees with a study on the hydrothermal vent plumes, where the distribution of the dMn plume was decoupled from the distribution of the pMn plume (Fitzsimmons et al., 2017). The fraction and concentration of LpCo showed linear

increases with turbidity. The LpCo fraction ranged between 0 and 0.75 indicating an influence of particle load on Co size fractionation, similar to Fe.

The increase in LpFe with increasing turbidity was weaker in the surface waters compared to depths below 50 m. This suggests a large additional LpFe source at depth with either a higher Fe content of particles or the presence of different type or sizes of particles causing different responses in turbidity measurements. The large additional LpFe source at depths is likely associated with benthic dFe inputs, with a subsequent transfer to the particulate phase by adsorption or oxidation with subsequent formation of Fe(oxihydr)oxides. In contrast, the increase in LpCo and LpMn concentrations with turbidity was similar in the surface 50 m and below and suggests a much weaker influence of sediment release on the distribution of particulate Mn and Co, which might be influenced by a weaker release from sediments in the dissolved form and slower oxidation rates, in particular for Co (Noble et al., 2012).

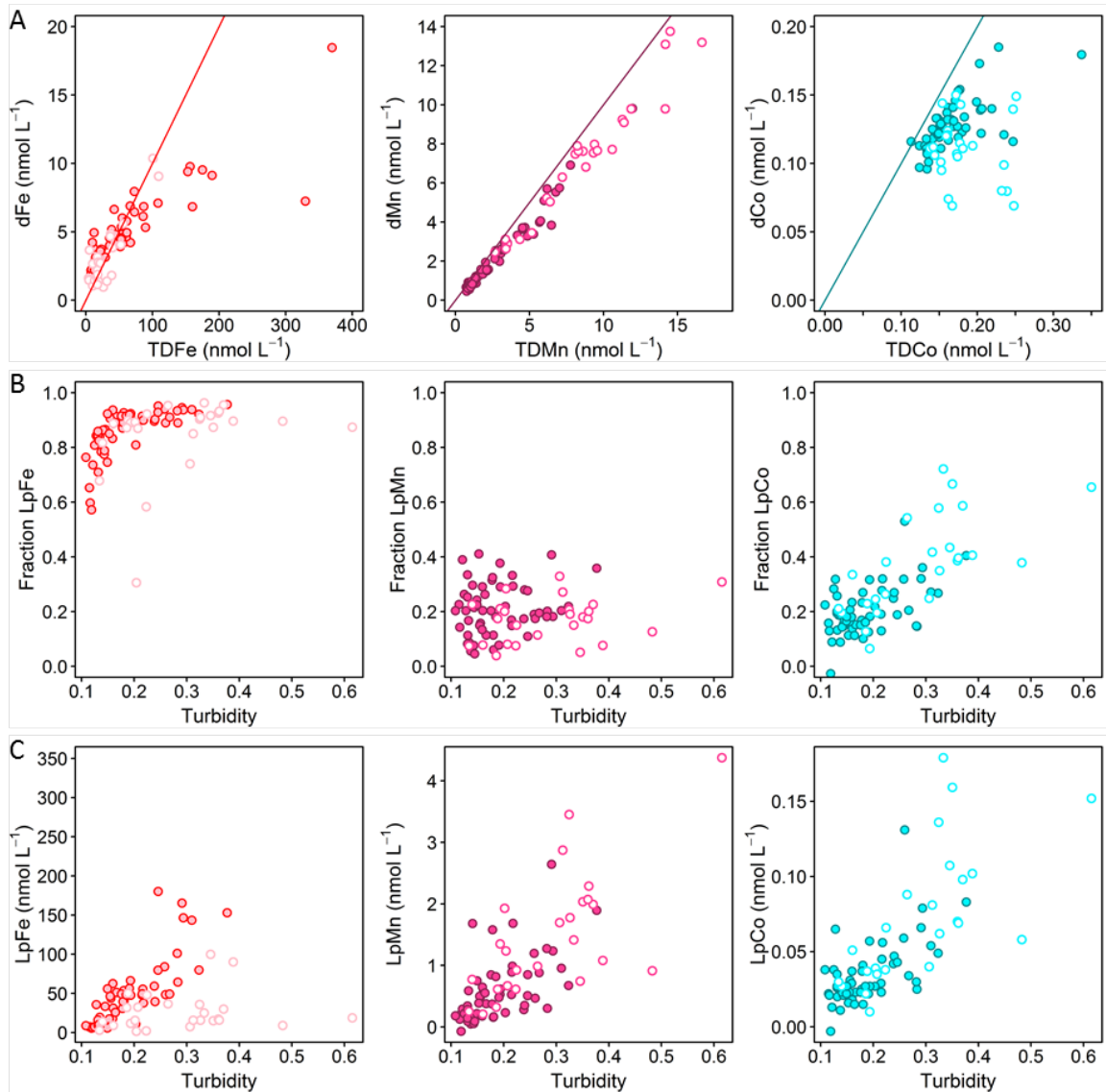


Figure 4.6: Distributions of TMs between dissolved and leachable particulate phase and compared to turbidity A) dissolved against total dissolvable trace metal concentrations for Fe (left; red line: $TDFe = 10 \cdot dFe$), Mn (middle; purple line: $TDMn = dMn$) and Co (right; turquoise line: $TDCo = dCo$). B) Fraction of leachable particulate trace metals (Lp/TD) against turbidity and C) Leachable particulate concentrations against turbidity for Fe (left), Mn (middle) and Co (right). Filled circles display all data points below 50 m depth, open circles at depths shallower than 50 m.

4.3.6 Temporal variability in redox sensitive trace metals

Large temporal changes in O_2 , turbidity and redox-sensitive TMs were observed on a short time scale of a few days at two repeat stations, station 3A/3B and station 8A/8B (Figure 4.7).

Station 3 and 8 were sampled with a difference of 9 days (Figure 4.7A), and 2 days (Figure 4.7B), respectively, between deployments. At station 3, O₂ concentrations in the upper 50 m were very similar between the deployments, whereas below 50 m O₂ had increased from 30 μmol kg⁻¹ during the first deployment to 50 μmol kg⁻¹ 9 days later. At the same time, turbidity at these depths had decreased from 0.35 to below 0.2, and dFe concentrations from a maximum of 10 to 5 nmol L⁻¹. Also dMn and dCo concentrations had decreased from 5 to 3 nmol L⁻¹ and 0.14 to 0.12 nmol L⁻¹, respectively. Particularly large changes were also observed for Lp concentration with a decrease from 147–322 nmol L⁻¹ to 31–51 nmol L⁻¹ for LpFe, from 0.066–0.114 nmol L⁻¹ to 0.015–0.031 nmol L⁻¹ for LpCo and from 1.24–2.64 to 0.16–0.54 for LpMn. No changes in water masses occurred, as indicated by relationships between salinity and temperature below 50 m.

Similar changes in O₂ and turbidity were observed at station 8. During the first deployment a local minimum in O₂ below 30 μmol kg⁻¹ was present between 105–120 m water depths and coincided with a maximum in turbidity of 0.4. In contrast O₂ concentrations and turbidity during the second deployment were relatively constant (50 and 60 μmol kg⁻¹ O₂ and turbidity 0.2) at water depths between 20 and 185 m (bottom sample). At depth of the local minimum in O₂ and maximum in turbidity, concentrations of dFe, dMn and dCo were elevated during the first deployment with concentrations of 9.4 nmol L⁻¹ for dFe, 3.7 nmol L⁻¹ for dMn and 0.145 nmol L⁻¹ for dCo in comparison to 4.6 nmol L⁻¹ for dFe, 2.6 nmol L⁻¹ for dMn, and 0.122 nmol L⁻¹ for dCo at similar depth during the second deployment.

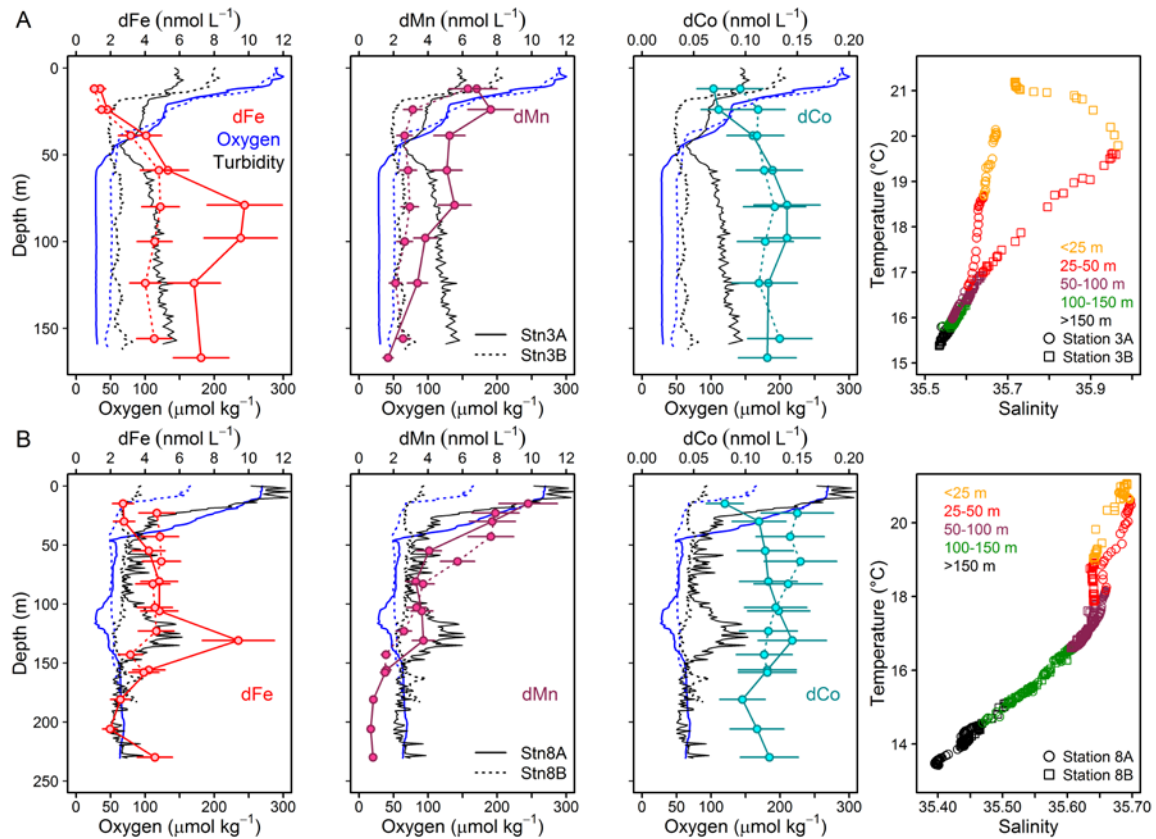


Figure 4.7: Repeated stations: oxygen concentration, turbidity and dissolved trace metals (Fe, Mn and Co) and temperature vs salinity plots. A) Station 3 (18.23 °N, 16.52 °W, 170 m water depth, 9 days between deployments). B) Station 8 (18.22°N, 16.55°N, 189–238 m water depth, 2 days between deployments).

1) Remineralization

We compared the results of the redox-sensitive TMs to other nutrient-like TMs and NO₃ and PO₄. For both repeated stations only minimal changes in dCd (Stn3A: 0.107–0.231 nmol L⁻¹; Stn3B: 0.135–0.150 nmol L⁻¹) and NO₃ (Stn3A: 23.5–26.3 μmol L⁻¹; Stn3B: 25.9–26.4 μmol L⁻¹) concentrations could be observed (Figure 4.8), suggesting that only a small fraction of increased dFe under lower O₂ conditions can be explained by increased remineralization of biogenic particles in the water column.

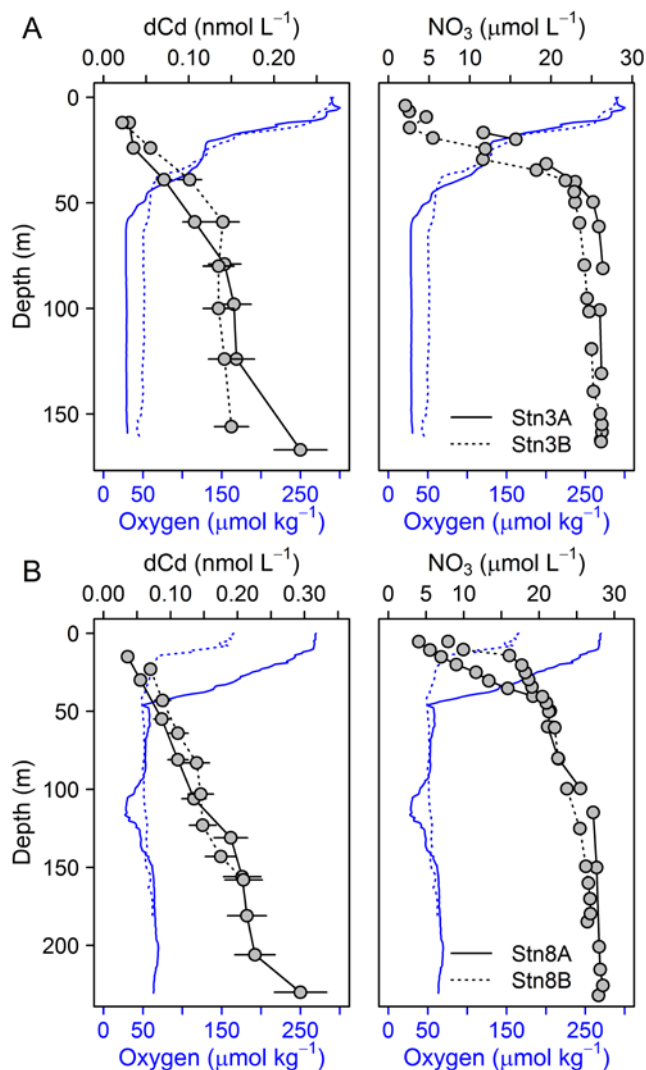


Figure 4.8: Depth profiles of dCd and nitrate (NO_3^-) of repeated stations. First deployment displayed as solid black line and second deployment displayed as dashed black line. Oxygen concentrations are indicated as blue solid line for the first deployment and dashed blue line for the second deployment. A) Station 3 (18.23°N , 16.52°W , 170 m water depth, 9 days between deployments) and B) Station 8 (18.22°N , 16.55°W , 189–238 m water depth, 2 days between deployments).

A weak influence of remineralization processes on the variability in dFe concentrations was confirmed by substantially higher dFe/C ratios at lower O_2 concentrations (40–72 $\mu\text{mol mol}^{-1}$ at Stn 3A compared to 33–41 $\mu\text{mol mol}^{-1}$ at Stn 3B, both below 50 m water depth). Assuming a dFe/C ratio of around 12 from remineralization, only about 0.25 nmol L^{-1} of the difference in dFe concentrations between repeated deployments can be explained by the difference in AOU.

In contrast, dCo/C ratios were similar between repeated deployments within the OMZ (0.90–1.04 at Stn 3A and 0.92–1.06 $\mu\text{mol mol}^{-1}$ at Stn 3B). Thus changes in remineralization could be the major reason for the changes in observed dCo concentrations during repeated deployments, indicating that the sensitivity of dCo sediment input or change in oxidation rates is low at an O_2 shift from 30 to 50 $\mu\text{mol kg}^{-1}$.

Similar to Fe, higher dMn/C ratios were observed at lower O_2 concentrations (3.4–5.5 $\mu\text{mol mol}^{-1}$ at Stn 3A compared to 2.1–2.9 $\mu\text{mol mol}^{-1}$ at Stn 3B). These results indicate that other processes than remineralization are also important for the change in dMn concentrations. An additional factor compared to Fe, might involve changes in intensity of photoreduction which may be influenced by differences in surface turbidity observed at station 3 (lower dMn/C and higher surface turbidity during second deployment). This however cannot explain the changes in dMn/C at Station 8, where a higher surface turbidity coincided with a higher dMn/C ratio at the local minimum in O_2 .

2) Atmospheric dust deposition and sediment resuspension

Within the OMZ, dAl concentrations ranged between 10 and 15 nmol L^{-1} , and LpAl concentration between 1.2 and 11.1 nmol L^{-1} and no substantial changes were observed between deployments (Figure 4.9). As lithogenic material has a high Al content, no substantial changes in Al concentrations signify that lithogenic inputs didn't differ much between deployments and consequently neither increased atmospheric input, nor sediment resuspension are likely to explain the differences in turbidity and TM concentrations. Consequently changes in turbidity might mainly be caused by biogenic and authigenic particles. This finding can be confirmed by substantial changes in TM/Al ratios observed during the deployments (Table 4.3 and Appendix Figure A1). The Fe/Al ratios in the solid phase of underlying sediments during that cruise were 0.23–0.30 (Lomnitz et al., in review) and Mn/Al ratios were 0.0015–0.0020 (Lomnitz, pers. com.).

Overall much higher TM/Al ratios compared to crustal ratios and ratios in underlying sediment suggest a weak influence of atmospheric dust and sediment resuspension on Fe, Co and Mn concentrations in the OMZ close to the shelf.

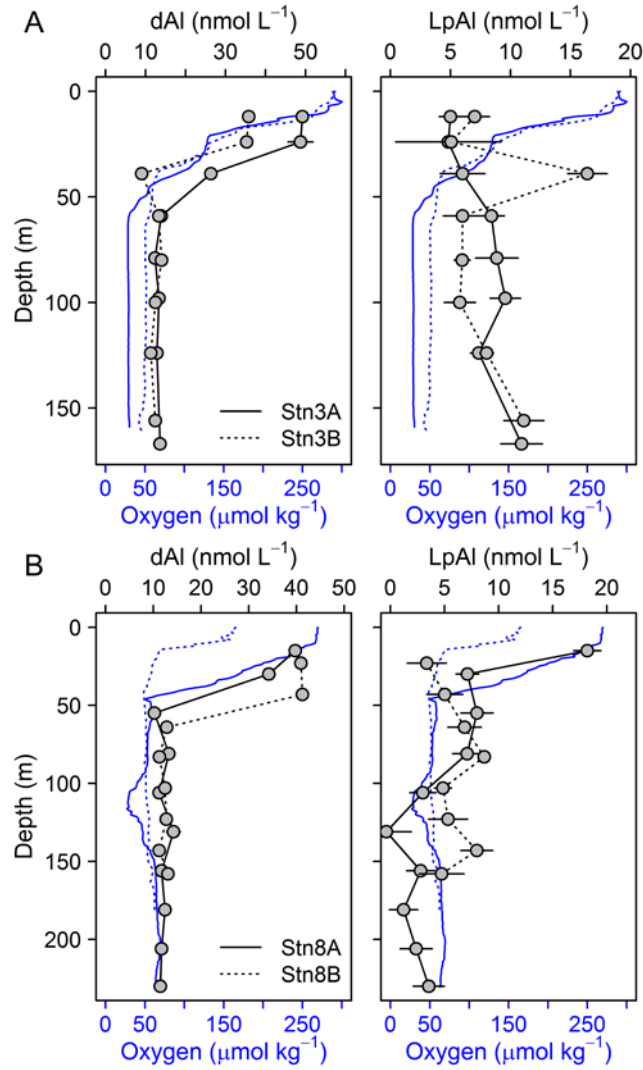


Figure 4.9: Repeated stations: oxygen concentration, dissolved and LpAl. A) Station 3 (18.23°N, 16.52°W, 170 m water depth, 9 days between deployments) and B) Station 8 (18.22°N, 16.55°N, 189–238 m water depth, 2 days between deployments).

Table 4.3: TM/Al ratios of different fractions for the repeated deployments at station 3 within the OMZ below 50 m water depth.

Parameter	Stn 3A	Stn 3B
dFe/dAl	0.382–0.789	0.349–0.365
TDFe/TDAI	4.00–13.42	1.83–2.81
LpFe/LpAl	10.00–29.501	3.64–8.59
dCo/dAl	0.009–0.011	0.009–0.011
TDCo/TDAI	0.009–0.010	0.006–0.008
LpCo/LpAl	0.007–0.011	0.001–0.005
dMn/dAl	0.263–0.447	0.186–0.213
TDMn/TDAI	0.261–0.319	0.115–0.173
LpMn/LpAl	0.139–0.276	0.015–0.086

3) Other possible causes for TM variability

From the comparison above, we can conclude that the changes in Fe during repeated deployments is not caused by increased remineralization nor changes in lithogenic input from atmospheric dust or sediment resuspension. The large changes in the Lp fractions must therefore be of biogenic or authigenic origin. If all LpCo would be present in biogenic particles of sinking phytoplankton cells, we would expect around 4.6 nmol L^{-1} LpFe in sinking phytoplankton at our observed maximum of $0.114 \text{ nmol L}^{-1}$ LpCo at station 3A, using an average Fe/Co ratio in phytoplankton of 40 (Moore et al., 2013) (observed ratios close to our study area were 20–40; Twining et al., 2015). However LpFe concentrations were 70 times larger, revealing that the majority of LpFe must be authigenically formed. Altogether our results suggest that changes in particle load as indicated by changes in turbidity do not comprise a major source of Fe, moreover a sink of previously dissolved Fe. Therefore, higher dissolved and Lp concentrations during the first deployment with lower O_2 concentrations must be caused by a stronger sediment source of dissolved Fe.

It is not possible to extract from our data whether the stronger sediment source under low oxygen conditions is directly driven by lower O₂ concentrations in surface sediments and in the water column resulting in higher benthic Fe fluxes and slower oxidation rates in the water column or by a longer residence time of the water mass on the shelf. However increased benthic fluxes are in accordance with previous findings from ex-situ sediment incubation experiments, where Fe fluxes increased with decreasing O₂ concentrations (Homoky et al., 2012). Therefore we hypothesize, that at a bottom water O₂ decrease from 50 to 30 μmol kg⁻¹, drastically more Fe is effectively released from the sediments by reduced oxidation at the sediment-water interface, but that a large fraction gets directly adsorbed onto particles. Therefore, particles do not compose a major source of Fe here, but may play an important role in Fe offshore transport.

Due to much lower changes in concentrations of dissolved and LpCo, and the additional effect of photoreduction and strong scavenging for Mn, we are unable to clearly resolve the main mechanisms for changes in Co and Mn concentrations with changes in O₂ and turbidity. Nevertheless, due to their similar redox-sensitive behavior and distribution in OMZs, it is likely that they are also affected by reduced O₂ conditions. The magnitude of response however, is much lower.

4.4 Conclusion

Sediments are an important source of Fe, Co and Mn to oxygen minimum waters in the Mauritanian shelf region, and remineralization and atmospheric dust deposition appear less important for Fe with vertical fluxes exceeding atmospheric fluxes but gain importance with distance from shelf. We were able to show that small changes in O₂ concentrations (from 30 to 50 μmol kg⁻¹) had a substantial influence on dissolved and LpFe concentrations and to a lower extent Co and Mn concentrations by increasing the

sediment source strength. The presence of a large part of sediment derived Fe in the leachable particulate phase highlights the importance of offshore particle transport on the Fe inventory, also in the dissolved form by reversible scavenging. To our knowledge, this is the first field study that could demonstrate strong short-term variability in redox-sensitive TMs over a few days to be directly linked to changes in O₂. These findings demonstrate that predicted long-term changes in oceanic O₂ distribution will largely impact biogeochemical cycles and will have a high implication for modelling global TM distributions. Current models do not account for small changes in O₂ on TM distribution and TM sediment fluxes. Determining the processes involved and quantifying the effect of O₂ will be crucial for the implementation into current modeling approaches. Not all processes, as e.g. the influence of the residence time of the water mass on the shelf compared to the direct influence of O₂, could be resolved in this study and it is unclear whether the changes observed on a small scale are readily transferable to a global scale. Therefore, we suggest further investigations on short-term variability of O₂ and particle load in the Mauritanian and other dynamic OMZs including water column TM measurement in combination with benthic TM fluxes and more detailed analysis of amount and types/composition of present particles.

5 El Niño reduces Peruvian shelf trace metal supply to the ocean

Insa Rapp¹, Christian Schlosser¹, Thomas J. Browning¹, Fabian Wolf¹, Frédéric A.C. Le Moigne¹, Martha Gledhill¹ and Eric P. Achterberg¹

Submitted to *Nature Geoscience*

¹Marine Biogeochemistry Division, GEOMAR Helmholtz Centre for Ocean Research
Kiel, Kiel 24148, Germany

Abstract

Upwelling ocean currents associated with oxygen minimum zones (OMZs) supply nutrients fuelling intense marine productivity. Perturbations in the extent and intensity of OMZs are projected in the future, but it is currently uncertain how this will impact fluxes of redox-sensitive Fe and other trace metal micronutrients to the surface ocean. Here we report the seawater concentrations of bioessential (Fe, Mn, Co, Zn, Cd) and process-diagnostic (Mn) trace metals in dissolved and acid-leachable fractions from the Peruvian OMZ (Equatorial Pacific) during a natural perturbation of seawater redox state accompanying the 2015 El Niño. El Niño drove atypical upwelling of oxygen-enriched water over the wide North Peruvian Shelf, resulting in strongly depleted reduced Fe(II), total dissolved Fe, and acid-leachable particulate Fe concentrations relative to non-El Niño conditions. Conversely, sustained oxygen-depleted conditions over the narrow South Peruvian Shelf led to Fe distributions typical of non-El Niño conditions. Observations of Fe were matched by the redox-sensitive micronutrients Co and Mn, but not by less redox-sensitive Cd, Ni and Zn. Collectively these observations show that oxygenation of OMZs significantly reduces water column inventories of redox-sensitive micronutrients, with potential impacts on ocean productivity.

5.1 Introduction

Coastal waters associated with eastern boundary currents receive high inputs of macronutrients (N, P, Si) and bioessential trace elements (Fe, Mn, Co, Zn, Cd) as deeper waters upwell to the surface (Bruland et al., 2005; Lohan and Bruland, 2008; Noble et al., 2012). Consequently, phytoplankton productivity in these regions is amongst the highest globally (Carr, 2001), which in turn reduces the fugacity of upwelled CO₂ and sustains up to 20% of global fish catch (Pauly and Christensen, 1995). However, taking into account phytoplankton requirements, upwelled waters are deficient in Fe relative to macronutrients (Bruland et al., 2005; Moore et al., 2013). Therefore, during off shelf transport of surface waters phytoplankton growth depletes Fe to limiting levels, leading to sharp reductions in phytoplankton productivity (Browning et al., 2017; Hutchins et al., 2002; Moore et al., 2013). Further offshore, concentrations of both Fe and macronutrients are depleted (Noble et al., 2012) and can co-limit growth (Bonnet et al., 2008; Browning et al., 2017; Ward et al., 2013). Constraining the factors that determine Fe supply from OMZs is therefore critical for projecting biogeochemical feedbacks to physical-chemical perturbations in these systems (Capone and Hutchins, 2013).

The Peruvian shelf in the eastern tropical South Pacific (ETSP) is one such OMZ coastal upwelling system, which itself alone accounts for ~10% of global fish landings (Christensen et al., 2014). Here, depleted bottom water oxygen levels (<5 μmol L⁻¹ O₂ over ~100–500 m water depth; Karstensen et al., 2008) on the continental shelf typically lead to very high benthic Fe fluxes (up to ~300 mmol m⁻¹ yr⁻¹; Noffke et al., 2012) that constitute the dominant Fe source to surface waters (Chever et al., 2015). Diagenetic processes in anoxic sediment pore waters reduce particulate Fe(III) species to soluble Fe(II), which is subsequently released into overlying bottom waters by diffusion, pore water efflux and sediment resuspension (Burdige, 1993; Chaillou et al., 2002; Froelich et

al., 1979). Fe(II) is rapidly oxidized in the presence of oxygen (Millero et al., 1987), and potentially also in the absence of oxygen by Fe(II)-oxidizing microbial nitrate reduction (Heller et al., 2017; Scholz et al., 2016). Conversely, particularly high bottom water dFe concentrations (up to 300 nmol L⁻¹) under sulfidic conditions indicate Fe(II) being stable in the absence of both oxygen and nitrate/nitrite (Scholz et al., 2016). Despite the presence of oxidation mechanisms, the combination of a strong sedimentary source and reduced oxidation kinetics under low oxygen conditions typically lead to elevated dissolved Fe (dFe) concentrations within OMZ waters over the Peruvian shelf (from a few nmol L⁻¹ up to ~80 nmol L⁻¹ under non-sulfidic conditions) (Bruland et al., 2005; Chever et al., 2015; Vedamati et al., 2014).

The complexity of the processes regulating sedimentary Fe release, water column Fe removal, and dynamics of offshore transport in OMZs means that current projections of net changes in water column Fe concentrations with modified oxygen levels—projected in the future (Schmidtke et al., 2017)—are highly uncertain. However, pronounced shifts in the strength and oxygenation of coastal upwelling over the Peruvian Shelf occur every 2–8 years, naturally, as part of the El Niño Southern Oscillation (ENSO). Specifically, El Niño events induce enhanced oxygen concentrations and an overall deepening of the oxycline (Helly and Levin, 2004; Stramma et al., 2016), thereby offering a realistic system-scale test on the sensitivity of water column Fe to changes in the oxygenation state of seawater.

5.2 Methods

5.2.1 Sampling

Samples were collected on RV Sonne cruise SO243 (8–19 October 2015) at 12 stations on four cross-shelf transects off the Peruvian coast between 9 and 17°S. El Niño events

are defined by a three-month running mean sea surface temperature (SST) anomaly of $>0.5^{\circ}\text{C}$ in the El Niño 3.4 region (5°N – 5°S , 120° – 170°W), relative to a centred 30-year base period 1986–2015 (NOAA, 2017). In October 2015 the SST anomaly was $>+2.0^{\circ}\text{C}$ near the equator and therefore considered a strong El Niño (Stramma et al., 2016). SST anomalies above $+0.5^{\circ}\text{C}$ prevailed between March 2015 and June 2016, and peaked from November 2015 and to January 2016 (NOAA, 2017).

Samples for trace metals (TMs) and iodide/iodate were collected using Ocean Test Equipment (OTE) samplers deployed on a Kevlar wire. After deployment, the OTE samplers were transferred in a DIN 5 TM clean container and pressurized with nitrogen gas (class/purity $>99.999\%$, Air Liquide, 0.2 atm overpressure). TM samples were collected in acid-cleaned (Achterberg et al., 2001b) 125 mL low density polyethylene (LDPE) bottles (Nalgene), either unfiltered (total dissolvable TMs) or filtered ($0.2\ \mu\text{m}$ Acropack 500 cartridge filters, Pall; dissolved TMs). The samples were acidified to pH 1.9 using ultra-pure HCl (OPTIMA grade, Fisher Scientific) and stored double-bagged for >6 months. Samples for Fe(II) determination were collected unfiltered in acid-cleaned opaque 125 mL high density polyethylene (HDPE) bottles (Nalgene) and immediately analyzed on-board (Hopwood et al., 2017b). Samples for iodide and iodate measurements were filtered ($0.2\ \mu\text{m}$ Acropack 500 cartridge filter), collected in opaque 60 mL HDPE bottles (Nalgene), and stored frozen at -20°C until analysis.

5.2.2 Trace metal analysis

Dissolved (d) and total dissolvable (TD) TM samples were preconcentrated and analyzed for Fe, Co, Mn, Cd, Ni, Pb, Zn and Cu as previously described (Rapp et al., 2017). Briefly, samples were preconcentrated using an automated preconcentration device (SeaFAST, Elemental Scientific Inc. (ESI)) with online buffering of samples using 1.5 M ammonium acetate buffer prior to loading onto a cation exchange resin (WAKO)

(Kagaya et al., 2009). After washing off the seawater matrix using de-ionized water (Milli-Q, Millipore), TMs were eluted from the resin using 1 M HNO₃ (SpA grade, Romil; distilled in a sub-boiling PFA distillation system (DST-1000, Savillex)) into acid-cleaned 4 mL scintillation vials (Novodirect). Preconcentrated samples were analyzed using high resolution sector field ICP-MS (Element XR, Thermo Fisher Scientific) with calibration by isotope-dilution for Fe, Cd, Ni, Cu and standard addition for Co, Mn and Pb. The concentration of leachable particulate (Lp) TMs was determined as the difference between total dissolvable and dissolved TM concentrations. Measurement uncertainties were determined after the Nordtest approach (Naykki et al., 2015; Rapp et al., 2017). Uncertainties on the TM measurements calculated after the Nordtest approach are 22% for Fe (excluding Fe(II)), 11% for Ni, 21% for Cu, 23% for Co, 17% for Mn, 13% for Cd and 13% for Zn. Standard deviation for LpFe was determined as combined error of dFe and LpFe and was between 22–33%. Uncertainties using the Nordtest approach are larger than uncertainties using the standard deviations in count rates and isotopic ratios of the measurements (1–10%), but are accounting for random and systematic effects by incorporating within-lab reproducibility and the bias obtained from determined reference materials. Reference seawater standards SAFe S (surface, ~10 m), D1 and D2 (deep, 1000 m) were analyzed in order to assess the accuracy of the analytical procedure. Obtained results and available consensus values are listed in Table 3.5.

Fe(II) was analyzed using luminol chemiluminescence flow injection analysis (FIA) without preconcentration (Hopwood et al., 2017b). The reagent (0.13 g L⁻¹ Luminol (98%, Carl Roth), 0.53 g L⁻¹ K₂CO₃ (reagent grade, Roth), 40 mL L⁻¹ NH₄OH solution (Trace Metal grade, Fisher) and 11 mL L⁻¹ concentrated HCl (Trace Metal grade, Fisher) in de-ionized water) was prepared in 2 L batches and stored for >24 h in the dark before usage to increase the chemiluminescent reagent (Luminol) response (King et al., 1995).

Briefly, analysis of Fe(II) was performed by loading one of two alternating reagent loops with Fe(II) reagent, while a second loop was utilized for H₂O₂ measurements (results not reported here). The reagent mixes with the sample after switching of the valve and is transported to the detector. Mixing of the sample and the reagent occurs after switching of the valve position. Fe(II) was analyzed in at least four replicates for each sample. Analysis was completed within 45 min after sub-sampling from OTE samplers. Standard additions were performed for each analytical run by spiking aged seawater with increasing amounts of an Fe(II) solution. An Fe(II) stock solution was prepared from ammonium Fe(II) sulfate hexahydrate (99.997% purity, Sigma Aldrich) in de-ionized water and acidified using 1 µL concentrated HCl (Trace Metal grade, Fisher) per mL. This stock solution was diluted daily in de-ionized water to be used for standard addition.

5.2.3 Iodide/Iodate analysis

Iodide and iodate analyses were undertaken from the same sample bottle. Frozen samples were defrosted overnight at room temperature for iodide. Afterwards samples were stored refrigerated for a maximum of 5 days until iodate analysis. Iodide was analyzed by cathodic stripping square wave voltammetry (Luther et al., 1988). The voltammetry unit consisted of a voltammeter stand (663 VA, Metrohm), an autosampler and a unit (Dosino, Metrohm) for automated spike addition. The system was controlled by a 797 VA Computrace (Metrohm).

Before analysis of iodate, samples were equilibrated to room temperature. Iodate concentrations were analyzed spectrophotometrically using sulphamic acid to reduce iodate to iodine (Chapman and Liss, 1977). The reaction of iodine with excess iodide forms a coloured I₃⁻ ion, which was measured using a USB 4000 detector (Ocean Optics) and a light source (Ocean Optics) with Spectra Suite (Ocean Optics) software.

5.2.4 Oxygen and nutrient analysis

Water sampling for macronutrients was performed using a stainless steel rosette with 24 x 10 L water bottles with a Seabird (SBE 02) CTD system. On-board nutrient measurements of nitrite (NO_2^-), nitrate (NO_3^-), phosphate (PO_4^{3-}) and silicic acid (Si(OH)_4) were conducted using a QuAatro autoanalyzer (Seal Analytical) (analytical precisions were 5.5, 1.3, 0.4 and 0.5%, respectively). Oxygen, temperature and salinity were measured with double sensors on the CTD system. Oxygen concentrations of discrete water samples were determined using Winkler titration with a non-electronic titration stand (Hansen, 2007; Winkler, 1988) and were used to calibrate the CTD oxygen sensor. Complete details on oxygen and nutrient analysis from this cruise are provided in Stramma et al. (2016).

5.3 Results & Discussion

In this study seawater samples were collected on a cruise that traversed the Peruvian shelf in October 2015 (Figure 5.1), several months after the start of the strong 2015/16 El Niño event (Stramma et al., 2016). Four cross-shelf transects along the Peruvian coast from 9°S to 16°S exhibited different magnitudes of El Niño-induced water column oxygenation (Figure 5.2 and Figure 5.3). El Niño induced atypical warmer, lighter, relatively oxygen-rich surface waters over Transect 1 occupying the North Peru shelf, with lowest oxygen values only observed in deeper waters ($4\text{--}5 \mu\text{mol L}^{-1} \text{O}_2$ at 240–600 m depth) (Stramma et al., 2016). Additionally, full seawater reduction of the redox indicator iodine (Wong and Brewer, 1977), exhibited as 500–600 nmol L^{-1} iodide concentrations, was only found within a narrow zone around 400 m depth (Figure 5.2a). In contrast, the three transects to the south (Transects 2–4) were characterized by sharp, shallow oxyclines ($\text{O}_2 < 5 \mu\text{mol L}^{-1}$ below 50 m) and upwelling of cold, oxygen-depleted,

macronutrient-enriched waters over the shelf (Stramma et al., 2016), which is typical of non-El Niño conditions (Stramma et al., 2016). Near-complete iodine reduction (iodide $>500 \text{ nmol L}^{-1}$) was also found over a broader and shallower depth range in the more southerly transects (200–400 m at Transects 2 and 3, and 150–400 m at Transect 4; Figure 5.2b–d).

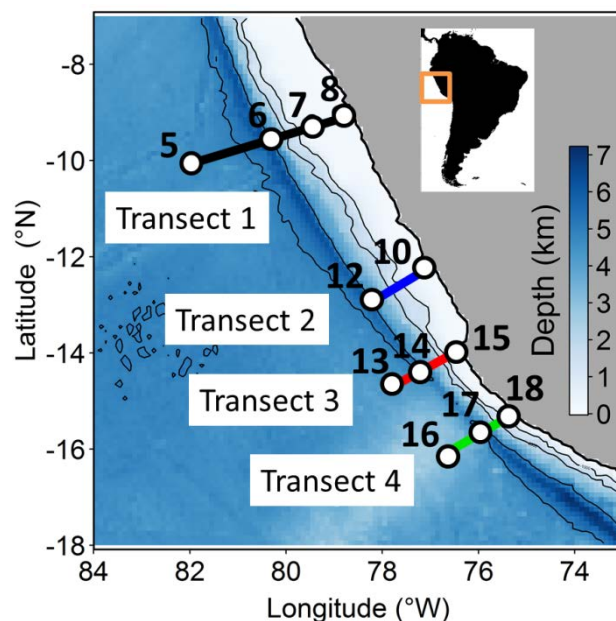


Figure 5.1: Map of sampling sites along the four cross-shelf transects. Blue colour shading indicates bathymetry, with decreasing shelf width in north to south direction.

Three fractions of water column Fe concentrations were determined on the cruise transects: (i) reduced Fe (Fe(II)), (ii) dFe ($<0.2 \mu\text{m}$ pore size filtered, Fe(II)+Fe(III)), and (iii) acid-leachable particulate Fe (LpFe) from unfiltered seawater samples. All Fe fractions for all four transects showed enhanced concentrations over the shelf and a decrease beyond the shelf break (Figure 5.2e–h)—consistent with studies reporting strong removal of benthic-derived Fe reducing offshore transport (Bruland et al., 2005; Vedamati et al., 2014). An additional observation common to all transects was the presence of elevated dFe and LpFe at the upper part of the OMZ from 100 m to 300 m (density anomalies of $26.0\text{--}26.5 \text{ kg m}^{-3}$; Figure 5.3a,b and Figure 5.6b). This feature has been previously documented for dFe, particulate Fe, and Fe(II) in the region, and was

related to a laterally transported shelf source (Heller et al., 2017). In our study we also found that concentrations of other redox-sensitive trace metals (TMs), dCo and dMn, were elevated (Figure 5.3c,d), while less redox-sensitive TMs, dCd and dNi, remained unchanged, instead exhibiting profiles resembling macronutrients (Figure 5.3 and Figure 5.6).

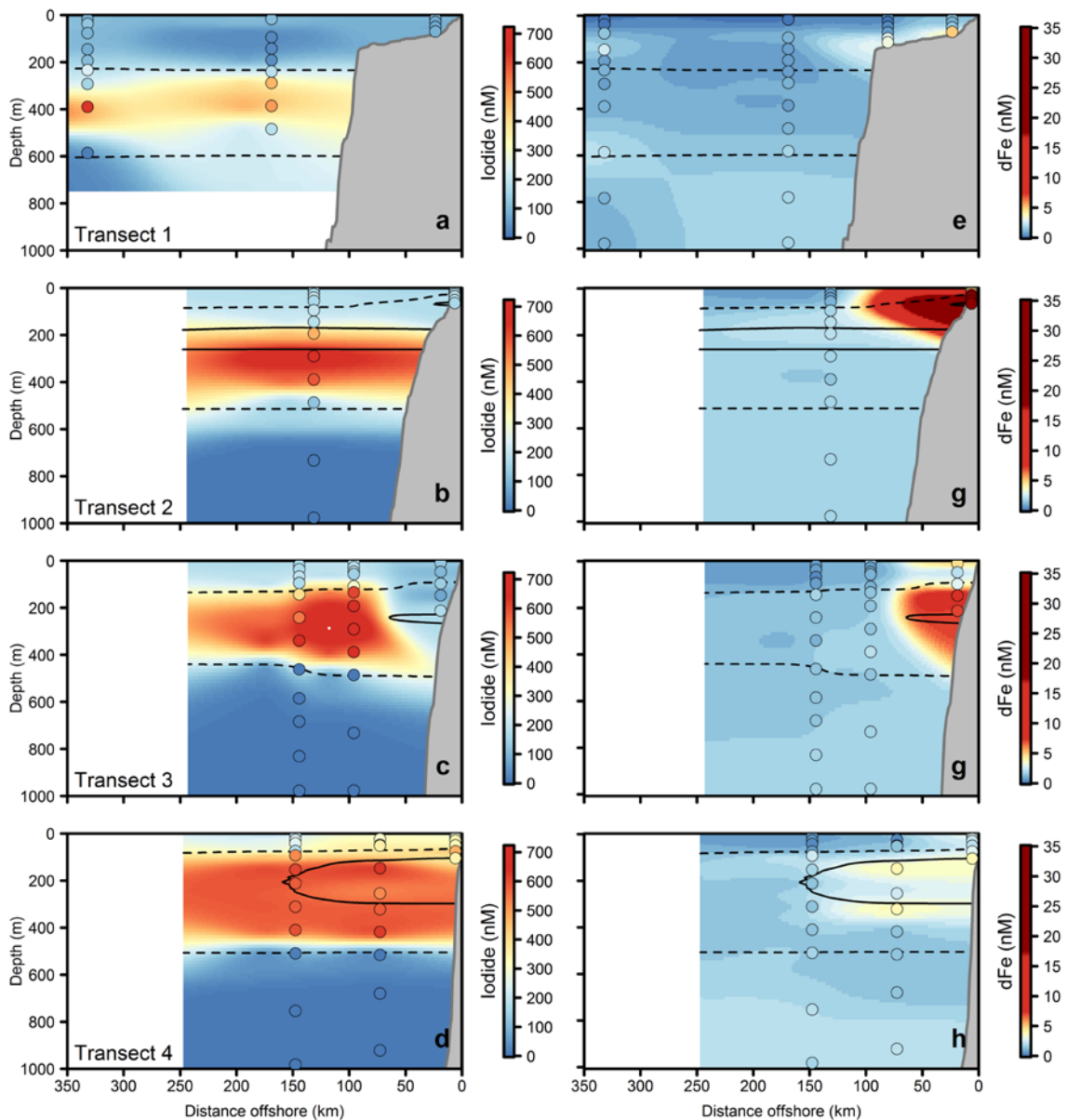


Figure 5.2: Elevated dissolved Fe concentrations under reducing conditions. (a–d) The redox indicator iodide (higher concentrations indicate more reducing conditions) and (e–h) dFe distributions along the four cross shelf transects arranged from north to south (top to bottom). Dots represent determined concentrations and background colourings are weighted average gridded fields generated in Ocean Data View. Oxygen contours are displayed for $0 \mu\text{mol L}^{-1}$ (solid line) and $5 \mu\text{mol L}^{-1}$ (dashed lines).

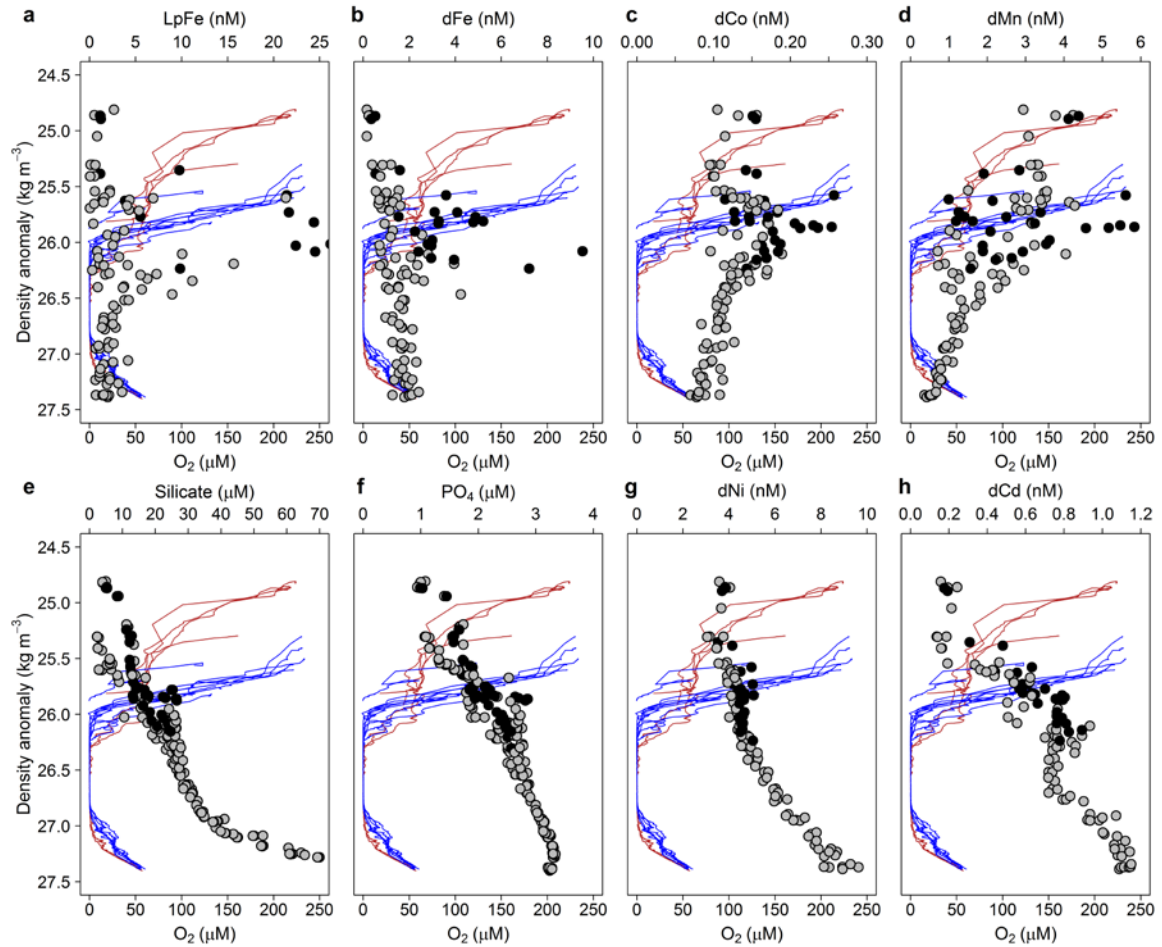


Figure 5.3: Oxygen and (micro)nutrient density distributions. Data from all stations are shown: grey and black dots indicate nutrient concentrations at offshore (bottom depth >2000 m) and onshore (bottom depth <300 m) stations, respectively. Lines indicate oxygen concentrations from Transect 1 (red) and Transects 2–4 (blue). Highest Fe concentrations at onshore stations for Transects 1–3 exceeded the scale (up to 124 nmol L⁻¹ LpFe and 30.4 nmol L⁻¹ dFe).

Part of the LpFe maxima in the upper OMZ may have formed *in situ*, by two mechanisms: adsorption of dFe onto the surface of suspended and sinking particles, and oxidation of Fe(II) to amorphous Fe(oxyhydr)oxides by traces of oxygen, hydrogen peroxide, or in connection with microbial nitrate reduction (Heller et al., 2017). As Fe, Mn and Co have a common sediment source (Noble et al., 2012), the enhanced concentrations of these metals in this density layer however points towards a dominant role of elevated benthic release on the shelf at shallower OMZ depths followed by offshore transport (Noffke et al., 2012). Increased activities of benthic-derived ²²⁸Ra, which indicate relatively recent contact with the shelf (²²⁸Ra half-life 5.75 yr), have also

been observed in the Peruvian upwelling system within the upper 200 m relative to greater depths (Sanial et al., 2018), supporting this interpretation. Collectively these observations point towards the highest net flux of benthic-derived trace metals at the top of the OMZ, where dissolved redox-sensitive trace metal concentrations are subsequently stabilized by lower oxygen concentrations (compared to shallower waters where increased removal by oxidation and microbial uptake occurs) (Boyd and Ellwood, 2010; Lohan and Bruland, 2008). Enhanced surface water concentrations were only found for Mn, which is due to sustained photoreduction of insoluble Mn(IV) to soluble Mn(II) (Sunda and Huntsman, 1994).

The upwelled flux of Fe over coastal shelves is strongly influenced by both shelf width (Bruland et al., 2001; Bruland et al., 2005) and the redox state of overlying waters (Lohan and Bruland, 2008; Pakhomova et al., 2007; Severmann et al., 2010), however the relative influence of these two factors is not well constrained. Our cross-shelf transects occupied a southward decline in shelf width, whilst the prevalent El Niño conditions induced a reverse gradient in deoxygenation. This allows us to evaluate the relative importance of these two controls on Fe distributions in this system. Despite showing similar on-shelf to off-shelf trends, absolute concentrations of all Fe fractions showed substantial variability between the four cross-shelf transects, and this variability corresponded to seawater oxygenation state (Figure 5.4). Lowest on-shelf Fe concentrations were found over the widest portion of the Peruvian shelf along Transect 1, where, uncharacteristically for the region, bottom water oxygen concentrations did not drop below $18 \mu\text{mol L}^{-1}$ (with $\text{Fe(II)} < 0.29 \text{ nmol L}^{-1}$ close to sediments, $\text{dFe} < 5.2 \text{ nmol L}^{-1}$, and $\text{LpFe} < 32.6 \text{ nmol L}^{-1}$; Figure 5.4b,c,d). Highest on-shelf concentrations of all Fe fractions were found along Transect 2, where oxygen concentrations were $< 2 \mu\text{mol L}^{-1}$ below 26 m (maximum Fe concentrations of

12.4 nmol L⁻¹ Fe(II) (52 m), 30.4 nmol L⁻¹ dFe (52 m), and 124 nmol L⁻¹ LpFe (36 m)). Between Transects 2–4, on-shelf concentrations of Fe(II), dFe and LpFe all decreased southwards with declining shelf width, to maximum values of 2.9 nmol L⁻¹ Fe(II), 3.9 nmol L⁻¹ dFe and 41.3 nmol L⁻¹ LpFe along Transect 4.

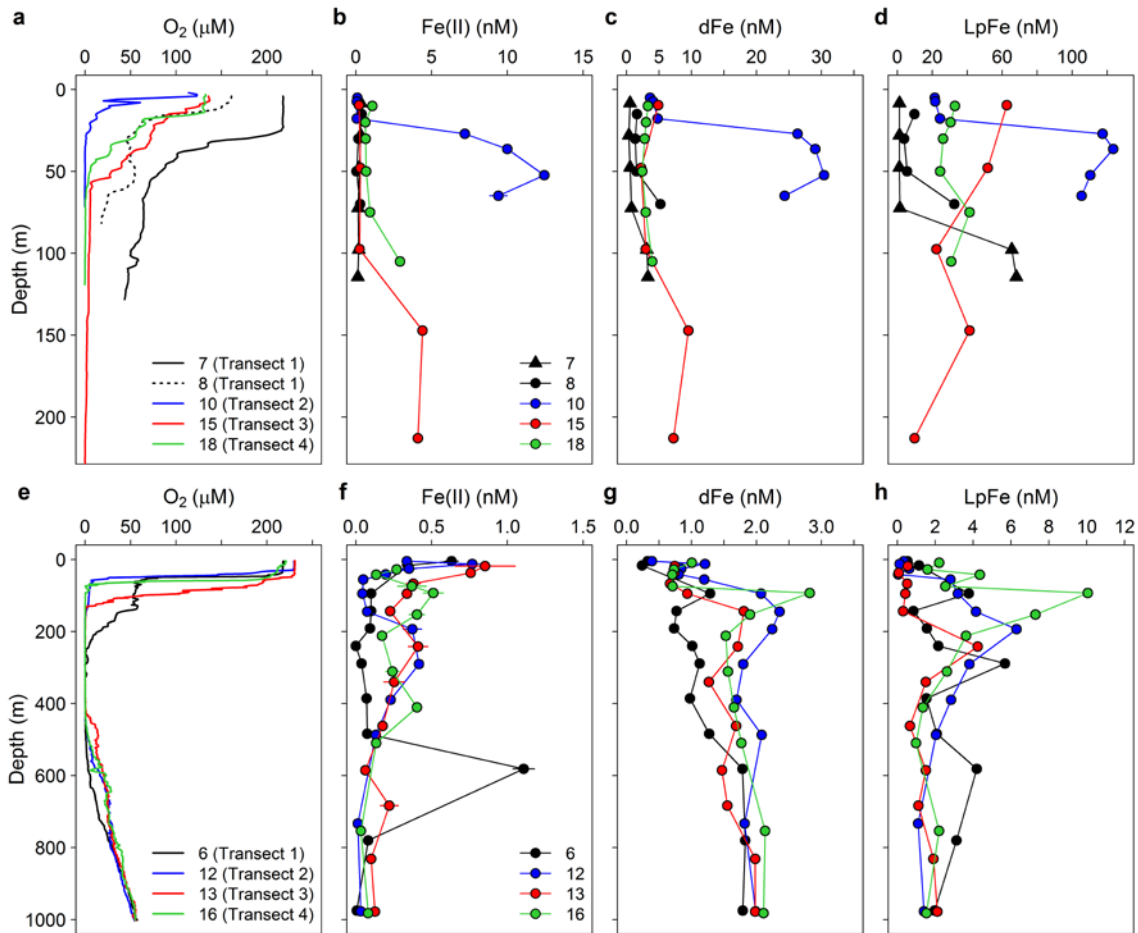


Figure 5.4: Oxygen and Fe profiles at on- and off shore stations. (a–d) Depth profiles of oxygen, Fe(II), dFe and LpFe at the five onshore stations and (e–h) at offshore stations with similar distances from the coast (130–170 km). Relative standard deviations for Fe(II) measurements are shown as error bars.

Moreover, in addition to overall concentrations, the contribution of the reduced, and most soluble Fe(II) species to dFe close to the seafloor was much lower over the shelf in the north (Fe(II):dFe=0.06 at Transect 1) relative to the three transects to the south, with progressively increasing contributions upon transitioning into more reducing conditions (Fe(II):dFe of 0.41, 0.57 and 0.74 for Transects 2, 3 and 4, respectively). Whereas bottom

water oxygen concentrations at Transects 2, 3 and 4 were all below detection limit ($<3 \mu\text{mol kg}^{-1}$) and therefore could not be used as an indicator for more subtle changes in redox status, ratios of reduced iodine (iodide) to total inorganic iodine (iodide+iodate) revealed a shift to more reducing conditions between Transects 2–4 that correlated with Fe(II):dFe ratios (iodide:(iodide+iodate) of 0.26, 0.47 and 0.72 for Transects 2, 3 and 4, respectively). The contribution, and thereby the stability, of the most soluble Fe(II) species was therefore enhanced by more reducing conditions existing below the detection limit of oxygen concentrations.

The coastal distribution of Fe concentrations along the cross shelf transects contrasts with previous studies in coastal upwelling sites with associated OMZs. Specifically, previous studies have reported highest Fe concentrations over the widest portions of continental shelves (Bruland et al., 2001; Bruland et al., 2005). Shelf width has accordingly been interpreted as a dominant control on Fe fluxes to the water column (Bruland et al., 2001; Bruland et al., 2005). For the widest section of the Peruvian shelf (Transect 1) we observed dFe concentrations that were ~ 10 times lower than previously reported values of $\sim 50 \text{ nmol L}^{-1}$ at almost exactly the same location (9°S , 52 m water depth) under anoxic conditions ($\sim 0\%$ oxygen saturation) during a La Niña event (Bruland et al., 2005). At $\sim 12^\circ\text{S}$, the approximate location of Transect 2, we measured dFe concentrations 2.5–10 times lower than the previously reported 75 nmol L^{-1} dFe (neutral ENSO; $\text{O}_2 < 5 \mu\text{mol L}^{-1}$; Vedamati et al., 2014) and 300 nM dFe (sulfidic conditions, neutral ENSO; Scholz et al., 2016). Further to the south, concentrations were similar to reported near-bottom dFe concentrations of $1.4\text{--}4.3 \text{ nmol L}^{-1}$ at $15\text{--}18^\circ\text{S}$ (Bruland et al., 2005; Vedamati et al., 2014). Collectively these trends can be attributed to the strong influence of prevailing oxidizing conditions over the northern Peru shelf under El Niño during our occupation, reflecting the net effect of diminished sedimentary Fe efflux and retention in

the overlying water column despite hosting the widest surface area of shelf sediment for release to occur.

The distribution of other TMs supported El Niño redox control of dFe. As for Fe, the redox-sensitive micronutrients dCo and dMn displayed lowest concentrations along the northern Transect 1 (Figure 5.5), whereas concentrations of dCd, a non-scavenged trace metal with depth profiles strongly regulated by biological uptake and remineralization, showed a general increase in concentration with increasing density (Figure 5.5). The latter is consistent with remineralization control at individual stations and a shift to generally higher concentrations at more southerly stations with stronger upwelling of deeper (denser) waters hosting enhanced dCd.

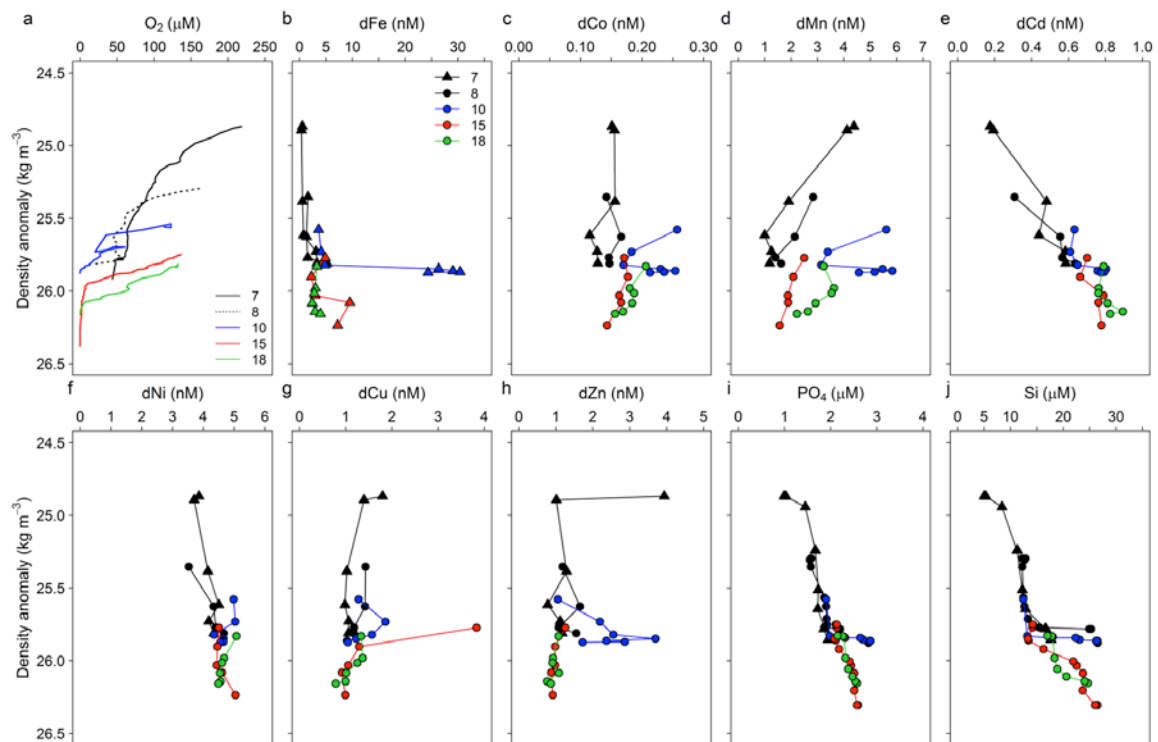


Figure 5.5: Oxygen, dissolved trace metals (dFe, dCo, dMn, dCd, dNi, dCu and dZn), phosphate (PO_4) and silicic acid (Si) density profiles of the five onshore stations. Relative standard deviations were 22% for Fe, 23% for Co, 17% for Mn, 13% for Cd, 11% for Ni, 21% for Cu and 13% for Zn.

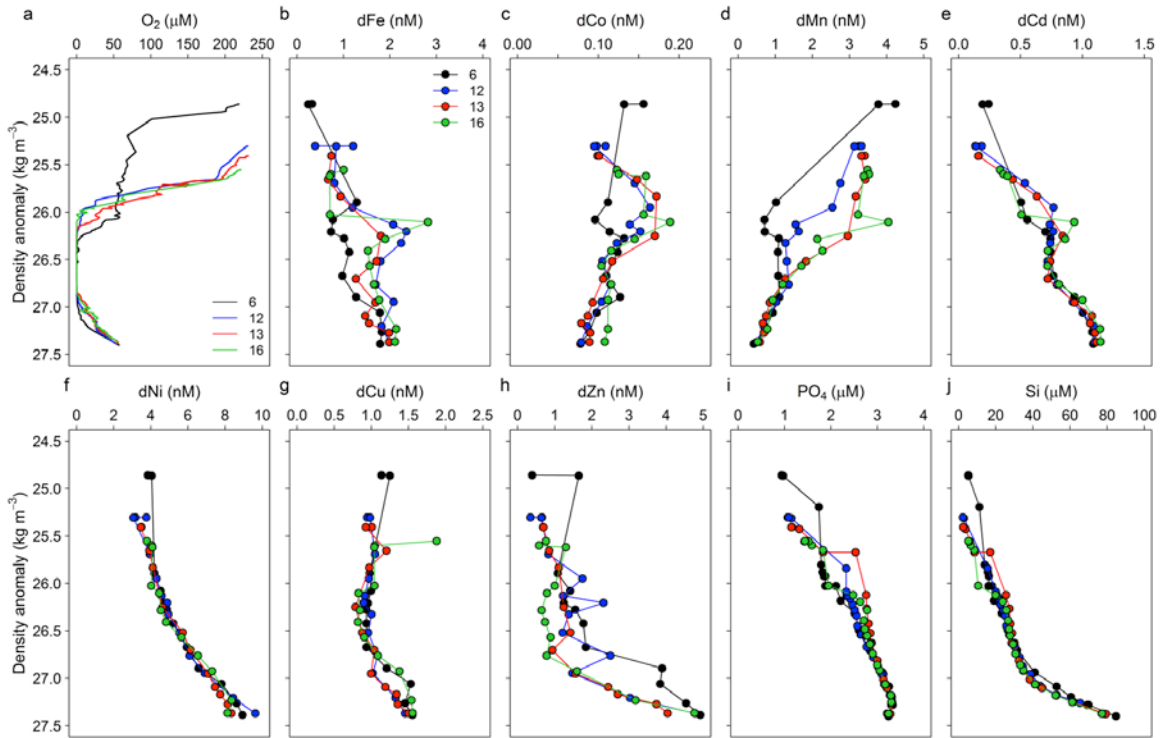


Figure 5.6: Oxygen, dissolved trace metals (dFe, dCo, dMn, dCd, dNi, dCu and dZn), phosphate (PO_4) and silicic acid (Si) density profiles of four offshore stations with similar distance from the coast (130–170 km).

The influence of El Niño on the distribution of redox-sensitive trace metals directly over the shelf appears to have been propagated offshore (Figure 5.4e–h). Within the offshore OMZ, Fe(II) was below the limit of detection at offshore stations of Transect 1 (Fe(II) $<0.2 \text{ nmol L}^{-1}$ at Stations 6 and 5, 170 and 330 km offshore respectively), whereas enhanced concentrations of $0.4\text{--}0.5 \text{ nmol L}^{-1}$ Fe(II) were present along Transects 2–3, and highest offshore Fe(II) concentrations of 4.2 and 4.6 nmol L^{-1} at station 17 of Transect 4 (depths of 148 m and 322 m respectively). Comparing offshore concentrations of dFe and LpFe within the OMZ at similar distances from the coast (130–170 km), further showed the lowest concentrations for Transect 1 (dFe $<1.3 \text{ nmol L}^{-1}$; LpFe $<5.7 \text{ nmol L}^{-1}$; $\text{O}_2 \sim 0 \text{ } \mu\text{mol L}^{-1}$ between 291 and 480 m depths) and the highest concentrations at Transect 4 (up to 2.8 nmol L^{-1} dFe; 10.1 nmol L^{-1} LpFe, $\text{O}_2 \sim 0 \text{ } \mu\text{mol L}^{-1}$ between 93 and 440 m depth). This trend was matched by redox-sensitive dCo and dMn

(Figure 5.6). In contrast, less redox-sensitive macronutrients and TMs with nutrient-like behaviour (dCd, dNi, dCu, dZn, phosphate and silicic acid) showed much less offshore variation between the transects (Figure 5.6).

Phytoplankton growth is restricted to illuminated surface waters and an important question therefore relates to how El Niño conditions influence micronutrient, and in particular dFe, supply to sunlit waters. We found higher surface dFe concentrations in less oxygenated water columns (0.73–1.2 nmol L⁻¹, three southern transects, Figure 5.2) relative to more oxygenated waters (0.24–0.32 nmol L⁻¹ at station 6, northern transect, Figure 5.2), despite the wider shelf and therefore sedimentary surface area for Fe release in the north. Direct interpretation of Fe supply to surface waters based on concentration data alone is complicated by anticipated rapid and complete phytoplankton uptake of supplied Fe in this system independent of the supply rate (Ward et al., 2013). However, the overall lower dFe in both surface and subsurface waters (in density layers that subsequently upwell; Figure 5.4), combined with higher ratios of nitrate+nitrite to dFe (Figure 5.7), at on- and off shore stations along Transect 1 compared to Transects 2–4, strongly indicates that the more oxidizing water column conditions induced by the El Niño result in a faster off-shelf transition into Fe limiting conditions, possibly driving overall reductions in productivity (Bruland et al., 2005; Johnson et al., 1999).

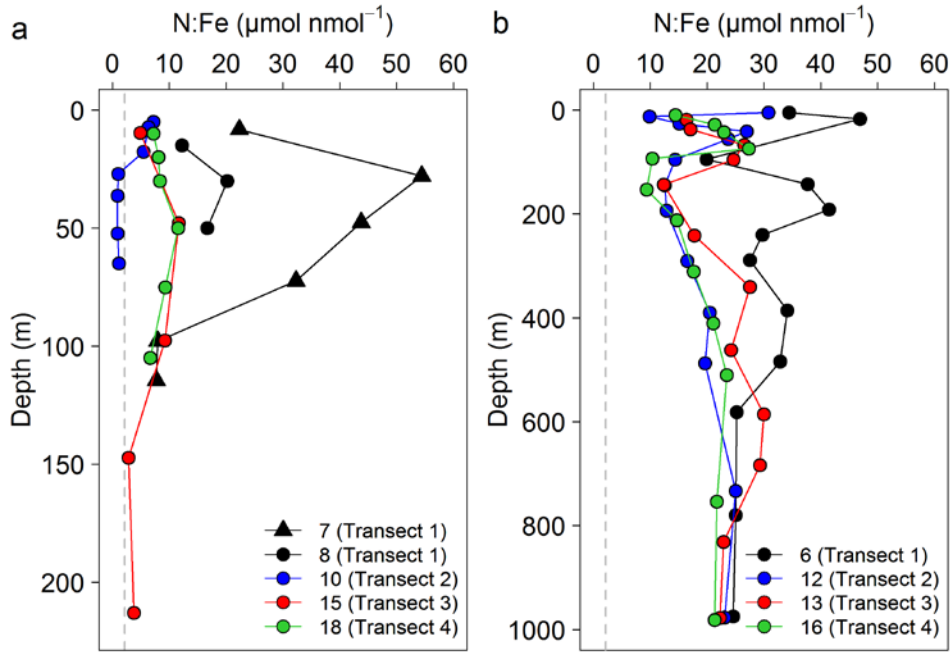


Figure 5.7: Depth profiles of nitrogen ($\text{NO}_3 + \text{NO}_2$) to Fe ratios along the four transects for (a) onshore stations, and (b) offshore stations. Vertical dashed line shows assumed average phytoplankton N:Fe requirement (from synthesis values in Moore et al. 2013).

5.4 Conclusion

Our observations have demonstrated the critical control of seawater oxidation state, within the context of shelf width (Bruland et al., 2005; Johnson et al., 1999), on water column concentrations of redox-sensitive micronutrient metals in the Peruvian Upwelling zone. Such data should constitute a vital part of evaluating on-going changes in biogeochemistry and overall productivity of eastern boundary upwelling zones (Capone and Hutchins, 2013). In the future, OMZs are however proposed to be more, rather than less, oxygen-depleted (Schmidtko et al., 2017), whereas El Niño events may become more frequent (Cai et al., 2014). Considerable uncertainty therefore remains in predicting future changes in Fe concentrations under conditions of more widespread and intense oxygen depletion punctuated by more frequent, transient, oxygenation. Intermittent oxic events in OMZs, which leads to Fe precipitation from the water column, have been suggested to play a critical role in resupplying Fe to sediments that can subsequently be

released following resumption of anoxia (Noffke et al., 2012; Scholz et al., 2011). Therefore, the importance of episodic oxygenation events may need to be considered when evaluating the knock-on feedbacks of deoxygenation (Schmidtko et al., 2017), Fe supply (Noffke et al., 2012), phytoplankton productivity (Moore et al., 2013), and the associated network of interconnected biogeochemical cycles (Capone and Hutchins, 2013) into the future.

Acknowledgements

The authors thank the Captain, crew and chief scientists, C.A. Marandino, T. Steinhoff and D. Grundle of the RV Sonne SO243 cruise. M. Hopwood is thanked for useful discussions and advice for the Fe(II) measurements. This work was funded by the Deutsche Forschungsgemeinschaft as part of Sonderforschungsbereich (SFB) 754: 'Climate-Biogeochemistry Interactions in the Tropical Ocean'. T.J.B. was funded by a Marie Skłodowska-Curie Postdoctoral European Fellowship (OceanLiNES; grant number 658035). The cruise was funded by the Bundesministerium für Bildung und Forschung (03G0243A). F.A.C.L.M. was funded by a DFG Fellowship of the Excellence Cluster 'The Future Ocean' (TRANSFER; grant number CP1403).

6 Conclusions and future directions

6.1 Summary

The major aim of this study was to improve our understanding of trace metal (TM) cycling in coastal low oxygen waters, and in particular factors that influence sources, stabilisation and removal of TMs. A focus was on the effect of variability in O₂ concentrations on the sediment-derived, redox-sensitive TMs Fe, Co and Mn, which is of particular interest in the context of improving our model parameterisation of the consequences of projected expansion of oxygen minimum zones (OMZs). We observed the distributions of a suite of TMs (Al, Co, Mn, Ni, Cu, Cd, Pb and Zn) with different physical, chemical and biological behaviours in two distinct OMZs: (i) off Mauritania in the eastern tropical North Atlantic (ETNA); and (ii) off Peru in the eastern tropical South Pacific (ETSP).

In Chapter 3 a newly developed and optimized method for the simultaneous analysis of Fe, Co, Mn, Ni, Cu, Cd, Pb and Zn was described. This method enabled high throughput and accurate quantification of the suite of TMs from a small seawater volume and was verified by matching SAFe S, D1 and D2 reference seawaters for TM concentrations. This method was then used for the analyses of the samples collected as part of the studies described in Chapter 4 and 5.

The TM distribution in the Mauritanian shelf region, described in Chapter 4, revealed Fe, Co and Mn concentration maxima within water layers with low O₂ concentrations. The observed maxima were caused by enhanced benthic inputs rather than remineralization of sinking particles from surface waters, as the enhanced TM concentrations were

decoupled from major nutrients and nutrient-like TMs. Temporal changes in Fe, Co and Mn concentrations within a few days at repeated coastal stations coincided with changes in O₂ concentrations and were likely driven by variations in their sediment-to-water column fluxes, with higher benthic fluxes under lower O₂ conditions. Variability in organic matter remineralization and lithogenic inputs appeared to be of minor importance for the TM variability in the deeper water column. Additionally, on the shelf we identified benthic Fe fluxes as the dominant source of dFe to surface waters, whereas the relative influence of atmospheric deposition of dust as an additional source increased with distance from the shelf.

The main finding of Chapter 5 was the strong influence of El Niño conditions at the northern Peruvian coast in the ETSP on the distribution of redox-sensitive TMs. TM distributions along four cross-shelf transects along the Peruvian coast with different shelf-widths and oxygenation states revealed a primary influence of the seawater oxygenation state on the distribution of Fe(II), dFe, dCo and dMn and a secondary influence of the shelf-width. Higher than usual water column O₂ concentrations, caused by the El Niño event, resulted in much lower concentrations of dFe and a much lower fraction of dFe present as Fe(II) at the northern Peruvian shelf compared to concentrations observed in previous studies under lower O₂ conditions. At the southern Peruvian shelf, bottom waters remained oxygen-depleted and Fe concentrations were in agreement with previous studies. Independent of the different oxygenation state of the shelf and shelf-width, plots of other bioessential TMs (e.g. Cd) as a function of density on the four transects revealed very similar distributions. The difference between redox-sensitive TMs and nutrient-like TMs suggested redox-influenced processes, such as sediment release and oxidation, instead of biological uptake and remineralization to cause the Fe, Co and Mn variability.

6.2 Comparison of the two study regions

Increasing concentrations of the redox-sensitive TMs Fe, Co and Mn with decreasing O₂ concentrations were observed in both study regions. These changes were not reflected by changes in less redox-sensitive nutrient-like TMs, supporting a strong direct dependency of the distribution of Fe, Co and Mn on oxygen concentrations.

However, a simple correlation between TM concentrations and O₂ was not observed, either for one of the regions or for both regions combined (Figure 6.1A–C). In fact, the overall trends in correlations between redox-sensitive TMs and O₂ varied largely. In the Mauritanian OMZ, dFe, dCo and dMn concentrations tend to decrease within increasing oxygen concentration between 30 and 70 μmol L⁻¹ O₂, whereas highest dFe, dCo and dMn concentrations in the Peruvian OMZ were observed at almost anoxic conditions and were drastically lower at >10 μmol L⁻¹ O₂. The differences might be partly explained by offshelf stations being sampled further away from the coast in the Peruvian OMZ (up to 380 km) compared to the Mauritanian OMZ (<77 km). However, even for comparable shelf stations with similar bottom water O₂ concentrations (~30 μmol L⁻¹), bottom depths, and distance from the sediments, dFe concentrations on the Peruvian shelf were ~5 nmol L⁻¹ in comparison to ~9 nmol L⁻¹ on the Mauritanian shelf. On the Mauritanian shelf dFe concentration as high as 18 nmol L⁻¹ were observed at ~50 μmol L⁻¹ O₂, whereas at the Peruvian shelf dFe concentrations >6 nmol L⁻¹ were only observed at O₂ <10 μmol L⁻¹.

Comparing the distribution of Fe, Co and Mn between the dissolved and total dissolvable phases also revealed differences between the two regions (Figure 6.1D–F). All three TMs showed a higher fraction in the leachable particulate phase in the Mauritanian OMZ. This may indicate elevated oxidation and particle scavenging in the Mauritanian OMZ

compared to the Peruvian OMZ, or a larger additional input of particulate TMs, for example by atmospheric dust deposition. In Chapter 4, however, we were able to identify a large amount of LpFe in the Mauritanian OMZ to be derived from an authigenic source, such as adsorption of dFe to particle surfaces or the formation of Fe(oxy)hydroxides.

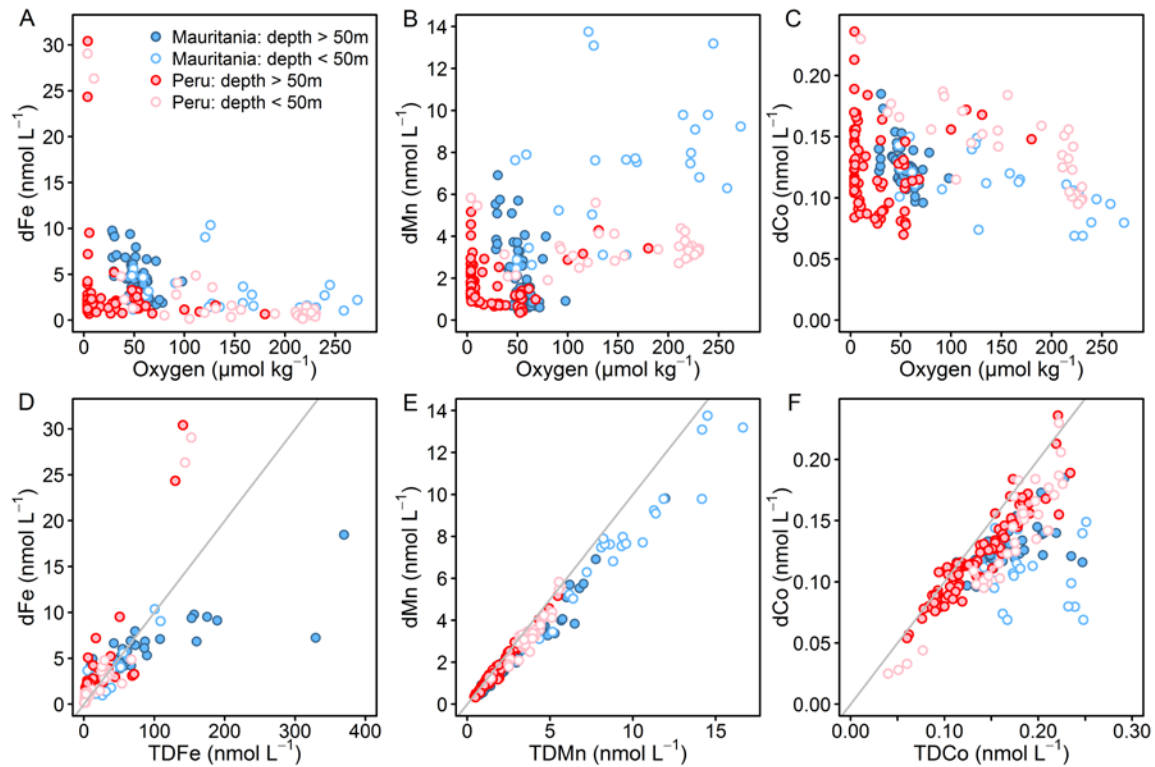


Figure 6.1: Comparison of TM (Fe, Co and Mn) distribution of the two study regions. A-C) Dissolved TM concentrations plotted against oxygen concentrations, D-F) dissolved TM concentrations plotted against total dissolvable TM concentrations. Grey lines indicate $TDFe = 10 \times dFe$ (D), $TDMn = dMn$ (E) and $TDCo = dCo$ (F).

The overall depth distributions, plotted as density profiles in Figure 6.2, show large differences in concentrations and distributions for all TMs as well as for macronutrients.

The macronutrients, silicic acid and phosphate (PO_4) and the nutrient-like TMs Cd and Ni, generally increase with depth in both regions, but show overall lower concentrations in the Mauritanian region than in the Peruvian region. This observation matches with the global oceanic distribution of these micronutrient metals, with generally lower concentrations found in the Atlantic Ocean compared to the Pacific Ocean, due to younger water mass ages in the Atlantic Ocean and therefore less time for input from

rem mineralization (Bruland and Lohan, 2006). In contrast, Fe, Co and Mn do not reveal increased concentrations in the Pacific compared with the Atlantic, as they are influenced by scavenging processes (Mn) or a balance between scavenging and remineralization processes (Fe and Co) (Bruland and Lohan, 2006). Co concentrations are similar in both regions and did not show a significant decrease with distance to the coast, indicating that the removal process for Co are much slower compared to Fe (Noble et al., 2012). LpFe and dFe concentrations were generally higher throughout the water column in the Mauritanian OMZ, and dMn were higher in surface waters of the Mauritanian OMZ but revealed a faster decrease with depth compared to the Peruvian OMZ. The slower decrease of dMn with depth in the Peruvian OMZ might partly be driven by the overall lower concentrations of Mn and by slower oxidation rates under lower O₂ concentrations (von Langen et al., 1997). The density profiles of the two regions additionally show differences in the distribution of Fe, Co and Mn along low oxygen waters. In the Peruvian shelf region, concentration maxima of Fe, Co and Mn were not present throughout the entire depth of the OMZ, more so at the top of the OMZ. In the Mauritanian shelf region, increased concentrations of these metals were present across the entire vertical extent of the two OMZ layers with decreased concentrations in between the two layers.

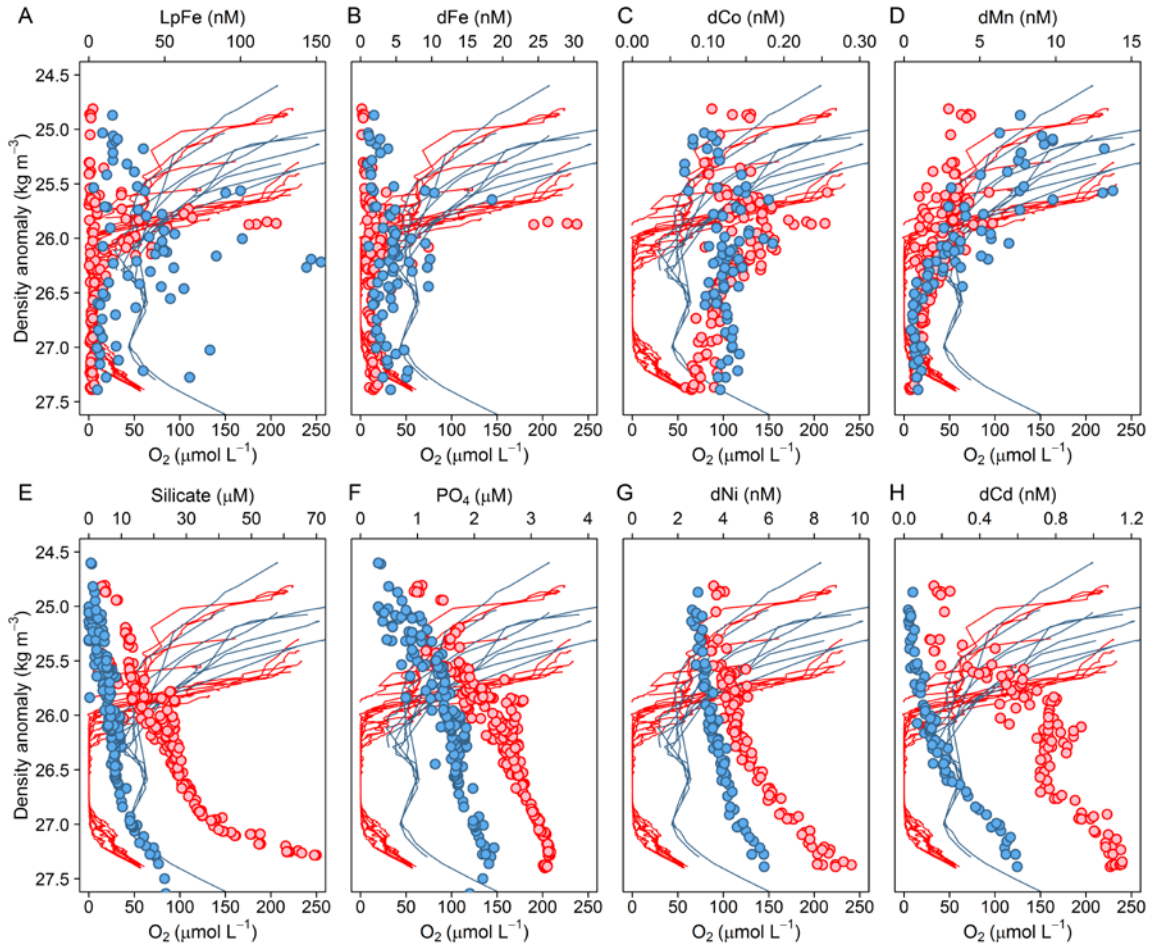


Figure 6.2: Density plots of redox-sensitive TMs (LpFe, dFe, dCo, dMn), macronutrients (silicic acid and phosphate) and nutrient-like TMs (dNi and dCd) for all data from the Mauritanian OMZ (blue circles) and the Peruvian OMZ (red circles). The oxygen distributions are plotted as blue lines for the Mauritanian OMZ and red lines for the Peruvian OMZ.

The differences in the TM distributions between the two regions and different correlations with O_2 concentrations should perhaps not be surprising, as multiple factors other than O_2 have an important influence on TM distributions, as discussed in detail in Chapters 1, 4 and 5. In the following the two study regions are compared with regards to their particular environmental characteristics, in addition to O_2 concentrations, which could have had important influences on TM distribution.

6.2.1 Additional TM inputs

The ETNA receives a large amount of atmospheric dust input from the Saharan desert, whereas dust deposition in the ETSP is very low. Dissolved atmospheric Fe deposition

fluxes to surface waters of the Mauritanian OMZ are between 0.12–2.12 $\mu\text{mol Fe m}^{-2} \text{d}^{-1}$ (Rijkenberg et al., 2012; Ussher et al., 2013, this study), whereas soluble atmospheric deposition fluxes to surface waters of the Peruvian OMZ are an order of magnitude lower, between 0.016–0.107 $\mu\text{mol Fe m}^{-2} \text{d}^{-1}$ (Baker et al., 2016). Estimates of averaged soluble Fe fluxes were 0.05–0.12 $\mu\text{mol Fe m}^{-2} \text{d}^{-1}$ (Powell et al., 2015) in the ETNA and 0.015 $\mu\text{mol Fe m}^{-2} \text{d}^{-1}$ off Peru (Krishnamurthy et al., 2009). Accordingly, whilst the major source of TMs in the Peruvian OMZ are considered to be from sediment input (e.g. Chever et al., 2015), in the ETNA a combination of sediment and atmospheric input are considered to both influence the water column TM inventory (Milne et al., 2017; Rijkenberg et al., 2012; Ussher et al., 2013).

6.2.2 Sediment release

The sediment release of redox-sensitive TMs is strongly influenced by bottom water O_2 concentrations (Pakhomova et al., 2007; Severmann et al., 2010). However, other factors than bottom water O_2 concentrations influence the sediment release of TMs, including shelf topography, sediment type and organic matter input to the sediments (Homoky et al., 2016). Accordingly, despite the large differences in oxygenation state of the shelf, benthic Fe fluxes in the Mauritanian and Peruvian shelf are comparable in their magnitude (Lomnitz et al., in review). Observed diffusive Fe(II) fluxes (determined from porewater Fe(II) concentrations) in the Mauritanian shelf were 0–0.05 $\text{mmol m}^{-2} \text{d}^{-1}$ (Lomnitz et al., in review), whereas reported diffusive Fe(II) fluxes in the Peruvian shelf were typically around 0–0.065 $\text{mmol m}^{-2} \text{d}^{-1}$ at bottom depth <400 m (Noffke et al., 2012; Scholz et al., 2016). However, episodically much larger benthic Fe fluxes of up to 0.5 $\text{mmol m}^{-2} \text{d}^{-1}$ have been observed on the Peruvian shelf (Noffke et al., 2012).

1) Organic matter input

The organic matter input to the shelf sediments influences TM sediment fluxes, as the organic carbon input determines the O₂ consumption by remineralization within the sediments and consequently results in the enhanced reduction of Fe and Mn oxides after O₂ and nitrate are fully depleted as electron acceptors (Homoky et al., 2016). Additionally, organic matter is a transporter of TMs to sediments. Higher DIC fluxes from the sediments and POC content of the sediments in the Peruvian OMZ than in the Mauritanian OMZ indicate higher organic matter inputs and thereby faster oxygen consumption in marine sediments. For example, the POC content of sediments off the coast off Mauritania is 1–3 wt% (Hartmann et al., 1976; Martinez et al., 2000) and 2.5–20 wt% off Peru (Suess, 1981). This would imply Peruvian sediments would have the potential to release more redox-sensitive TMs.

2) Sediment type

In some regions a correlation between organic carbon oxidation rates and benthic Fe fluxes has been observed (Elrod et al., 2004). As a result this relationship is often used in global extrapolations in ocean models to parameterize sedimentary Fe flux to seawater (Blain and Tagliabue, 2016). However, an extrapolation of this relationship to global shelf sediments might not be justified, as shelf regions with a low reactive Fe content have been shown to exhibit much lower Fe fluxes than predicted from organic carbon oxidation rates (Homoky et al., 2013). This highlights the importance of the sediment type and in particular, the reactive TM inventory of the sediment. The inventory of reactive TMs in sediments is determined by the provenance of the lithogenic sediment material and the mixture and amount of lithogenic and biogenic material input.

For example, sediments in the Peruvian OMZ contain slightly younger, more soluble, igneous rock material than the Mauritanian OMZ (as indicated by heavier ϵNd values)

(Jeandel et al., 2007). Sediments underlying the Peruvian OMZ can broadly be classified as clays and diatom ooze, whereas sediments underlying the Mauritanian OMZ can be classified as clays and fine-grained calcareous sediments (Dutkiewicz et al., 2015). Also sediment grain size influences TM release by influencing the amount of reactive surface area available for TM exchange with an increase in reactive surface and therefore TM exchange in fine-grained sediments (Homoky et al., 2016). Additionally, the solute exchange between sediment and bottom waters and the entrainment of oxygen into the seafloor are influenced by grain size with a larger exchange in coarse sandy sediments compared to fine sediments (Homoky et al., 2016). The distribution in grain size is largely influenced by shelf topography (see below). In the core of the Peruvian OMZ, continuous reductive dissolution of Fe and transport into the water column results in a depletion of sediments in Fe, as indicated by decreased Fe/Al ratios (Noffke et al., 2012; Scholz et al., 2016). In contrast, below and above anoxic bottom waters, in bottom waters with oxygen levels above a few $\mu\text{mol L}^{-1}$, an enrichment in Fe/Al ratios was observed, as a result of Fe(oxy)hydroxide precipitation (Scholz et al., 2016). Depletion in OMZ sediment Fe content through increased dissolution may ultimately result in decreased Fe fluxes, although it is not clear how significant flux changes would be and over what timescales.

3) Shelf topography

The topography of the shelf influences the formation of waves and the bottom current energy and thereby sediment resuspension (Homoky et al., 2016). The shelf topography also influences the distribution of sediment particle size (Homoky et al., 2016). Finer particles are preferentially transported further distances and thereby deposit to deeper seafloor regions, typically resulting in more sandy shallow sediments and more fine-

grained muddy deeper sediments. Additionally, shallower sediments experience a higher input of organic matter which enhances trace metal fluxes (Noffke et al., 2012).

4) Sediment communities

Organisms living in the sediments or at the sediment-water interface can have an additional influence on the sediment TM release into the overlying water column. Shelf sediments in the Mauritanian OMZ are inhabited by burrow-dwelling microfauna, which can facilitate the solute exchange between sediments and seawater by bioirrigation (Dale et al., 2014; Kristensen et al., 2012).

5) Shelf width

As mentioned in Chapter 5, the shelf width has an important influence on the overall flux of sediment released TMs. The shelf width does not directly influence sediment fluxes per unit area, but determines the total seafloor surface area available for TM release compared to the overlying water volume, and thereby results in increased concentrations of sediment released TMs. The Mauritanian shelf is narrower than the northern Peruvian Shelf but much wider than the southern Peruvian shelf. The shelf break (region where the slope of the seafloor increases) of our study region in the Mauritanian OMZ was at a distance of ~40 km from the coast and at ~250 m water depth. The shelf break at the most northern transect of the Peruvian coast was ~100 km off the coast and at ~200 m water depth. The shelf width decreased drastically towards the southern Peruvian coast where the bottom depth drops to over 400 m within 20 km distance to the coast. Just on basis of the shelf width, TM input on the northern (southern) Peruvian shelf would therefore be expected to be larger (smaller) than on the Mauritanian shelf.

6.2.3 Physical transport

As oxidation and scavenging processes are time dependant, the efficiency of the (offshore) transport away from the sources compared to removal processes is strongly influenced by the offshore velocity of physical transport. In the Mauritanian OMZ, a local offshore maximum in dFe, dCo and dMn and $^{224}\text{Ra}/^{223}\text{Ra}$ indicated locally rapid transport of waters that had been in recent contact with the sediments and could be explained by local and short-term variabilities in the dynamic current system in this region (Schafstall et al., 2010). Vertical fluxes of TMs to surface waters are influenced by diapycnal mixing and vertical advection related to upwelling and eddy pumping (e.g. Steinfeldt et al., 2015). And also the offshore transport might be largely influenced by eddy movement (Czeschel et al., 2011).

6.2.4 Primary productivity and remineralization

Primary production (PP) in surface waters influences the uptake rates of TMs and thereby their removal from surface waters. PP coupled to export efficiency, the fraction of PP exported downwards out of the surface layer, also determines the amount of organic matter which is transported to deeper depths, with subsequent release of dissolved TMs during remineralization. The PP off the coast of Peru is reported as $1.8\text{--}3.6 \text{ g C m}^{-2} \text{ d}^{-1}$ (Pennington et al., 2006; Quiñones et al., 2010; Walsh, 1981), perhaps slightly higher than that off the coast of Mauritania $0.3\text{--}2.3 \text{ g C m}^{-2} \text{ d}^{-1}$ (Morel et al., 1996). The remineralization length scale (RLS; the ‘vertical distance over which organic particle flux declines by 63%’; Boyd and Trull (2007)) also differs between regions (e.g. Marsay et al., 2015). OMZs for example are characterized by larger RLS compared to oxygenated waters (Devol and Hartnett, 2001; Keil et al., 2016; Van Mooy et al., 2002). Especially in anoxic OMZs, such as the Peruvian OMZ, RLS are large due to the absence or strong reduction in grazing activity by zooplankton (Cavan et al., 2017) as most metazoans

cannot tolerate very low O₂ concentrations (Wright et al., 2012). Therefore, the input of dissolved TMs by remineralization might be lower in the Peruvian OMZ compared to the Mauritanian OMZ despite higher PP at the Peruvian margin. The high surface Fe concentrations in the ETNA, mainly caused by high atmospheric Fe deposition, may result in an enhanced ratio of Fe to major nutrients in phytoplankton cells in the ETNA due to luxury uptake of Fe (Sunda and Huntsman, 1995). Increased Fe/C ratios of sinking organic matter may therefore result in enhanced release of dFe during organic matter remineralization within the Mauritanian OMZ and may help to explain the overall higher dFe concentrations in this region in comparison to the Peruvian OMZ.

6.2.5 Removal rates

Oxidation of sediment-derived reduced Fe, Co and Mn species transforms the TMs into the less soluble oxidized form. Abiotic oxidation processes are dependent on the prevalent O₂ concentrations (e.g. King et al., 1995). However, the oxidation by electron acceptors other than O₂ may occur and influence removal rates of dissolved TMs (e.g. Moffett and Zika, 1987). In addition, biogenic oxidation processes, as known to occur for Fe(II), Mn(II) and Co(II), might show a different dependency on O₂ concentrations and may occur in the absence of oxygen. Especially for Mn(II), oxidation by microbial processes likely dominates Mn(II) oxidation rates (Moffett, 1994; Tebo and Emerson, 1986). An example is nitrate reduction by Fe-oxidizing bacteria, as has been suggested to occur in the Peruvian OMZ (Scholz et al., 2016). In addition to oxidation processes, removal rates are influenced by the type and the amount of particle surfaces present for adsorption (Honeyman and Santschi, 1987) and the amount and character of organic complexation (ligands) preventing loss by scavenging (Gledhill and Buck, 2012).

6.3 Predicting long term effects of ocean deoxygenation on TM distributions

In both of our study regions short term-variability in O_2 resulted in pronounced concentration changes in redox-sensitive TMs, with generally enhanced concentrations under lower O_2 conditions. However, the magnitude in response and long-term effects might vary largely between the two regions studied here. In the Mauritanian OMZ, decreases in O_2 are likely to result in a significant increase in benthic Fe fluxes. A decrease in sediment fluxes by depletion of the reactive Fe inventory is less likely to occur due to the enhanced TM input originating from atmospheric deposition of mineral dust. In contrast, Fe depletion of sediments has been observed in the Peruvian OMZ and could cause reduced benthic Fe fluxes in the core of the OMZ (Noffke et al., 2012; Scholz et al., 2016). If during an expansion of the Peruvian OMZ the sedimentary-released Fe flux becomes larger than its resupply, then the increase in benthic Fe fluxes might be lower compared to the Mauritanian OMZ. In general the results of this PhD thesis indicate that anoxic and suboxic regimes and regions with different magnitudes of TM inputs to the sediments need to be considered differently in terms of seawater TM changes in response to enhanced deoxygenation.

An increase in benthic TM release as a result of deoxygenation might have a large influence on biogeochemical cycles (Capone and Hutchins, 2013). For example, predicted future increases in deoxygenation and thereby enhanced redox-sensitive TM concentrations (Chapter 3 and 4) could result in enhanced PP if the region is currently limited by TMs and if the enhanced benthic TM release reaches the surface ocean. This effect therefore may only be significant in regions where limitation of phytoplankton by Fe (or potentially Co or Mn) occurs (Boyd et al., 2007; Moore et al., 2013). In very close proximity to coastlines the supply rates of Fe and other nutrients typical exceed

phytoplankton demand, with growth restricted by light availability or top down grazing control, however due to rapid removal by scavenging Fe limitation can develop rapidly within tens of kilometres from coastlines (Hutchins et al., 1998; Moore et al., 2013). In the Peruvian OMZ, Fe limitation has been observed less than 100 km offshore (Browning et al., in review) and productivity may therefore be enhanced by increased Fe release from sediments. In the ETNA, under the Saharan dust plume, surface dFe concentrations are usually elevated out into the open ocean (e.g. Schlosser et al., 2014). In regions currently subjected to large atmospheric inputs of Fe, any enhanced sediment fluxes may not have a large impact on phytoplankton productivity, unless those waters are advected to low Fe regions, for example from the ETNA to the South Atlantic gyre (Ussher et al., 2013). Overall, the biological impact of changes in sediment TM release might be anticipated to largely depend on the nature of the biogeochemical system in which the changes occur.

In addition to changes in TMs, ocean deoxygenation may also influence the distribution of the major nutrients. For example, in OMZs denitrification and annamox result in a loss of nitrogen (Gruber and Sarmiento, 1997), whereas enhanced benthic fluxes of phosphate are observed under low O₂ conditions (Ingall and Jahnke, 1994). Therefore projected changes in TMs, nitrogen and phosphorous accompanying O₂ changes, alongside changes in other factors such as irradiance and temperature, need to be considered together in order to successfully predict the net effect on phytoplankton productivity.

Ocean deoxygenation is not the only climate change scenario that has an influence on TM distribution. For example increased stratification of the surface water column, predicted as a result of global warming, may decrease vertical mixing fluxes of nutrients to surface waters (e.g. Bopp et al., 2005). Ocean acidification influences TM speciation and solubility and therefore may influence oceanic TM cycling (Breitbarth et al., 2010;

Gledhill et al., 2015; Millero et al., 2009). The inorganic solubility of some TMs (e.g. Fe, Cu and Al) is predicted to increase with decreases in seawater pH, caused by an increase in atmospheric CO₂, whereas complexation by organic ligands was shown to decrease for Fe and Cu (Gledhill et al., 2015). Also non-sedimentary inputs of TMs may change significantly in the future. Altered precipitation may modify riverine inputs in some regions and changes in wind speed, aridity, precipitation, and land use may alter atmospheric deposition fluxes (Jickells et al., 2005).

6.4 Future directions

This thesis has demonstrated what appears to be a direct dependency of redox-sensitive TMs released from sediments on O₂ concentrations in two distinct OMZs of the ETNA and the ETSP. However, important details constraining to what extent TMs are influenced by the aforementioned parameters relative to O₂ are still lacking. It was also not possible to extract from our dataset to what extent the O₂ concentrations affect sediment TM release itself and to what extent changes in removal rates under modified O₂ conditions impact these concentration changes. Therefore there are still missing gaps and an urgent requirement for future studies to focus on the interaction of TM release, stabilisation and cycling under varying oxygen conditions. In the following, several suggestions are made for future studies addressing this topic and improving methods available for TM analysis.

Firstly, the interpretation of the results in our study would have benefited from supporting data of benthic TM fluxes under the varying O₂ conditions. In the Mauritanian OMZ, sediment fluxes were available at most stations but were not performed for the repeated profiles at the same location where the large short-term variability in O₂ and TMs was observed. In the Peruvian OMZ there was no supporting sediment TM flux data

from the same cruise (SO243). Therefore, further cruises are recommended, to focus on combined collection of both seawater samples and the measurement of benthic TM fluxes, with a focus on OMZs that undergo temporal variability in O₂ concentrations in order to improve the spatial and temporal coverage available of combined data sets for benthic fluxes and water column TM concentrations. A significant effort to address this in the Peruvian OMZ system has been conducted by a series of cruises from March to July 2017 off the coast of Peru, initiated by the Collaborative Research Centre 754 (SFB754—Climate-Biogeochemistry Interactions in the Tropical Ocean; samples currently under analysis). The GEOTRACES programme has launched a large number of basin-scale cruises that have significantly improved our understanding about TM sources, sinks and internal cycling in the world's oceans (Henderson et al., 2016). However in order to improve our understanding of processes occurring close to a local source, such as sediment release at continental margins, higher-resolution sampling close to the source is required. Additionally, a large focus of previous studies on TM distribution in OMZs and benthic fluxes has been on Fe. Available benthic Co and Mn flux data in OMZs are sparse. As water column data also indicate a large dependency of dCo and dMn on O₂ concentrations (Hatta et al., 2015; Hawco et al., 2016; Noble et al., 2012), we suggest future benthic flux studies include quantification of Co and Mn fluxes.

The collection of a large number of seawater TM samples requires a fast and reliable method for the analysis of TM in seawater. In Chapter 2, we presented an automated offline preconcentration method with analysis of Fe, Co, Mn, Cd, Cu, Ni, Pb and Zn by ICP-MS. This method requires a small sample volume, has low detection limits and is highly accurate. However, this method could further be improved by online coupling to ICP-MS. The benefits of online preconcentration are (i) even lower detection limits by direct injection of the eluent into the plasma, as the smaller volume of eluent utilized

results in higher TM concentrations in the analyte entering the ICP-MS, (ii) the method is faster and (iii) elimination of one step causing potential contamination from the 4 mL scintillation vials and additional sample handling (opening procedure and storage open in autosampler).

Secondly, a rapid decrease in Fe(II) offshore within the anoxic Peruvian OMZ suggests a removal mechanism other than oxidation by oxygen (Bruland et al., 2005; Vedamati et al., 2014). The processes causing this however are still largely uncertain. The occurrence of Fe oxidation during microbial nitrate reduction has been suggested to occur (Scholz et al., 2016). Other oxidizing species, such as H₂O₂ or superoxide, might be present within the OMZ in sufficient amounts to result in significant Fe(II) oxidation. Although measurements of H₂O₂ have been undertaken in OMZs and showed enhanced concentrations of up to 10 nM during our study in the Peruvian OMZs, methodological interferences (related to reduced V species) make it impossible to fully exclude that an overestimation in H₂O₂ concentrations occurred (Hopwood et al., 2017b). Understanding of Fe(II) oxidation within OMZ could be improved by measuring a range of possible oxidizing agents in the OMZ and, if necessary, optimize available methods and quantify possible interferences. For example, the addition of the enzyme catalase, which degrades H₂O₂, could be used in order to determine the contribution of actual H₂O₂ to the apparent H₂O₂ signal by analyzing H₂O₂ in the unmodified sample and after the addition of catalase (Hopwood et al., 2017b). The influence of microbial nitrate reduction on dissolved Fe could be tested in anoxic incubation experiments using seawater from the nitrite maximum in OMZs and simultaneously measuring Fe(II) oxidation rates and the concentrations of different nitrogen species (M. J. Hopwood, pers. comm.).

Thirdly, combined studies of Fe isotopes, including assessment of isotopic fractionation, from sediments and pore waters, and dissolved and particulate Fe in seawater, could

further help to identify the influence of the shelf source and Fe cycling in the water column. Several studies have been performed using Fe isotopes in an attempt to quantify the magnitude of different Fe sources to the ocean and to understand specific features in Fe distribution (e.g. Chever et al., 2015; Conway and John, 2014; Homoky et al., 2013; John et al., 2017). The assessment of different Fe sources through Fe isotope studies is possible due to the different characteristic Fe isotopic signature from different input sources (Conway and John, 2014). For example, particularly light Fe isotope signatures (expressed as $\delta^{56}\text{Fe}: \left[\frac{(^{56}\text{Fe}/^{54}\text{Fe})_{\text{sample}}}{(^{56}\text{Fe}/^{54}\text{Fe})_{\text{IRMM-14}}} - 1 \right] \times 10^3$, IRMM-14: international iron isotope reference material) are observed in anoxic sediment pore waters ($\delta^{56}\text{Fe}$: -1.82 to -3.45‰; Bergquist and Boyle, 2006; Homoky et al., 2009; Severmann et al., 2006), compared to heavier isotope ratios from atmospheric dust dissolution ($\delta^{56}\text{Fe}$: $+0.13 \pm 0.18\%$; Waeles et al., 2007) and non-reductive dissolution from sediments ($\delta^{56}\text{Fe}$: $+0.22 \pm 0.18\%$; Homoky et al., 2013). Observed isotope ratios in sediment pore waters and in bottom waters close to the sediment source however show large variations, which are likely to be driven by a) different magnitudes of reductive and non-reductive dissolution processes in the sediments, b) quantitative dissolution of sedimentary Fe and c) abiotic and biotic processes, such as Fe oxidation, which might alter the Fe isotope signature at the sediment water interface (John et al., 2017, and references therein). Also Fe cycling within the water column (ligand complexation, photoreduction, biological uptake, oxidation and scavenging) results in an alteration of Fe isotope signatures (Chever et al., 2015, and references therein). While, these processes complicate the estimation of the different source inputs, it also raises the possibility to use the isotope data to better understand water column Fe cycling.

Finally, understanding and estimating TM removal processes and the influence of oxygen on these processes is a crucial task. Calculating an empirical removal of Fe(II) after

Chapter 6: Conclusions and future directions

sediment release through abiotic oxidation by O_2 under changing oxygen conditions after equations provided by Millero et al. (1987) is theoretically possible; however actual removal might depend on several additional parameters such as abiotic oxidation by other oxidizing agents than O_2 , biotic oxidation mechanisms and microbial uptake (Moffett and Zika, 1987; Scholz et al., 2016). In a system where input fluxes, such as atmospheric deposition and sediment fluxes, and also remineralization rates and ocean circulation are well quantified, numerical models would be well-suited to quantify removal processes via a mass balance. In addition, different hypothesis for removal processes and source mechanisms could be tested in a model environment.

References

- Abadie, C., Lacan, F., Radic, A., Pradoux, C. and Poitrasson, F., 2017. Iron isotopes reveal distinct dissolved iron sources and pathways in the intermediate versus deep Southern Ocean. *Proceedings of the National Academy of Sciences of the United States of America*, 114(5): 858-863.
- Achterberg, E.P., Braungardt, C.B., Sandford, R.C. and Worsfold, P.J., 2001a. UV digestion of seawater samples prior to the determination of copper using flow injection with chemiluminescence detection. *Analytica Chimica Acta*, 440(1): 27-36.
- Achterberg, E.P. et al., 2001b. Determination of iron in seawater. *Analytica Chimica Acta*, 442(1): 1-14.
- Achterberg, E.P. and Van Den Berg, C.M., 1997. Chemical speciation of chromium and nickel in the western Mediterranean. *Deep Sea Research Part II: Topical Studies in Oceanography*, 44(3-4): 693-720.
- Aguilar-Islas, A.M. and Bruland, K.W., 2006. Dissolved manganese and silicic acid in the Columbia River plume: A major source to the California current and coastal waters off Washington and Oregon. *Marine Chemistry*, 101(3-4): 233-247.
- Aguilar-Islas, A.M., Wu, J., Rember, R., Johansen, A.M. and Shank, L.M., 2010. Dissolution of aerosol-derived iron in seawater: Leach solution chemistry, aerosol type, and colloidal iron fraction. *Marine Chemistry*, 120(1): 25-33.
- Baker, A.R. and Croot, P.L., 2010. Atmospheric and marine controls on aerosol iron solubility in seawater. *Marine Chemistry*, 120(1-4): 4-13.
- Baker, A.R., Jickells, T.D., Witt, M. and Linge, K.L., 2006. Trends in the solubility of iron, aluminium, manganese and phosphorus in aerosol collected over the Atlantic Ocean. *Marine Chemistry*, 98(1): 43-58.
- Baker, A.R., Thomas, M., Bange, H.W. and Plasencia Sánchez, E., 2016. Soluble trace metals in aerosols over the tropical south-east Pacific offshore of Peru. *Biogeosciences*, 13(3): 817-825.
- Balistrieri, L., Brewer, P.G. and Murray, J.W., 1981. Scavenging Residence Times of Trace-Metals and Surface-Chemistry of Sinking Particles in the Deep Ocean. *Deep-Sea Research Part a-Oceanographic Research Papers*, 28(2): 101-121.
- Barbeau, K., Rue, E.L., Bruland, K.W. and Butler, A., 2001. Photochemical cycling of iron in the surface ocean mediated by microbial iron(III)-binding ligands. *Nature*, 413(6854): 409-413.

References

- Barbeau, K., Rue, E.L., Trick, C.G., Bruland, K.W. and Butler, A., 2003. Photochemical reactivity of siderophores produced by marine heterotrophic bacteria and cyanobacteria based on characteristic Fe(III) binding groups. *Limnology and Oceanography*, 48(3): 1069-1078.
- Barton, E.D., 1989. The Poleward Undercurrent On The Eastern Boundary Of The Subtropical North Atlantic. In: S.J. Neshyba, C.N.K. Mooers, R.L. Smith and R.T. Barber (Editors), *Poleward Flows Along Eastern Ocean Boundaries*. Springer-Verlag, New York, pp. 82-95.
- Barton, E.D. et al., 1998. The transition zone of the Canary Current upwelling region. *Progress in Oceanography*, 41(4): 455-504.
- Becagli, S. et al., 2012. Evidence for heavy fuel oil combustion aerosols from chemical analyses at the island of Lampedusa: a possible large role of ships emissions in the Mediterranean. *Atmos. Chem. Phys.*, 12(7): 3479-3492.
- Bergquist, B. and Boyle, E., 2006. Iron isotopes in the Amazon River system: weathering and transport signatures. *Earth and Planetary Science Letters*, 248(1): 54-68.
- Berman-Frank, I., Cullen, J.T., Shaked, Y., Sherrell, R.M. and Falkowski, P.G., 2001. Iron availability, cellular iron quotas, and nitrogen fixation in *Trichodesmium*. *Limnology and Oceanography*, 46(6): 1249-1260.
- Bianchi, D., Weber, T.S., Kiko, R. and Deutsch, C., 2018. Global niche of marine anaerobic metabolisms expanded by particle microenvironments. *Nature Geoscience*, 11(4): 263-268.
- Biller, D.V. and Bruland, K.W., 2012. Analysis of Mn, Fe, Co, Ni, Cu, Zn, Cd, and Pb in seawater using the Nobias-chelate PA1 resin and magnetic sector inductively coupled plasma mass spectrometry (ICP-MS). *Marine Chemistry*, 130: 12-20.
- Biller, D.V. and Bruland, K.W., 2013. Sources and distributions of Mn, Fe, Co, Ni, Cu, Zn, and Cd relative to macronutrients along the central California coast during the spring and summer upwelling season. *Marine Chemistry*, 155: 50-70.
- Blain, S. and Tagliabue, A., 2016. Modeling Methods. In: S. Blain and A. Tagliabue (Editors), *Iron Cycle in Oceans*. ISTE Ltd, London.
- Bonnet, S. et al., 2008. Nutrient limitation of primary productivity in the Southeast Pacific (BIOSOPE cruise). *Biogeosciences*, 5(1): 215-225.
- Bonnet, S. et al., 2013. Geographical gradients of dissolved Vitamin B₁₂ in the Mediterranean Sea. *Frontiers in Microbiology*, 4: 126.

References

- Bopp, L., Aumont, O., Cadule, P., Alvain, S. and Gehlen, M., 2005. Response of diatoms distribution to global warming and potential implications: A global model study. *Geophysical Research Letters*, 32: L19606.
- Boyd, P.W., 2007. Biogeochemistry - Iron findings. *Nature*, 446(7139): 989-991.
- Boyd, P.W. and Ellwood, M.J., 2010. The biogeochemical cycle of iron in the ocean. *Nature Geoscience*, 3(10): 675-682.
- Boyd, P.W. et al., 2007. Mesoscale iron enrichment experiments 1993-2005: Synthesis and future directions. *Science*, 315(5812): 612-617.
- Boyd, P.W. and Trull, T.W., 2007. Understanding the export of biogenic particles in oceanic waters: Is there consensus? *Progress in Oceanography*, 72(4): 276-312.
- Boyle, E.A., Chapnick, S.D., Shen, G.T. and Bacon, M.P., 1986. Temporal Variability of Lead in the Western North-Atlantic. *Journal of Geophysical Research-Oceans*, 91(C7): 8573-8593.
- Boyle, E.A., Edmond, J.M. and Sholkovitz, E.R., 1977. The mechanism of iron removal in estuaries. *Geochimica et Cosmochimica Acta*, 41(9): 1313-1324.
- Boyle, E.A. et al., 2014. Anthropogenic lead emissions in the ocean: The evolving global experiment. *Oceanography*, 27(1): 69-75.
- Brandt, P. et al., 2015. On the role of circulation and mixing in the ventilation of oxygen minimum zones with a focus on the eastern tropical North Atlantic. *Biogeosciences*, 12(2): 489-512.
- Breitbarth, E. et al., 2010. Ocean acidification affects iron speciation during a coastal seawater mesocosm experiment. *Biogeosciences*, 7(3): 1065-1073.
- Breitburg, D., 2002. Effects of hypoxia, and the balance between hypoxia and enrichment, on coastal fishes and fisheries. *Estuaries*, 25(4b): 767-781.
- Breitburg, D. et al., 2018. Declining oxygen in the global ocean and coastal waters. *Science*, 359(46): eaam7240.
- Bridgestock, L. et al., 2016. Return of naturally sourced Pb to Atlantic surface waters. *Nature Communications*, 7: 12921.
- Bristow, L.A. et al., 2017. N₂ production rates limited by nitrite availability in the Bay of Bengal oxygen minimum zone. *Nature Geoscience*, 10: 24-29.
- Broecker, W.S. and Peng, T.H., 1982. *Tracers in the Sea*. Lamont-Doherty Geological Observatory, Columbia University, New York.

References

- Broecker, W.S., Sutherland, S. and Peng, T.H., 1999. A possible 20th-century slowdown of Southern Ocean deep water formation. *Science*, 286(5442): 1132-1135.
- Browning, T.J. et al., 2017. Nutrient co-limitation at the boundary of an oceanic gyre. *Nature*, 551: 242-246.
- Browning, T.J. et al., in review. Influence of iron, cobalt, and vitamin B₁₂ supply on phytoplankton growth in the tropical East Pacific during the 2015 El Niño. *Geophysical Research Letters*.
- Bruland, K.W., 1980. Oceanographic Distributions of Cadmium, Zinc, Nickel, and Copper in the North Pacific. *Earth and Planetary Science Letters*, 47(2): 176-198.
- Bruland, K.W., 1989. Complexation of Zinc by Natural Organic-Ligands in the Central North Pacific. *Limnology and Oceanography*, 34(2): 269-285.
- Bruland, K.W., 1992. Complexation of Cadmium by Natural Organic-Ligands in the Central North Pacific. *Limnology and Oceanography*, 37(5): 1008-1017.
- Bruland, K.W., 2009. GEOTRACES and SAFe INTERCALIBRATIONS, Consensus Values for the GEOTRACES 2008 and SAFe Reference Samples, <http://es.ucsc.edu/~kbruland/GeotracesSaFe/kwbGeotracesSaFe.html>.
- Bruland, K.W., Franks, R.P., Knauer, G.A. and Martin, J.H., 1979. Sampling and Analytical Methods for the Determination of Copper, Cadmium, Zinc, and Nickel at the Nanogram Per Liter Level in Sea-Water. *Analytica Chimica Acta*, 105(1): 233-245.
- Bruland, K.W. and Lohan, M.C., 2006. Controls of Trace Metals in Seawater. In: H. Elderfield (Editor), *The Oceans and Marine Geochemistry. Treatise on Geochemistry*. Elsevier, Oxford, pp. 23-47.
- Bruland, K.W., Rue, E.L. and Smith, G.J., 2001. Iron and macronutrients in California coastal upwelling regimes: Implications for diatom blooms. *Limnology and Oceanography*, 46(7): 1661-1674.
- Bruland, K.W., Rue, E.L., Smith, G.J. and DiTullio, G.R., 2005. Iron, macronutrients and diatom blooms in the Peru upwelling regime: brown and blue waters of Peru. *Marine Chemistry*, 93(2-4): 81-103.
- Buck, C.S., Landing, W.M., Resing, J.A. and Measures, C.I., 2010. The solubility and deposition of aerosol Fe and other trace elements in the North Atlantic Ocean: Observations from the A16N CLIVAR/CO₂ repeat hydrography section. *Marine Chemistry*, 120(1-4): 57-70.
- Buffle, J., 1990. The analytical challenge posed by fulvic and humic compounds. *Analytica Chimica Acta*, 232(Supplement C): 1-2.

References

- Burdige, D.J., 1993. The Biogeochemistry of Manganese and Iron Reduction in Marine-Sediments. *Earth-Science Reviews*, 35(3): 249-284.
- Byrne, R.H., Kump, L.R. and Cantrell, K.J., 1988. The influence of temperature and pH on trace metal speciation in seawater. *Marine Chemistry*, 25(2): 163-181.
- Cai, W. et al., 2014. Increasing frequency of extreme El Niño events due to greenhouse warming. *Nature Climate Change*, 4: 111-116.
- Capone, D.G. and Hutchins, D.A., 2013. Microbial biogeochemistry of coastal upwelling regimes in a changing ocean. *Nature Geoscience*, 6(9): 711-717.
- Carr, M.-E., 2001. Estimation of potential productivity in Eastern Boundary Currents using remote sensing. *Deep Sea Research Part II: Topical Studies in Oceanography*, 49(1): 59-80.
- Cavan, E.L., Trimmer, M., Shelley, F. and Sanders, R., 2017. Remineralization of particulate organic carbon in an ocean oxygen minimum zone. *Nature Communications*, 8: 14847.
- Chaillou, G., Anschutz, P., Lavaux, G., Schafer, J. and Blanc, G., 2002. The distribution of Mo, U, and Cd in relation to major redox species in muddy sediments of the Bay of Biscay. *Marine Chemistry*, 80(1): 41-59.
- Chance, R., Malin, G., Jickells, T. and Baker, A.R., 2007. Reduction of iodate to iodide by cold water diatom cultures. *Marine Chemistry*, 105(1): 169-180.
- Chapman, P. and Liss, P.S., 1977. Effect of Nitrite on Spectrophotometric Determination of Iodate in Seawater. *Marine Chemistry*, 5(3): 243-249.
- Charette, M.A., Morris, P.J., Henderson, P.B. and Moore, W.S., 2015. Radium isotope distributions during the US GEOTRACES North Atlantic cruises. *Marine Chemistry*, 177: 184-195.
- Chavez, F.P. et al., 1999. Biological and chemical response of the equatorial Pacific Ocean to the 1997-98 El Niño. *Science*, 286(5447): 2126-2131.
- Chever, F. et al., 2015. Total dissolvable and dissolved iron isotopes in the water column of the Peru upwelling regime. *Geochimica Et Cosmochimica Acta*, 162: 66-82.
- Christensen, V., de la Puente, S., Sueiro, J.C., Steenbeek, J. and Majluf, P., 2014. Valuing seafood: The Peruvian fisheries sector. *Marine Policy*, 44(Supplement C): 302-311.
- Coale, K.H. and Bruland, K.W., 1990. Spatial and temporal variability in copper complexation in the North Pacific. *Deep Sea Research Part A. Oceanographic Research Papers*, 37(2): 317-336.

References

- Conway, T.M. and John, S.G., 2014. Quantification of dissolved iron sources to the North Atlantic Ocean. *Nature*, 511: 212-215.
- Croot, P.L., Andersson, K., Ozturk, M. and Turner, D.R., 2004. The distribution and speciation of iron along 6 degrees E in the Southern Ocean. *Deep-Sea Research Part II -Topical Studies in Oceanography*, 51(22-24): 2857-2879.
- Cutter, G. et al., 2014. Sampling and sample-handling protocols for GEOTRACES cruises. *GEOTRACES*.
- Cyr, F., Bourgault, D., Galbraith, P.S. and Gosselin, M., 2015. Turbulent nitrate fluxes in the Lower St. Lawrence Estuary, Canada. *Journal of Geophysical Research-Oceans*, 120(3): 2308-2330.
- Czeschel, R. et al., 2011. Middepth circulation of the eastern tropical South Pacific and its link to the oxygen minimum zone. *Journal of Geophysical Research-Oceans*, 116: C01015.
- Dale, A.W. et al., 2015. A revised global estimate of dissolved iron fluxes from marine sediments. *Global Biogeochemical Cycles*, 29(5): 691-707.
- Dale, A.W. et al., 2014. Benthic nitrogen fluxes and fractionation of nitrate in the Mauritanian oxygen minimum zone (Eastern Tropical North Atlantic). *Geochimica et Cosmochimica Acta*, 134: 234-256.
- Dammshäuser, A., Wagener, T. and Croot, P.L., 2011. Surface water dissolved aluminum and titanium: Tracers for specific time scales of dust deposition to the Atlantic? *Geophysical Research Letters*, 38: L24601.
- Danielsson, L.G., Magnusson, B. and Westerlund, S., 1978. Improved Metal Extraction Procedure for Determination of Trace-Metals in Sea-Water by Atomic-Absorption Spectrometry with Electrothermal Atomization. *Analytica Chimica Acta*, 98(1): 47-57.
- de Baar, H. and de Jong, J., 2001. Distribution, Sources and Sinks of Iron in Seawater. In: D.R. Turner and K.A. Hunter (Editors), *The Biogeochemistry of Iron in Seawater*. John Wiley & Sons Ltd., Hoboken.
- de Jong, J., Schoemann, V., Lannuzel, D., Tison, J.L. and Mattielli, N., 2008. High-accuracy determination of iron in seawater by isotope dilution multiple collector inductively coupled plasma mass spectrometry (ID-MC-ICP-MS) using nitrilotriacetic acid chelating resin for pre-concentration and matrix separation. *Analytica Chimica Acta*, 623(2): 126-139.
- Devol, A.H. and Hartnett, H.E., 2001. Role of the oxygen - deficient zone in transfer of organic carbon to the deep ocean. *Limnology and Oceanography*, 46(7): 1684-1690.

References

- Diaz, R.J. and Rosenberg, R., 2008. Spreading dead zones and consequences for marine ecosystems. *Science*, 321(5891): 926-929.
- Duggen, S. et al., 2010. The role of airborne volcanic ash for the surface ocean biogeochemical iron-cycle: a review. *Biogeosciences*, 7(3): 827-844.
- Dutkiewicz, A., Müller, D., O'Callaghan, S. and Jónasson, H., 2015. Census of seafloor sediments in the world's ocean. *Geology*, 43(9): 795-798.
- Eby, L.A. and Crowder, L.B., 2002. Hypoxia-based habitat compression in the Neuse River Estuary: context-dependent shifts in behavioral avoidance thresholds. *Canadian Journal of Fisheries and Aquatic Sciences*, 59(6): 952-965.
- Elderfield, H. and Truesdale, V.W., 1980. On the Biophilic Nature of Iodine in Seawater. *Earth and Planetary Science Letters*, 50(1): 105-114.
- Elrod, V.A., Berelson, W.M., Coale, K.H. and Johnson, K.S., 2004. The flux of iron from continental shelf sediments: A missing source for global budgets. *Geophysical Research Letters*, 31: L12307.
- Eriksen, C.C., 1982. Observations of Internal Wave Reflection Off Sloping Bottoms. *Journal of Geophysical Research-Oceans*, 87(C1): 525-538.
- Falkowski, P.G., 1997. Evolution of the nitrogen cycle and its influence on the biological sequestration of CO₂ in the ocean. *Nature*, 387(6630): 272-275.
- Falkowski, P.G., Barber, R.T. and Smetacek, V., 1998. Biogeochemical controls and feedbacks on ocean primary production. *Science*, 281(5374): 200-206.
- Field, C.B., Behrenfeld, M.J., Randerson, J.T. and Falkowski, P., 1998. Primary production of the biosphere: Integrating terrestrial and oceanic components. *Science*, 281(5374): 237-240.
- Fitzsimmons, J.N. et al., 2017. Iron persistence in a distal hydrothermal plume supported by dissolved-particulate exchange. *Nature Geoscience*, 10(3): 195-201.
- Fitzsimmons, J.N., Zhang, R.F. and Boyle, E.A., 2013. Dissolved iron in the tropical North Atlantic Ocean. *Marine Chemistry*, 154: 87-99.
- Frank, M., 2011. Oceanography: chemical twins, separated. *Nature Geoscience*, 4: 220-221.
- Froelich, P.N. et al., 1979. Early Oxidation of Organic-Matter in Pelagic Sediments of the Eastern Equatorial Atlantic - Suboxic Diagenesis. *Geochimica Et Cosmochimica Acta*, 43(7): 1075-1090.

References

- Garcia-Solsona, E., Garcia-Orellana, J., Masqué, P. and Dulaiova, H., 2008. Uncertainties associated with ^{223}Ra and ^{224}Ra measurements in water via a Delayed Coincidence Counter (RaDeCC). *Marine Chemistry*, 109(3-4): 198-219.
- German, C.R. and Von Damm, K.L., 2006. Hydrothermal Processes. In: H. Elderfield (Editor), *The Oceans and Marine Geochemistry*. Elsevier, Oxford, pp. 181-222.
- Gerringa, L.J.A. et al., 2012. Iron from melting glaciers fuels the phytoplankton blooms in Amundsen Sea (Southern Ocean): Iron biogeochemistry. *Deep Sea Research Part II: Topical Studies in Oceanography*, 71-76(Supplement C): 16-31.
- Gill, A., 1982. *Atmosphere-Ocean Dynamics*. Academic Press, California, 662 pp.
- Gledhill, M., Achterberg, E.P., Li, K., Mohamed, K.N. and Rijkenberg, M.J., 2015. Influence of ocean acidification on the complexation of iron and copper by organic ligands in estuarine waters. *Marine Chemistry*, 177: 421-433.
- Gledhill, M. and Buck, K.N., 2012. The organic complexation of iron in the marine environment: a review. *Frontiers in Microbiology*, 3: 69.
- Grasshoff, K., Ehrhardt, M. and Kremling, K., 1983. *Methods of Seawater Analysis*. Verlag Chemie, Weinheim.
- Green, M.A., Aller, R.C., Cochran, J.K., Lee, C. and Aller, J.Y., 2002. Bioturbation in shelf/slope sediments off Cape Hatteras, North Carolina: the use of Th-234, Ch1-a, and Br- to evaluate rates of particle and solute transport. *Deep-Sea Research Part II -Topical Studies in Oceanography*, 49(20): 4627-4644.
- Gruber, N. and Sarmiento, J.L., 1997. Global patterns of marine nitrogen fixation and denitrification. *Global Biogeochemical Cycles*, 11(2): 235-266.
- Gutiérrez, D. et al., 2008. Oxygenation episodes on the continental shelf of central Peru: Remote forcing and benthic ecosystem response. *Progress in Oceanography*, 79(2): 177-189.
- Hahn, J., Brandt, P., Schmidtke, S. and Krahnemann, G., 2017. Decadal oxygen change in the eastern tropical North Atlantic. *Ocean Science*, 13(4): 551-576.
- Hansen, H.P., 2007. Determination of oxygen. *Methods of Seawater Analysis*, Third Edition: 75-89.
- Hartmann, M., Müller, P.J., Suess, E. and van der Weijden, C.H., 1976. Chemistry of Late Quaternary sediments and their interstitial waters of sediment cores from the North-West African continental margin, Meteor Forschungsergebnisse, Deutsche Forschungsgemeinschaft, Reihe C Geologie und Geophysik, Gebrüder Bornträger, Berlin, Stuttgart, C24, 1-67. PANGAEA.

References

- Hatta, M. et al., 2015. An overview of dissolved Fe and Mn distributions during the 2010-2011 US GEOTRACES north Atlantic cruises: GEOTRACES GA03. *Deep-Sea Research Part II -Topical Studies in Oceanography*, 116: 117-129.
- Hawco, N.J., Ohnemus, D.C., Resing, J.A., Twining, B.S. and Saito, M.A., 2016. A dissolved cobalt plume in the oxygen minimum zone of the eastern tropical South Pacific. *Biogeosciences*, 13(20): 5697-5717.
- Heggie, D.T., 1982. Copper in Surface Waters of the Bering Sea. *Geochimica Et Cosmochimica Acta*, 46(7): 1301-1306.
- Heller, M.I. et al., 2017. Accumulation of Fe oxyhydroxides in the Peruvian oxygen deficient zone implies non-oxygen dependent Fe oxidation. *Geochimica Et Cosmochimica Acta*, 211: 174-193.
- Helly, J.J. and Levin, L.A., 2004. Global distribution of naturally occurring marine hypoxia on continental margins. *Deep-Sea Research Part I-Oceanographic Research Papers*, 51(9): 1159-1168.
- Henderson, G., Boyle, E., Lohan, M., Rijkenberg, M. and Sarthou, G., 2016. Biological and climatic impacts of the ocean trace element chemistry. Discussion meeting issue organised and edited by Gideon Henderson, Ed Boyle, Maeve Lohan, Michal Rijkenberg and Géraldine Sarthou. *Phil. Trans. R. Soc. A*, 374(2081).
- Henderson, G.M. et al., 2007. GEOTRACES - An international study of the global marine biogeochemical cycles of trace elements and their isotopes. *Chemie Der Erde-Geochemistry*, 67(2): 85-131.
- Henderson, P., Morris, P., Moore, W. and Charette, M., 2013. Methodological advances for measuring low-level radium isotopes in seawater. *Journal of Radioanalytical and Nuclear Chemistry*, 296: 357-362.
- Homoky, W., Severmann, S., Mills, R., Statham, P. and Fones, G., 2009. Pore-fluid Fe isotopes reflect the extent of benthic Fe redox recycling: Evidence from continental shelf and deep-sea sediments. *Geology*, 37(8): 751-754.
- Homoky, W.B., John, S.G., Conway, T.M. and Mills, R.A., 2013. Distinct iron isotopic signatures and supply from marine sediment dissolution. *Nature Communications*, 4: 2143.
- Homoky, W.B. et al., 2012. Dissolved oxygen and suspended particles regulate the benthic flux of iron from continental margins. *Marine Chemistry*, 134: 59-70.
- Homoky, W.B. et al., 2016. Quantifying trace element and isotope fluxes at the ocean-sediment boundary: a review. *Philosophical Transactions of the Royal Society a-Mathematical Physical and Engineering Sciences*, 374(2081): 20160246.

References

- Honeyman, B.D. and Santschi, P.H., 1987. The Effect of Particle Concentration on the Rate of Thorium Adsorption. Abstracts of Papers of the American Chemical Society, 193: 61.
- Hopwood, M.J. et al., 2017a. A Comparison between Four Analytical Methods for the Measurement of Fe(II) at Nanomolar Concentrations in Coastal Seawater. *Frontiers in Marine Science*, 4: 192.
- Hopwood, M.J., Rapp, I., Schlosser, C. and Achterberg, E.P., 2017b. Hydrogen peroxide in deep waters from the Mediterranean Sea, South Atlantic and South Pacific Oceans. *Scientific Reports*, 7: 43436.
- Hurst, M.P., Aguilar-Islas, A.M. and Bruland, K.W., 2010. Iron in the southeastern Bering Sea: Elevated leachable particulate Fe in shelf bottom waters as an important source for surface waters. *Continental Shelf Research*, 30(5): 467-480.
- Hutchins, D.A., DiTullio, G.R., Zhang, Y. and Bruland, K.W., 1998. An iron limitation mosaic in the California upwelling regime. *Limnology and Oceanography*, 43(6): 1037-1054.
- Hutchins, D.A. et al., 2002. Phytoplankton iron limitation in the Humboldt Current and Peru Upwelling. *Limnology and Oceanography*, 47(4): 997-1011.
- Hydes, D.J. and Liss, P.S., 1976. Fluorimetric Method for Determination of Low Concentrations of Dissolved Aluminum in Natural-Waters. *Analyst*, 101(1209): 922-931.
- Ingall, E. and Jahnke, R., 1994. Evidence for Enhanced Phosphorus Regeneration from Marine-Sediments Overlain by Oxygen Depleted Waters. *Geochimica Et Cosmochimica Acta*, 58(11): 2571-2575.
- Jeandel, C., Arsouze, T., Lacan, F., Téchiné, P. and Dutay, J.C., 2007. Isotopic Nd compositions and concentrations of the lithogenic inputs into the ocean: A compilation, with an emphasis on the margins. *Chemical Geology*, 239(1): 156-164.
- Jensen, H.S., Mortensen, P.B., Andersen, F., Rasmussen, E. and Jensen, A., 1995. Phosphorus cycling in a coastal marine sediment, Aarhus Bay, Denmark. *Limnology and Oceanography*, 40(5): 908-917.
- Jickells, T.D. et al., 2005. Global iron connections between desert dust, ocean biogeochemistry, and climate. *Science*, 308(5718): 67-71.
- John, S.G. and Adkins, J., 2012. The vertical distribution of iron stable isotopes in the North Atlantic near Bermuda. *Global Biogeochemical Cycles*, 26: GB2034.

References

- John, S.G. et al., 2017. Biogeochemical cycling of Fe and Fe stable isotopes in the Eastern Tropical South Pacific. *Marine Chemistry*, 201: 66-76.
- Johnson, G.C., Sloyan, B.M., Kessler, W.S. and McTaggart, K.E., 2002. Direct measurements of upper ocean currents and water properties across the tropical Pacific during the 1990s. *Progress in Oceanography*, 52(1): 31-61.
- Johnson, K.S., Chavez, F.P. and Friederich, G.E., 1999. Continental-shelf sediment as a primary source of iron for coastal phytoplankton. *Nature*, 398(6729): 697-700.
- Kagaya, S. et al., 2009. A solid phase extraction using a chelate resin immobilizing carboxymethylated pentaethylenehexamine for separation and preconcentration of trace elements in water samples. *Talanta*, 79(2): 146-152.
- Kagaya, S. et al., 2013. Potential of Presep (R) PolyChelate as a Chelating Resin: Comparative Study with Some Aminocarboxylic Acid-type Resins. *Analytical Sciences*, 29(11): 1107-1112.
- Karstensen, J., Stramma, L. and Visbeck, M., 2008. Oxygen minimum zones in the eastern tropical Atlantic and Pacific oceans. *Progress in Oceanography*, 77(4): 331-350.
- Keeling, R.F., Kortzinger, A. and Gruber, N., 2010. Ocean Deoxygenation in a Warming World. *Annual Review of Marine Science*, 2: 199-229.
- Keil, R.G., Neibauer, J.A., Biladeau, C., van der Elst, K. and Devol, A.H., 2016. A multiproxy approach to understanding the "enhanced" flux of organic matter through the oxygen-deficient waters of the Arabian Sea. *Biogeosciences*, 13(7): 2077-2092.
- Kessler, W.S., 2006. The circulation of the eastern tropical Pacific: A review. *Progress in Oceanography*, 69(2): 181-217.
- Kessler, W.S. and McPhaden, M.J., 1995. The 1991–1993 El Niño in the central Pacific. *Deep Sea Research Part II: Topical Studies in Oceanography*, 42(2): 295-333.
- King, D.W., Lounsbury, H.A. and Millero, F.J., 1995. Rates and Mechanism of Fe(II) Oxidation at Nanomolar Total Iron Concentrations. *Environmental Science & Technology*, 29(3): 818-824.
- Klenz, T., Dengler, M. and Brandt, P., submitted. Seasonal variability of the Mauritanian Undercurrent at 18°N from shipboard current and hydrographic measurements. *Journal of Geophysical Research: Oceans*.
- Köllner, M., Visbeck, M., Tanhua, T. and Fischer, T., 2016. Diapycnal diffusivity in the core and oxycline of the tropical North Atlantic oxygen minimum zone. *Journal of Marine Systems*, 160: 54-63.

References

- Kremling, K. et al., 2007. Determination of trace elements. In: K. Grasshoff, K. Kremling and M. Ehrhardt (Editors), *Methods of Seawater Analysis*. Wiley-VCH Verlag GmbH, pp. 253-364.
- Krishnamurthy, A. et al., 2009. Impacts of increasing anthropogenic soluble iron and nitrogen deposition on ocean biogeochemistry. *Global Biogeochemical Cycles*, 23: GB3016.
- Kristensen, E. et al., 2012. What is bioturbation? The need for a precise definition for fauna in aquatic sciences. *Marine Ecology Progress Series*, 446: 285-302.
- Labatut, M. et al., 2014. Iron sources and dissolved-particulate interactions in the seawater of the Western Equatorial Pacific, iron isotope perspectives. *Global Biogeochemical Cycles*, 28(10): 1044-1065.
- Lagerstrom, M.E. et al., 2013. Automated on-line flow-injection ICP-MS determination of trace metals (Mn, Fe, Co, Ni, Cu and Zn) in open ocean seawater: Application to the GEOTRACES program. *Marine Chemistry*, 155: 71-80.
- Lam, P.J. and Bishop, J.K.B., 2008. The continental margin is a key source of iron to the HNLC North Pacific Ocean. *Geophysical Research Letters*, 35: L07608.
- Lam, P.J., Ohnemus, D.C. and Marcus, M.A., 2012. The speciation of marine particulate iron adjacent to active and passive continental margins. *Geochimica Et Cosmochimica Acta*, 80: 108-124.
- Landing, W.M. and Bruland, K.W., 1980. Manganese in the North Pacific. *Earth and Planetary Science Letters*, 49(1): 45-56.
- Lee, J.-M. et al., 2011. Analysis of trace metals (Cu, Cd, Pb, and Fe) in seawater using single batch nitrilotriacetate resin extraction and isotope dilution inductively coupled plasma mass spectrometry. *Analytica Chimica Acta*, 686(1-2): 93-101.
- Lis, H. and Shaked, Y., 2009. Probing the bioavailability of organically bound iron: a case study in the *Synechococcus*-rich waters of the Gulf of Aqaba. *Aquatic Microbial Ecology*, 56(2-3): 241-253.
- Liu, X. and Millero, F.J., 1999. The solubility of iron hydroxide in sodium chloride solutions. *Geochimica et Cosmochimica Acta*, 63(19): 3487-3497.
- Liu, X.W. and Millero, F.J., 2002. The solubility of iron in seawater. *Marine Chemistry*, 77(1): 43-54.
- Lohan, M.C. and Bruland, K.W., 2008. Elevated Fe(II) and dissolved Fe in hypoxic shelf waters off Oregon and Washington: An enhanced source of iron to coastal upwelling regimes. *Environmental Science & Technology*, 42(17): 6462-6468.

References

- Lomnitz, U. et al., in review. Dissolved benthic phosphate, iron and carbon fluxes in the Mauritanian upwelling system and implications for ongoing deoxygenation. Deep-Sea Research Part I.
- Long, M.C., Deutsch, C. and Ito, T., 2016. Finding forced trends in oceanic oxygen. *Global Biogeochemical Cycles*, 30(2): 381-397.
- Luther, G.W., Swartz, C.B. and Ullman, W.J., 1988. Direct Determination of Iodide in Seawater by Cathodic Stripping Square-Wave Voltammetry. *Analytical Chemistry*, 60(17): 1721-1724.
- Luyten, J.R., Pedlosky, J. and Stommel, H., 1983. The Ventilated Thermocline. *Journal of Physical Oceanography*, 13(2): 292-309.
- Magnusson, B., Näykki, T., Hovind, H. and Krysell, M., 2012. Handbook for Calculation of Measurement Uncertainty in Environmental Laboratories. 537, Nordic Innovation, Oslo, Norway, www.nordtest.info.
- Marsay, C.M. et al., 2015. Attenuation of sinking particulate organic carbon flux through the mesopelagic ocean. *Proceedings of the National Academy of Sciences of the United States of America*, 112(4): 1089-1094.
- Martin, J.H., Gordon, R.M., Fitzwater, S. and Broenkow, W.W., 1989. Vertex - Phytoplankton Iron Studies in the Gulf of Alaska. *Deep-Sea Research Part a-Oceanographic Research Papers*, 36(5): 649-680.
- Martinez, P. et al., 2000. Spatial variations in nutrient utilization, production and diagenesis in the sediments of a coastal upwelling regime (NW Africa): Implications for the paleoceanographic record. *Journal of marine research*, 58(5): 809-835.
- Mawji, E. et al., 2015. The GEOTRACES Intermediate Data Product 2014. *Marine Chemistry*, 177: 1-8.
- McLennan, S.M., 2001. Relationships between the trace element composition of sedimentary rocks and upper continental crust. *Geochemistry Geophysics Geosystems*, 2: 1021.
- McPhaden, M.J., Zebiak, S.E. and Glantz, M.H., 2006. ENSO as an integrating concept in Earth science. *Science*, 314(5806): 1740-1745.
- Measures, C.I. and Vink, S., 2000. On the use of dissolved aluminum in surface waters to estimate dust deposition to the ocean. *Global Biogeochemical Cycles*, 14(1): 317-327.
- Middag, R., de Baar, H.J.W., Laan, P. and Huhn, O., 2012. The effects of continental margins and water mass circulation on the distribution of dissolved aluminum and

References

- manganese in Drake Passage. *Journal of Geophysical Research-Oceans*, 117: C01019.
- Millero, F.J., Sotolongo, S. and Izaguirre, M., 1987. The oxidation kinetics of Fe(II) in seawater. *Geochimica et Cosmochimica Acta*, 51(4): 793-801.
- Millero, F.J., Woosley, R., Ditrolio, B. and Waters, J., 2009. Effect of ocean acidification on the speciation of metals in seawater. *Oceanography*, 22(4): 72-85.
- Millero, F.J., Yao, W. and Aicher, J., 1995. The speciation of Fe(II) and Fe(III) in natural waters. *Marine Chemistry*, 50(1): 21-39.
- Milne, A., Landing, W., Bizimis, M. and Morton, P., 2010. Determination of Mn, Fe, Co, Ni, Cu, Zn, Cd and Pb in seawater using high resolution magnetic sector inductively coupled mass spectrometry (HR-ICP-MS). *Analytica Chimica Acta*, 665(2): 200-207.
- Milne, A. et al., 2017. Particulate phases are key in controlling dissolved iron concentrations in the (sub)tropical North Atlantic. *Geophysical Research Letters*, 44(5): 2377-2387.
- Mittelstaedt, E., 1983. The Upwelling Area Off Northwest Africa - a Description of Phenomena Related to Coastal Upwelling. *Progress in Oceanography*, 12(3): 307-331.
- Mittelstaedt, E., 1991. The Ocean Boundary Along the Northwest African Coast - Circulation and Oceanographic Properties at the Sea-Surface. *Progress in Oceanography*, 26(4): 307-355.
- Moffett, J.W., 1994. The Relationship between Cerium and Manganese Oxidation in the Marine-Environment. *Limnology and Oceanography*, 39(6): 1309-1318.
- Moffett, J.W. and Ho, J., 1996. Oxidation of cobalt and manganese in seawater via a common microbially catalyzed pathway. *Geochimica Et Cosmochimica Acta*, 60(18): 3415-3424.
- Moffett, J.W. et al., 2015. Biogeochemistry of iron in the Arabian Sea. *Limnology and Oceanography*, 60(5): 1671-1688.
- Moffett, J.W. and Zika, R.G., 1987. Reaction kinetics of hydrogen peroxide with copper and iron in seawater. *Environmental Science & Technology*, 21(8): 804-810.
- Moore, C.M. et al., 2009. Large-scale distribution of Atlantic nitrogen fixation controlled by iron availability. *Nature Geoscience*, 2(12): 867-871.
- Moore, C.M. et al., 2013. Processes and patterns of oceanic nutrient limitation. *Nature Geoscience*, 6(9): 701-710.

References

- Moore, J.K. and Braucher, O., 2008. Sedimentary and mineral dust sources of dissolved iron to the world ocean. *Biogeosciences*, 5: 631-656.
- Moore, J.K. and Doney, S.C., 2007. Iron availability limits the ocean nitrogen inventory stabilizing feedbacks between marine denitrification and nitrogen fixation. *Global Biogeochemical Cycles*, 21: BG2001.
- Moore, W.S., 1987. ^{228}Ra in the South-Atlantic Bight. *Journal of Geophysical Research-Oceans*, 92(C5): 5177-5190.
- Moore, W.S., 2000a. Ages of continental shelf waters determined from ^{223}Ra and ^{224}Ra . *Journal of Geophysical Research-Oceans*, 105(C9): 22117-22122.
- Moore, W.S., 2000b. Determining coastal mixing rates using radium isotopes. *Continental Shelf Research*, 20(15): 1993-2007.
- Moore, W.S., 2007. Seasonal distribution and flux of radium isotopes on the southeastern U.S. continental shelf. *Journal of Geophysical Research: Oceans*, 112: C10013.
- Moore, W.S. and Arnold, R., 1996. Measurement of ^{223}Ra and ^{224}Ra in coastal waters using a delayed coincidence counter. *Journal of Geophysical Research-Oceans*, 101(C1): 1321-1329.
- Moore, W.S. and Cai, P., 2013. Calibration of RaDeCC systems for ^{223}Ra measurements. *Marine Chemistry*, 156: 130-137.
- Moran, S.B. and Moore, R.M., 1991. The Potential Source of Dissolved Aluminum from Resuspended Sediments to the North-Atlantic Deep-Water. *Geochimica Et Cosmochimica Acta*, 55(10): 2745-2751.
- Morel, A., Antoine, D., Babin, M. and Dandonneau, Y., 1996. Measured and modeled primary production in the northeast Atlantic (EUMELI JGOFS program): the impact of natural variations in photosynthetic parameters on model predictive skill. *Deep Sea Research Part I: Oceanographic Research Papers*, 43(8): 1273-1304.
- Morel, F.M.M., Milligan, A.J. and Saito, M.A., 2003. *Marine Bioinorganic Chemistry: The Role of Trace Metals in the Oceanic Cycles of Major Nutrients*. In: H. Elderfield (Editor), *The Oceans and Marine Geochemistry*. Treatise on Geochemistry. Elsevier, Oxford, pp. 113-143.
- Morel, F.M.M. and Price, N.M., 2003. The biogeochemical cycles of trace metals in the oceans. *Science*, 300(5621): 944-947.
- Naykki, T. et al., 2015. Application of the Nordtest method for "real-time" uncertainty estimation of on-line field measurement. *Environmental Monitoring and Assessment*, 187(10): 360.

References

- NOAA, 2017. Historical El Nino / La Nina episodes (150-present). NOAA Centre for Weather and Climate Prediction.
http://origin.cpc.ncep.noaa.gov/products/analysis_monitoring/ensostuff/ONI_v5.php.
- Noble, A.E. et al., 2015. Dynamic variability of dissolved Pb and Pb isotope composition from the US North Atlantic GEOTRACES transect. *Deep-Sea Research Part II - Topical Studies in Oceanography*, 116: 208-225.
- Noble, A.E. et al., 2012. Basin-scale inputs of cobalt, iron, and manganese from the Benguela-Angola front to the South Atlantic Ocean. *Limnology and Oceanography*, 57(4): 989-1010.
- Noble, A.E., Ohnemus, D.C., Hawco, N.J., Lam, P.J. and Saito, M.A., 2017. Coastal sources, sinks and strong organic complexation of dissolved cobalt within the US North Atlantic GEOTRACES transect GA03. *Biogeosciences*, 14(11): 2715-2739.
- Noffke, A. et al., 2012. Benthic iron and phosphorus fluxes across the Peruvian oxygen minimum zone. *Limnology and Oceanography*, 57(3): 851-867.
- Nriagu, J.O. and Pacyna, J.M., 1988. Quantitative assessment of worldwide contamination of air, water and soils by trace metals. *Nature*, 333(6169): 134-139.
- Oksanen, J. et al., 2017. vegan: Community Ecology Package. Ordination methods, diversity analysis and other functions for community and vegetation ecologists. Version 2.4-4. <https://CRAN.R-project.org/package=vegan>.
- Oldham, V.E., Jones, M.R., Tebo, B.M. and Luther, G.W., 2017. Oxidative and reductive processes contributing to manganese cycling at oxic-anoxic interfaces. *Marine Chemistry*, 195: 122-128.
- Orians, K.J. and Bruland, K.W., 1985. Dissolved Aluminum in the Central North Pacific. *Nature*, 316(6027): 427-429.
- Orians, K.J. and Bruland, K.W., 1986. The Biogeochemistry of Aluminum in the Pacific-Ocean. *Earth and Planetary Science Letters*, 78(4): 397-410.
- Osborn, T.R., 1980. Estimates of the Local-Rate of Vertical Diffusion from Dissipation Measurements. *Journal of Physical Oceanography*, 10(1): 83-89.
- Pakhomova, S.V. et al., 2007. Fluxes of iron and manganese across the sediment-water interface under various redox conditions. *Marine Chemistry*, 107(3): 319-331.
- Panzeca, C. et al., 2008. Potential cobalt limitation of vitamin B₁₂ synthesis in the North Atlantic Ocean. *Global Biogeochemical Cycles*, 22: GB2029.

References

- Parker, D.L. et al., 2007. Inter-relationships of MnO₂ precipitation, siderophore-Mn(III) complex formation, siderophore degradation, and iron limitation in Mn(II)-oxidizing bacterial cultures. *Geochimica Et Cosmochimica Acta*, 71(23): 5672-5683.
- Patey, M.D., Achterberg, E.P., Rijkenberg, M.J. and Pearce, R., 2015. Aerosol time-series measurements over the tropical Northeast Atlantic Ocean: Dust sources, elemental composition and mineralogy. *Marine Chemistry*, 174: 103-119.
- Pauly, D. and Christensen, V., 1995. Primary Production Required to Sustain Global Fisheries (Vol 374, Pg 255, 1995). *Nature*, 376(6537): 279-279.
- Peña-Izquierdo, J. et al., 2015. Water mass pathways to the North Atlantic oxygen minimum zone. *Journal of Geophysical Research-Oceans*, 120(5): 3350-3372.
- Pennington, J.T. et al., 2006. Primary production in the eastern tropical Pacific: A review. *Progress in Oceanography*, 69(2-4): 285-317.
- Powell, C. et al., 2015. Estimation of the atmospheric flux of nutrients and trace metals to the eastern tropical North Atlantic Ocean. *Journal of the Atmospheric Sciences*, 72(10): 4029-4045.
- Prohaska, T., Irrgeher, J., Zitek, A. and Jakubowski, N., 2014. Sector Field Mass Spectrometry for Elemental and Isotopic Analysis. Royal Society of Chemistry.
- Quiñones, R.A. et al., 2010. The Humboldt Current System. In: K.-K. Liu, L. Atkinson, R.A. Quiñones and L. Talaue-McManus (Editors), *Carbon and Nutrient Fluxes in Continental Margins: A Global Synthesis*. Springer-Verlag, Berlin, pp. 44-64.
- Rama and Moore, W.S., 1996. Using the radium quartet for evaluating groundwater input and water exchange in salt marshes. *Geochimica Et Cosmochimica Acta*, 60(23): 4645-4652.
- Rapp, I., Schlosser, C., Rusiecka, D., Gledhill, M. and Achterberg, E.P., 2017. Automated preconcentration of Fe, Zn, Cu, Ni, Cd, Pb, Co, and Mn in seawater with analysis using high-resolution sector field inductively-coupled plasma mass spectrometry. *Analytica Chimica Acta*, 976: 1-13.
- Resing, J.A. et al., 2015. Basin-scale transport of hydrothermal dissolved metals across the South Pacific Ocean. *Nature*, 523: 200-203.
- Rijkenberg, M.J.A. et al., 2014. The Distribution of Dissolved Iron in the West Atlantic Ocean. *Plos One*, 9(6): e101323.
- Rijkenberg, M.J.A. et al., 2012. Fluxes and distribution of dissolved iron in the eastern (sub-) tropical North Atlantic Ocean. *Global Biogeochemical Cycles*, 26: GB3004.

References

- Ring, G., O'Mullane, J., O'Riordan, A. and Furey, A., 2016. Trace metal determination as it relates to metallosis of orthopaedic implants: Evolution and current status. *Clinical Biochemistry*, 49(7-8): 617-635.
- Rose, A.L. and Waite, T.D., 2001. Chemiluminescence of Luminol in the Presence of Iron(II) and Oxygen: Oxidation Mechanism and Implications for Its Analytical Use. *Analytical Chemistry*, 73(24): 5909-5920.
- Rudnick, R.L. and Gao, S., 2006. Composition of the continental crust. In: H.D. Holland and K.K. Turekian (Editors), *Treatise on geochemistry*. Pergamon, Oxford, UK, pp. 1-64.
- Rue, E.L. and Bruland, K.W., 1995. Complexation of Iron(III) by Natural Organic-Ligands in the Central North Pacific as Determined by a New Competitive Ligand Equilibration Adsorptive Cathodic Stripping Voltammetric Method. *Marine Chemistry*, 50(1-4): 117-138.
- Rue, E.L., Smith, G.J., Cutter, G.A. and Bruland, K.W., 1997. The response of trace element redox couples to suboxic conditions in the water column. *Deep-Sea Research Part I-Oceanographic Research Papers*, 44(1): 113-134.
- Rusiecka, D. et al., 2018. Anthropogenic Signatures of Lead in the Northeast Atlantic. *Geophysical Research Letters*, 45(6): 2734-2743.
- Ryan-Keogh, T.J. et al., 2013. Spatial and temporal development of phytoplankton iron stress in relation to bloom dynamics in the high-latitude North Atlantic Ocean. *Limnology and Oceanography*, 58(2): 533-545.
- Saito, M.A., Goepfert, T.J. and Ritt, J.T., 2008. Some thoughts on the concept of colimitation: Three definitions and the importance of bioavailability. *Limnology and Oceanography*, 53(1): 276-290.
- Saito, M.A. and Moffett, J.W., 2001. Complexation of cobalt by natural organic ligands in the Sargasso Sea as determined by a new high-sensitivity electrochemical cobalt speciation method suitable for open ocean work. *Marine Chemistry*, 75(1-2): 49-68.
- Saito, M.A. and Moffett, J.W., 2002. Temporal and spatial variability of cobalt in the Atlantic Ocean. *Geochimica Et Cosmochimica Acta*, 66(11): 1943-1953.
- Sanial, V. et al., 2018. Radium-228 as a tracer of dissolved trace element inputs from the Peruvian continental margin. *Marine Chemistry*, 201: 20-34.
- Schafstall, J., Dengler, M., Brandt, P. and Bange, H., 2010. Tidal-induced mixing and diapycnal nutrient fluxes in the Mauritanian upwelling region. *Journal of Geophysical Research-Oceans*, 115: C10014.

References

- Schaule, B.K. and Patterson, C.C., 1981. Lead Concentrations in the Northeast Pacific - Evidence for Global Anthropogenic Perturbations. *Earth and Planetary Science Letters*, 54(1): 97-116.
- Schlosser, C., De La Rocha, C.L. and Croot, P.L., 2011. Effects of iron surface adsorption and sample handling on iron solubility measurements. *Marine Chemistry*, 127(1-4): 48-55.
- Schlosser, C. et al., 2014. Seasonal ITCZ migration dynamically controls the location of the (sub)tropical Atlantic biogeochemical divide. *Proceedings of the National Academy of Sciences of the United States of America*, 111(4): 1438-1442.
- Schmidtko, S., Stramma, L. and Visbeck, M., 2017. Decline in global oceanic oxygen content during the past five decades. *Nature*, 542(7641): 335-339.
- Scholten, J.C. et al., 2010. Preparation of Mn-fiber standards for the efficiency calibration of the delayed coincidence counting system (RaDeCC). *Marine Chemistry*, 121: 206-214.
- Scholz, F., 2015. *Voltammetric techniques of analysis: the essentials*. ChemTexts, 1(4): 17.
- Scholz, F. et al., 2011. Early diagenesis of redox-sensitive trace metals in the Peru upwelling area - response to ENSO-related oxygen fluctuations in the water column. *Geochimica Et Cosmochimica Acta*, 75(22): 7257-7276.
- Scholz, F. et al., 2016. Nitrate-dependent iron oxidation limits iron transport in anoxic ocean regions. *Earth and Planetary Science Letters*, 454: 272-281.
- Scholz, F., McManus, J., Mix, A.C., Hensen, C. and Schneider, R.R., 2014. The impact of ocean deoxygenation on iron release from continental margin sediments. *Nature Geoscience*, 7(6): 433-437.
- Severmann, S., Johnson, C.M., Beard, B.L. and McManus, J., 2006. The effect of early diagenesis on the Fe isotope compositions of porewaters and authigenic minerals in continental margin sediments. *Geochimica et Cosmochimica Acta*, 70(8): 2006-2022.
- Severmann, S., McManus, J., Berelson, W.M. and Hammond, D.E., 2010. The continental shelf benthic iron flux and its isotope composition. *Geochimica Et Cosmochimica Acta*, 74(14): 3984-4004.
- Shelley, R.U., Landing, W.M., Ussher, S.J., Planquette, H. and Sarthou, G., 2018. Regional trends in the fractional solubility of Fe and other metals from North Atlantic aerosols (GEOTRACES cruises GA01 and GA03) following a two-stage leach. *Biogeosciences*, 15(8): 2271-2288.

References

- Shelley, R.U., Morton, P.L. and Landing, W.M., 2015. Elemental ratios and enrichment factors in aerosols from the US-GEOTRACES North Atlantic transects. *Deep-Sea Research Part II -Topical Studies in Oceanography*, 116: 262-272.
- Sherrell, R.M. and Boyle, E.A., 1992. The Trace Metal Composition of Suspended Particles in the Oceanic Water Column near Bermuda. *Earth and Planetary Science Letters*, 111(1): 155-174.
- Sholkovitz, E.R. and Copland, D., 1981. The coagulation, solubility and adsorption properties of Fe, Mn, Cu, Ni, Cd, Co and humic acids in a river water. *Geochimica et Cosmochimica Acta*, 45(2): 181-189.
- Sholkovitz, E.R., Sedwick, P.N., Church, T.M., Baker, A.R. and Powell, C.F., 2012. Fractional solubility of aerosol iron: Synthesis of a global-scale data set. *Geochimica et Cosmochimica Acta*, 89(Supplement C): 173-189.
- Soataert, K., Petzoldt, T. and Meysman, F., 2016. marelac: Tools for Aquatic Sciences. Version 2.1.6. <https://CRAN.R-project.org/package=marelac>.
- Sohrin, Y. et al., 2008. Multielemental determination of GEOTRACES key trace metals in seawater by ICPMS after preconcentration using an ethylenediaminetriacetic acid chelating resin. *Analytical Chemistry*, 80(16): 6267-6273.
- Spokes, L.J. and Liss, P.S., 1996. Photochemically induced redox reactions in seawater, II. Nitrogen and iodine. *Marine Chemistry*, 54(1): 1-10.
- Steinfeldt, R., Sultenfuss, J., Dengler, M., Fischer, T. and Rhein, M., 2015. Coastal upwelling off Peru and Mauritania inferred from helium isotope disequilibrium. *Biogeosciences*, 12(24): 7519-7533.
- Stramma, L. et al., 2008a. Oxygen minimum zone in the North Atlantic south and east of the Cape Verde Islands. *Journal of Geophysical Research-Oceans*, 113: C04014.
- Stramma, L. et al., 2016. Observed El Nino conditions in the eastern tropical Pacific in October 2015. *Ocean Science*, 12(4): 861-873.
- Stramma, L., Hüttl, S. and Schafstall, J., 2005. Water masses and currents in the upper tropical northeast Atlantic off northwest Africa. *Journal of Geophysical Research: Oceans*, 110: C12006.
- Stramma, L., Johnson, G.C., Sprintall, J. and Mohrholz, V., 2008b. Expanding oxygen-minimum zones in the tropical oceans. *Science*, 320(5876): 655-658.
- Stramma, L., Oschlies, A. and Schmidtko, S., 2012a. Mismatch between observed and modeled trends in dissolved upper-ocean oxygen over the last 50 yr. *Biogeosciences*, 9(10): 4045-4057.

References

- Stramma, L. et al., 2012b. Expansion of oxygen minimum zones may reduce available habitat for tropical pelagic fishes. *Nature Climate Change*, 2(1): 33-37.
- Stramma, L., Visbeck, M., Brandt, P., Tanhua, T. and Wallace, D., 2009. Deoxygenation in the oxygen minimum zone of the eastern tropical North Atlantic. *Geophysical Research Letters*, 36: L20607.
- Stumm, W. and Morgan, J.J., 1995. *Aquatic Chemistry: Chemical Equilibria and Rates in Natural Waters*. John Wiley & Sons, New York, 1040 pp.
- Suess, E., 1981. Phosphate regeneration from sediments of the Peru continental margin by dissolution of fish debris. *Geochimica et Cosmochimica Acta*, 45(4): 577-588.
- Sunda, W.G. and Huntsman, S.A., 1988. Effect of Sunlight on Redox Cycles of Manganese in the Southwestern Sargasso Sea. *Deep-Sea Research Part a-Oceanographic Research Papers*, 35(8): 1297-1317.
- Sunda, W.G. and Huntsman, S.A., 1994. Photoreduction of Manganese Oxides in Seawater. *Marine Chemistry*, 46(1-2): 133-152.
- Sunda, W.G. and Huntsman, S.A., 1995. Iron uptake and growth limitation in oceanic and coastal phytoplankton. *Marine Chemistry*, 50(1-4): 189-206.
- Sundby, B. et al., 1986. The Effect of Oxygen on Release and Uptake of Cobalt, Manganese, Iron and Phosphate at the Sediment-Water Interface. *Geochimica Et Cosmochimica Acta*, 50(6): 1281-1288.
- Tagliabue, A., 2014. More to hydrothermal iron input than meets the eye. *Proceedings of the National Academy of Sciences of the United States of America*, 111(47): 16641-16642.
- Tagliabue, A., Aumont, O. and Bopp, L., 2014. The impact of different external sources of iron on the global carbon cycle. *Geophysical Research Letters*, 41(3): 920-926.
- Tagliabue, A. et al., 2010. Hydrothermal contribution to the oceanic dissolved iron inventory. *Nature Geoscience*, 3(4): 252-256.
- Tagliabue, A. et al., 2017. The integral role of iron in ocean biogeochemistry. *Nature*, 543(7643): 51-59.
- Tebo, B.M. et al., 2004. Biogenic manganese oxides: Properties and mechanisms of formation. *Annual Review of Earth and Planetary Sciences*, 32: 287-328.
- Tebo, B.M. and Emerson, S., 1986. Microbial Manganese(II) Oxidation in the Marine Environment - a Quantitative Study. *Biogeochemistry*, 2(2): 149-161.

References

- Thomas, P., Rahman, M.S., Picha, M.E. and Tan, W.X., 2015. Impaired gamete production and viability in Atlantic croaker collected throughout the 20,000 km² hypoxic region in the northern Gulf of Mexico. *Marine Pollution Bulletin*, 101(1): 182-192.
- Tomczak, M., 1981. An analysis of mixing in the frontal zone of South and North Atlantic Central Water off North-West Africa. *Progress in Oceanography*, 10(3): 173-192.
- Turner, D.R., Whitfield, M. and Dickson, A.G., 1981. The equilibrium speciation of dissolved components in freshwater and sea water at 25°C and 1 atm pressure. *Geochimica et Cosmochimica Acta*, 45(6): 855-881.
- Twining, B.S., Rauschenberg, S., Morton, P.L. and Vogt, S., 2015. Metal contents of phytoplankton and labile particulate material in the North Atlantic Ocean. *Progress in Oceanography*, 137: 261-283.
- Ussher, S.J. et al., 2013. Impact of atmospheric deposition on the contrasting iron biogeochemistry of the North and South Atlantic Ocean. *Global Biogeochemical Cycles*, 27(4): 1096-1107.
- Van Mooy, B.A.S., Keil, R.G. and Devol, A.H., 2002. Impact of suboxia on sinking particulate organic carbon: Enhanced carbon flux and preferential degradation of amino acids via denitrification. *Geochimica et Cosmochimica Acta*, 66(3): 457-465.
- Vedamati, J., Goepfert, T. and Moffett, J.W., 2014. Iron speciation in the eastern tropical South Pacific oxygen minimum zone off Peru. *Limnology and Oceanography*, 59(6): 1945-1957.
- Vega, M. and van den Berg, C.M.G., 1997. Determination of cobalt in seawater by catalytic adsorptive cathodic stripping voltammetry. *Analytical Chemistry*, 69(5): 874-881.
- Veron, A., Patterson, C. and Flegal, A., 1994. Use of stable lead isotopes to characterize the sources of anthropogenic lead in North Atlantic surface waters. *Geochimica et Cosmochimica Acta*, 58(15): 3199-3206.
- Voelker, B.M. and Sedlak, D.L., 1995. Iron Reduction by Photoproduced Superoxide in Seawater. *Marine Chemistry*, 50(1-4): 93-102.
- von Langen, P.J., Johnson, K.S., Coale, K.H. and Elrod, V.A., 1997. Oxidation kinetics of manganese (II) in seawater at nanomolar concentrations. *Geochimica et Cosmochimica Acta*, 61(23): 4945-4954.

References

- Waeles, M., Baker, A.R., Jickells, T. and Hoogewerff, J., 2007. Global dust teleconnections: aerosol iron solubility and stable isotope composition. *Environmental Chemistry*, 4(4): 233-237.
- Walsh, J.J., 1981. A carbon budget for overfishing off Peru. *Nature*, 290: 300-304.
- Ward, B.A., Dutkiewicz, S., Moore, C.M. and Follows, M.J., 2013. Iron, phosphorus, and nitrogen supply ratios define the biogeography of nitrogen fixation. *Limnology and Oceanography*, 58(6): 2059-2075.
- Watson, A.J., Bakker, D.C.E., Ridgwell, A.J., Boyd, P.W. and Law, C.S., 2000. Effect of iron supply on Southern Ocean CO₂ uptake and implications for glacial atmospheric CO₂. *Nature*, 407(6805): 730-733.
- Weber, T. and Deutsch, C., 2014. Local versus basin-scale limitation of marine nitrogen fixation. *Proceedings of the National Academy of Sciences of the United States of America*, 111(24): 8741-8746.
- Wedepohl, K.H., 1995. The composition of the continental crust. *Geochimica Et Cosmochimica Acta*, 59(7): 1217-1232.
- Weiss, R.F., 1970. The solubility of nitrogen, oxygen and argon in water and seawater. *Deep Sea Research and Oceanographic Abstracts*, 17(4): 721-735.
- Williams, R.G. and Follows, M.J., 2011. *Ocean dynamics and the carbon cycle: Principles and mechanisms*. Cambridge University Press.
- Windom, H.L., Moore, W.S., Niencheski, L.F.H. and Jahnke, R.A., 2006. Submarine groundwater discharge: A large, previously unrecognized source of dissolved iron to the South Atlantic Ocean. *Marine Chemistry*, 102(3): 252-266.
- Winkler, L.W., 1988. Bestimmung des im Wasser gelösten Sauerstoffs. *Ber. Dtsch. Chem. Ges.*, 21: 2843-2855.
- Wong, G.T.F. and Brewer, P.G., 1977. Marine Chemistry of Iodine in Anoxic Basins. *Geochimica Et Cosmochimica Acta*, 41(1): 151-159.
- Wright, J.J., Konwar, K.M. and Hallam, S.J., 2012. Microbial ecology of expanding oxygen minimum zones. *Nature Reviews Microbiology*, 10: 381-394.
- Wu, J.F., 2007. Determination of picomolar iron in seawater by double Mg(OH)₂ precipitation isotope dilution high-resolution ICPMS. *Marine Chemistry*, 103(3-4): 370-381.
- Wu, J.F. and Boyle, E.A., 1997. Low blank preconcentration technique for the determination of lead, copper, and cadmium in small-volume seawater samples by isotope dilution ICPMS. *Analytical Chemistry*, 69(13): 2464-2470.

References

- Wu, J.F. and Luther, G.W., 1994. Size-Fractionated Iron Concentrations in the Water Column of the Western North-Atlantic Ocean. *Limnology and Oceanography*, 39(5): 1119-1129.
- Wyrтки, K., 1962. The Oxygen Minima in Relation to Ocean Circulation. *Deep-Sea Research*, 9(1): 11-23.
- Xie, R.F.C. et al., 2015. The cadmium-phosphate relationship in the western South Atlantic - The importance of mode and intermediate waters on the global systematics. *Marine Chemistry*, 177: 110-123.
- Yuan, J. and Shiller, A.M., 1999. Determination of Subnanomolar Levels of Hydrogen Peroxide in Seawater by Reagent-Injection Chemiluminescence Detection. *Analytical Chemistry*, 71(10): 1975-1980.
- Zenk, W., Klein, B. and Schroder, M., 1991. Cape-Verde Frontal Zone. *Deep-Sea Research Part a-Oceanographic Research Papers*, 38: S505-S530.
- Zhu, Q.Z., Aller, R.C. and Kaushik, A., 2011. Analysis of vitamin B12 in seawater and marine sediment porewater using ELISA. *Limnology and Oceanography-Methods*, 9: 515-523.

Appendix

Appendix

Table A1: Pearson correlations of all data below 50 m water depth for the same parameters as used for the principle component analysis.

	dFe	dMn	dCo	dNi	dCd	dPb	oxy	I ⁻	depth	turb	PO ₄	NO ₃	AOU	dCu	Si(OH) ₄	temp	sal
dFe	1																
dMn	0.57	1															
dCo	0.60	0.65	1														
dNi	-0.08	-0.62	-0.10	1													
dCd	-0.13	-0.64	-0.06	0.96	1												
dPb	0.09	-0.34	0.01	0.78	0.69	1											
oxy	-0.55	-0.61	-0.58	0.43	0.36	0.42	1										
I ⁻	0.43	0.78	0.40	-0.67	-0.65	-0.42	-0.52	1									
depth	-0.11	-0.58	-0.11	0.97	0.95	0.79	0.45	-0.61	1								
turb	0.76	0.56	0.41	-0.32	-0.36	-0.27	-0.64	0.53	-0.35	1							
PO ₄	0.23	-0.37	0.15	0.85	0.84	0.68	-0.12	-0.49	0.84	0.00	1						
NO ₃	-0.03	-0.65	-0.09	0.92	0.93	0.63	0.11	-0.68	0.89	-0.22	0.89	1					
AOU	0.29	-0.29	0.30	0.62	0.67	0.39	-0.22	-0.22	0.58	0.08	0.76	0.74	1				
dCu	0.29	-0.02	0.36	0.59	0.51	0.74	0.12	-0.16	0.55	-0.10	0.57	0.44	0.42	1			
Si(OH) ₄	0.17	-0.41	0.11	0.93	0.90	0.77	0.08	-0.50	0.95	-0.09	0.94	0.88	0.71	0.65	1		
temp	0.15	0.70	0.20	-0.97	-0.97	-0.73	-0.45	0.71	-0.96	0.37	-0.85	-0.95	-0.61	-0.50	-0.90	1	
sal	0.06	0.68	0.21	-0.93	-0.92	-0.74	-0.48	0.64	-0.93	0.25	-0.79	-0.89	-0.55	-0.45	-0.86	0.96	1

Appendix

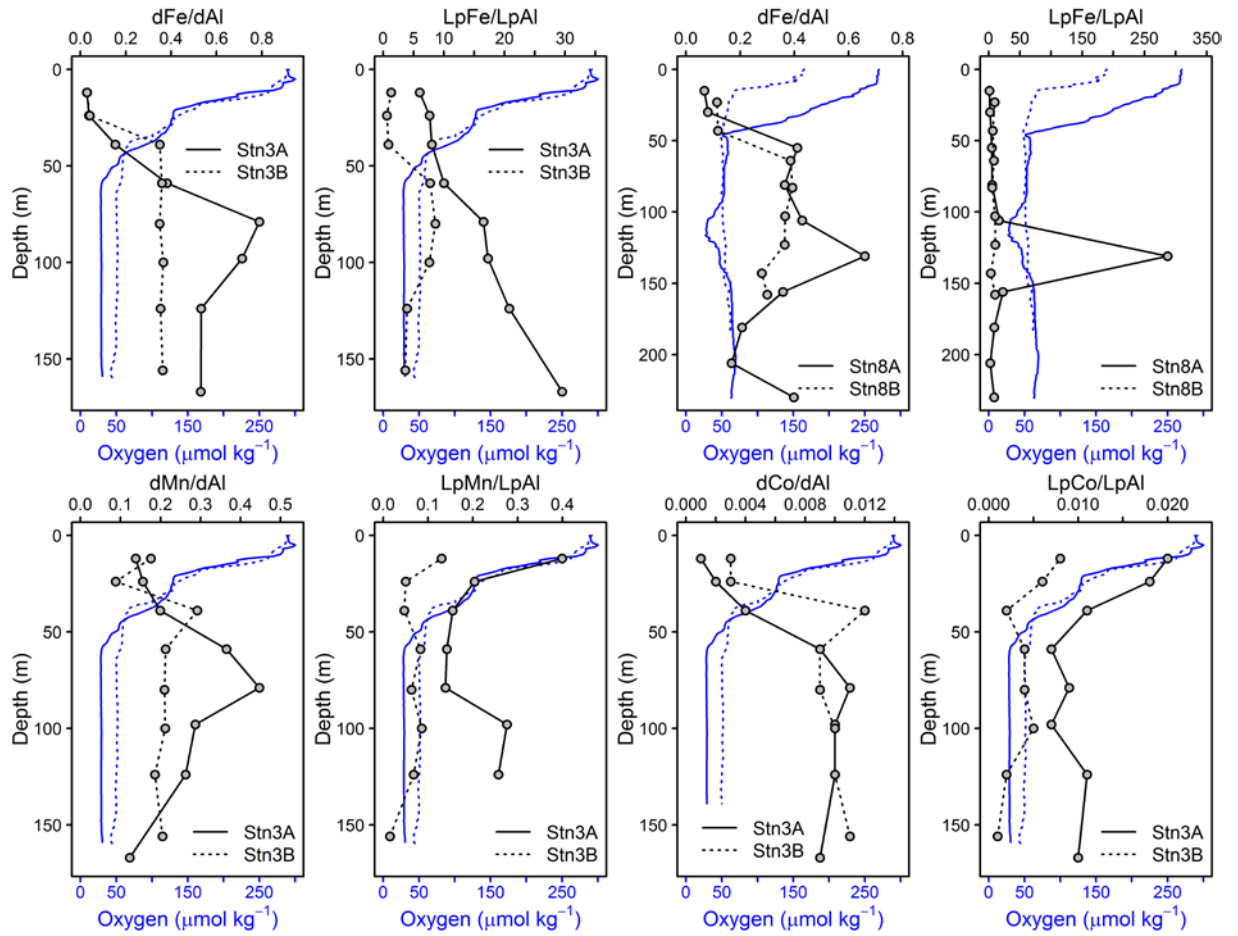


Figure A1: Dissolved and leachable particulate Fe to Al ratios for repeated profiles at Station 3 (A+B) and Station 8 (A+B) and dissolved and leachable particulate Co and Mn to Al ratios for repeated profiles at Station 3 (A+B).

Statement of declaration

I hereby declare that I have produced the PhD thesis at hand with the title

*"Trace metal sources and cycling in tropical
oxygen minimum zones"*

independently and without improper external assistance and that I have listed all relevant sources. Moreover, I assure that the PhD thesis has been written under compliance of the rules for good scientific practice of the German Research association and that the PhD thesis has not been submitted before to an examination procedure. Published or submitted for publication manuscripts are identified at the relevant places.

Insa Rapp

Kiel, 29.05.2018

Curriculum Vitae

Personal Information

Date of birth: 16.07.1987
Place of birth: Duisburg, Germany
Nationality: German

Education

03/2014–05/2018 PhD candidate

Chemical Oceanography Department
GEOMAR Helmholtz Centre for Ocean Research, Kiel
Collaborative Research Centre 754

10/2011–10/2013 MSc in Water Science

University Duisburg-Essen
Areas of study: Environmental Chemistry, Analytics,
Geomicrobiology

05/2013–10/2013 Master Thesis Project

UFZ Helmholtz Centre for Environmental Research, Leipzig
Department of Isotope Biogeochemistry
Title: “Effect of cell membranes on the carbon isotope fractionation
during reductive dehalogenation of chlorinated ethenes”

10/2008–09/2011 BSc in Water Science

University Duisburg-Essen
Areas of study: Chemistry, Analytics, Microbiology

06/2011–09/2011 Bachelor Thesis Project

University of New South Wales, Sydney, Australia
School of Biotechnology and Biomolecular Sciences
Title: “Targeted isolation of TM7 bacteria from the environment”

Research Cruises

RV Sonne – SO243 Equatorial Pacific, Oct 2015
RV New Horizon – NH1417 North Pacific Aug – Sep 2014

Conferences and Summer schools

GEOTRACES summer school (Plouzané, France) 2017

Goldschmidt 2017, Paris: ‘Iron biogeochemistry in the Peruvian oxygen minimum zone during the 2015/16 El Niño’ (Oral)

Challenger Society Conference 2016, Liverpool: ‘Controls of redox-sensitive trace metals in two dynamic oxygen minimum zones’ (Oral)

Ocean Sciences Meeting 2016, New Orleans: ‘Distribution of soluble, colloidal and leachable particulate trace metals in dynamic and oxygen depleted Mauritanian shelf waters’ (Poster)

Royal Society Meeting 2016 – Ocean ventilation and deoxygenation in a warming world, London: ‘Regulation of redox-sensitive trace metals in the dynamic oxygen minimum zone off Mauritania’ (Poster)

Publication list

1. **Rapp I.**, Schlosser C., Rusiecka D., Gledhill M. and Achterberg E.P., ‘Automated preconcentration of Fe, Zn, Cu, Ni, Cd, Pb, Co, and Mn in seawater with analysis using high-resolution sector field inductively-coupled plasma mass spectrometry’, *Analytica Chimica Acta*, 2017, 976: 1–13.
2. Browning T.J., Achterberg E.P., **Rapp I.**, Engel A., Bertrand E.M., Tagliabue A., and Moore C. M., ‘Nutrient co-limitation at the boundary of an oceanic gyre’, *Nature*, 2017, 551: 242–246.
3. Browning T.J., Achterberg E.P., Yong J.C., **Rapp I.**, Utermann C., Engel A., and Moore C.M., ‘Iron limitation of microbial phosphorus acquisition in the tropical North Atlantic’, *Nature Communications*, 2017, 8: 15465.
4. Hopwood M.J., **Rapp I.**, Schlosser C., and Achterberg E.P., ‘Hydrogen peroxide in deep waters from the Mediterranean Sea, South Atlantic and South Pacific Oceans’, *Scientific Reports*, 2017: 43436.
5. Shilova I.N., Mills M.M., Robidart J.C., Turk-Kubo K.A., Björkman K.M., Kolber Z., **Rapp I.**, van Dijken G.L., Church M.J., Arrigo K.R., Achterberg E.P., and Zehr J.P., ‘Differential effects of nitrate, ammonium, and urea as N sources for microbial communities in the North Pacific Ocean’, *Limnology & Oceanography*, 2017, 62 (6): 2550–2574.
6. Renpenning J., **Rapp I.**, and Nijenhuis I., ‘Substrate Hydrophobicity and Cell Composition Influence the Extent of Rate Limitation and Masking of Isotope Fractionation during Microbial Reductive Dehalogenation of Chlorinated Ethenes’, *Environmental Science & Technology*, 2015, 49 (7): 4293–4301.

7. Lutze H.V., Bircher S., **Rapp I.**, Kerlin N., Bakkour R., Geisler M., von Sonntag C., and Schmidt T.C., 'Degradation of Chlorotriazine Pesticides by Sulfate Radicals and the Influence of Organic Matter', *Environmental Science & Technology*, 2015, 49 (3): 1673–1680.
8. **Rapp I.**, Schlosser C., Browning T.J., Wolf F., Le Moigne F.A.C., Gledhill M., Achterberg E.P., 'El Niño reduces Peruvian shelf trace metal supply to the ocean', *submitted to Nature Geoscience*
9. Browning T.J., **Rapp I.**, Schlosser C., Gledhill M., Achterberg E.P., Bracher A., Le Moigne F.A.C., 'Influence of iron, cobalt, and vitamin B₁₂ supply on phytoplankton growth in the tropical East Pacific during the 2015 El Niño', *in review for Geophysical Research Letters*
10. **Rapp I.**, Schlosser C., Menzel Barraqueta J.-L., Wenzel B., Lüdke J., Scholten J., Gasser B., Reichert P., Gledhill M., Dengler M., Achterberg E.P., 'Controls on redox-sensitive trace metals in the Mauritanian oxygen minimum zone', *in prep.*